Nucleosynthesis in extremely metal-poor and zero metallicity stars

Monique Alves Cruz

Nucleosynthesis in extremely metal-poor and zero metallicity stars

Monique Alves Cruz

Dissertation der Fakultät für Physik
Dissertation of the Faculty of Physics

der Ludwig-Maximilians-Universität München
at the Ludwig Maximilian University of Munich

für den Grad des
for the degree of

Doctor rerum naturalium

vorgelegt von Monique Alves Cruz
presented by

aus Itamaraju, Brasilien (Brazil)
from

Munich, 2012

1^{st} Evaluator: Prof. Dr. Achim Weiss
2^{nd} Evaluator: Prof. Dr. Joseph Mohr
Date of the oral exam: 20.12.2012

Zusammenfassung

Die wachsende Zahl an Beobachtungen metallarmer Sterne (engl. “metal-poor”, MP) hat eine Vielzahl von Fragen zur Elemententstehung in der Frühzeit unserer Galaxie aufgeworfen. In dieser Arbeit untersuchen wir die Entwicklung und die Nukleosynthese von extrem metallarmen und metallfreien Sternen. Für die Metallhäufigkeit von Interesse in dieser Arbeit ($0 \leq Z \leq 10^{-5}$) gibt es drei große Modelsätze in der Literatur (Campbell 2007; Lau et al. 2009; Suda & Fujimoto 2010). Trotzdem gibt nur eine Quelle Häufigkeiten für Elemente schwerer als Sauerstoff an. Unsere Modelle untersuchen nicht nur die leichten Elemente sondern auch die Nukleosynthese schwerer Elemente während der sogenannten “proton ingestion episode” (PIE) und die Unsicherheiten die sich für die nukleosynthetischen Vorhersagen ergeben.

Wir finden, dass der s-Prozess während der PIE sowohl in metallarmen als auch in Sternen mittlerer Metallhäufigkeit stattfindet. In massearmen Sternen geschieht die PIE während des Helium-Blitzes im Sternkern und hat großen Einfluß auf die s-Prozess Ausbeute falls Saatkerne aus dem Häufigkeitsmaximum um Eisen im Stern vorhanden sind. Mittelschwere Sterne dagegen durchleben die PIE während der TP-AGB Phase. Wir finden, dass die s-Prozess Ausbeute während der PIE in diesen Sternen sehr stark abhängig von der Dauer der PIE ist. Außerdem wird der Großteil der s-Prozess Häufigkeit in demjenigen und dem darauf folgendem TP produziert, in dem die PIE stattfindet. Wir vergleichen unsere Produktion leichter Elemente mit denen aus Campbell 2007 und finden eine erhebliche Abweichung. Die Unterschiede können hauptsächlich auf das (nicht-) Vorhandensein von “hot bottom burning” während der AGB Phase zurückgeführt werden.

Obwohl unsere Vorhersagen zum Auftreten von s-Prozess Elemententstehung während der PIE von massearmen Sternen qualitativ mit denen von Campbell et al. 2010 übereinstimmen, findet in unseren Modelle sehr viel weniger s-Prozess statt. Wir vergleichen diese Vorhersagen mit den zwei metallärmsten Sternen die bisher beobachtet wurden. Dazu nehmen wir an, dass Masse zum beobachteten Stern übertragen wurde und sich dann in dessen Sternhülle verteilt hat. Wir finden, dass massearme EMP Sterne mögliche Kandidaten für einen Begleitstern von HE0107-5240 sind. Trotzdem sind unsere Vorhersagen nicht in der Lage, die Häufigkeitsverteilung von HE1327-2326 zu erklären, im Gegensatz zun den Ergebnissen in Campbell et al. 2010.

Schließlich nutzen wir ein erweitertes Netzwerk in GARSTEC um uns mit den anomalen Häufigkeiten von Sternhaufen zu befassen. Wir fanden, dass “overshooting” eine maßgebliche Rolle für die endgültigen Häufigkeiten von O, Na, Mg und Al spielt. Wenn overshooting nicht in den Rechnung miteinbezogen wird, kann eine sehr viel bessere Übereinstimmung mit den Beobachtungen erhalten werden.

Abstract

The increasing number of metal-poor (MP) stars observed to date has raised numerous questions concerning the elemental production in the early stages of our Galaxy. In this thesis we study the evolution and nucleosynthesis of zero metallicity and extremely metal-poor stars. For the metallicity range covered in this thesis ($0 \leq Z \leq 10^{-5}$) there are three large grids of models in the literature (Campbell 2007; Lau et al. 2009; Suda & Fujimoto 2010). Nevertheless, only one study presents abundances for elements heavier than oxygen. Our models explore not only the light elements, but also the nucleosynthesis of heavy elements during the proton ingestion episode and the uncertainties affecting the nucleosynthesis predictions.

We have found that s-process does occur during the proton ingestion episode (PIE) in both low- and intermediate-mass stars. In low-mass stars, the PIE happens during the core He-flash and has a strong impact in the production of s-process if iron-peak seeds are available in the star. Intermediate-mass stars, on the other hand, undergo PIE during the TP-AGB phase. We have found that the s-process production during the PIE in these stars is strongly dependent on the duration of the ingestion. Moreover, the bulk of the surface s-process abundance is produced in the TP, in which PIE occurs, and in the subsequent TP. We have compared the yields of our light elements with those reported by Campbell 2007. We have found considerable discrepancies between the yields. This discrepancies can be mainly ascribed to the occurrence (or not) of hot bottom burning during the AGB.

Although our predictions qualitatively agree with those by Campbell et al. 2010 on the occurrence of s-process production during the PIE of low-mass stars, our models produce far less s-process than theirs. We compared these predictions to the two most iron-poor stars observed to date. We assumed that mass was tranferred to the observed star and it was then diluted in the stellar envelope. We have found that low-mass EMP stars are possible candidates as the companion of HE0107-5240. Nevertheless, our predictions are not able to explain the abundance patterns in HE1327-2326 in contrast to Campbell et al. 2010 results.

Finally, we have also employed the new extended network in GARSTEC to address the globular cluster anomalies issue. We have found that overshooting plays an important role in the final yields of O, Na, Mg, and Al. If overshooting is not included in the calculations a much better agreement with the observations can be obtained.

Contents

List of Figures

List of Tables

Chapter 1

Introduction

Stars are responsible for the production of all elements heavier than helium in the Universe. In astronomy, these elements are referred to as metals. The metallicity of a star is a measure of the amount of metals present in the star. The two definitions of metallicity commonly used are Z and [Fe/H]. Z is the total mass fraction of elements heavier than helium and [Fe/H][1] is the amount of iron with respect to hydrogen relative to the same quantity in the Sun. In the Big Bang only hydrogen, helium and traces of lithium and beryllium were produced. Hence, the metallicity of a star is an indicator of the degree of pollution its gas has been subjected to since the Big Bang. The primordial stars (also known as Population III stars) are the first stars formed in the Universe and have no metals (Z=0).

Stars that have less than 1/10th of the iron content observed in the Sun ([Fe/H] < -1, Beers & Christlieb 2005) are classified as metal-poor stars (hereafter, MP stars) and were vastly studied over the past decades. The search for MP stars in the Galactic halo has started in the seventies with (Bond 1970, 1980, 1981) and Bidelman & MacConnell (1973) spectroscopy surveys. However, it was in the nineties that deeper surveys, such as the HK (Beers et al. 1985, 1992, 1999) and the Hamburg/ESO (HES) Christlieb et al. (2001) surveys, have played an important role in the identification of numerous low metallicity stars.

Metal-poor candidates were selected using the line strength of the calcium II lines H and K, since iron lines cannot be observed in medium resolution spectrum. Figure 1.1 shows the decrease in the strength of the calcium II lines with decreasing metallicity for three stars in similar evolutionary stages. Using this method, the HK and HES surveys provided hundreds of MP candidates that were later confirmed to have low metallicity, including the two most iron-poor stars observed HE0107-5240 (Christlieb et al. 2004) and HE1327-2326 (Frebel et al. 2008) with metallicities [Fe/H]=-5.39 and [Fe/H]=-5.96, respectively.

A nomenclature used to describe differing levels of metal deficiency was proposed by Beers & Christlieb (2005) in order to avoid confusion among studies (See Table 1.1) and will be used throughout this thesis.

The metallicity of a star is an indicator of the degree of pollution of the interstellar medium (ISM) at the time of birth of the star. This implies that the atmospheres of low metallicity

[1] $[A/B] = \log_{10}(N_A/N_B)_* - \log_{10}(N_A/N_B)_\odot$, where N_A and N_B refer to the numbers of atoms of elements *A* and *B*, respectively. Iron was chosen as an indicator of metallicity due to the large amount of absorption lines found in the solar spectrum.

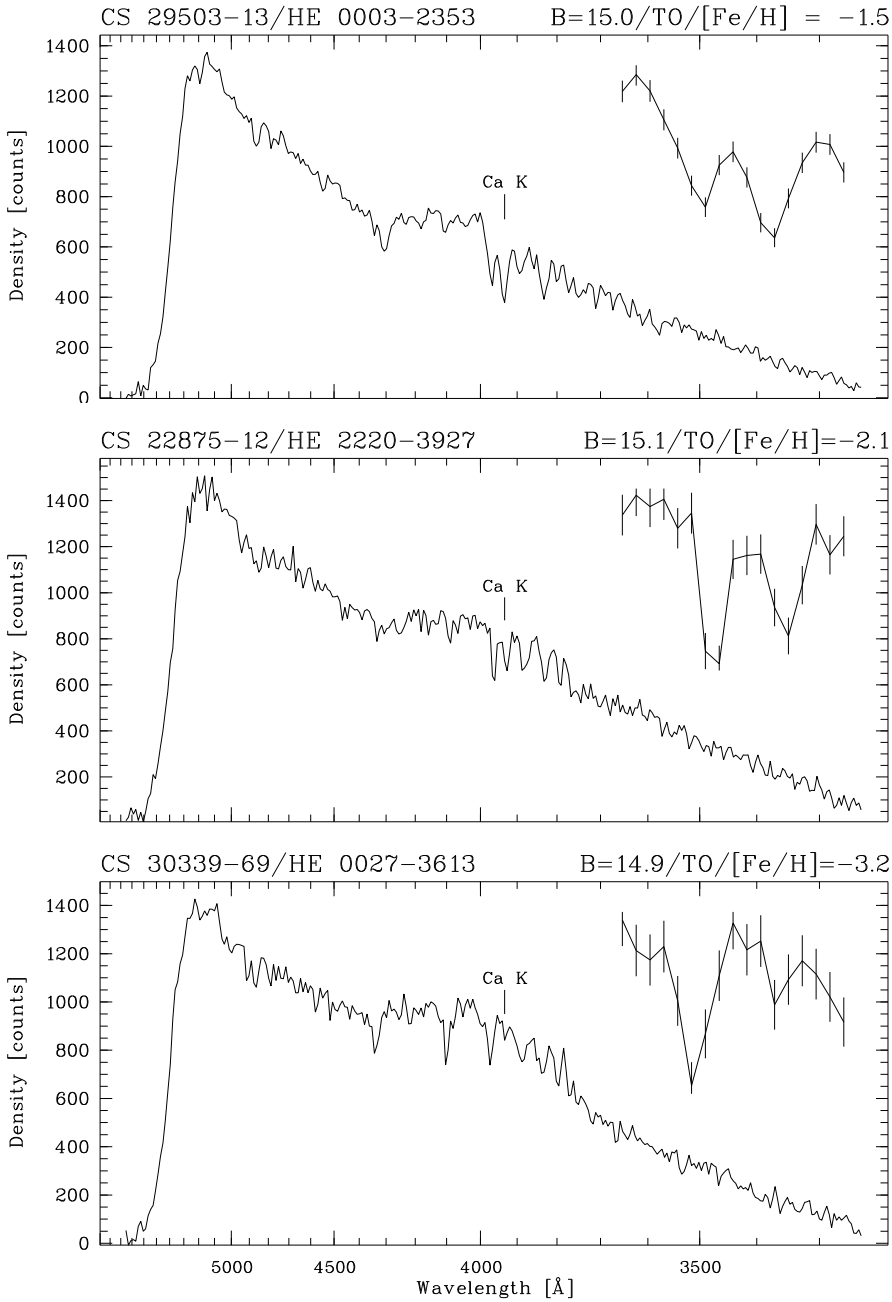

Figure 1.1: HES spectra of metal-poor stars found in the HK survey for different metallicities. Note that wavelength is *de*creasing from left to right and the variation in the line strength of the calcium lines with metallicity. Figure taken from Christlieb (2003). The labels in the upper part of each plot indicate: The name of the star using the nomenclature of the HK/HES surveys. B is the magnitude in the Johnson's filter. TO indicates the evolutionary stage of the star, in this case Turnoff. [Fe/H] is the metallicity of the star.

stars reflect the nucleosynthesis products of fewer stellar generations than the atmospheres of those stars more metal-rich. Extremely metal-poor stars, hereafter EMP stars, have less than

Term	Acronym	[Fe/H]
Super metal-rich	SMR	$> +0.5$
Solar	—	~ 0.0
Metal-poor	MP	< -1.0
Very metal-poor	VMP	< -2.0
Extremely metal-poor	EMP	< -3.0
Ultra metal-poor	UMP	< -4.0
Hyper metal-poor	HMP	< -5.0
Mega metal-poor	MMP	< -6.0

Table 1.1: Nomenclature for star of different metallicities from Beers & Christlieb (2005)

1/1000th of the iron content of the sun (Table 1.1) and are an important key to understand the chemical evolution of the Milky Way during its early stages. Their abundance patterns might shed light on individual nucleosynthesis processes, contrary to those more metal-rich stars, which reflect the well-mixed products of several nucleosynthesis processes in multiple generations of stars.

Several attempts have been made in order to explain the peculiarities of EMP abundance patterns; their origin, nevertheless, is still an unsolved puzzle. One of the first scenarios proposed to explain the overabundance of carbon and nitrogen in EMP stars involved the ingestion of protons into the helium convective zone (proton ingestion episode-PIE) that happens during the core He-flash in Pop. III and EMP stars (Fujimoto et al. 1990; Schlattl et al. 2001; Weiss et al. 2004; Picardi et al. 2004). The proton ingestion into the helium-rich convective layers during the core He-flash is a robust phenomenon in one dimensional stellar evolution calculations of low metallicity stars ([Fe/H] < -4.5) that subsequently leads to a large surface enrichment in CNO-elements (Hollowell et al. 1990; Schlattl et al. 2001; Campbell & Lattanzio 2008). However, the amount of C, N, and O dredged-up to the surface in the models is 1 to 3 dex larger than the observed [C/Fe], disfavoring the self-enrichment scenario. Besides, most EMP stars observed are not evolved past the helium-core flash to have undergone PIE.

1.1 CEMP stars

One import characteristic of EMP stars is the larger fraction of carbon-enhanced stars compared with those more metal-rich. While solar metallicity stars enriched in carbon represent $\sim 1\%$ of the total number of stars (Tomkin et al. 1989; Luck & Bond 1991), 20-30% of the stars with metallicity [Fe/H] < -2.5 are carbon enhanced (Rossi et al. 1999; Suda et al. 2011). There is no agreement between studies in the quantitative definition of CEMP stars, however, the difference in the definition is not sufficient to disprove the larger fraction of carbon enrichment among EMP stars. This finding was originally observed in medium resolution spectroscopy studies, which prompted numerous high resolution spectroscopy follow-up observations of carbon enhanced EMP stars in order to obtain detailed abundance patterns.

Carbon-enhanced metal-poor stars, known as CEMP stars, belong to a more complex class than initially thought. These stars present a wide variety of patterns in terms of neutron capture elements, with stars showing no signatures of these elements to others having large

enhancement in s-process or r-process[1] elements, or in both. Table 1.2 shows the CEMP stars subclasses (Beers & Christlieb 2005). Ba and Eu are mainly formed by s- and r-process, respectively. For this reason, they are used as tracers of each process and were chosen to categorize the CEMP subclasses. Figure 1.2 shows the Ba and Eu abundances for the CEMP stars observed in high resolution. The abundances were taken from the SAGA database (Suda et al. 2008). As it can be seen, the Ba/Fe and Eu/Fe abundance ratios can be up to three orders of magnitude larger than the ratios observed in the Sun. The stars enriched only in s-process elements tend to have lower [Ba/Fe] abundances than stars enriched in both neutron capture processes.

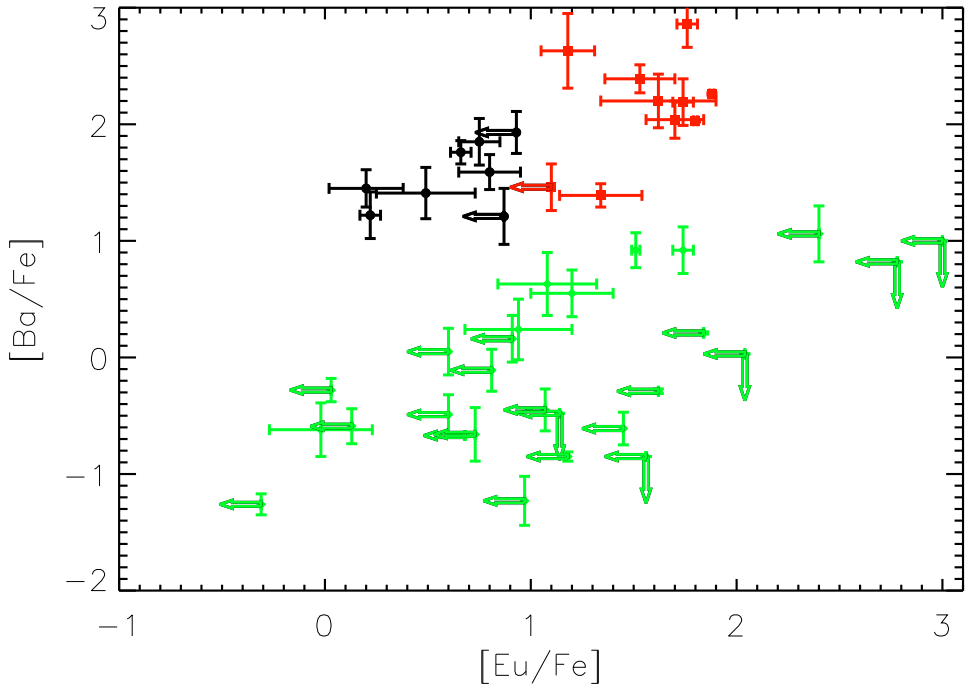

Figure 1.2: Overview of the observational data for CEMP stars. Black symbols represent the CEMP-s stars, green symbols represent the CEMP-rs stars, and red symbols represent the CEMP-r stars according to the classification of Masseron et al. (2010). Data points were taken from the SAGA database.

The majority of CEMP stars are enhanced in s-process elements ($\sim$ 80% - Aoki et al. 2008), being approximately equally distributed between CEMP-s and CEMP-rs stars. The positive correlation between carbon and s-process elements suggests that they might have the same production site (Aoki et al. 2002; Suda et al. 2004, 2011). Figure 1 from Masseron et al. 2010 shows that CEMP-s stars exhibit [Ba/Fe] and [Eu/Fe] ratios identical to classical Ba stars. Qualitatively the origin of carbon and s-process elements in CEMP-s stars can be explained by mass transfer from a AGB (Asymptotic Giant Branch) companion (now a white dwarf).

[1]Elements heavier than iron are formed by neutron capture into iron-seeds elemends. The neutron capture processes are divided into two: s(*low*)-process and r(*apid*)-process.

Subclass	
CEMP-r	$[Eu/Fe] > 1.0$
CEMP-s	$[Ba/Eu] > 0.5$ & $[Ba/Fe] > 1.0$
CEMP-rs	$0.0 < [Ba/Eu] < 0.5$
CEMP-no	$[Ba/Fe] < 0.0$

Table 1.2: Classification of CEMP stars as proposed by Beers & Christlieb (2005). The definition of a CEMP star is the star with [C/Fe] > 1.0. The CEMP definition varies between different studies: [C/Fe] > 0.9 according to Masseron et al. 2010, [C/Fe] > 0.7 according to Suda et al. 2011. The letter *s stands for s-process elements, and the letter r stands for r-process elements.*

Mass would be transferred via stellar winds or via Lobe-Roche overflow and products of AGB nucleosynthesis would be dumped onto the convective envelope of the observed star (Figure 1.3). Radial velocity monitoring has shown that a large fraction of CEMP-s stars exhibits radial velocity variations, strengthening the argument of a binary scenario for the formation of CEMP-s stars (Lucatello et al. 2005).

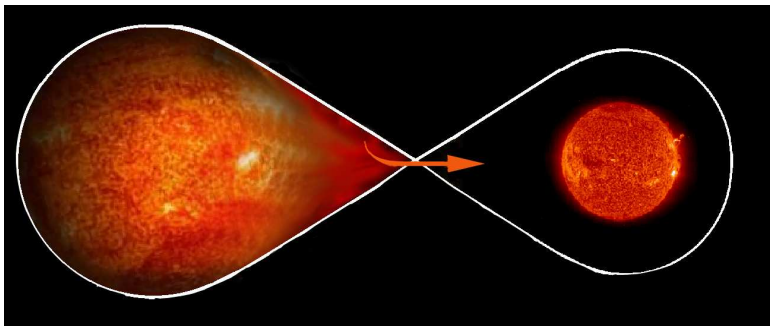

Figure 1.3: Mass Transfer in a binary system via Roche Lobe overflow. Adapted using the image of the Sun by NASA.

Quantitative results for s-process nucleosynthesis were presented by Bisterzo et al. 2010. They have performed s-process calculations based on AGB models with masses M $= 1.3 - 2.0$M$_\odot$ and metallicities $-3.6 \leq$ [Fe/H] ≤ -1.0. In these models, neutrons are burnt radiatively inside the ^{13}C pocket. The ^{13}C pocket was formulated as a region where the abundance of the main neutron source (^{13}C) is larger than the abundance of the main neutron poison (^{14}N). This region might form if protons from the bottom of the convective envelope penetrate the He intershell after the third dredge-up and are captured by the abundant ^{12}C (Gallino et al. 1998). The physical mechanism reponsible for the formation of the ^{13}C pocket is not yet established. For this reason, its efficiency is a free parameter in the models. Using different efficiencies of the ^{13}C pocket Bisterzo et al. 2011 are able to reproduce the general trend for the s-process abundance patterns of CEMP stars.

Lugaro et al. (2012) presented models for the s-process in AGB stars of masses M $= 0.9-$ 6.0M$_\odot$ and metallicity [Fe/H] $= -2.3$. In these models ^{13}C is mainly burnt in radiative conditions during the interpulse periods. Some models present mild proton ingestion, leading ^{13}C to burn in convective conditions during the thermal pulse. The inclusion of the ^{13}C pocket was done by forcing the code to mix a small amount of proton from the envelope into

the intershell. The proton abundance decreases from 0.7 in the envelope to 10^{-4} at a given point in mass located bellow the bottom of the envelope. The free parameter in the models is the mass between the bottom of the envelope and the point where the proton abundance is 10^{-4}. Models with masses $M \sim 2M_{\odot}$, where ^{13}C burns radiatively, produce a good match to the CEMP-s stars.

Suda et al. (2004) argued that the most likely production site for carbon and s-process elements is the PIE during the AGB phase of stars with mass $1.2M_{\odot} < M \leq 3.0M_{\odot}$ and metallicities $[Fe/H] \leq -2.5$. At the beginning of the AGB evolution, protons are dredged-down into the helium convective zone due to the low entropy barrier between the H- and He-rich layers. Neutrons are produced in a convective environment via $^{13}C(\alpha, n)^{16}O$. The high neutron densities achieved during the PIE ($N_n > 10^{13} cm^{-3}$) can lead to a large production of s-process elements. This phenomenon, that only happens in an extremely low metallicity environment in the 1D stellar evolution models, was not taken into account in Bisterzo et al. (2010) simulations. For metallicities $[Fe/H] < -2.5$ they used an extrapolated stellar structure from more metal-rich models. Therefore, more realistic models, taking PIE into account, for the nucleosynthesis during the AGB evolution of EMP stars are still missing in the literature.

1.2 The most iron-poor stars

The two hyper metal-poor stars (see Table 1.1) discovered to date (HE0107-5240 and HE1327-2326) have been subject of extensive theoretical and observational studies. Both stars are strongly enhanced in carbon, nitrogen and oxygen, despite their extremely low iron content. The exact CEMP class they belong to, however, is not yet determined since there are only upper limits values for the Ba and Eu abundances (Table 1.3).

Element	HE0107-5240	HE1327-2326
[Fe/H]	−5.39	−5.96
[C/Fe]	3.70	3.78
[N/Fe]	2.28	4.28
[O/Fe]	2.30	3.42
[Na/Fe]	0.81	2.73
[Mg/Fe]	0.15	1.97
[Al/Fe]	< −0.26	1.46
[Ti/Fe]	-0.36	0.91
[Sr/Fe]	< −0.52	1.17
[Ba/Fe]	< 0.82	< 1.40
[Eu/Fe]	< 2.78	< 4.64

Table 1.3: Relative abundances of HE0107-5240 (Bessell et al. 2004; Christlieb et al. 2004) and HE1327-2326 (Frebel et al. 2008).

The first question that rises from the observations is whether the carbon, nitrogen, and oxygen enhancements are the result of external pollution or internal processes. HE1327-2326 is an unevolved star, which exclude the possibility for a self-pollution scenario since the bottom of the convective envelope only reaches the ashes of burning regions when the star becomes a

giant. On the other hand, HE0107-5240 is a giant star. Nevertheless, comparisons between its position in the (log g,log T_{eff}) plane and theoretical tracks, have shown that it is far from the tip of the red giant branch, where the proton ingestion occurrs, and thus could not have yet produced the CNO elements observed in its atmosphere (Picardi et al. 2004; Weiss et al. 2004).

Therefore, other interpretations for the abundance patterns of HMP stars remain: 1) They are second generation stars and their photosphere reflects only the nucleosynthetic yields of Pop. III supernovae; 2) they are primordial stars which accreted material after their birth from the primordial cloud or their abundance patterns are the result of mass-transfer from a companion; 3) they are primordial or second generation stars which acquired most of their metals from the Galactic ISM.

Iwamoto et al. (2005) presented Pop. III supernovae yields for stars with initial mass $M = 25M_{\odot}$. Their models can reproduce the overabundance of CNO elements in the HMP stars. Heger & Woosley (2010) also performed supernovae nucleosynthesis calculation of metal-free stars with initial masses in the range $10 - 100M_{\odot}$. The best fits to HE1327-2326 and HE0107-5240 abundances were obtained for low energy explosions models and stars in the mass range $10 - 30M_{\odot}$. These results reinforce prior suggestions that primordial stars were formed with smaller masses.

Suda et al. (2004) discussed the possibility that HE0107-5240 is a primordial star that was polluted by CNO and s-process elements via mass-transfer from an AGB companion. In their scenario, the atmosphere of the stars in the binary system would be polluted in iron-peak elements via accretion of gas from the polluted primordial cloud. CNO and s-process elements would be formed during the PIE occurring at the beginning of the TP-AGB in the primary star and later dumped onto HE0107-5240 atmosphere. They have shown that the binary scenario is a viable possibility if HE0107-5240 is either a first or a second generation star and its companion has an initial mass in the range $1.2 \leq M/M_{\odot} \leq 3.0$. They have found that C, N, O, Na, and Mg can be produced during the PIE and, if iron-peak elements are present in the convective zone, s-process elements might also be formed. In order to determine whether HE0107-5240 is a first or a second generation star accurate measurements of s-process elements are necessary. In addition, recent nucleosynthesis model by Campbell et al. (2010) have shown that s-process production might happen also during the core He-flash, contradicting Fujimoto et al. (2000) results, and thus, low-mass stars might also be responsible for the abundance pattern observed in the HMP stars.

1.3 Primordial Stars

The nature of the primordial stars has been subject of intensive debate. It was a general idea that the metal-free environment could form only isolated stars with extremely large masses (Abel et al. 2002; Bromm et al. 2002; Bromm & Loeb 2004; O'shea & Norman 2007; Yoshida et al. 2008), since the cooling efficiency would be small due to the absence of metals.

Star formation depends on the competition between gravity and outwards forces (pressure gradient, magnetic fields, and turbulance). The mass distribution of the stars formed, i.e. the initial mass function - IMF, is controlled by the heating and cooling processes in the gas. Metals are responsible for most of the cooling in the present-day molecular clouds, decreasing their temperature down to $T \sim 10$ K. Metal atoms, excited by collisions, return to a lower

energy state by emitting a photon which, in turn, can leave the region, cooling the cloud. Nevertheless, in primordial clouds where there are no metals, cooling is produced by H_2 molecules which reduces the cloud temperature to $T = 100 - 200$ K.

The minimum mass that a cloud of gas must have to collapse under its gravity is called the Jeans mass:

$$M_J = 45 M_\odot T^{3/2} n_H^{-1/2}, \tag{1.1}$$

where T is the temperature in kelvins and n_H is the hydrogen density given in cm^{-3}.

Based on the above equation, it can be seen that the primordial stars should be more massive than $M > 100 M_\odot$. Contrary, the observed Populations I and II stars have much lower masses $M < 1.0 M_\odot$. The transition between these two modes of star formation should be mainly controlled by the increasing metallicity which is an indicative that there should be a critical metallicity, Z_c below which only massive stars were formed. Bromm & Loeb (2003) argued that since the two main coolants in the cloud are oxygen and carbon, the two modes of star formation should be separated by the critical abundances of these two elements, instead of a critical total metallicity. They found that all low metallicity stars observed at the time had larger oxygen abundance than the critical oxygen value, although some stars presented subcritical carbon abundance. This subcritical carbon abundance could be formed post-birth during the RGB phase, therefore, it would not invalidate their argument. However, the recent discovery of an EMP star with metallicity [Fe/H] $= -4.89$ and no enhancement in CNO elements (Caffau et al. 2011, 2012), which results in the lowest total metallicity $Z \leq 10^{-4} Z_\odot$ observed in a star, puts into question the claims of a minimum metallicity required for the formation of low-mass stars.

One important mechanism to form low-mass stars is the fragmentation of large clouds into smaller collapsing clumps. Fragmentation occurs if the free-fall compressional heating rate is smaller than the radiative cooling rate. Old numerical simulations of metal-free star formation have found no fragmentation which led to the general idea that Pop. III stars were isolated systems. These simulations were limited to a narrow timespan and the possible formation and fragmentation of a circumstellar disc could not be followed. Recent simulations, employing sink particles to represent the growing protostars, found strong fragmentation in the protostellar disc due to a very efficient cooling by H_2 lines and collision-induced emission (Stacy et al. 2010, 2012; Greif et al. 2011). They have shown that Pop. III stars can be formed in multiple systems with a flat protostellar mass function ($M \sim 0.1 - 10 M_\odot$). The sink particle approach is subjected to a large inaccuracy. The mass function derived using this approach is quite uncertain. Nonetheless, the occurrence of fragmentation found in the simulations shows that low-mass metal-free stars could be formed.

1.4 Outline

We focused on the study of the nucleosynthesis of stars with metallcities [Fe/H] < -3.0. In all these stars proton ingestion takes place, either during the core He-flash or the TP-AGB phase. The goal of this thesis is to study the s-process production during the proton

ingestion and its contribution to the abundance patterns observed in EMP stars. We explore the uncertainties in modelling such phenomenon and the AGB phase.

The thesis is structured as follows: In Chapter 2 we give an overview of stellar evolution and nucleosynthesis. Also, we give a literature overview of the proton ingestion episode and its characteristics. In Chapter 3 we give a brief overview of the evolutionary code, the input physics used in the models, and the modifications performed to the code. In Chapter 4 we give an overview of the post-processing code created for the purpose of this thesis. In Chapter 5 we presented our low-mass stars models and their influence on the HMP stars abundance patterns. In Chapter 6 we presented our intermediate-mass stars models. In Chapter 7 we use the extended network in the evolutionary code to understand the abundance anomalies in Globular Clusters. Finally in Chapter 8 we present the conclusions.

Chapter 2

On the Evolution of Moderate-Mass stars

The evolution of a star is strongly dependent on its initial mass. Throughout the course of its life, a star undergoes many evolutionary stages, amongst them, the Asymptotic Giant Branch, referred to as AGB phase. The AGB phase is the production site of heavy elements. In this chapter a sketch of the evolution prior and during the AGB phase will be discussed, together with a brief discussion on the formation of s-process elements. For a more detailed description we refer the reader to the standard textbooks: Clayton (1983), Kippenhahn & Weigert (1990).

2.1 Introduction

Stars classified as moderate-mass stars are those ending their lives as white dwarfs. They are divided into low- and intermediate-mass stars. This classification is based on the way helium is burnt in the core, if in a violent (He-flash) or a quiescent way. The mass boundary between low- and intermediate-mass stars is model and metallicity dependent. In general, stars with mass below $2M_{\odot}$ experience core He-flash and are classified as low-mass stars. Stars with masses between $2M_{\odot}$ and $10M_{\odot}$ are classified as intermediate-mass stars.

A protostar of mass larger than $0.08M_{\odot}$ will reach high enough temperatures in the center to start fusion and become a zero-age main sequence (ZAMS) star. In the ZAMS phase the star is assumed to be chemically homogenous and in equilibrium. The evolution at this point strongly depends on the stellar mass and will be described in 2.2.

As the star advances in the evolution, it assumes more and more an onion-like structure, with shells powered by different burning mechanisms on top of each other. In the AGB phase, for instance, the core is surrounded by He- and H-burning shells. The structure and nucleosynthesis of this evolutionary stage will be discussed in 2.3 and 2.4. 2.4 will focus on the formation of elements heavier than iron and its connection with the AGB phase.

2.2 Evolution pre-AGB phase

2.2.1 Low-Mass Stars

The main-sequence (MS) phase begins at the ZAMS and finishes when hydrogen is exhausted in the center, and corresponds to the majority of the stellar life. During the MS of low-mass stars, H-burning is dominated by the proton-proton (pp) chain reactions in a radiative core (for $M \geq 1.1M_{\odot}$ a convective core develops due to the increasing importance of the CNO cycle (Figure 2.1)). The pp chain, as can be seen in the panel (a) of Figure 2.1, involves the fusion of two protons into a deuterium, leading to the formation of helium via three different branches (PPI, PPII, PPIII). The frequency of the branches depends on chemical compositon, temperature, and density.

Figure 2.2 illustrates the evolution of a low-mass star in the Hertzsprung-Russel diagram (HRD). The MS is represented by the points A to D. The point where the star leaves the MS after the exhaustion of hydrogen in the core is the turn-off point (point D in Figure 2.2). From the turn-off point onwards, the energy source is H-burning (dominated by the CNO cycle) in a shell around the inert helium core. The envelope start expanding as a reaction to the contraction of the core. The star enters the subgiant phase (points E to G in Figure 2.2) and moves towards lower temperature in the HRD. The cooling of the stellar outer layers results in the formation of a convective envelope. The star moves towards lower effective temperatures and higher luminosities in the HR diagram. As the star climbs the giant branch, the convective envelope penetrates deeply inwards and material partially processed by H-burning is brought to the surface. This event, known as first dredge-up (FDU), results in an increase of the abundances of isotopes such as ^{4}He, ^{13}C, and ^{14}N (formed through the activation of the CNO cycles) and in a decrease of ^{12}C abundances (Figure 2.3). The decrease in the $^{12}C/^{13}C$ ratio is shown in panel (b) of Figure 2.3 and can be used to trace the FDU since ^{12}C is present in

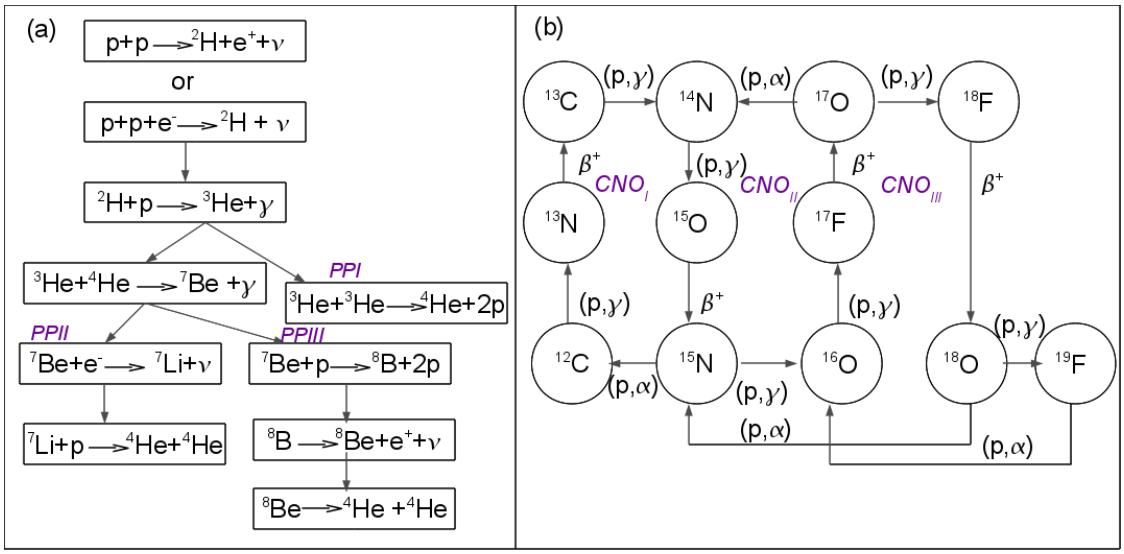

Figure 2.1: Panel (a) shows the reactions involved in the pp chain. The energies released by the branches are: 26.2 MeV (PPI), 25.7 MeV (PPII), and 19.2 MeV (PPIII). Panel (b) shows the reactions involved in the CNO cycles. The elements C, N , and O act as catalysts in these reactions. Their final abundances are those of equilibrium in the CNO cycles and the sum of these abundances is equal to the sum of the initial values.

the photosphere of MS stars, whilst ^{13}C is only present after products of the CNO cycle are dredged-up to the surface via convective mixing.

The core continues to contract while the star climbs the red giant branch (RGB) and at some point the core becomes dense enough to be degenerate. When the temperature is hot enough, He is burnt off-center in a violent way (core He-flash), as a result of the decoupling of temperature and density in the equation of state of the degenerate matter. The increase in temperature in the core is not compensated by its expansion and subsequent cooling. In this way, the energy released by nuclear burning heats up the core, which in turn will increase the reaction rates, until a thermonuclear runaway occurs. The off-center nature of the core He-flash is a result of neutrino energy loss, which cools the core in the hot and dense regions. The cooling efficiency decreases with density, leading to a higher temperature on the border of the cooled region.

After the He ignition the star moves in the HR diagram to higher temperatures and lower luminosities. Now, the core He-burning is surrounded by a H-burning shell. If the star has solar metallicity it is in a position in the HR diagram called red giant clump, on the other hand if it has lower metallicity it is on the horizontal branch (HB). After He exhaustion in the center the core starts to contract and the envelope expands. Helium is now burning in a shell surrounded by the H-burning shell and the star ascends again the giant branch (AGB) phase.

Zero Metallicity

For primordial stars the evolution can be quite different compared to the evolution of the metal-rich ones and even from the Population II case.

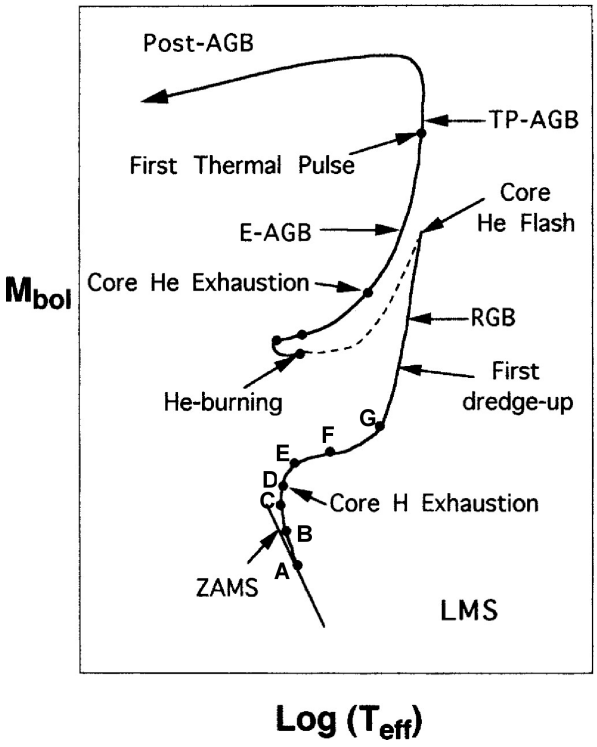

Figure 2.2: Illustrative evolutionary track of a $1M_{\odot}$ with solar metallicity. Figure taken from Busso et al. (1999). Temperature decrease from left to right.

Metal-free stars have only hydrogen and helium in their composition (and traces of Li, Be, and B). Since low-mass stars do not have a hot enough core to burn H via CNO cycles (even in the metal-rich regime), the lack of CNO catalysts does not affect their Main-Sequence nuclear burning. However, the absence of metals implies a decrease in opacity and, thus, energy escapes more easily. As a consequence, the burning rate to maintain hydrostatic equilibrium in zero-metallicity stars is larger, resulting in higher luminosities and effective temperatures and, hence, shorter lifetimes. The lack of CNO catalysts is also responsible for the delay in the ignition of the H-burning shell (powered by CNO), instead the shell is powered by the PP chains. Only after the He-flash, CNO elements are produced in a significant amount to dominate the H-burning in the shell.

Another difference between metal-rich and metal-free low-mass stars is the luminosity of the tip of the RGB. In the Z = 0 case, the conditions for He ignition are achieved earlier, leading to a shorter RGB evolution and a lower luminosity of the tip of the RGB (for instance, $\Delta log(L/L_{\odot}) \sim 1 dex$ between star of Z=0 and Z=0.002). For the Z=0 stars the He-flash occurs in a region much more off-center. In this case, as the convection zone is farther out in the star, the growth of the convection zone quickly reaches the H-burning shell, mixing H down into the hot He convective zone. The high temperature in the zone where protons were mixed leads to rapid H-burning, releasing a large amount of energy.

2.2.2 Intermediate-Mass Stars

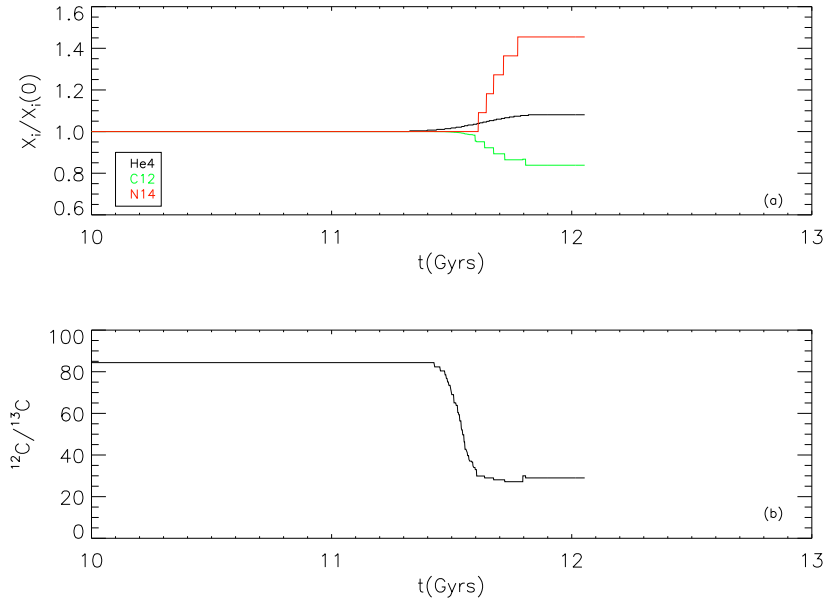

Figure 2.3: Panel (a) shows the surface abundances ratio of ^{4}He, ^{12}C, and ^{14}N and their initial value for a $1M_\odot$ star. Panel (b) shows the $^{12}C/^{13}C$ ratios for the same $1M_\odot$ star. The effects of the FDU are seen when the star reaches 11.4 Gyrs and they reflect the H-burning nucleosynthesis when powered by CNO cycles in the shell. Model computed using the Garching stellar evolution code.

The evolution of these stars already differs from the low-mass ones in the main-sequence: Hydrogen burns mainly through the CNO cycle (Figure 2.1) and the temperature-dependence from the CNO cycle reactions causes the development of a convective core.

The climbing and subsequent first dredge-up in these stars are similar to the low-mass case, however the ignition of helium is in the center and it is not under degenerate conditions.

After He exhaustion in the center, the core contracts and the envelope expands moving the star in the HR diagram toward larger luminosities: the star enters the early AGB phase. For intermediate-mass stars the bottom of the convective envelope penetrates beyond the H-He discontinuity, mixing H-burning products with the envelope. This mixing episode is called second dredge-up (SDU) and its position in the HR digram is shown in Figure (2.4). The surface abundance of ^{4}He, ^{12}C, and ^{14}N are significantly altered after the SDU.

Zero Metallicity

In the case of intermediate-mass stars the behavior in the HR diagram during the MS is completely different. While in metal-rich stars the temperature decreases with luminosity, in metal-free it increases, due to the fact that in $Z = 0$ stars the burning is powered by p-p chains. Another difference is that metal-free stars increase their luminosity by a large amount during the MS (Figure 6.5).

In the zero metallicity case, ^{12}C production occurs just as the star turns off the Main-Sequence, when there is a small amount of hydrogen in the core ($X_H \sim 0.01$). Once the ^{12}C abundance (in mass-fraction) reaches $\sim 10^{-12}$ there is a thermal runaway, giving rise

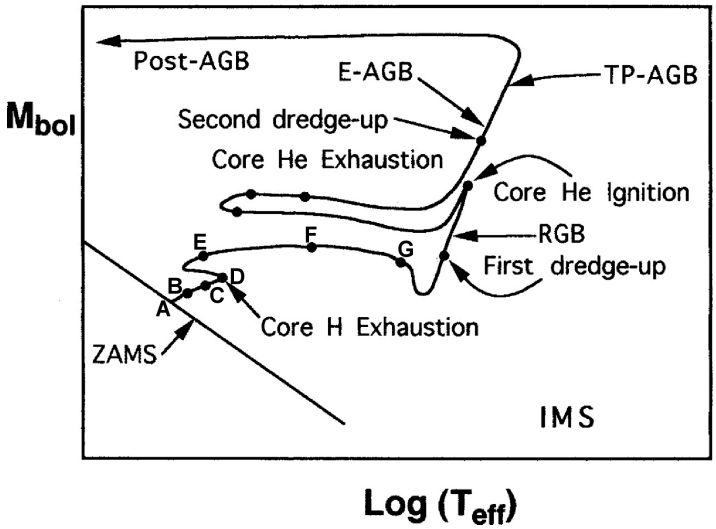

Figure 2.4: Illustrative evolutionary track of a $5M_{\odot}$ with solar metallicity. Figure taken from Busso et al. (1999). Points A to D illustrate the main sequence.

to a small convective core (Figure 2.6), which mixes some extra H, increasing its central abundance, and therefore, prolonging the MS.

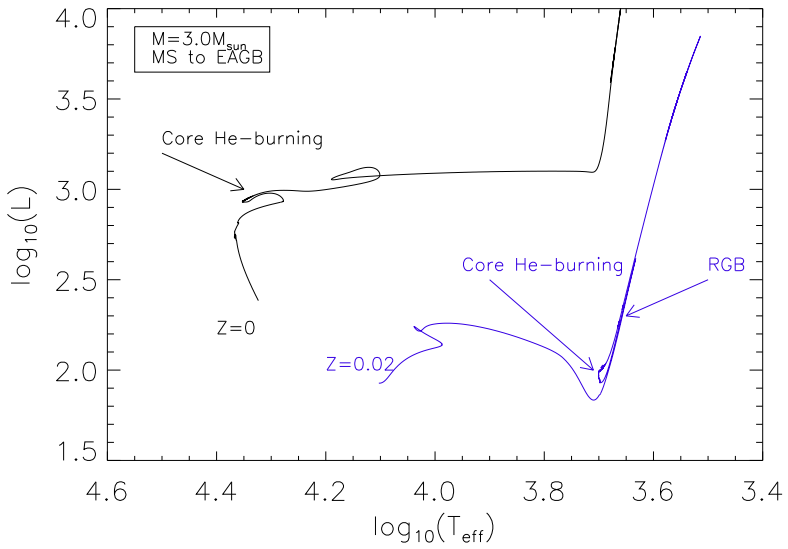

Figure 2.5: This HR diagram illustrates the differences between metal-free and solar metallicity Intermediate-Mass stars, such as the large increase in luminosity during the MS and the lack of an RGB. Core He burning also occurs at a higher luminosity in the Z=0 model, and at a much higher surface temperature. Models computed using the Garching stellar evolution code. The second loop in the Z=0 track corresponds to a small He shell flash that happens after the core He-burning.

The $Z = 0$ star reaches He-burning temperatures at much lower densities, leading to a

quiet ignition of He in the core. The star rapidly changes from core H-burning to core He-burning, avoiding a RGB configuration. Due to the lack of RGB, only one mixing episode occurs. The envelope goes deeply enough to reach regions that have been subjected to partial hydrogen burning. However, once the H-burning occurs via p-p chain the envelope is not enriched in ^{14}N as it occurs in the metal-rich regime and, also, the enrichment in ^{4}He is much stronger (Figure 2.7).

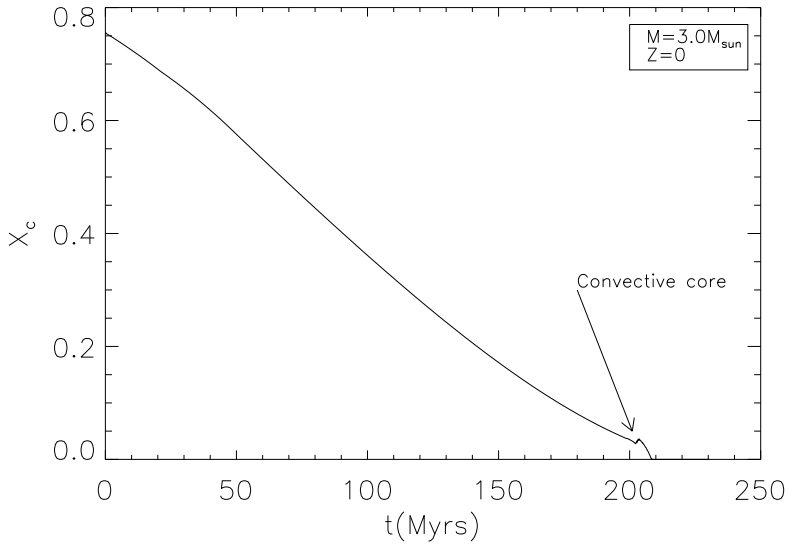

Figure 2.6: Mass fraction of hydrogen in the core as a function of time for a metal-free star. The development of the convective core can be seen by the increase in the mass fraction towards the end of the MS. Models computed using the Garching stellar evolution code.

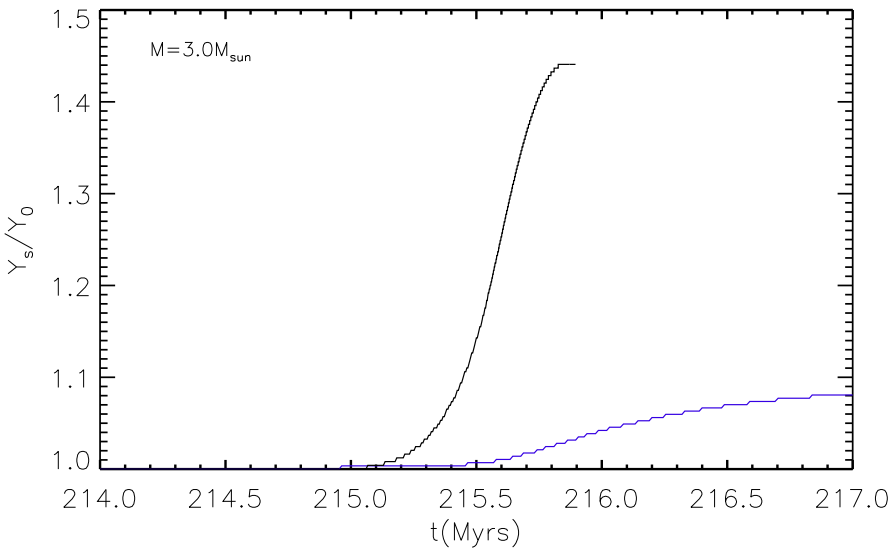

Figure 2.7: Ratio between He surface abundance after the FDU and the initial abundance. Blue line and black line represent Z=0.02 and Z=0, respectively. Models computed using the Garching stellar evolution code. The model with Z=0.02 was shifted by 125 Myrs for visualization purpose. The Z=0 calculation is shown only until the end of the dredge-up. The helium abundance will increase further in the AGB evolution.

2.3 Thermal-Pulse phase

One of the last evolutionary stages of low- and intermediate-mass stars is the Asymptotic Giant Branch. This phase is characterized by a degenerate carbon and oxygen (CO) core surrounded by He- and H-burning shells and a convective envelope, see Figure (2.8).

It is divided in two parts, the early AGB (E-AGB) and the thermally pulsing AGB (TP-AGB). During the E-AGB the two shells coexist and the main source of energy is the He-burning shell. During the TP-AGB phase, the energy source alternates between the H- and the He-burning shells.

In the TP-AGB phase the H shell dominates the energy production for most of the time. H is burnt into He at the top of the He intershell. As a consequence, the He intershell gets thicker. The bottom layers of the intershell are compressed until their temperature and density become high enough that helium burning is triggered. The thermal pulse generated by this sudden release of energy causes the whole intershell to become convective. This region, now known as pulse driven convective zone (PDCZ), homogenizes most of the intershell region, bringing material from the He-burning shell to a region closer to the surface below the H-burning shell. On the top of the intershell the H shell cools and hydrogen burning stops. A TP extinguishes after a few hundreds years and H burning starts again. The pulses are repeated several times with intervals between them of $10^3 - 10^4$ years. The total number of pulses depends on the initial stellar mass and the mass-loss prescription adopted. Figure (2.9) shows the stellar luminosity over time, during the TP-AGB. The luminosity produced

by H-burning and He-burning are also shown. During the pulse, a peak in the He luminosity can be seen. This luminosity, then, decreases and stays smaller than the hydrogen one during the entire interpulse period.

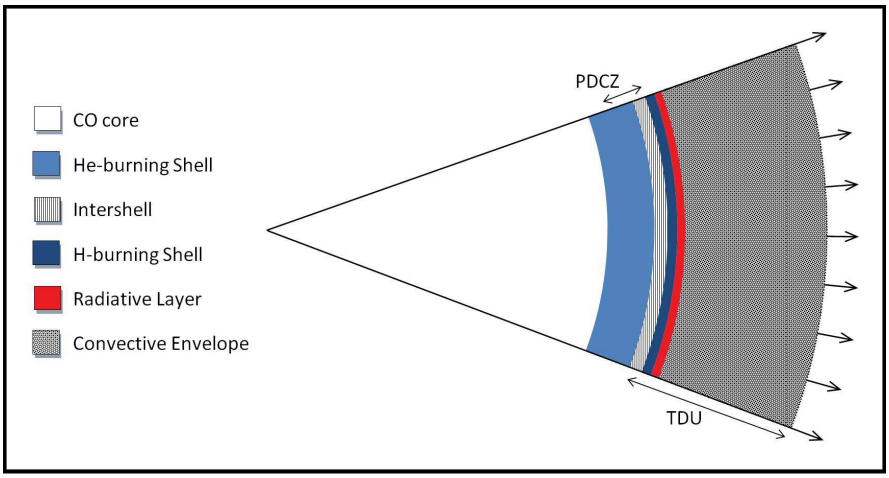

Figure 2.8: Schematic structure of an AGB star. The Pulse Driven Convective zone (PDCZ) and the third dregde-up (TDU) are indicated in the figure. (not to scale). [Adapted from figure 1.2 from Lugaro (2001)]

After the occurrence of a thermal pulse, mixing episodes may occur which bring the products of nuclear burning from deep inside the star to the stellar surface. These events, called third dredge-up (TDU), bring mostly ^{4}He, ^{12}C, and s-process elements to the stellar surface. The intershell contains much more C than O, and as a result, the envelope C/O ratio increases with each TDU until a C star is formed, C/O > 1, (Figure 2.10). In extremely low metallicity stars, dredge-up leads to significant surface enhancements for many other species, like O, ^{22}Ne, ^{23}Na, ^{25}Mg or ^{26}Mg (Herwig 2005).

The efficiency of the TDU depends on the adopted physics of mixing. The use of a constant solar calibrated value for the mixing-length parameter $\alpha_{\rm MLT}$ may not describe AGB envelopes accurately at all. It also depends on the treatment of convective boundaries and the reaction rates used.

During the AGB phase other mass-dependent phenomena occur and the classification of low- and intermediate-mass stars based on the He-flash is not useful anymore. In massive AGB stars the base of the convective envelope can dip into the H-shell with typical temperatures between $(0.5 - 1.0) \times 10^8$ K. The H-shell has, then, larger access to fuel, convectively mixed into its outer layers. This phenomena, known as HBB prevents C-star formation, since it transforms dredged-up C into N (Boothroyd et al. 1993). The decrease of the envelope mass towards the end of the AGB evolution, due to mass loss, reduces the HBB efficiency.

For AGB stars the usual classification is:

- Low-mass AGB stars: The stars that do not experience Hot-bottom Burning (HBB), become CO white dwarfs and produce s-process - M < 4.0M$_\odot$;
- Massive AGB stars: Do experience HBB and become CO white dwarfs - 4.0M$_\odot <$ M < 8.0M$_\odot$;
- Super AGB stars: Experience HBB, carbon burning and become ONeMg white dwarfs - 8.0M$_\odot <$ M < 10.0M$_\odot$.

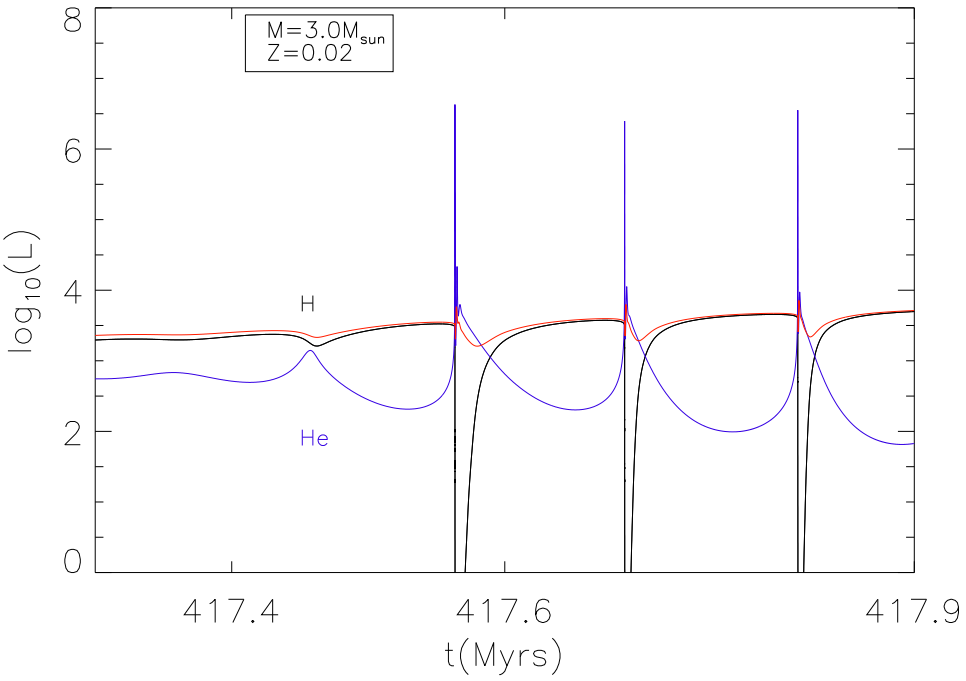

Figure 2.9: The evolution on the surface luminosity (red line) as a function of time for a $3M_{\odot}$ model computed with the Garching stellar evolution code. Blue line: Luminosity of He-burning shell. Black Line: Luminosity of H-burning shell.

The nucleosynthesis signature of HBB includes Li production, high N abundances, low C/O and $^{12}C/^{13}C$ ratios and enhancements of ^{23}Na, ^{25}Mg, ^{26}Mg and ^{26}Al (Ventura et al. 2002; Karakas & Lattanzio 2003; Denissenkov & Herwig 2003; Karakas & Lattanzio 2007; Karakas 2010).

The initial-mass boundary for HBB depends on metallicity. Forestini & Charbonnel (1997) find HBB for $M \geq 5.0$ for Z=0.02, while Siess et al. (2002) found HBB down to $3M_{\odot}$ for zero metallicity stars. In fact, the initial-mass boundary for low-metallicity stars is still model dependent: Campbell & Lattanzio (2008) found HBB in zero metallicities stars for $M \geq 2.0M_{\odot}$ in contrast to Lau et al. (2009), whose models with $M < 4.0M_{\odot}$ do not experience HBB.

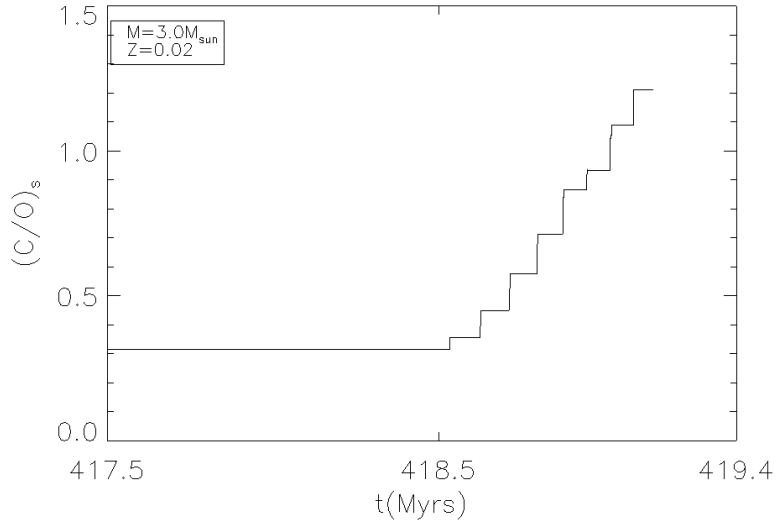

Figure 2.10: The evolution of the surface C/O ratio during the TP-AGB of a $3M\odot$ model with Z=0.02 solar-scaled composition.

2.4 Formation of Heavy Elements

Chemical elements are synthesized in the stellar interior through fusion of lighter elements into heavier elements for atomic numbers $1 \leq \mathrm{Z} \leq 56$. Elements heavier than ^{56}Fe can not be produced by fusion. This can be explained considering the mass of a nucleus given by:

$$m(Z,A) = Zm_p + (A-Z)m_n - \frac{B(Z,A)}{c^2}, \tag{2.1}$$

where $\mathrm{m_p}$ is the proton mass, $\mathrm{m_n}$ the neutron mass, *B(Z, A)* is the binding energy of nuclide *m(Z, A)*, *A* is the atomic mass, *Z* is the atomic number and *c* is the speed of light. Figure (2.11) shows that for nuclides with $\mathrm{A} \leq 56$, the reaction is exothermic, thus the binding energy of the heavier nuclide (final nuclide) is higher than the one of the lighter nuclide (original nuclide).

Above $\mathrm{A} = 56$ the behavior is the opposite: reactions are endothermic. Therefore, these nuclei can not be produced by fusion. In addition, fusion occurs when the kinetic energy of the seed nuclei is sufficient to overcome the Coulomb barrier. Since the Coulomb barrier increases with the electric charge of the colliding nuclei, fusion can be triggered more easily between nuclei with small number of protons. Hence neutrons do not need to overcome the Coulomb barrier, the main mechanism for the formation of heavy elements is the neutron capture.

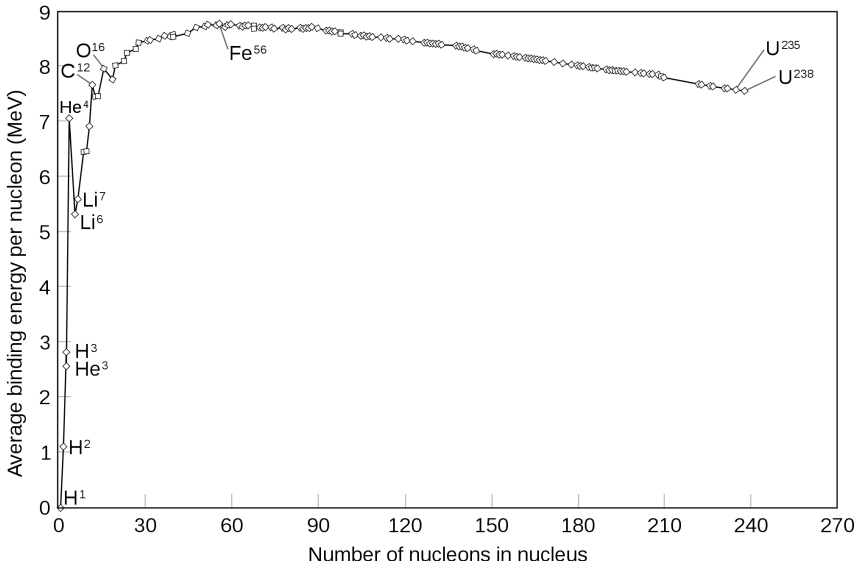

Figure 2.11: Binding energy per nucleon as a function of atomic mass.

The neutron capture process can be slow (s-process) or rapid (r-process) relative to the beta decay rate[1]. The occurrence of one or another process depends on physical parameters, such as temperature and neutron density, which are closely connected to the evolutionary stage.

In the s-process stable isotopes are produced along the valley of beta stability, whereas in the r-process neutron-rich atomic nuclei are created (Figure 2.12).

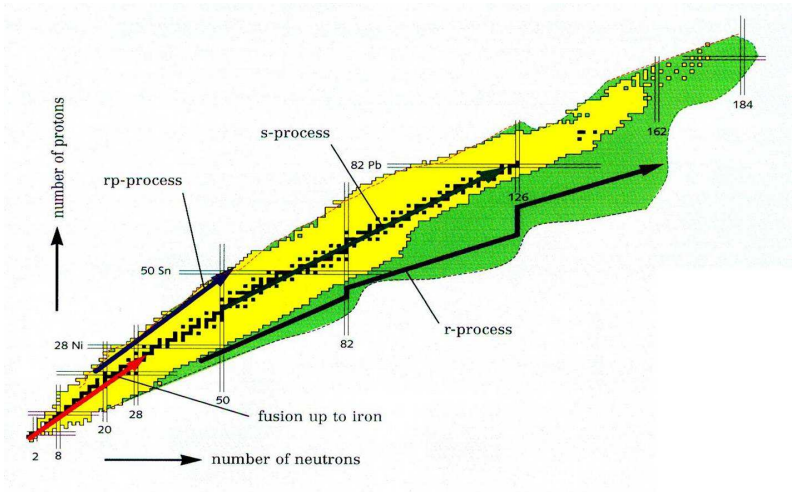

Figure 2.12: S-process and r-process paths. Black symbols represent stable isotopes, green and yellow symbols represent unstable ones. Figure taken from: http : //www − alt.gsi.de/fair/overview/research/nuclear − structure$_e$.html.

[1]The decay β^- is the transformation of a neutron into a proton (which remains in the nucleus), an electron (which is ejected), and an anti neutrino, as described by the reaction: $(Z, A) \rightarrow (Z + 1, A) + e^- + \overline{\nu_e}$.

2.4.1 S-process

The s-process is characterized by a slow neutron capture, i.e, the average rate of neutron capture by a certain nucleus is much smaller than the β decay rate. It is estimated that, in average, $10^2 - 10^5$ years may pass between successive neutrons captures. This process is also characterized by a neutron density of the order of $10^5 - 10^{11}\mathrm{ncm}^{-3}$, which can be provided by two astrophysical sites:

- Core He-burning in massive stars, where the main neutron source is given by the reaction (2.2)

$$^{22}Ne +^4 He \rightarrow ^{25}Mg + n; \tag{2.2}$$

- The He-shell in the AGB phase, during the thermal pulses, where the main neutron source is the following reaction:

$$^{13}C +^4 He \rightarrow ^{16}O + n. \tag{2.3}$$

The main products of the s-process are: Sr-Y-Zr, Ba-La-Ce-Pr-Nd and Pb, corresponding to its three largest abundance peaks. The reason for the existence of these three peaks lies in the fact that for number of neutrons N = 50, 82, 126 the neutron capture cross-sections are much smaller than for other N. These "magic numbers" of neutrons are a quantum effect of closed shells in the same way that electrons in complete shells produce high chemical stability for noble gases.

2.4.2 Classical Model and The S-process Components

In the classical model, the formation of s-process elements happens in a chain, starting with iron seed nuclei. The changes in the abundances $\mathrm{N_i}$ over time are given by equation 2.4, where τ is the neutron exposure[1] (which is the integral of the flux over time) and σ_i is the neutron capture cross-section by isotope i.

$$\frac{dN_i}{d\tau} = \sigma_{i-1}N_{i-1} - \sigma_i N_i, \qquad 56 \leq i \leq 209. \tag{2.4}$$

In a steady state, $\mathrm{dN_i/d}\tau = 0$, the product σN is constant. Clayton et. al 1961 showed that a simple neutron exposure τ can not reproduce the abundances of elements in the solar system. However, a good adjustment of σN for the solar system is obtained when an exponential distribution for the neutron expositions is assumed (Seeger et al. 1965):

[1] $\tau = \int \mathrm{v_T N_n(t)dt}$, where $\mathrm{v_T}$ is the thermal velocity and $\mathrm{N_n(t)}$ is the neutron density

$$\rho(\tau) = \frac{GN_{56}}{\tau_0} e^{-\frac{\tau}{\tau_0}}, \tag{2.5}$$

where τ_0 is the mean neutron exposure, G is the iron fraction exposed to neutrons and N_{56} is the initial ^{56}Fe abundance.

The curve σN decreases slowly with the mass number, once the product $\tau_0\sigma_i$ increases with it. However, when σ is very small (in the magic numbers), there is a sudden drop in the curve. This effect is shown in Figure (2.13).

The exponential distribution of neutron exposures in equation (2.5) can reproduce the solar abundances if three values of τ_0 are adopted. These values depend on the atomic mass A and are often referred to as s-process components. The main component is responsible for the production of isotopes in the atomic mass range $90 < A < 204$. A good fit for the solar abundances in this atomic range is obtained with $\tau_0 \approx 0.30\text{mb}^{-1}$.The weak component ($A \leq 90$), which most likely environment is the core of massive stars ($M \geq 10M\odot$) nicely fits the solar curve if $\tau_0 \simeq 0.06\text{mb}^{-1}$ (Meyer 1994). It was also proposed the existence of a strong component ($204 < A < 209$) in order to reproduce more than 50% of solar Lead abundance ^{208}Pb (Käppeler et al. 1989). In this case $\tau_0 = 7.0\text{mb}^{-1}$.

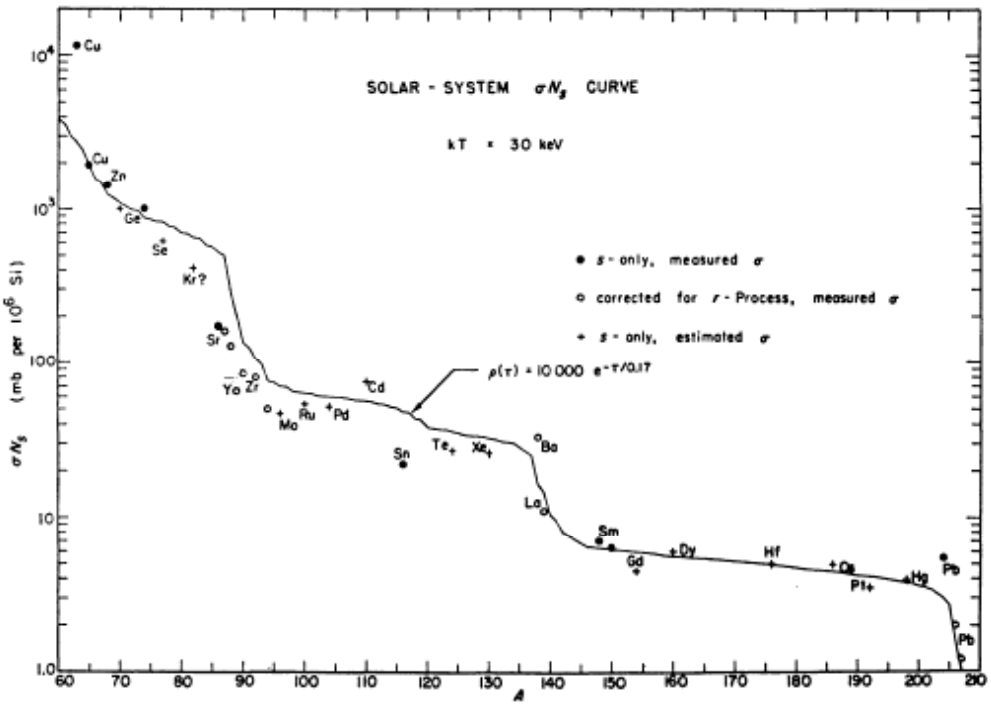

Figure 2.13: Solar s-process $\sigma_i N_i$ distribution. The curve was obtained with an exponential distribution of neutron exposures. Figure taken from Seeger et al. (1965).

In the classical model, no hypotheses on the s-process site were formulated. Ulrich (1973) proposed the pulse driven convective zone in the TP-AGB phase as the astrophysical site for s-process production. An exponential distribution of neutron exposures would be achieved by

the recurrent TPs, in agreement with the classical model assumption. However Straniero et al. (1995) demonstrated that the $^{13}C(\alpha, n)^{16}O$ reaction is burning in radiative conditions during the interpulse period. In this case, the distribution of neutrons exposures changes and the resulting distribution is a superposition of a few single exposures. The limitations of the classical model were revealed with improved new studies and therefore, the necessity of s-process calculations considering its possible sites. For this purpose, full stellar evolution models are required, becoming the usual approach nowadays when performing s-process calculations. S-process calculations are performed, in general, in a post-processing code which uses the thermodynamic output from the full evolutionary models as the input for the s-process network.

2.4.3 The ^{13}C Pocket

In the current scenario, s-process occurs in a thin radiative layer on top of the He-intershell. Protons from the envelope are mixed down to a tiny region above the He-intershell during the TDU. This region, also enriched in ^{12}C, will be re-ignited during the interpulse period, leading to the formation of ^{13}C through the reaction chain $^{12}C(p, \gamma)^{13}N(\beta)^{13}C$. This ^{13}C-rich layer, known as ^{13}C Pocket, is depleted in ^{14}N and it is the production site of s-process elements (Figure 2.14). The pocket can partially overlap an outer ^{14}N pocket.

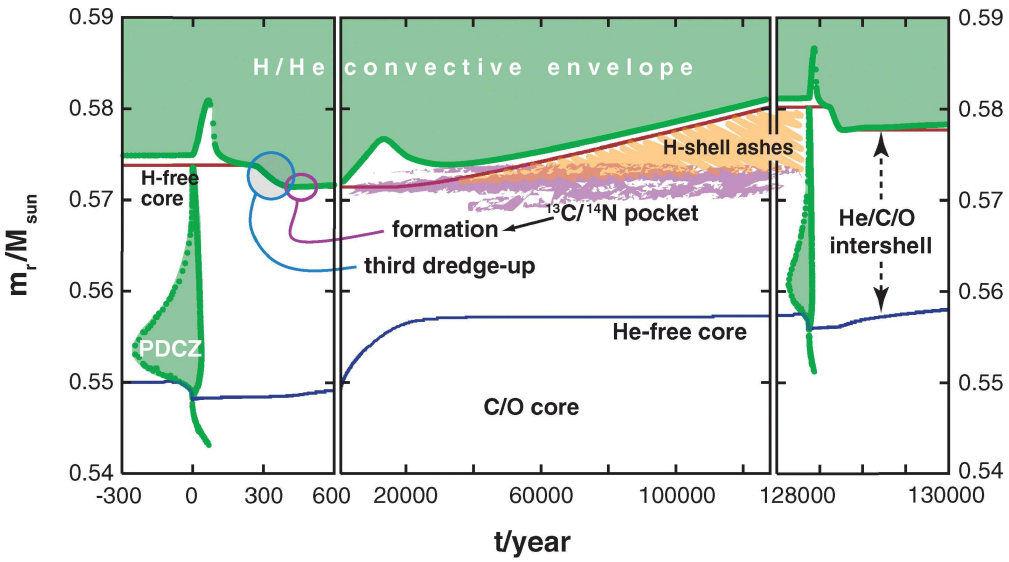

Figure 2.14: This figure shows the time evolution of two thermal pulses. The red line indicates the position (in mass) of the H-free core, while the blue one shows the position of the He-free core. In the first panel the development of the TP and the pulse driven convective zone are shown (green color indicates convection). The convective envelope deepens, dredge-up products of the past TP and mixes protons down. The second panel shows the interpulse period and the development of the pocket, whose products are going to be dredged-up to the surface by the subsequent TP (third panel). Figure taken from Herwig (2005).

A description of the physical phenomena driven the mixing of protons into the He-intershell is still missing. Three mechanisms were proposed (Herwig 2005): diffusive overshooting

(Herwig et al. 1997), mixing induced by rotation (Langer et al. 1999) and mixing induced by gravity waves (Denissenkov & Tout 2003). None of them can be definetly appointed as the mechanism responsible for the ^{13}C pocket formation. For this reason, in the AGB calculations found in the literature the amount of ^{13}C in the pocket is used as a free parameter (Gallino et al. 1998). Other groups opted to introduce an exponentially decaying profile for the velocity at the bottom of the convective envelope, calibrating the free parameter in order to get the maximum ^{13}C efficiency (Cristallo et al. 2004).

2.5 Proton Ingestion Episode

The proton ingestion episode (PIE) was first discussed by Dantona & Mazzitelli (1982). In their simulation of low-mass zero metallicity stars, they observed a very far off-center ignition of the core He-flash and suggested that the He convective zone would break through the He-H discontinuity, leading to surface enrichment in carbon and nitrogen. Only a decade later the PIE was fully simulated by Fujimoto et al. (1990) and Hollowell et al. (1990). Since then, many groups have succeeded in simulating this phenomenon. These works are summarized in Table 2.1.

The huge amount of energy released during the core He-flash results in the formation of a convective zone at the position of maximum energy release, the so called Helium Convective Zone (HeCZ). The point of ignition, i.e. the inner boundary of the HeCZ, is off-center due to neutrino cooling in the core. The outer boundary of the convective zone advances in mass during the development of the flash. At extremely low metallicities, the low entropy barrier between the He- and H-burning layers allows the HeCZ to reach H-rich layers. Protons are dredged-down into the HeCZ and burnt via $^{12}\mathrm{C}(\mathrm{p},\gamma)^{13}\mathrm{N}(\beta)^{13}\mathrm{C}$. The convective zone continues to advance until a secondary flash due to hydrogen burning happens, the H-flash (see Figure 2.15).

The H-flash causes a splitting of the HeCZ at the position of maximum energy release by hydrogen burning (Figure 2.16). The upper convective zone, known as hydrogen convective zone (HCZ), continues to expand. Between $10^2 - 10^3$ years the envelope reaches deeper regions of the star and products of the nucleosynthesis during and after the PIE are dredged-up to the surface. The stellar surface is then strongly enhanced in carbon, nitrogen, and oxygen.

The PIE can also happen at the beginning of the TP-AGB phase, depending on the mass and metallicity. It might happen at one or more thermal-pulses. The dredge-up following the PIE enhances the envelope in CNO elements. Once the envelope reaches $\mathrm{Z_{CNO}} \sim 10^{-4}$, the AGB evolution proceeds similarly to the evolution of a star with higher metallicity. Figure 2.17 shows the behavior of the models as a function of mass and metallicity for three different studies. Apart from minor differences, the mass-metallicity boundaries for the occurrence of the PIE during the core He-flash or the TP-AGB phases are consistent between Suda & Fujimoto (2010) and Campbell & Lattanzio (2008). For instance, in stars with masses $\mathrm{M} = 1.0\mathrm{M}_\odot$, PIE switches from core He-flash to the TP-AGB at metallicity $[\mathrm{Fe/H}] = -5.45$ for the models by Campbell & Lattanzio (2008). On the other hand, in Suda & Fujimoto (2010) models, PIE happens during the core He-flash for metallicities up to $[\mathrm{Fe/H}] = -5.0$. In the $\mathrm{M} = 2.0\mathrm{M}_\odot$ case, models by Suda & Fujimoto (2010) undergo PIE during the TP-AGB for metallicities $[\mathrm{Fe/H}] \leq -3.0$, while models by Lau et al. (2009) and Campbell & Lattanzio

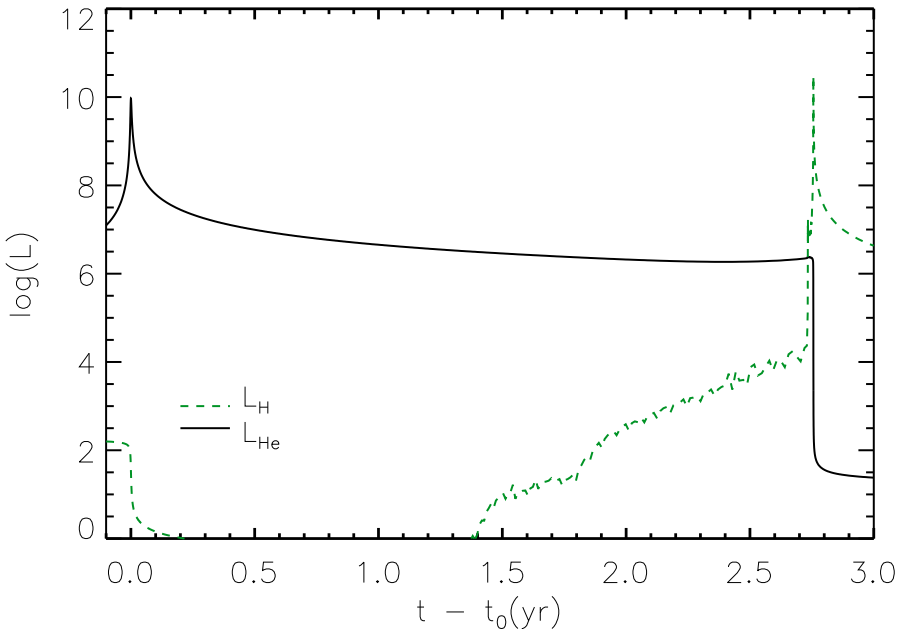

Figure 2.15: H- and He-burning luminosities (in solar luminosity units) for a star with mass $M = 1.0M_{\odot}$ and zero metallicity during the core He-flash. t_0 represents the time when He-burning luminosity reaches its maximum value. The secondary H-flash happens approximately 3 years after the maximum He-burning luminosity.

(2008) undergo PIE for metallicities [Fe/H] < -3.5.

Campbell & Lattanzio (2008) and Lau et al. (2009) results for the $3.0M_{\odot}$ models show the largest differences. While Campbell & Lattanzio (2008) models undergo PIE during the AGB phase, Lau et al. (2009) models undergo a somewhat different ingestion process, the carbon injection. During the carbon injection a convective pocket opens up above the H-shell and its lower border penetrates C-rich region. Carbon surface enrichment is also observed after the carbon injection, however, its abundance is lower than those observed in models that undergo PIE (Lau et al. 2009). The uncertainties in the treatment of mixing and convection are responsible for the differences found between different studies. Campbell & Lattanzio (2008) suggested that multidimensional simulations are necessary to model a violent event such as PIE. Stancliffe et al. (2011) have performed three-dimensional simulations of the PIE during the AGB phase for a $1M_{\odot}$ star with metallicity $Z = 10^{-4}$. In this simulation, they observed a more prominent proton ingestion than those obtained by the 1D models, resulting in a much more violent H-flash. The larger convective velocities observed in the 3D models results in a high H-burning close to the He-burning shell. Also, despite the larger H-burning luminosity observed in the 3D models, there is no evidence for the HeCZ splitting into two zones. They argued, however, that the absence of splitting might be a result of the low spatial resolution used in the calculation or the insufficient timespan of the calculation. One important conclusion from the 3D simulations is that the use of an advective mixing scheme, instead of the diffusive approximation usually used in the 1D models, would provide a more

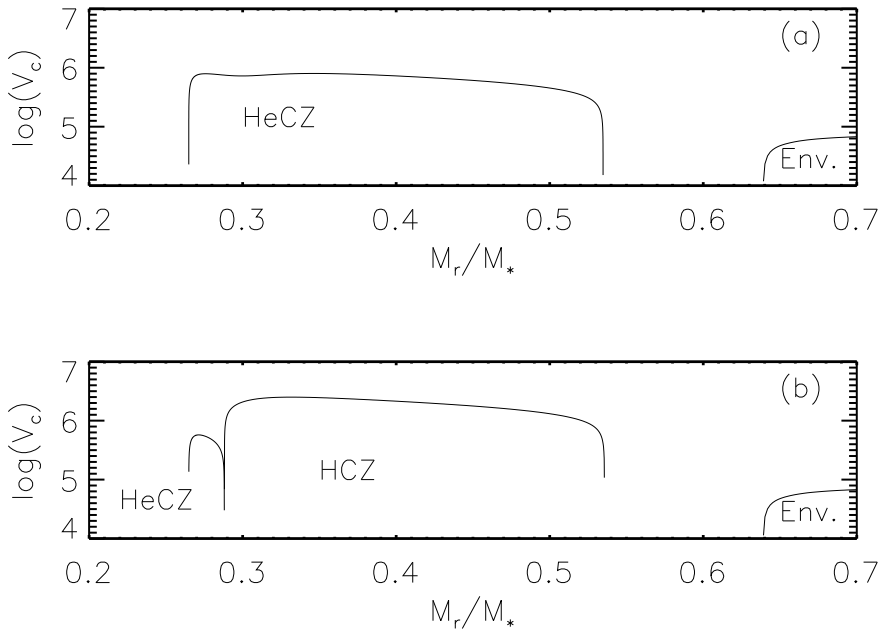

Figure 2.16: Convective zones during the PIE of a star with mass $\mathrm{M} = 1.0\mathrm{M}_{\odot}$ and metallicity $\mathrm{Z} = 10^{-8}$. Panel (a) shows the HeCZ before the H-flash. Panel (b) shows the splitting of the HeCZ after the H-flash. The upper convective zone is known as hydrogen convective zone (HCZ). The velocity is given in cms^{-1}.

realistic description of the PIE.

During the PIE, ^{13}C is formed by proton capture on ^{12}C and mixed throughout the entire HeCZ. Neutrons are produced by the reaction $^{13}\mathrm{C}(\alpha,\mathrm{n})^{16}\mathrm{O}$ and s-process might take place inside the convective zone. Until recently, there was no s-process simulation for this particular phenomenon. However, the s-process model of a star with $1\mathrm{M}_{\odot}$ and metallicity $\mathrm{Z} = 10^{-8}$ obtained by Campbell et al. (2010) has shown that the high neutron density achieved during the PIE leads to a strong production of heavy elements. Therefore, PIE might be an important site of s-process production during the early Galaxy. The work by Campbell et al. (2010), nonetheless, is limited to one single mass and metallicity. Therefore, a broader study of the s-process production during the PIE is necessary and is developed in this thesis.

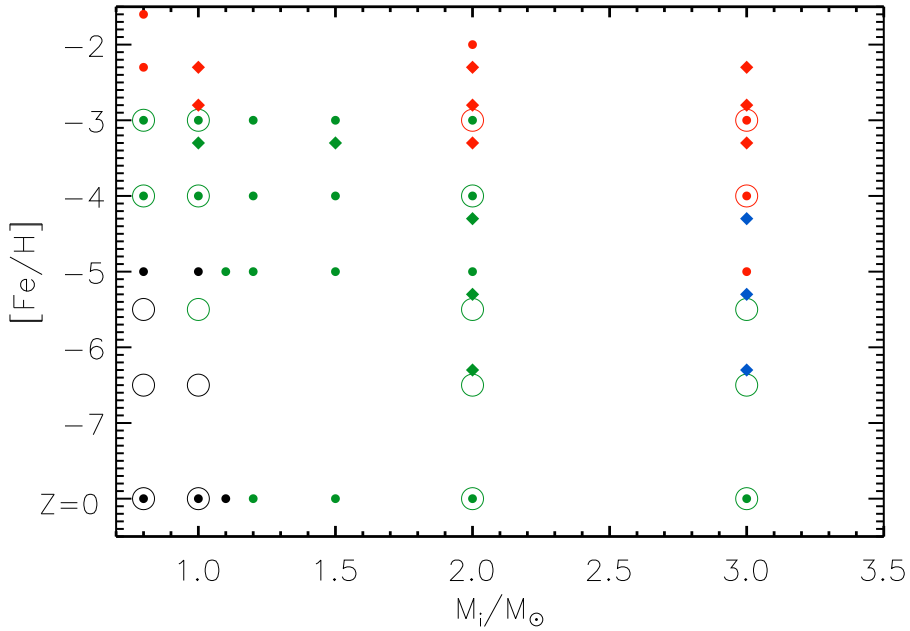

Figure 2.17: Mass-metallicity diagram for models produced by Campbell & Lattanzio (2008) (open circles), Suda & Fujimoto (2010) (filled circles), and Lau et al. (2009) (filled diamonds). Black symbols represent models that undergo PIE during the core He-flash, green symbols represent models that undergo PIE during the TP-AGB phase, red symbols represent models that do not undergo PIE, and blue symbols represent models that undergo carbon injection during the TP-AGB phase.

Author	Year	Mass	Metallicity	PIE?
Fujimoto et al.	1990	1.0	zero	yes
Hollowell et al.	1990	1.0	zero	yes
Cassisi et al.	1996	0.7 - 1.1	-8,-4,-3	yes
Fujimoto et al.	2000	0.8-4.0	zero, -4,-2	yes
Weiss et al.	2000	0.8-1.2	zero	no
Chieffi et al.	2001	4.0-8.0	zero	yes
Goriely & Siess	2001	3.0	zero	no
Schlattl et al.	2001	0.8-1.0	zero	yes
Siess et al.	2002	0.8-20	zero	no
Schlattl et al.	2002	0.8	zero,-3, -2	yes
Herwig	2003	2.0 & 5.0	zero	yes
Iwamoto et al.	2004	1.0-3.0	-2.7	yes
Picardi et al.	2004	0.8-1.5	zero,-6,-5,-4	yes
Weiss et al.	2004	0.82	zero, -5	yes
Suda et al.	2004	0.8-4.0	zero	yes
Suda et al.	2007	0.8-1.2	zero	yes
Campbell & Lattanzio	2008	0.8-3.0	zero,-6,-5,-4,-3	yes
Lau et al.	2009	1.0-7.0	-6.3,-5.3,-4.3,-3.3,-2.3	yes
Suda & Fujimoto	2010	0.8-9.0	zero, -5,-4,-3,-2	yes

Table 2.1: Literature theoretical studies of EMP and zero metallicity stars. The mass is given in solar mass unit. The metallicity is given in terms of [Fe/H], except when Z=0.

2.6 Summary

In this chapter the evolution throughout the life of a star was described. The main features of each evolutionary stage prior to the AGB phase were discussed, emphasizing the differences between solar metallicity and metal-free stars. More differences resulting from the low amount of metals are going to be discussed in forthcoming chapters. Special attention in the description of the main structural properties was given to the AGB phase, which is the subject of the present thesis.

An introduction to the s-process from the classical analytical works to the current approach was given. A thin ^{13}C-rich layer burnt during the interpulse period in the TP-AGB phase is currently believed to be the site of the main s-process component. The physical mechanism driving the formation of the ^{13}C pocket is still missing, therefore, most of the s-process calculations are performed assuming the amount of ^{13}C in the pocket as a free parameter.

The evolution of metal-free and EMP stars deviate considerably from the evolution of their metal-rich counterparts. Extra mixing of protons into He-rich layers, occurring in such stars, can lead to the production of heavy elements. This thesis focus on the study of the s-process production by metal-free and EMP stars and its implications to the formation of carbon enhanced stars in the early stages of the Galaxy.

Chapter 3

The evolutionary Code

In this chapter we will give a brief description of the stellar evolution code and the main physical ingredients used in the models. During the AGB evolution, due to the third dredge-up, carbon is constantly brought up to the stellar surface. Eventually the star becomes carbon-rich. This enrichment affects the stellar structure, and consequently, affects the evolution of subsequent TPs. The treatment of opacity and mass-loss used to account consistently for the effects of surface variations in carbon abundance will be described in this chapter.

3.1 Evolutionary Code: Basics

In stellar evolution theory, the structure of a star can be described by four first-order spatial differential equations. These four basic stellar structure equations are, in order of appearance, the mass conservation equation, the hydrostatic equilibrium equation, the energy conservation equation, and the energy transport equation:

$$\frac{\partial r}{\partial m} = \frac{1}{4\pi r^2 \rho}, \tag{3.1}$$

where r is the stellar radius, ρ the density, and m the mass within a sphere of radius r.

$$\frac{\partial P}{\partial m} = -\frac{Gm}{4\pi r^4}, \tag{3.2}$$

where P is the pressure and G is the gravitational constant.

$$\frac{\partial l}{\partial m} = \epsilon_{nucl} + \epsilon_g - \epsilon_\nu, \tag{3.3}$$

where l is the luminosity at radius r, ϵ_{nucl} is the nuclear energy generation rate, ϵ_g is the gravothermal energy generation rate, and ϵ_ν is the neutrino energy loss rate.

$$\frac{\partial T}{\partial m} = -\frac{GmT}{\partial 4\pi r^4 P}\nabla, \tag{3.4}$$

where $\nabla = \frac{\partial \mathrm{lnT}}{\partial \mathrm{lnP}}$.

If the star is in radiative equilibrium, the energy is transported outwards by photons and the temperature gradient can be written as:

$$\nabla_{rad} = \frac{3\kappa l P}{16\pi a c G m T^4} \tag{3.5}$$

where a is the radiation-density constant, c is speed of light, and κ is the Rosseland mean opacity.

Due to nuclear burning processes taking place in the stellar interior the solutions of the set of equations (3.1-3.4) evolve in time. Nuclear reactions are responsible for the energy and the elemental production during the life of a star. Time evolution of nuclear species is taking into account in the evolutionary calculations by solving the equation:

$$\frac{\partial X_i}{\partial t} = \sum_{jk} X_j X_k r_{jk} - \sum_{ik} X_i X_k r_{ik} \tag{3.6}$$

where X_i is the mass fraction of isotope i, r_{jk} and r_{ik} are the reaction rates for the creation and destruction of isotope i, respectively. This set of equations must satisfy the condition: $\sum_i X_i = 1$.

The coupled solution of the structure equations and the nuclear burning network is extremely time consuming if hundreds of isotopes are considered in the network. Since few reactions are responsible for the energy production (mainly pp chains, CNO cycle, and He reactions), only isotopes lighter than ^{28}Si are usually included in the evolutionary code.

In the set of equations (3.1-3.4) there are four structure equations, but five unknowns (r, ρ, T, L, and P). Thus, additional information is required. This extra information is the equation of state (EOS) which provides one of the thermodynamical quantities as a function of the others ($\rho = \rho(\mathrm{T}, \mathrm{P}, \mu)$). An accurate description of the stellar structure and evolution requires an accurate knowledge of the physical processes taking plase in the stellar interior. On the other hand, a correct description of these physical processes depends on the properties of the stellar matter. Therefore, other quantities necessary to obtain accurate stellar models are:

$\kappa_\nu = \kappa_\nu(\mathrm{P}, \mathrm{T}, \mu)$ - the opacity,

$\mathrm{c_p} = \mathrm{c_p}(\mathrm{P}, \mathrm{T}, \mu)$ - the specific heat at constant pressure,

$\epsilon = \epsilon(\mathrm{P}, \mathrm{T}, \mu)$ - the energy production rate.

Boundary conditions at the center ($M_r = 0$) and at the surface ($M_r = M$) of the star are also necessary, as well as the initial conditions.

In the GARching STellar Evolution Code (GARSTEC - An extended description of the code can be found in Weiss & Schlattl 2008), the so called Heyney method is used to solve the equations (3.1 - 3.4). The method consists in solving the system of equations by imposing a set of test values (in our case, $P(M_r)$, $R(M_r)$, $T(M_r)$, $l(M_r)$) and then applying iterative corrections.

Let us write the previous four differential equations as:

$$\frac{dy^i}{dm} = f^i(m, y^1, ...y^4), \tag{3.7}$$

where i correspond to a mesh point of mass m^i and $y^1...y^4$ are the dependent variables (P, R, T, l).

Discretizing the equations (3.7):

$$A^i_j = \frac{y^i_{j+1} - y^i_j}{m_{j+1} - m_j} - f^i(m_j, m_{j+1}, y^1_j, y^1_{j+1}, ...y^4_j, y^4_{j+1}), \tag{3.8}$$

where f^i are computed by calculating mean values between times j and *j+1*.

The solution would be reached if the condition $A_j^i = 0$ is fulfilled for all j. In reality, however, $A_j^i = c_j^i \neq 0$, and the system is solved by modifying test values of y_j^i in order to fulfill the condition: $c_j^i \leq \epsilon$ for all j and i (where ϵ is the desired accuracy). The solution $P(M_r)$, $R(M_r)$, $T(M_r)$, $l(M_r)$, $\rho(M_r)$, and $X_i(M_r)$ at a given time t for all M_r ϵ [0,M] is referred to as a **stellar model**

Time-dependent equations related to burning and mixing are solved between two evolutionary models. The burning and mixing timesteps are subdivisions of the evolutionary timestep and structure quantities such as temperature and pressure are kept constant. Mixing and burning can be solved simultaneously, making it possible for GARSTEC to follow proton ingestion episodes when the mixing and burning timescales are comparable.

3.2 Physical Input

In this section the main physical ingredients used in the stellar evolution codes will be discussed.

3.2.1 Opacity

The propagation of radiation through a medium is affected by absorption, emission and scattering processes. Absorption is the removal of radiation by a process which changes the degrees of freedom of an atom or molecule. One example of this process is the bound-bound absorption, in which a photon is removed from the radiation beam by an atom, leading to the excitation from one bound state to another bound state. A measurement of the amount of absorption (including scattering) in a certain medium is given by its opacity (κ $[cm^2g^{-1}]$[1]). The opacity depends on the wavelength and on the conditions in the medium (temperature, density, and chemistry): $\kappa_\nu = \kappa_\nu(T, \rho, \mu)$.

At the present time, due to high computational cost, opacities can not be calculated in the evolutionary code for a given density, temperature, and frequency. Instead, what it is done is to use tabulated Rosseland[2] mean opacities. For each set of chemical composition (X,Y,Z) opacities are stored in tables for a grid of temperature and density. In the code, the opacity at a given grid point is obtained through interpolation of the existing table in the temperature-density space.

For high temperatures we used opacities tables from Iglesias & Rogers (1996) (OPAL96). In the low temperature regime, molecules must be taken into account as an opacity source. In Alexander & Ferguson (1994) and Ferguson et al. (2005) the molecular opacities are calculated assuming a solar-scaled composition for the metals, and composition changes in the metal-group elements are not considered.

At high temperatures, the mean opacity is dominated by free-free and bound-free transitions from atoms. As the temperature decreases the atoms become more neutral, decreasing their importance as an opacity source. On the other hand, molecules are formed, becoming

[1]Definition: $\rho\kappa = n\sigma$, where σ is the cross section for scattering/absorption of radiation and n is the absorber density.

[2]Definition: $1/\kappa = \frac{\int_0^\infty \frac{1}{\kappa_\nu} \frac{\partial B_\nu}{\partial T} d\nu}{\int_0^\infty \frac{\partial B_\nu}{\partial T} d\nu}$, where κ_ν is the monochromatic opacity and B_ν is the Planck function.

the main source of opacity, with the H_2O molecule being the most important source in the temperature range $3.0 \leq \log T \leq 3.4$.

During the TP-AGB phase carbon is brought to the surface by the third dredge-up and the stellar envelope changes from the oxygen-rich to the carbon-rich (C/O > 1) regime. In the former regime, the envelope is dominated by molecules such as H_2O, TiO, while in the latter oxygen is bound in CO and molecules such as CN and C_2 are formed from the remaining carbon (Weiss & Ferguson 2009). The increase in carbon abundance leads to a decrease in the oxygen (now bound to carbon) available for water molecules, and therefore to a decrease in the mean opacity at temperatures important for absorption by H_2O. The available CN starts to dominate the mean opacity at the temperature range $3.2 \leq \log T \leq 3.6$.

Marigo (2002) has shown the influence of molecular opacities with varying C/O ratios in the envelope structure of AGB stars, using analytical fit relations for the opacities in a synthetic TP-AGB code. This work was able to reproduce several observational properties of C-rich stars in the solar neighborhood, where other models failed as they considered the changes in C/O only as an increase in the overall metallicity. Weiss & Ferguson (2009), on the other hand, published the first large grid of full AGB models using opacities tables for different C/O ratios. They found that for the same metallicity, the variable C/O opacities leads to higher effecive temperature ($T_{\rm eff}$), compared to the fixed C/O opacities, while the C/O-ratio is less than 1. When the ratio is larger than unity the $T_{\rm eff}$ for the variable case starts to decrease in comparison to the fixed one.

Differences in the effective temperature lead to differences in the mass-loss, thus, differences in the duration of the TP-AGB phase. The efficiency of the third dredge-up is also affected by the different treatment of opacities. Consequently, the surface abundance patterns derived from the calculations using variable C/O opacities differ from the ones using fixed-C/O.

Weiss & Ferguson (2009) have shown that C-enriched opacities have an important effect in the AGB evolution even for stars with metallicity down to $Z = 0.0005$. Similar results were obtained by Cristallo et al. (2007) for a slightly lower metallicity ($Z = 0.0001$), using the molecular opacities of Lederer & Aringer (2008). Although our models have much lower initial metallicities than those of Weiss & Ferguson (2009), they undergo a proton mixing episode in the early phases of the TP-AGB that results in surface enrichment in C, N, and O isotopes. This enrichment increases the envelope abundance to the level of $Z \sim 0.0001$. Thefore, the AGB evolution of extremelly metal-poor and metal-free stars should be strongly affected by the opacity treatment used.

The AGB calculations performed in this thesis use the opacities with varying C/O ratios (implemented by Kitsikis 2008), unless stated otherwise, since it is consistent with the carbon enhancement caused by the third dredge-up.

3.2.2 Nuclear Network

The version of GARSTEC from Weiss & Schlattl (2008) follows the evolution of stable isotopes involved in the p-p chain, the CNO cycles, and the standard helium burning reactions. For this work the network in GARSTEC has been extended to include all relevant nucleosynthesis processes for intermediate mass elements ($A < 30$) during H-burning. This is

important because it has been suggested that in metal-free primordial stars elements in this mass range can be produced during H-burning (e.g. by NeNa and MgAl chains) and then act as seeds for the s-process (Goriely & Siess 2001). Also, reactions that govern the production of neutrons during the He-burning have been incorporated in the network. In total, the network comprises 34 isotopes linked by 120 reactions, including proton, alpha, and neutron captures, and beta decays (See Figure 3.1 for a list of isotopes involved in the network).

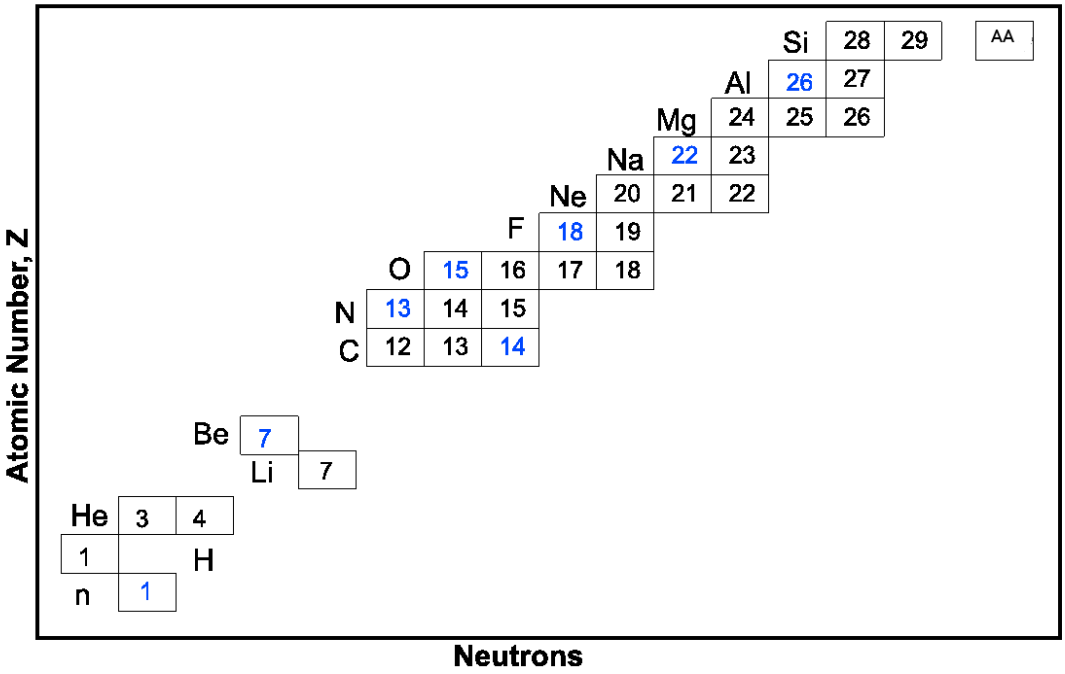

Figure 3.1: Isotopes considered in the nuclear network used in the evolutionary code. The stable isotopes are in black and the unstable isotopes are in blue.

The ground state and the meta-stable state of ^{26}Al were treated as two separated isotopes in the network ($^{26}\mathrm{Al_g}$, $^{26}\mathrm{Al_m}$). In order to accurately compute the abundance of neutrons during the evolutionary calculations, the effect of neutron captures on all isotopes not included in the network is accounted for by using a neutron sink, which we call ^{30}AA, as described in Jorissen & Arnould (1989). The number fraction and the neutron capture cross-section of the sink are given by

$$Y_{AA} = \sum_{i=^{30}\mathrm{Si}}^{^{211}\mathrm{Po}} Y_i \tag{3.9}$$

$$\sigma_{(AA,n)} = \sum_{i=^{30}\mathrm{Si}}^{^{211}\mathrm{Po}} \frac{Y_i \sigma_{(i,n)}}{Y_{AA}}, \tag{3.10}$$

respectively, where the summation extends over all the relevant isotopes not included in the evolutionary calculations.

One of the difficulties in the neutron sink approach is the calculation of the sink cross-section ($\sigma_{(\mathrm{AA,n})}$), which has to be known beforehand in order to get accurate estimates of the number of neutrons captured by heavy elements in the evolutionary calculations. This cross-section, however, depends on the distribution of heavy elements, and therefore on the neutron capture path. Thus, detailed s-process calculations are necessary to estimate values for $\sigma_{(\mathrm{AA,n})}$.

In AGB stars with metallicity [Fe/H] > -2.5, s-process happens in a radiative environment and the typical neutron exposure is smaller than 1.0 mbarn^{-1}. A fixed value for $\sigma_{(\mathrm{AA,n})}$ of 80 mbarn can reproduce the neutron exposure from the parametrized s-process calculation within 10%. A better agreement is achieved using a fitting formula for the cross-section as a function of the neutron exposure based on the parametrized calculation (Figure 3.4). In EMP stars, during the PIE, neutrons are produced and consumed in convective regions. The large ingestion of protons that occurs in EMP stellar models, either during the core He-flash for low stellar masses or early in the AGB for intermediate mass-stars leads to the production of a significant amount of ^{13}C through the reaction $^{12}\mathrm{C}(\mathrm{p},\gamma)^{13}\mathrm{N}(\beta^-)^{13}\mathrm{C}$ and might result in neutron exposures much larger than those achieved in more metal-rich stars. In order to test the dependence of the neutron exposure on the choice of $\sigma_{(\mathrm{AA,n})}$ in this case, we have used the abundance of light elements from evolutionary calculations of EMP stars with 1 $\mathrm{M}_\odot$.

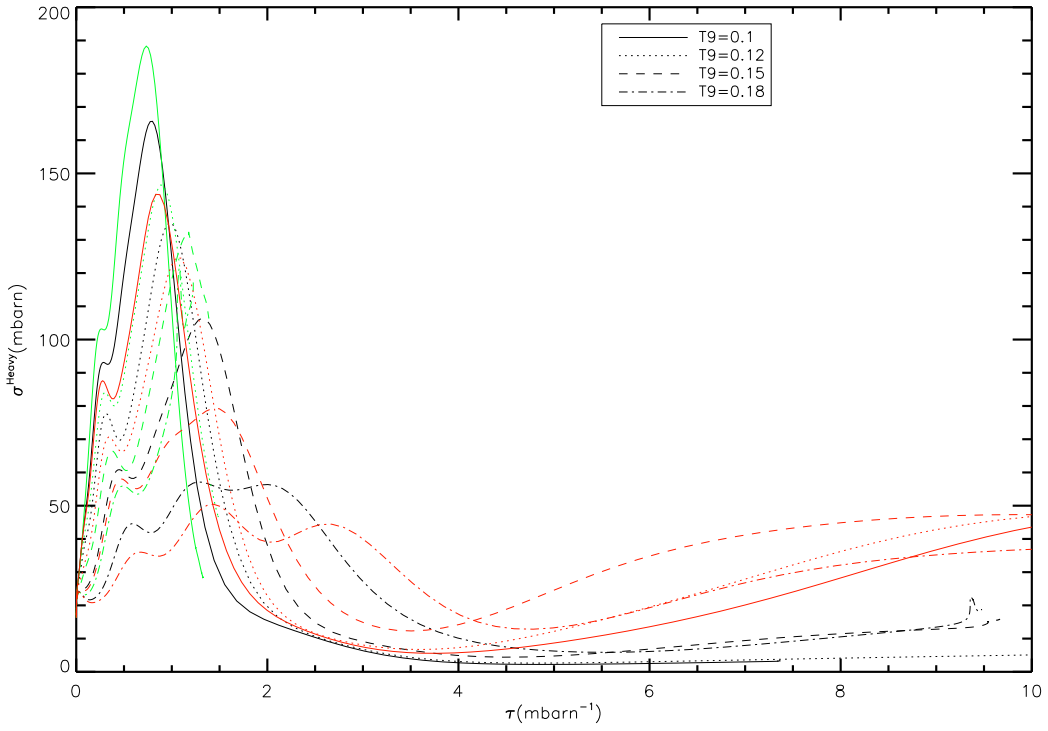

Figure 3.2: Neutron cross-section of the sink particle as a function of neutron exposure for different temperatures and compositions. Green line: C2 composition, black line: C1 composition, and red line: C3 composition. For details on the composition see Table 3.1.

Under the conditions reigning during the PIE in the core He-flash, the choice of a fixed value for $\sigma_{(\mathrm{AA,n})}$ should have little influence in the resulting neutron exposure. The reason

is the following. We assume for our extremely metal poor models a solar scaled abundance pattern with initial metallicity Z = 10^{-8}. When protons are ingested into the helium-burning region during the PIE, light metals have already been produced. These primary metals, predominantly carbon, amount to a mass fraction of about 0.05 and they are about 10^8 times more abundant than metals with A≥30. The average neutron cross-section for the light and heavy elements are 0.01 mb and 1000 mb, respectively. Therefore, the average contribution to the neutron capture by light elements is much larger than by heavy elements in such environment. We estimate $\sigma_{\rm light}{\rm X}_{\rm light}/\sigma_{\rm heavy}{\rm X}_{\rm heavy} \sim 1500$.

In order to test this, we have performed network calculations (we refer to these calculations in the text as parametrized s-process calculations) for fixed values of temperature and density in the ranges T = $1.0 - 2.5 \times 10^8$ K and $\rho = 100 - 5000$ g cm^{-3}, respectively. In the parametrized s-process network calculations we have combined the small network used in the evolutionary code with the s-process network used in the post-processing unit in order to check the difference between using the sink approach and solving a full network. In these calculations 613 isotopes, from neutrons to ^{211}Po, were used. Proton and alpha captures were included for the light elements (A < 30), while neutron captures were included for all isotopes. The initial distribution of metals is as follows: for metals with A ≥ 30 we take a solar distribution pattern that has been scaled down to reflect an initial total metallicity Z = 10^{-8}, whereas for metals with A < 30 abundances are taken from the stellar model at the moment and location in which the PIE takes place. The only exception is for ^{13}C that determines the neutron flux, for which we have assumed two different mass fraction values, 10^{-2} and 10^{-4}. In Figure 3.5 we show, for the case T = 10^8 K and $\rho = 500$ g cm^{-3}, the evolution of the resulting neutron exposures where we compare results of the full parametric calculations with two calculations with a neutron sink. In one of them $\sigma_{\rm (AA,n)}$ is fixed to 80 mb and in the other $\sigma_{\rm (AA,n)}$ is given as a function of the neutron exposure as obtained from the full parametric calculation. Differences between the full parametric study and the two calculations using the neutron sink approach are smaller than a few parts per thousand, negligible for practical purposes.

Composition	^{13}C	$A > 30$
$C1$	1.6×10^{-1}	$solar$
$C2$	4.5×10^{-4}	$solar - scaled/Z = 10^{-8}$
$C3$	4.5×10^{-2}	$solar - scaled/Z = 10^{-8}$
$C4$	4.5×10^{-4}	0.0

Table 3.1: Initial compositions for the parametrized s-process calculations. The C1 composition is the same used by Jorissen & Arnould (1989). C2 represents the typical composition in our evolutionary models of a one solar mass star with metallicity Z = 10^{-8}. C3 is similar to C2, except for the ^{13}C abundance.

Figure (3.2) shows the dependence of the cross-section of the sink particle with the neutron exposure for different temperatures and initial compositions. For $\tau < 0.05$ mbarn^{-1}, the neutron path is the same in all considered conditions. When the neutron exposure is larger than this value, the details of the neutron-capture path start to depend on the physical conditions, as can be seen in the separation of the curves. Figure (3.3) shows that the higher the temperature the flatter the dependence of $\sigma_{\rm AA}$ with the neutron exposure. This is due to the fact that, at higher temperatures the neutron fluxes are larger, leading to neutron paths that involve more neutron-rich nuclei with smaller cross sections. For the composition C2

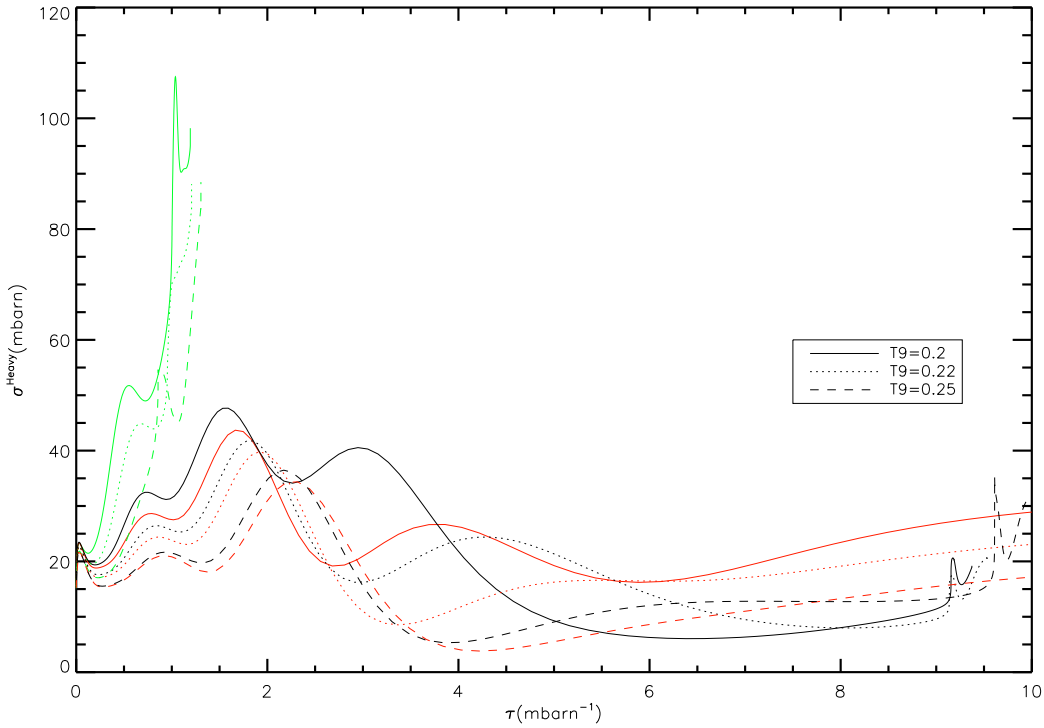

Figure 3.3: Description is the same as in Figure (3.2).

this does not happen, because its maximum neutron flux is around two orders of magnitude smaller than in the C1 and C3 cases, due to its lower ^{13}C abundance.

For the solar composition Jorissen & Arnould (1989) have shown that the use of a fixed value for $\sigma_{\rm AA}$ can lead to differences up to 60% between the full s-process calculations and the sink approach. However this large difference occurs for neutron exposure values larger than 1.0 mbarn^{-1}, which are never achieved in the radiative ^{13}C pocket during the AGB phase.

In our calculations the cross-section used is a function of the neutron exposure ($\sigma_{\rm (AA,n)}(\tau)$) and was estimated based on network calculations using a solar-scaled initial composition for isotopes with A$\geq$30 and the abundances obtained from the modeling of the PIE for the lighter isotopes.

The reaction rates used for the isotopes are mainly from the NACRE (Angulo et al. 1999) compilation and from the JINA REACLIB library (Cyburt et al. 2010) with the following exceptions:

- $^{14}N(p,\gamma)^{15}O$ rate - Adelberger et al. (2011);
- $^{17}O(p,\gamma)^{18}F$ and $^{17}O(p,\alpha)^{14}N$ rates - Moazen et al. (2007);
- $^{22}Ne(p,\gamma)^{23}Na$ - Hale et al. (2002);
- $^{23}Na(p,\gamma)^{24}Mg$ and $^{23}Na(p,\alpha)^{20}Ne$ rates - Hale et al. (2004);
- $^{13}C(\alpha,n)^{16}O$ - Kubono et al. (2003);

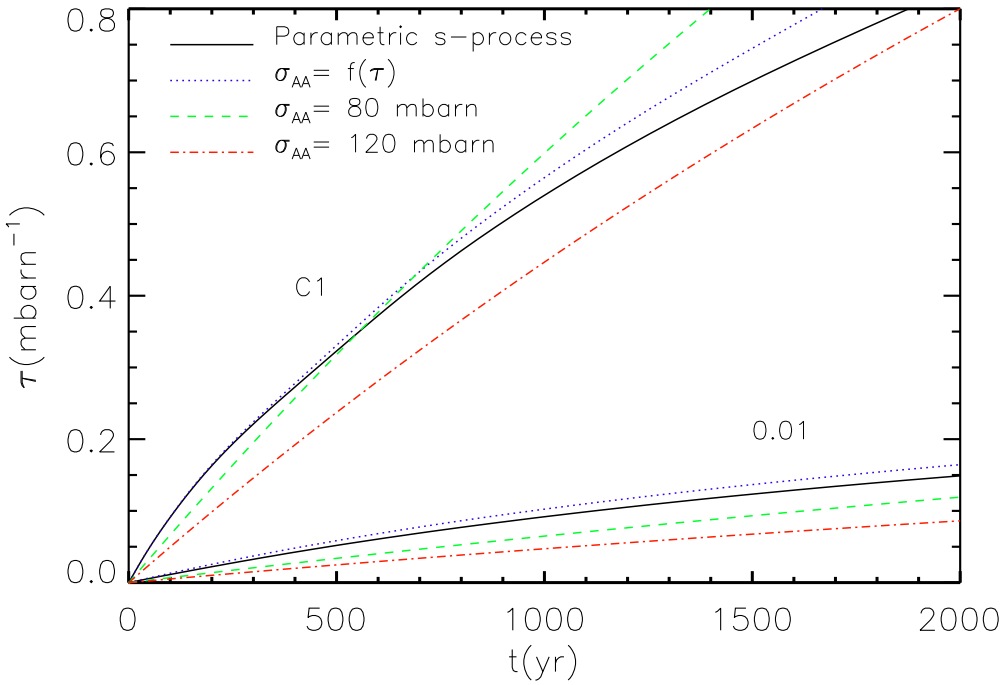

Figure 3.4: Neutron exposure calculated using the parametrized s-process network in comparison with the sink approach for different values of cross-section: Two cases with fixed cross-section values and one case in which the cross-section was calculated as a function of the neutron exposure. Physical conditions used in this calculations: $\mathrm{T} = 10^8\mathrm{K}$, $\rho = 500\ \mathrm{gcm}^{-3}$. Initial compositions are indicated in the plot. The lines with labe "0.01" have the same initial composition as C1 except for the $^{13}\mathrm{C}$ mass fraction which is equal to 0.01.

- $^{22}Ne(\alpha,n)^{25}Mg$ - Jaeger et al. (2001);
- $^{12}C(\alpha,\gamma)^{16}O$ - Kunz et al. (2002).

3.2.3 Mass-Loss

One of the main uncertainties in the stellar evolution calculations is the mass-loss. Observations support the idea that negligible mass is lost during the Main Sequence. On the other hand, mass-loss plays an important role in cool giants (RGB and AGB stars): Winds are driven by radiation pressure on the dust grains formed in their cool atmospheres. Several observational studies have found a correlation between the mass-loss rate and the pulsation period of AGB stars (Schöier & Olofsson 2001; Whitelock et al. 2003; Winters et al. 2003), supporting the idea that mass-loss is enhanced by the pulsation occurring in this evolutionary stage.

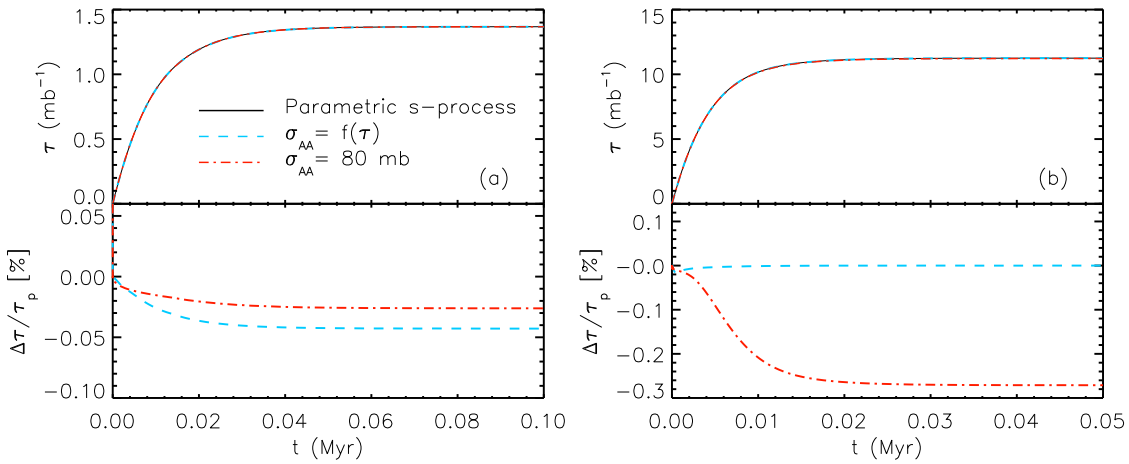

Figure 3.5: Neutron exposure calculated using the parametrized s-process network in comparison with the sink approach for different values of cross-section: Two cases with fixed cross-section values and one case in which the cross-section was calculated as a function of the neutron exposure. Physical conditions used in this calculations: $\mathrm{T} = 10^8\mathrm{K}$, $\rho = 500\ \mathrm{gcm}^{-3}$. Panel (a) refers to the initial composition C2, while panel (b) refers to initial composition C3.

The rate at which mass is lost during the AGB evolution varies from $10^{-8}\mathrm{M}_{\odot}\mathrm{yr}^{-1}$ to $10^{-4}\mathrm{M}_{\odot}\mathrm{yr}^{-1}$ and it is usually estimated from infrared color indices or molecular CO rotational lines.

The most used mass-loss prescription in evolutonary calculations is the empirical relation for RGB stars derived by Reimers (1975):

$$\dot{M}(M_{\odot}yr^{-1}) = 4 \times 10^{-13}\eta_R \frac{(R/R_{\odot})(L/L_{\odot})}{(M/M_{\odot})}, \tag{3.11}$$

where L is the luminosity, R is the radius, and M is the mass of the star. η_{R} is the Reimers parameter.

We adopted ($\eta_{\mathrm{R}} = 1.0$) for intermediate-mass stars in agreement with Bloecker (1995) and ($\eta_{\mathrm{R}} = 0.4$) for low-mass stars in agreement with Karakas & Lattanzio (2003) and Campbell & Lattanzio (2008). This prescription is used in all evolutionary phases, although in the AGB phase it is used only when its contribution for the mass-loss is more important than the contribution from dust-driven wind.

Over the past decade, models of dust-driven winds have been developed, leading to the conclusion that the high AGB mass-loss rate observed is a result of the interaction between the pulsation and dust grains formed in the atmosphere. Observations corroborate this idea since all stars with dust-driven winds show pulsations (Willson 2000).

Vassiliadis & Wood (1993) derived an empirical formula based on observations of AGB stars, correlating the mass-loss rate and the pulsation period, which is largely used in AGB modelling. However, this and other early formulations (Bloecker 1995; Bowen 1988) did not take into account the chemistry of the dust formation process which is strongly temperature dependent (Wachter et al. 2002).

Wachter et al. (2002) derived mass-loss rate for solar metallicity using dynamical wind models for dust-forming carbon-rich atmospheres. This work includes detailed descriptions of formation, growth and evaporation of dust grains. They provide fitting formulae for the mass-loss rate depending on the stellar parameters ($T_{\rm eff}$,log(L),$M_\star$). Mattsson et al. (2010) argued that the use of fitting formulae for the mass-loss rates that take into account only the stellar parameters may not be correct. These fitting formulas do not take into account the mass-loss dependence with the amount of condensible carbon ($\epsilon_{\rm c}$), for instance. Mattsson et al. (2010) calculations shows an increase in the mass-loss rate by an order of magnitude if $\epsilon_{\rm c}$ is increased by a factor of five.

In a more recent study, Wachter et al. (2008) performed mass-loss simulations for lower metallicities (Z=0.001 and Z=0.01) stars. They have concluded that lower metallicities do not result in lower mass-loss rates. The average mass-loss rates found in their models are very similar to the solar ones. This result was confirmed by Mattsson et al. (2008) simulations using an independent wind code. In the light of this, extremelly metal-poor and metal free AGB stars might have non-negligible mass loss, since their envelope metallicity is increased up to Z=0.0001 already in the beggining of the TP-AGB phase due to the proton ingestion episode and continue to increase throughout the TP-AGB evolution.

In our calculations the mass-loss rate derived by (Wachter et al. 2002) is used in stellar evolution code during the TP-AGB phase for stars with pulsation period P > 100 days. Previous AGB calculations using this mass-loss prescription adopted a limiting period of P > 400 days (Kitsikis 2008). This cutoff period was used in order to be consistent with the O-rich prescription adopted, which is valid only for this regime. In the calculations performed by Weiss & Ferguson (2009) the stars were still in the O-rich regime when the pulsation period reached 400 days, thus the choice of P=400 days as a critical period also for C-rich regime did not imply any additional error. In contrast, in the metal-poor regime, due to extra proton mixing, the envelope is quickly enriched with carbon isotopes in the beginning of the TP-AGB phase. The choice of a smaller cutoff period is more consistent with the carbon enrichment in this case.

The prescription is given as a function of the stellar parameters:

$$log(\dot{M}) = -4.52 + 2.47\log\left(10^{-4}\frac{L}{L_\odot}\right) - 6.81\log\left(\frac{T_{eff}}{2600K}\right) - 1.95\log\left(\frac{M}{M_\odot}\right). \qquad (3.12)$$

For the oxygen-rich regime the empirical relation from van Loon et al. (2005) was adopted:

$$log(\dot{M}) = -5.65 + 1.05\log\left(10^{-4}\frac{L}{L_\odot}\right) - 6.3\log\left(\frac{T_{eff}}{3500K}\right). \qquad (3.13)$$

3.3 Overshooting

Convection is usually described in stellar evolution calculations by the Mixing Length Theory (MLT). In the MLT, the fluid element loses its identity and mixes with the surroundings after traveling a certain distance, the mixing length. The mixing length is treated as a

free parameter in the evolutionary code. In fact, the mixing length parameter $\alpha_{\rm MLT}$, defined as the ratio between the mixing length and the pressure scale height[1], is the adjustable parameter in the code and is calibrated using a solar model. The unstable regions of a star are, then, defined by means of the Schwarzschild criterion: if $\nabla_{\rm rad} < \nabla_{\rm ad}$ the region is considered stable. $\nabla_{\rm ad}$ is the temperature gradient when the bubble moves adiabatically.

The convective boundary is defined at the point of neutral stability ($\nabla_{\rm rad} = \nabla_{\rm ad}$), where the acceleration of the fluid element is zero. However, at this layer the fluid element has non-zero velocity and, therefore, is able to travel (overshoot) beyond the convective boundary. A crucial problem rises then: How far is the extension of the mixing beyond the formal convective boundaries? The usual approach to answer this question is to introduce a free parameter which is a fraction of the pressure scale height, representing the amount of penetration into the stable regions, and calibrate it using observables affected by the inclusion of overshooting. Schaller et al. (1992) found that in order to reproduce the observed main sequence width using instantaneous mixing in the overshooting region a value of $\rm d_{over}/H_p = 0.2$ should be adopted to the overshooting parameter.

The two-dimensional numerical radiation hydrodynamics simulations performed by Freytag et al. (1996) have shown extra mixing beyond the Schwarzschild borders. Moreover, they found that the velocity declines exponentially at the stable region and that the mixing in the overshoot region can be described as a diffusive process. In GARSTEC a relation between the diffusion coefficient and the depth of the convective zone was derived.

$$D = D_0 e^{\frac{-2z}{f H_p}}, \tag{3.14}$$

where z is the distance from the border of the convective zone, $\rm H_p$ is the pressure scale height, $\rm D_0$ is the diffusion coefficient near the edge of the convective zone, and f is a free parameter.

Freytag et al. (1996) found from their simulation a value of f=0.25 for convective envelopes of A-stars and f=1.0 for DA white dwarfs, showing that f strongly depends on the stellar parameters. Herwig et al. (1997) on the other hand, found that an overshooting parameter of f=0.016 reproduces the observed main sequence width. In this same study they found that the application of the diffusive overshooting during the AGB results in the occurrence of the third dredge-up in low-mass stars.

Another important issue regarding overshooting is that it does not have the same efficiency in all convective borders. For instance, in order to reproduce the solar s-process abundance patterns Lugaro et al. (2003) have shown that the overshooting parameter value at the bottom of the pulse-driven-convective-zone (PDCZ) should be smaller than the value used at the base of the convective envelope.

In this thesis diffusive overshooting as described by Freytag et al. (1996) is used in all convective boundaries. One single value for the free parameter f is used, unless stated otherwise. When applied, overshooting is considered in all evolutionary phases.

[1] $\alpha_{\rm MLT} = \ell/\rm H_p$

Chapter 4

SPNUC: The s-process Code

In this chapter we will give a brief description of the post-processing s-process code. The code solves a nuclear network which contains neutron capture and beta decay reactions between isotopes heavier than ^{29}Si between two stellar models. We have used the s-process network provided by Dr. Aldo Serenelli in the post-processing code.

The calculation of s-process nucleosynthesis coupled to an evolutionary code is quite time consuming, since a s-process network contains hundreds of isotopes. A post-processing unit, which uses the thermodynamical output from an evolutionary code as input to solve the network, is then the favored choice when simulating s-process.

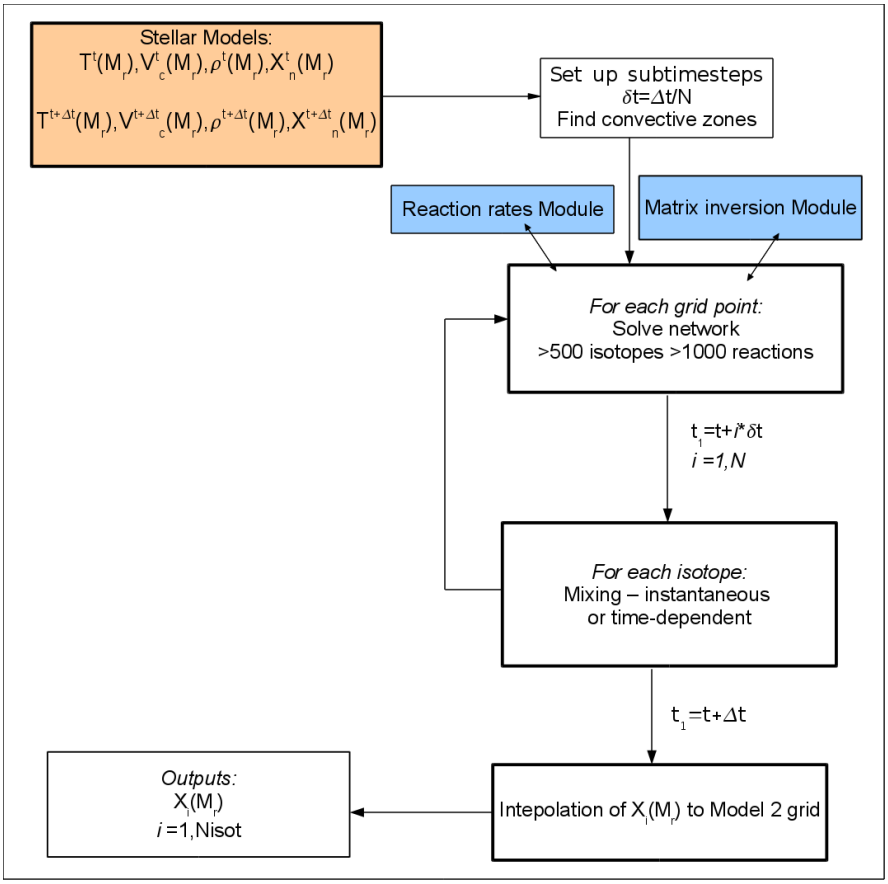

Figure 4.1: Schematic diagram of the post-processing code. The code uses the thermodynamical information from two stellar models, separated by Δt, as input for the network. The network is solved for each grid point. The mixing is done after each subtimestep (δt).

The post-processing code uses the model structure (temperature, density, neutron abundance, and convection velocity) from evolutionary calculations as input for the s-process calculations. The calculations are done between two structural models and the evolutionary timestep between them is divided into smaller burning and mixing steps. All structural quantities are kept constant between the two stellar models (Figure 4.2). Within each substep, we first compute changes in chemical composition due to nuclear burning and then mix the convective (and overshooting) regions.

During the PIE the burning and mixing timescale might be comparable, therefore, the use of a time-dependent mixing scheme is required. We adopted the time-dependent mixing prescription described in Chieffi et al. (2001).

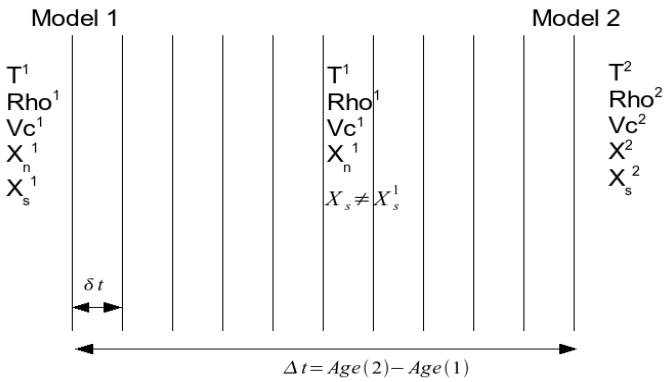

Figure 4.2: Schematic diagram of the code. This figure shows the divison of the evolutionary timestep into smaller burning timesteps. For each burning timestep the physical quantities are kept constant and equal to the values of Model 1.

$$\mathrm{X_i^k} = {}^0\mathrm{X_i^k} + \frac{1}{\mathrm{M_{mixed}}} \sum_{\mathrm{j=mixed}} ({}^0\mathrm{X_j^k} - {}^0\mathrm{X_i^k})\mathrm{f_{ij}}\Delta\mathrm{M_j}, \tag{4.1}$$

where the sum extends over the mixed region (including overshooting regions if present), $\Delta\mathrm{M_j}$ is the mass of the shell j, ${}^0\mathrm{X_i^k}$ and ${}^0\mathrm{X_j^k}$ are, respectively, the abundances of isotope k in the shells i and j before mixing, $\mathrm{M_{mixed}}$ is the mass of the entire mixed region, and $\mathrm{f_{ij}}$ is a damping factor given by

$$\mathrm{f_{ij}} = \min(\frac{\Delta\mathrm{t}}{\tau_{\mathrm{ij}}}, 1) \tag{4.2}$$

that accounts for partial mixing between zones i and j when the mixing timescale between them, τ_{ij}, is longer than the timestep used in the calculations, Δt. Here, τ_{ij} is assumed to be the convective turn-over timescale between grid points i and j and the convective velocity is determined using MLT. With this scheme we account for partial mixing occurring when the convective turn-over timescale between two shells in the model is longer than the mixing timestep.

4.1 The network

A s-process network consists of a system of ordinary differential equations as described below:

$$\frac{dY_i}{dt} = \sum_j N_j^i \lambda_j Y_j + \sum_j N_{j,n}^i \rho N_A \langle \sigma v \rangle_{j,n} Y_j Y_n, \tag{4.3}$$

where Y_i is the mole fraction, definied as $= X_i/A_i$, being X_i the mass fraction and A_i the atomic mass $[gmole^{-1}]$. The numerical factors are:

$N_j^i = N_i$,

$N_{j,n}^i = N_i/(|N_j|!|N_n|!)$,

where the numbers, N_m, are positive or negative and specify the number of isotopes m created (positive) or destroyed in the reaction.

The categories of thermonuclear reactions involved in equation (4.3) are:

1. Decays, photodisintegrations, electron and positron captures ($\rightarrow \lambda_j$)

2. Two-particle reactions ($\rightarrow N_A\langle\sigma v\rangle_{j,n}$) - in our case neutron capture reactions

Reactions rates were taken from different sources. The majority of them are used in the parametrization formula of Thielemann et al. (1987):

$$r = exp[a_0 + a_1/T_9 + a_2(T_9^{-1/3}) + a_3(T_9^{1/3}) + a_4T_9 + a_5(T_9^{5/3}) + a_6lnT_9], \tag{4.4}$$

where $T_9 = T/10^9$, and a_i are the coefficients varying for each reaction.

The values for the coefficients a_i were taken mainly from the JINA database[1] (Cyburt et al. 2010), which uses the most up to date experimental and theoretical cross-sections to derive the coefficients values, or were calculated by Dr. Aldo Serenelli using the newest measurements of neutron capture cross-section by the KADONIS 3.0 project (Dillmann et al. 2006). Weak interactions rates (electron captures and β decays) were taken mainly from Takahashi & Yokoi (1987) and are interpolated as a function of temperature and electron density. At temperatures lower than 10^6 K we assumed a constant value equal to the laboratory value.

The network used in the code is softwired, making changes in the number of isotopes and reactions used, easy to perform. It was written and kindly provided by Dr. Aldo Serenelli.

Since the neutron fluxes achieved in the calculations presented in this thesis are much higher than the "canonical" AGB values ($N_n > 10^{14}$ cm^{-3}), the isotopes were selected way beyond the valley of beta stability. In a crude estimate, the timescale for neutron capture is given by:

$$\tau = \frac{1}{Y_n\rho < \sigma v > Na}, \tag{4.5}$$

where $Y_n\rho$Na is the neutron density, Na is the Avogrado constant, Y_n is the neutron number fraction, and σ is the neutron capture cross-section. For typical temperatures during the AGB phase, a neutron density equal to 10^{14}cm^{-3} and an average neutron cross-section of $< \sigma > \sim$ 1000mb, the neutron capture timescale is approximately $\tau \sim$ 3s.

All isotopes with decay lifetimes comparable or longer to the lifetime against neutron captures have been included in the network, leading to a network with 580 isotopes and more than 1000 reactions.

[1] http://groups.nscl.msu.edu/jina/reaclib/db/

Branching points

If the β decay rate is comparable to the neutron capture one, a branching appears in the s-process. Branching points can also appear when there is a competition between β^+ and β^- rates, or when the nucleus decay rate has a strong dependence with temperature and/or density, and it can also appear when isomeric states can be produced.

Sometimes the excited state of a nucleus does not de-excite rapidly to the ground state. This excited nucleus is known as isomer and its existence leads to ramifications of the s-process (Ward, Newman & Clayton 1976). Figure (4.3) shows an important s-process branching point, which involves the isomeric state of ^{85}Kr. The probability for the neutron capture onto ^{84}Kr to result in the isomeric state of ^{85}Kr is given by the isomeric ratio (IR):

$$IR = \frac{\sigma(^{84}Kr(n,\gamma)^{85}Kr^{m})}{\sigma_{tot}(^{84}Kr(n,\gamma)^{85}Kr)} = 0.42 \tag{4.6}$$

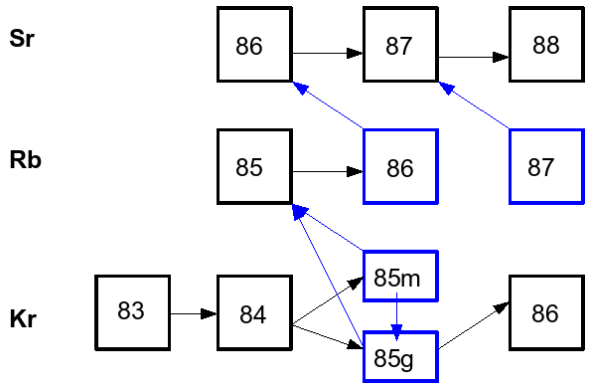

Figure 4.3: Krypton branching point is shown. Black boxes indicate stable isotopes, while blue unstable ones. Black arrows represent neutron capture reactions while the blue ones represent beta decays.

If the nucleus is non-thermalized the isomeric and the ground states must be treated as two separate isotopes. Other isomeric states included in our calculations are: ^{113}Cd, ^{115}Cd, ^{114}In, ^{115}In, ^{148}Pm, ^{176}Lu, ^{180}Hf, ^{180}Ta.

4.2 The number of subtimesteps

We have performed calculations varying the number of subtimesteps in order to test the abundances dependence with this parameter. As explained before, the code takes the evolutionary timestep (Δt) between two subsequent models and divide it into smaller subtimesteps (δt - Figure 4.2). We have chosen two stellar models with different neutron densities (10^7cm^{-3} and 10^{14}cm^{-3}), during the PIE of a 1M$_\odot$ star with metallicity Z = 10^{-8}. We did not evolve the test calculations through the entire PIE evolution, instead, we evolved each stellar model only one timestep (Δt) forward.

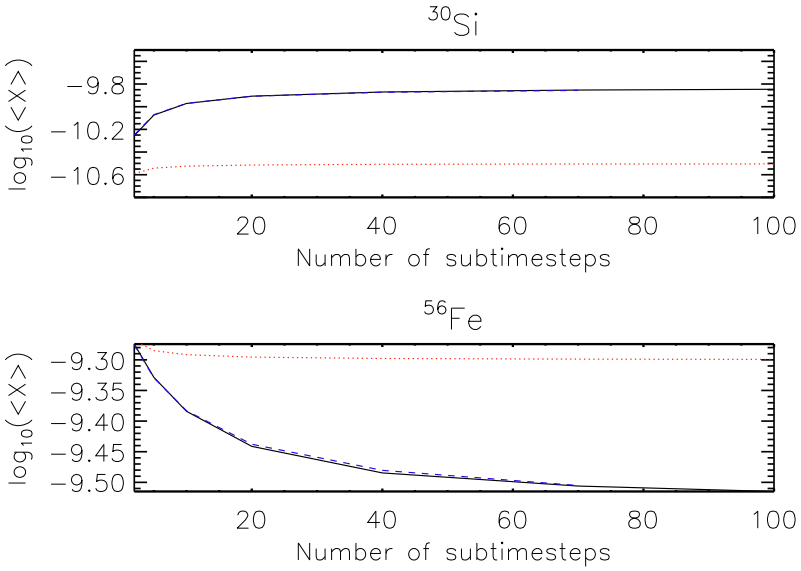

Figure 4.4: The mass-fraction averaged over the helium convective zone as a function of the number of subtimesteps for the isotopes: ^{30}Si and ^{56}Fe. The black line represents the case with $\mathrm{N_n} = 10^{14}\mathrm{cm}^{-3}$, while the red line represents the case with $\mathrm{N_n} = 10^{7}\mathrm{cm}^{-3}$. The blue line indicates the calculations using a diffusive mixing scheme for the case with $\mathrm{N_n} = 10^{14}\mathrm{cm}^{-3}$.

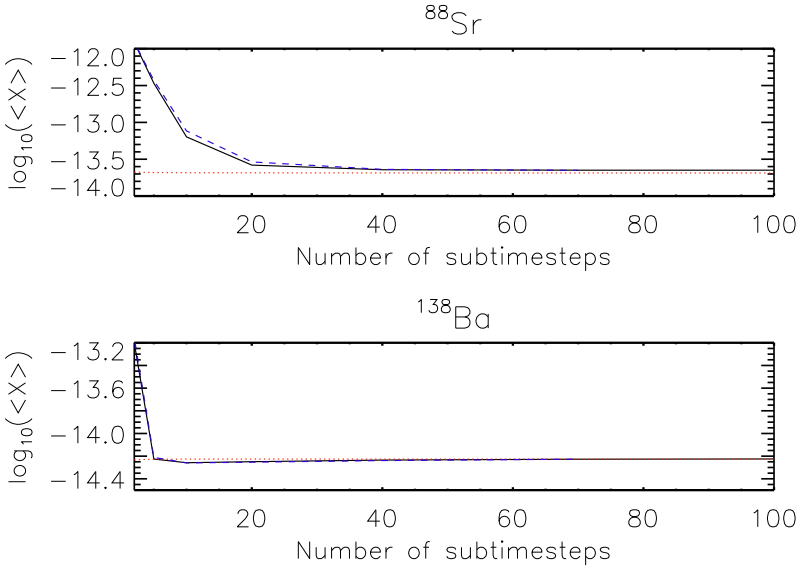

Figure 4.5: Same as Figure 4.4 for isotopes: ^{88}Sr and ^{138}Ba.

Figures 4.4 and 4.5 shows the abundance for some selected stable isotopes averaged over the convective zone. When the neutron density is $10^{7}\mathrm{cm}^{-3}$ the number of subtimesteps used has no influence in the final abundances. For neutron densities larger than the canonical AGB value, the difference between dividing the timestep into two or more subtimesteps can

be larger than one order of magnitude. Different isotopes converge for different number of subtimesteps (Figures 4.4 and 4.5). Therefore, we decided to divide the timesteps into 50 subtimesteps in order to be closer to the convergence values for most of the isotopes. We have also tested a diffusive approach for the mixing scheme (Blue lines in Figures 4.4 and 4.5).

Diffusive Mixing

Convection in stars is in general highly turbulent. As discussed in chapter 2 the MLT is the most used formalism to describe convection in stellar models. Modelling the PIE requires the use of a time dependent mixing, since the H-burning timescale is comparable to the mixing timescale. In the evolutionary code, mixing is treated as a diffusive process. In this case, the equation for composition change can be written as:

$$\frac{dX_i}{dt} = \left(\frac{\partial X_i}{\partial t}\right)_{nuc} + \frac{\partial}{\partial m_r}\left(\sigma D \frac{\partial X_i}{\partial m_r}\right) \tag{4.7}$$

where $\mathrm{X_i}$ is the mass-fraction of isotopes i, $\sigma = (4\pi \mathrm{r}^2\rho)^2$ and $\mathrm{D} = -1/3\mathrm{vl_m}$ is the diffusion coefficient.

We have applied an implicit method to solve the diffusion equation and performed the mixing after each burning timestep. Figures 4.4-4.5 shows the abundance dependence with the number of subtimesteps for the diffusive approach as well. The difference between using the time-dependent scheme by Chieffi et al. (2001) and the diffusive approach is very small. For two subtimesteps, the differences can be as large as 20%. However, the differences decrease with an increasing number of subtimesteps ($\sim 1\%$).

Chapter 5

Low-Mass Stars

The bulk of this chapter forms part of an article submitted to Astronomy & Astrophysics.

5.1 Introduction

The peculiar abundance patterns observed in EMP stars are usually attributed to mass-transfer from an AGB companion. AGB stars synthesize carbon and s-process elements, during the thermal-pulses, which are brought up to the surface at each TDU. The discovery of the proton ingestion episode, however, prompted several attempts to explain the carbon enrichment in such stars by means of internal processes. In this scenario, the observed EMP star would have undergone PIE during the core He-flash and, then, polluted its own atmosphere with CNO elements in the post-PIE dredge-up. Core He-flash models have shown, however, that the resulting carbon enhancement is usually 1.0-3.0 dex larger than the observed values (Schlattl et al. 2001; Weiss et al. 2004; Picardi et al. 2004). Simulations by Fujimoto et al. (2000) indicated that s-process does not occur during the core He-flash. In these simulations, the timescale of the PIE was too short to make the s-process production viable. Thus, low-mass stars could not be the companion of most carbon enriched EMP stars, since most of these stars shows enhancement in s-process elements.

However, recent simulations by Campbell et al. (2010) have shown that PIE during the core He-flash results in a large neutron production and, therefore, in a large s-process production. A recent observational discovery also strengthened the necessity of understanding the evolution of EMP low-mass stars. A star with metallicity [Fe/H] $= -4.89$ and no enhancement in CNO elements was found in the Galactic halo (Caffau et al. 2011, 2012). This iron abundance corresponds to a total metallicity of $Z \leq 7.40 \times 10^{-7}$, which makes SDSS J102915+172927, the star with the lowest metallicity ever detected. The two hyper metal-poor stars ([Fe/H] < -5.0) found in the past decade are in fact more metal rich than SDSS J102915+17292 ($Z \sim 10^{-4}$), since they present high levels of carbon, nitrogen, and oxygen enhancement. The extremely low metallicity found for SDSS J102915+172927 puts into question the claims of a minimum metallicity required for the formation of low-mass stars (Bromm & Loeb 2003; Schneider et al. 2003).

Up to now, simulations of s-process during the PIE are limited to one mass and one metallicity ($M = 1.0M_{\odot}/Z = 10^{-8}$ - Campbell et al. (2010)). Fujimoto et al. (2000) did not

perform actual s-process calculations. In reality, they suggested the absence of s-process during the core He-flash PIE based on the short duration of this phenomenon in their models. It is important, then, to understand the nucleosynthesis during the PIE which might be an important source of s-process production during the early stages of the Galaxy. In order to do this, we have performed evolutionary and post-processing s-process calculations of low-mass stars with metallicities ($Z \leq 10^{-7}$) and explored the model uncertainties (especially convection) and their impact in the s-process.

5.2 The Models

We performed evolutionary calculations of 1 $M_\odot$ stellar models from the zero-age main sequence to the dredge-up after the PIE. The composition is solar-scaled with metallicities $Z = 0$, $Z = 10^{-8}$, and $Z = 10^{-7}$. Our "standard" models (M1, M2, M6, and M7 - see Table 5.1) do not included overshooting or metal diffusion. In order to check the s-process dependence with stellar mass, we computed an additional model with metallicity $Z = 10^{-8}$ and mass $M = 0.82M_\odot$ (M6 in Table 5.1). Due to convergence problems, it was not possible to continue the simulation beyond the H-flash for model M5.

Mixing in convective regions is modeled as a diffusive process. The diffusion coefficient in convective regions is taken as $D_c = 1/3v \times \ell$, where v is the convective velocity derived from MLT and ℓ is the mixing length. It has been suggested that during the PIE, the reactive nature of the hydrogen material adds some buoyancy to the sinking elements and this results in a reduced efficiency of the mixing (Herwig et al. 2011). We have mimicked this situation by using a reduced diffusion coefficient by dividing the above relation by 10 in a model with $Z = 10^{-8}$ (model M3 - Table 5.1).

Finaly, we have also computed additional models with metallicity $Z = 10^{-8}$ including overshooting. Overshooting has been modeled as an exponentially decaying diffusive coefficient, as described in Freytag et al. (1996), and has been included in all convective boundaries. In order to test the influence and associated uncertainties of this poorly-understood phenomenon, two values of the free parameter f that determines the extension of the overshooting regions have been chosen: $f = 0.016$ and 0.07 (models M4 and M5 respectively - Table 5.1). The first value is a standard choice for this prescription of overshooting because it gives comparable results in the main sequence as the canonical choice of 0.2 pressure scale heights (Magic et al. 2010), a value known to reproduce different observational constraints such as the the width of the main sequence observed in different open clusters. The higher value is intended to represent a case where overshooting is much larger than in convective cores and deep stellar envelopes, and closer to what was originally found by Freytag et al. (1996) for thin convective envelopes of A-type stars. Incidentally, this amount of overshooting gives the right lithium depletion in solar models (Weiss et al. 2000).

Model	Mass ($M_\odot$)	Metallicity (Z)	
M1	1.0	zero	—
M2	1.0	10^{-8}	—
M3	1.0	10^{-8}	R.M.E
M4	1.0	10^{-8}	OV.
M5	1.0	10^{-8}	OV.
M6	0.82	10^{-8}	—
M7	1.0	10^{-7}	—

Table 5.1: List of low-mass stars models. R.M.E stands for Reduced Mixing Efficiency and OV stands for overshooting. A detailed description of the models is found in the text.

5.3 From the ZAMS to the PIE

The main sequence evolution of EMP and zero metallicity stars does not differ significantly from the evolution of their metal-rich counterparts, since the H-burning in the core is dominated by the pp chain in all cases. Figure 5.1 shows the HRD for the computed models. There is no difference in the morphology of the HRD up to the tip of the RGB for the models with mass $1.0M_\odot$ and metallicity $10^{-8} \leq Z \leq 10^{-7}$. The model with metallicity Z=0 shows a loop at the SGB, not observed in other models (point A in Figure 5.1). This loop results from a thermal runaway happening due to the increase importance of the CNO cycle in the H-burning. Just before H is exhausted in the center, the core contracts, increasing its temperature and density. The increase in temperature and density in the core, results in an increase in the efficiency of the 3α reactions and, therefore, in the production of ^{12}C. The energy released by the CNO cycle strongly increases, due to the increase in ^{12}C abundance, and a flash occurs. This flash produces the loop in the HRD.

In Table 5.2 we present the stellar lifetimes of various evolutionary stages corresponding to the tracks of Figure 5.1. We compare our results mainly to the results by Campbell (2007) which calculated a grid of models with metallicities [Fe/H] ≤ -3.0 and masses $0.85 \leq M \leq 3.0$. Zero metallicity models will also be compared to (Marigo et al. 2001; Siess et al. 2002), who published an extensive grid of models for this metallicity. We have defined the MS lifetime as the time between the ZAMS and the turn-off. For the zero metallicity model (M1), we have found MS lifetimes 8% and 11% smaller than the values given by Marigo et al. (2001) and Siess et al. (2002), respectively. These differences could be the result of a larger initial hydrogen content used in these studies (X=0.77,Y=0.23). In comparison to Campbell (2007) results, which used the same initial H abundance (X=0.755,Y=0.245), the MS lifetime of model M1 is only 3% smaller than the value provided. Our standard models M2 and M7 are in good agreement with similar models ([Fe/H] $= -6.5$ and [Fe/H] $= -5.45$) simulated by Campbell (2007), showing differences smaller than 7%. The MS lifetime slightly decreases with increasing metallicity, which is probably due to a larger contribution of the CNO cycle to the H-burning.

Lifetime values for the subgiant branch and the red giant branch phases are provided only by Campbell (2007). The SGB lifetime is defined as the time bewteen the turn-off and the base of the RGB. Our models have SGB lifetimes usually 20% smaller than models by Campbell (2007), except for M1 which has slightly larger lifetime and M7 which is about 30% shorter.

Model	$\tau_{\rm ms}$	$\tau_{\rm SGB}$	$\tau_{\rm RGB}$
M1	5501	508	101
M2	5335	364	111
M3	5335	364	104
M4	5336	360	117
M5	5400	356	95
M6	10433	775	184
M7	5277	282	125

Table 5.2: Various lifetimes for all low-mass stars models. $\tau_{\rm ms}$ is the time between ZAMS and MS Turn-off. $\tau_{\rm SGB}$ is the time bewteen the MS turn-off and the base of the RGB. $\tau_{\rm RGB}$ is the time spent in the RGB. In this case the first and the second RGB (except for model M5). All ages are given in Myr unless stated otherwise.

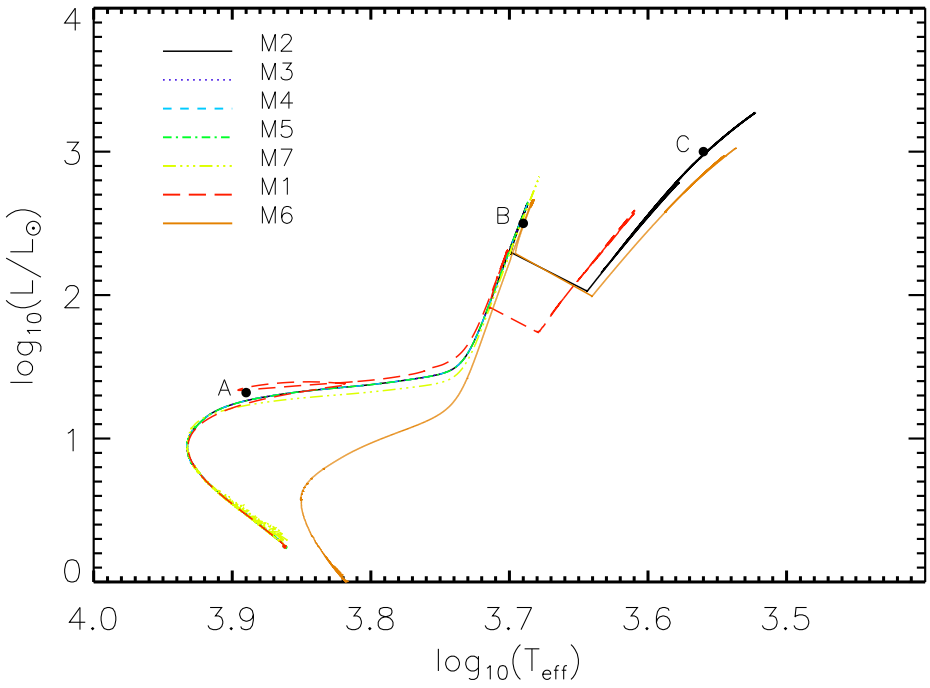

Figure 5.1: Comparison between the different models in the HR diagram. Point A shows the loop that occurs in models with zero metallicity. Point B shows the position of the RGB and point C shows the position of the secondary RGB.

The RGB lifetime is defined as the time between the base of the RGB and the tip of the RGB. EMP models usually present a secondary RGB, then, the RGB lifetime discussed here takes into consideration both RGB phases: prior and after the PIE. The differences between our RGB lifetimes and the values by Campbell (2007) are not larger than 15%.

As mentioned in Chapter 2, the luminosity at the tip of the RGB is larger for higher metallicities. Figure 5.2 shows a zoom in the last portion of the RGB for the models with

$1.0M_{\odot}$. It can be seen that the zero metallicity model has the lowest luminosity. Also, the luminosity at the tip of the RGB varies by almost 0.6 dex over this metallicity range.

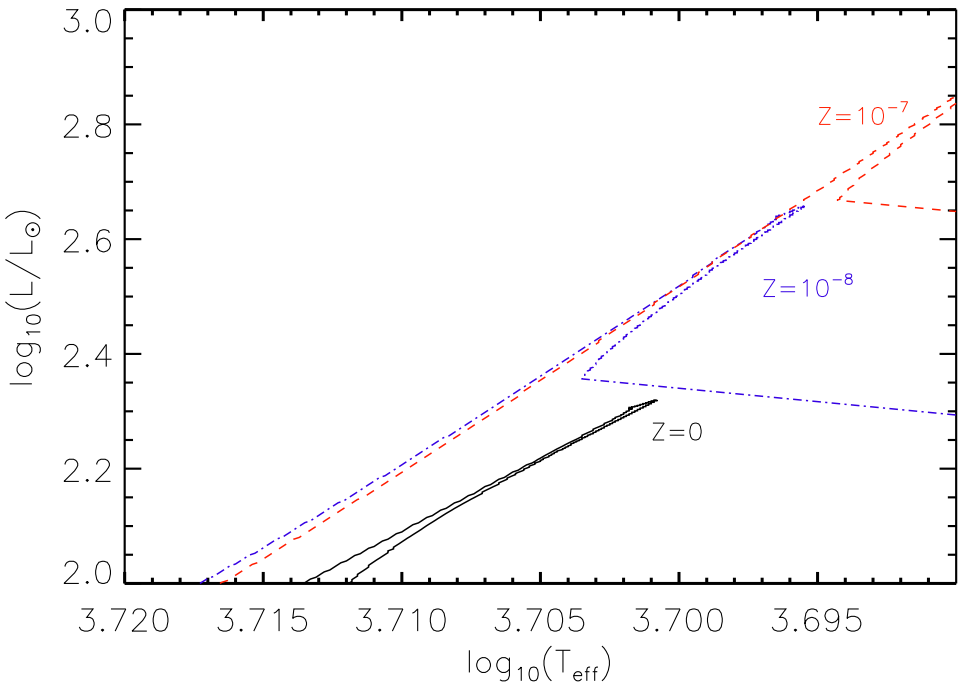

Figure 5.2: The last portion of the RGB in the HR Diagram for all the standard $1.0M_{\odot}$ models. The luminosity at the tip of the RGB varies by ~ 0.6 dex over this metallicity range.

The PIE happens when the star is located at the tip of the RGB (point B in Figure 5.1). After the PIE, the envelope deepens and products of H- and He-burning are dredged-up to the surface. This results in an increase of the total metallicity to values between 10^{-3} and 10^{-2}. This large increase in metallicity causes a strong increase in the low-temperature opacity, producing an abrupt jump in the effective temperature. He-burning ceases after the H-flash which reassumes a RGB configuration with H-burning in a shell (point C in Figure 5.1 - Hollowell et al. (1990)) - the secondary RGB.

5.4 Main Characteristics of the Proton Ingestion Episode

In this and following sections we will use model M2 (See Table 5.4) to illustrate the characteristics of the PIE, unless stated otherwise.

Low-mass stars ignite He-burning under degenerate conditions, leading to the well known core He-flash. Due to stronger neutrino cooling in the innermost core the ignition point is off-center, as shown by the position of maximum energy release by He-burning $M^{He}_{max} = 0.265M_{\odot}$ (Fig. 5.3). Ignition of He-burning results in the formation of the so-called helium convective zone (HeCZ) the outer boundary of which advances in mass during the development of the He-flash. In Figure 5.3 we show the evolution of the convective HeCZ (light grey region

extending from $M_r/M_\odot = 0.265$ up to 0.535) during the time following the maximum helium-burning luminosity up the the moment where the PIE starts. The combination of an off-center He-burning ignition and a low entropy barrier between the He- and H-burning shells in the very metal-poor environment allows the HeCZ to reach hydrogen-rich layers (Hollowell et al. 1990) and giving rise to the PIE.

The HeCZ reaches the radiatively stratified H-rich layers on top (initially represented by white region above $M_r/M_\odot = 0.535$) soon after the He-burning luminosity reaches its maximum value. Protons are then mixed down into the HeCZ and are captured by the abundant ^{12}C, creating ^{13}C. The H-burning luminosity increases while the HeCZ continues expanding (in mass). Note that the penetration of the HeCZ into the H-rich region occurs in a narrow region of only a few parts per thousand of solar masses and it is barely visible around 0.535 $M_\odot$ in Figure 5.3. Around 0.23 years after the He-luminosity reached its maximum a secondary flash happens, the H-flash, with a H-burning luminosity comparable or larger than the He-burning luminosity ($\log_{10}(L^{He}_{max}/L_\odot) = 10.67$, $\log_{10}(L^{H}_{max}/L_\odot) = 10.73$). The burning timescale for hydrogen through the $^{12}C(p,\gamma)$ reaction becomes shorter as protons travel downwards in the HeCZ until a point inside the HeCZ is reached where the burning and mixing timescales are comparable. At this position ($M^{H}_{max} = 0.29M_\odot$) the energy released by H-burning is maximum and temperature rises quickly, resulting in an inversion in the temperature profile that eventually leads to the splitting of the convective zone. This prevents the penetration of protons further down into the He-CZ.

The splitting results in two convective zones: a small HeCZ and an upper convective zone which is referred to as hydrogen convective zone (HCZ). The outer boundary of the HCZ continues to advance in mass. In about 700 years, the envelope deepens and products of burning during and after the PIE are dredged-up to the surface. The envelope is enriched mainly in C, N, and O. Similarly to results by other authors, the amount of C and N brought up to the surface is too large compared to the abundances observed in EMP stars (values in Table 5.7 are more than 3 dex larger than the average CEMP's carbon abundance). Enrichment in s-process depends strongly on the nucleosynthesis before the splitting of the HeCZ and will be discussed in the following section. The long-term evolution before and after the PIE is illustrated in Figure 5.4, where time has been set to zero at the moment when L^{He} reaches its maximum.

The time between maximum He-burning luminosity and the onset of hydrogen mixing (Δt_{mix}) in our calculations is usually larger than the interval found in other studies (Hollowell et al. 1990; Suda et al. 2007; Picardi et al. 2004). This might partially be the result of the larger mass between the bottom of the HeCZ and the location of the base of the H-rich layer in our models. Our predicted Δt_{mix} varies from 10^{-2} to 1 year (depending on the metallicity and the convection efficiency assumed in the models), while in other studies this value ranges from 10^{-3} to 10^{-2} years. The main properties of the core helium flash and the PIE are summarized in Table 5.4. In can be seen in Table 5.4 that, for a given stellar mass, the larger the mass between the He-flash ignition point and the H-shell (ΔM_{ig}) the higher is Δt_{mix}.

Table 5.3 shows a summary of the literature theoretical studies of low-mass stars. Our values of ΔM_{ig} are usually larger than the values found in the literature, with the exception of the models by (Schlattl et al. 2001, 2002) that used a slightly different version of GARSTEC. The maximum ΔM_{ig} reported by other groups in the literature for which PIE happens is 0.24. On the other hand, our models present ΔM_{ig} only larger than this value. Suda et al. (2007) suggested that the inner He-flash ignition point obtained by Schlattl et al. (2001),

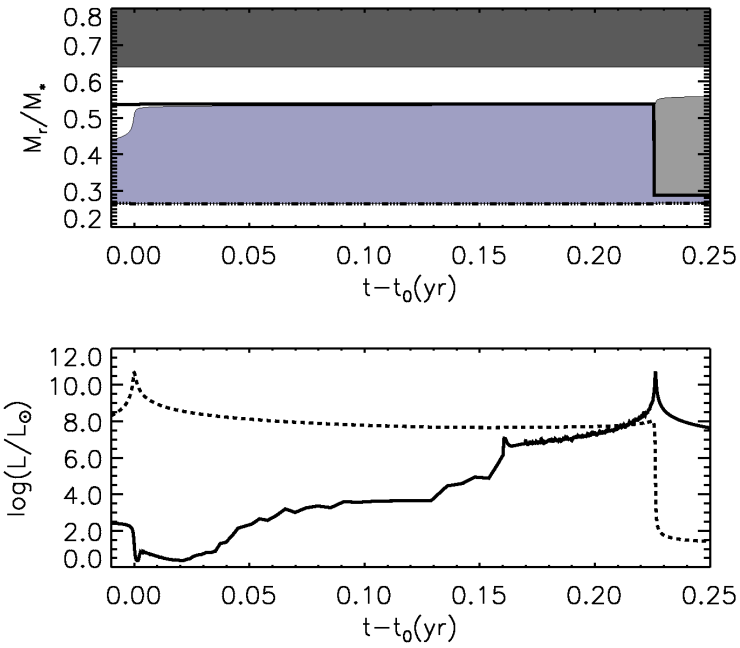

Figure 5.3: Upper Panel: Time evolution of convective zones (grey areas) in our model M2 during the PIE. Thick solid and dot-dashed lines represent the position of maximum energy release due to H-burning and He-burning, respectively. The splitting of the HeCZ around $t - t_0 = 0.225$ yr is evident with the formation of a detached HCZ (dark grey area). Bottom Panel: Evolution of H-burning (solid line) and He-burning (dashed line) luminosities. $t = t_0$ corresponds to the time of maximum He-burning luminosity.

and also observed in our models, might have two sources: the neutrino bremsstrahlung, not included in the fitting formula for neutrino energy-loss rates given by Munakata et al. (1985) and the equation of state. Suda et al. (2007) performed an evolutionary model using the fitting formula by Munakata et al. (1985) in order to check if the absence of neutrino bremsstrahlung would cause the inward shift of the ignition point. They found a ignition point only 10% smaller than the models including neutrino bremsstrahlung. This 10% reduction is, however, too small to account for the inner position found by Schlattl et al. (2001). We have performed an evolutionary calculation using Irwin's EOS (Cassisi et al. 2003) for the zero metallicity case: the ignition point is only 3% larger than found in M1.

An interesting diagnostic is the distance, in mass, that protons are mixed down before the splitting of the HeCZ occurs (ΔM_c - Campbell 2007). It appears that, for a given mass, this quantity is an indicator of the amount of pollution that occurs after the PIE (Campbell 2007). Table 5.4 shows that the larger ΔM_c, the larger is the abundance of CNO elements in the surface, with the exception of model M4.

An important property of the PIE for the s-process is the time between the onset of hydrogen mixing and the splitting of the convective zone, here referred to as Δt_{PIE}. After the splitting of the HeCZ, the abundance of ^{14}N, the main neutron poison in this environment, in the HCZ rapidly builds up. As the ^{13}C to ^{14}N ratio drops below unity neutrons are predominantly captured by ^{14}N(n, p)^{14}C and the s- process is effectively shut down. Therefore, Δt_{PIE} determines the timescale for s-processing. In our calculations Δt_{PIE} is in the range $\sim$0.1 to 1 yr (Table 5.4), about an order of magnitude larger than in some other studies

Authors	M_*	Z	M^{He}_{max}	M_c	ΔM_{ig}
Fujimoto et al. 1990	0.77	zero	0.41	0.53	0.12
Schlattl et al. 2001	1.00	zero	0.15	0.48	0.33
Schlattl et al. 2002	0.82	zero	0.31	0.61	0.30
Siess et al. 2002	1.00	zero	0.31	0.49	0.18
Picardi et al. 2004	0.80	zero	0.35	0.52	0.17
	0.80	10^{-8}	0.38	0.54	0.16
	0.80	10^{-7}	0.35	0.55	0.20
	1.00	zero	0.26	0.50	0.24
Campbell 2007	0.85	$\sim 10^{-7}$	0.30	0.53	0.23
	0.85	$\sim 10^{-8}$	0.33	0.52	0.19
	0.85	zero	0.28	0.49	0.21
	1.00	$\sim 10^{-8}$	0.31	0.52	0.21
	1.00	zero	0.25	0.49	0.23
Suda et al. 2007	0.80	zero	0.36	0.51	0.15
	1.00	zero	0.33	0.50	0.17
Suda & Fujimoto 2010	0.80	$\sim 10^{-7}$	—	0.54	—
	0.80	zero	—	0.51	—
	1.00	$\sim 10^{-7}$	—	0.53	—
	1.00	zero	—	0.50	—

Table 5.3: A summary of the literature for theoretical studies of low-mass stars of extremelly low and zero metallicity. All masses are given in solar mass unit.

(e.g. Hollowell et al. (1990)). In contrast, Campbell et al. (2010) presented a model with metallicity [Fe/H] $= -6.5$ in which $\Delta t_{PIE} \sim 20$ yrs, about two orders of magnitude larger than our findings. The large differences in Δt_{PIE} may be at the core of the seemingly contradictory results regarding the production of s-process elements during the core He-flash found by different authors.

We note here that splitting of the He-CZ is ubiquitous in all 1-dimensional simulations of the PIE during the core helium flash (Hollowell et al. 1990; Schlattl et al. 2001; Campbell & Lattanzio 2008). Splitting of the HeCZ (shell) is also found in PIE resulting from very late thermal pulses in post-AGB stars (Herwig 2001; Althaus et al. 2005) as well as in simulations of the early phases of the TP-AGB in very metal-poor stars (Fujimoto et al. 2000; Serenelli 2006; Cristallo et al. 2009a). On the other hand, recent hydrodynamic 3-dimensional simulations of the TP-AGB phase for a low-mass star (Stancliffe et al. 2011) have not shown splitting of the HeCZ, although the authors argued this might be an artifact of the low resolution used in the calculations.

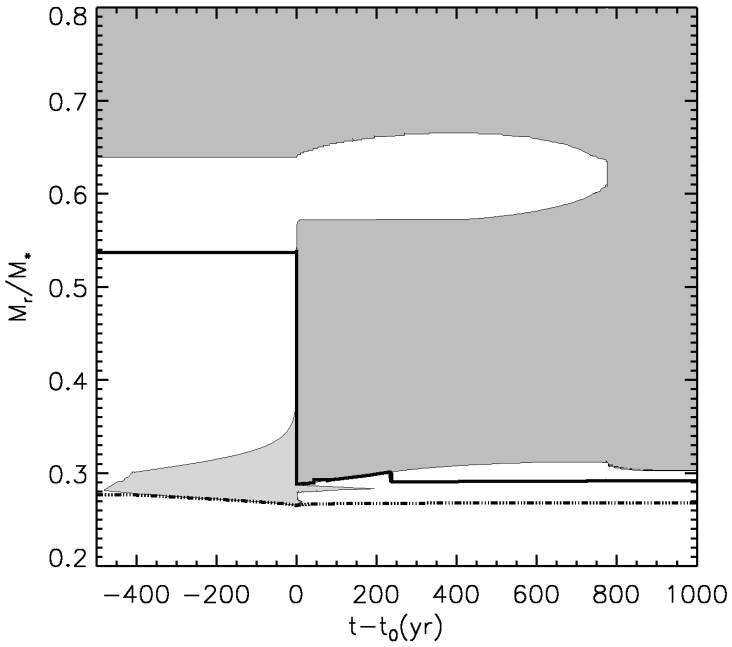

Figure 5.4: Long-term evolution of the 1 $M_\odot$, Z=10^{-8} stellar model during the development of the core He-flash, the PIE, and the subsequent dredge-up event. $t = t_0$ corresponds to the time of maximum He-burning luminosity. As in Figure 5.3, thick solid and dot-dashed lines represent the position of maximum energy release due to H-burning and He-burning, respectively. Merging of the HCZ and the stellar envelope occurs around 770 yr after the PIE takes place.

Model	L^{He}_{max}	L^{H}_{max}	M^{He}_{max}	M^{He}_{c}	Δt_{mix}	Δt_{PIE}	M^{H}_{max}	ΔM_c	ΔM_{ig}	Z_{CNO}
M1	9.972	10.48	0.175	0.488	1.400	1.356	0.290	0.198	0.313	0.010
M2	10.67	10.73	0.265	0.535	0.024	0.202	0.288	0.247	0.270	0.018
M3	10.67	9.828	0.265	0.535	0.028	0.234	0.333	0.202	0.270	0.017
M4	10.68	10.87	0.263	0.536	0.019	0.104	0.281	0.255	0.273	0.015
M5	10.68	11.17	0.261	0.534	6.5×10^{-3}	0.041	0.267	0.267	0.273	—
M6	10.68	11.05	0.277	0.562	0.002	0.075	0.298	0.264	0.285	0.025
M7	11.10	10.37	0.289	0.572	0.200	2.204	0.293	0.279	0.283	0.023

Table 5.4: Main properties of the proton ingestion episode. L^{He}_{max} and L^{H}_{max} are the logarithm of the maximum He-burning luminosity and the maximum H-burning luminosity in units of solar luminosity, respectively. M^{He}_{max} is the position of maximum energy released by He-burning. M^{He}_{c} is the core mass. Δt_{mix} is the time between maximum He-burning luminosity and the onset of hydrogen mixing in years. Δt_{PIE} is the time between maximum He-burning luminosity and the splitting of the convective zone in years. M4 and M5 are the models including overshooting with overshooting parameters f=0.016 and f=0.07, respectively.M^{H}_{max} is the position of maximum energy release by H-burning. ΔM_c is the distance, in mass, that the H-shell moves inwards during the PIE ($M_\odot$). ΔM_{ig} is the distance, in mass, between the He-flash ignition point and the H-shell ($M_\odot$). All masses are given in units of solar mass. Z_{CNO} is the surface mass-fraction of CNO elements.

5.5 Neutron Production and the s-process

During the PIE, ^{13}C is formed by proton captures on ^{12}C and mixed throughout the entire HeCZ. The abundance of ^{13}C in the convective zone increases by several orders of magnitude during Δt_{PIE} (from $X_{13C} \sim 10^{-10}$ to $X_{13C} \sim 10^{-3}$ in mass-fraction).

Neutrons are produced by the reaction $^{13}C(\alpha, n)^{16}O$, near the bottom of the convective zone, reaching maximum neutron density values larger than $10^{14}cm^{-3}$. ^{12}C is the most abundant isotope, besides ^{4}He, in the HeCZ and thus neutrons are mainly captured by it and enter into the recycling reaction $^{12}C(n, \gamma)^{13}C(\alpha, n)^{16}O$. At the beginning of the proton ingestion, ^{13}C is much less abundant than ^{14}N, and neutrons not captured by ^{12}C are captured by ^{14}N. As the PIE progresses, the ^{13}C abundance increases and so does the $^{13}C/^{14}N$ abundance ratio and the neutron density (Fig. 5.5 and Fig. 5.6). Eventually, $^{13}C/^{14}N$ abundance ratio gets larger than unity and more neutrons are free to be captured by heavy elements. The $^{13}C/^{14}N$ abundance ratio reaches a maximum value around $\Delta t \sim 0.10$ yrs after the PIE starts. Hydrogen abundance is now large enough to enhance the competition between $^{13}C(p, \gamma)^{14}N$ and $^{13}C(\alpha, n)^{16}O$. Thus, the $^{13}C/^{14}N$ abundance ratio starts to decrease, leading to a shallower increase in neutron density than before. After the splitting, the bottom of the HeCZ moves slightly outwards and cools down and the supply of fresh protons into the HeCZ stops, consequently the neutron flux is quickly suppressed (Fig. 5.5).

Regarding the production of s-process elements in a given environment (which determines, among others, the number of seed nuclei present), the key quantity is the time-integrated neutron flux, or neutron exposure, given by

$$\tau = \int_{ti}^{tf} v_T n_n dt \tag{5.1}$$

where v_T is the thermal velocity of neutrons, ti is the beginning of the neutron flux, tf is the end of the neutron flux, and n_n their number density. In the case of the PIE, the other relevant

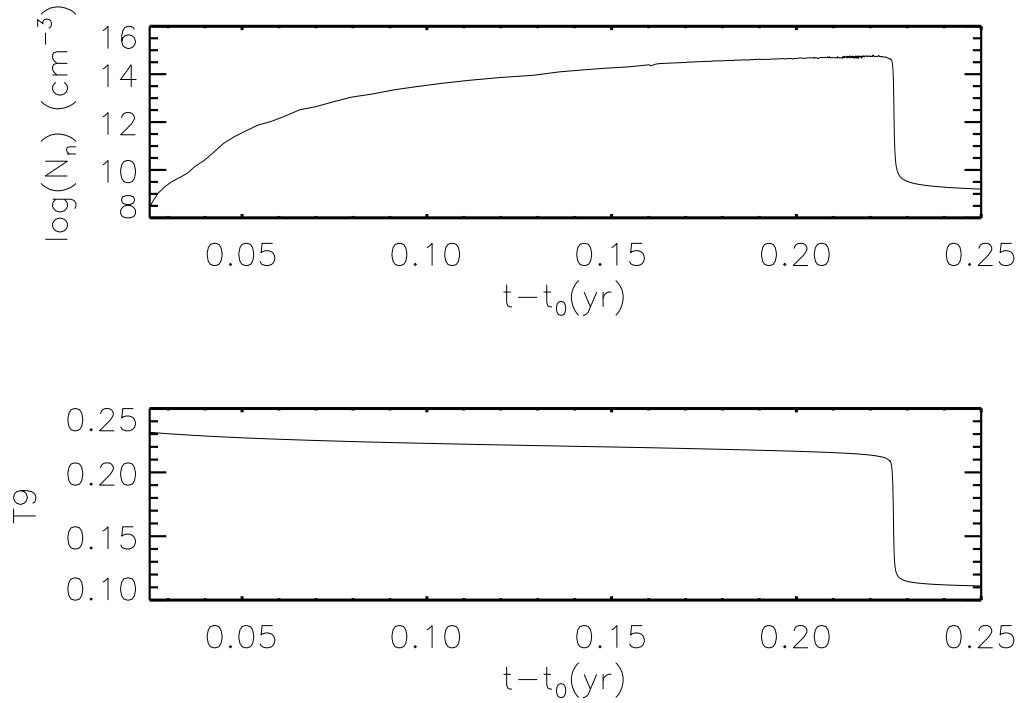

Figure 5.5: Upper Panel: Time evolution of maximum neutron density in our $\mathrm{Z} = 10^{-8}$ model (M2) at M=0.265 $\mathrm{M}_{\odot}$. Bottom Panel: Evolution of the temperature near the bottom of the HeCZ. In both cases the sudden change at $t - t_0 \approx 0.225$ yr reflects the splitting of the HeCZ.

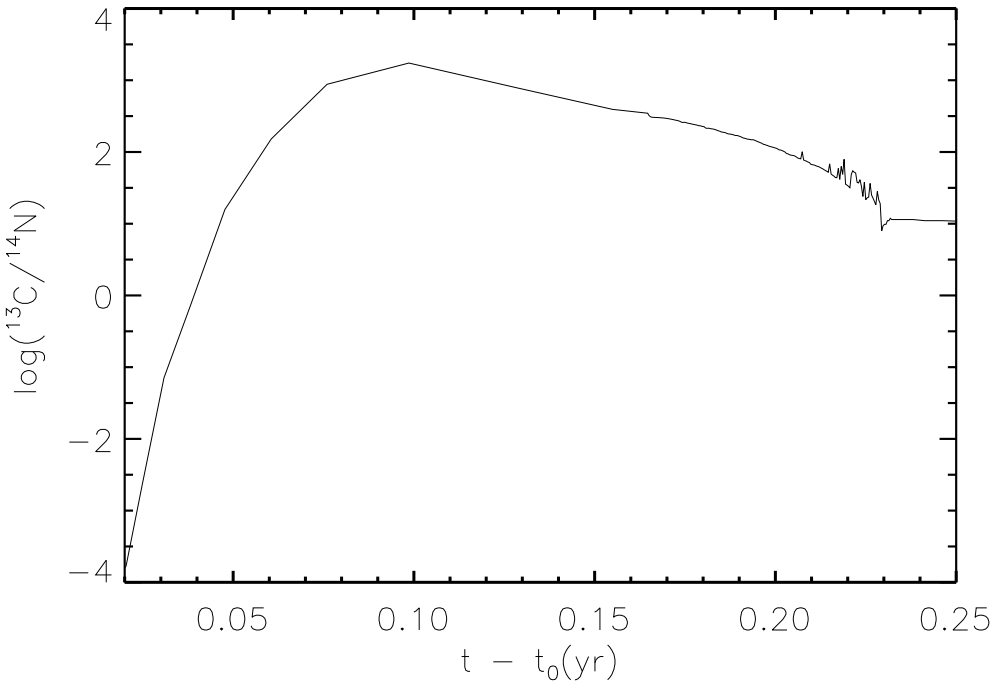

Figure 5.6: $^{13}\mathrm{C}/^{14}\mathrm{N}$ ratio near the bottom of the HeCZ. t_0 is the same as in Fig. 5.3 and 5.5.

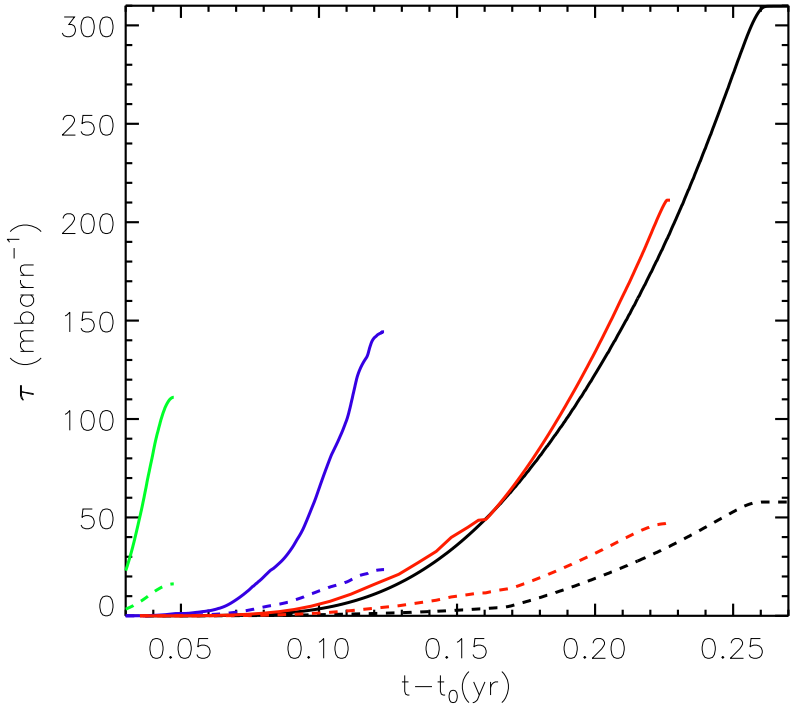

Figure 5.7: Time evolution of neutron exposure. Solid lines represent the neutron exposure at the position of maximum neutron density (i.e. near the bottom of the HeCZ) and dashed lines represent the average neutron exposure in the convective zone. Blue line: model including overshooting (f=0.016 - M4), red line: standard $Z = 10^{-8}$ model (M2), black line: reduced convection efficiency (M3), and green line: model including overshooting (f=0.07).

quantity is the splitting timescale Δt_{PIE} which, as we discuss below, determines the timespan over which neutrons are effectively produced and is therefore the cutoff to the integration in Equation 5.1.

In Figure 5.7 we show, in solid lines, the neutron exposure as a function of time near the bottom of the HeCZ, where the maximum neutron flux is achieved. Results for the reference model, M2, are depicted in red. In the same figure, dashed lines denote the neutron exposure averaged across the entire convective zone. For comparison, typical values for the neutron exposure during the AGB phase are roughly two orders of magnitude smaller than the maximum neutron exposure at the bottom of the HeCZ.

At the beginning of the PIE iron-peak elements (mainly ^{56}Fe) are converted to elements of the first s-process peak (Sr, Y, Zr). The ^{56}Fe abundance is strongly reduced, reaching its minimum value at about 0.17 yrs after the maximum helium-burning luminosity. Between 0.17 and 0.22 yrs after the He-flash, strontium is converted into barium and, subsequently into lead. The mass fraction of Fe, Sr, Ba, and Pb in the convective zone are shown in Figure 5.8. Near the end of the PIE, as the outer boundary of the HCZ advances, freshly dredged-down iron increases the ^{56}Fe abundance by an order of magnitude.

After the splitting of the HeCZ, the upper convective zone, HCZ, penetrates further into the H-rich layers above and ^{12}C is converted into ^{14}N. The cooling of the HCZ effectively

switches off α-captures by ^{13}C, and ^{14}N captures most of the remaining neutrons available, effectively quenching s-processing. Therefore, the abundances of heavy elements in the HCZ remain unchanged by nuclear burning after the splitting. They do not change until the HCZ merges with the stellar envelope and the processed material is dredged-up to the surface.

5.5.1 The influence of convective mixing

The treatment of convection and the associated mixing in stellar evolution calculations is subject to fundamental uncertainties that can not be properly addressed in 1D models. Nevertheless, we can try to understand how varying the mixing efficiency in convective regions or the extent of the mixing regions (e.g. by including overshooting) affect the basic properties of the PIE. In turn, this will affect neutron production and the ensuing creation of s-process elements.

Let us first discuss models including overshooting. Model M4 is computed by using a moderate amount of overshooting characterized by $f = 0.016$ (Sect. 5.2). The extended convective boundary in this model allows a larger penetration of the HeCZ into H-rich layers. More fuel is ingested into the HeCZ and thus a faster, but shorter, evolution of the proton ingestion episode is achieved. In Figure 5.7 solid lines represent the time evolution of the neutron exposure at the location of maximum neutron density. Comparison of models M2 and M4 (red and blue lines respectively) show that the more vigorous entrainment of hydrogen into the HeCZ in model M4 produces an early and steeper increase in the neutron exposure. Also, the maximum neutron flux is almost a factor of two larger in model M4 than in model M2. However, the faster release of nuclear energy by hydrogen burning leads to the PIE lasting less than half the time it does in the case of no overshooting. This leads to a significantly smaller final neutron exposure in the case of M4 as seen in Figure 5.7. To confirm this trend, we have computed an additional model with a large overshooting parameter $f = 0.07$. For this model, results shown in green in Figure 5.7 confirm that a larger overshooting region leads to a more violent hydrogen ingestion (as seen by the quick and steep rise in neutron production) but of shorter duration and, overall, reduced efficiency in the final neutron exposure. Quantitatively, the difference between the final neutron exposure for the two models with overshooting is not too large, despite the $\sim 50\%$ difference in $\Delta t_{\rm PIE}$ (see blue and gree solid lines in Figure 5.7).

As mentioned before, we have found shorter splitting timescales than other recent calculations (e.g. those of Campbell et al. (2010)). In order to mimic these longer splitting timescales, we computed a model with a reduced convective mixing efficiency. In our calculations we have simply achieved this by dividing the diffusion coefficient by a constant factor. In model M3 this reduction is by one order of magnitude. As expected, a reduced mixing efficiency results in a larger $\Delta t_{\rm PIE}$, although the difference is not too significant compared to the standard case (see Models M2 and M3 in Table 5.4). This increase in time, however, is enough to produce a total neutron exposure at maximum (black solid line) about 50% larger than in the standard case; this should favor the production of the heaviest s-process isotopes. In terms of structure properties, while the inclusion of overshooting moves the splitting position inwards, the reduced mixing efficiency moves this position outwards ($M^{\rm H}_{\rm max}$ in Table 5.4). This slightly reduces the amount of CNO elements dredged-up.

In a radiative environment, the neutron exposure at the position of maximum neutron density would result in a strong enhancement in Pb, due to the repeated neutron captures in a static environment, in all cases. However, in a convective environment, the interplay between burning and convection is important. The mixing timescale is shorter than the

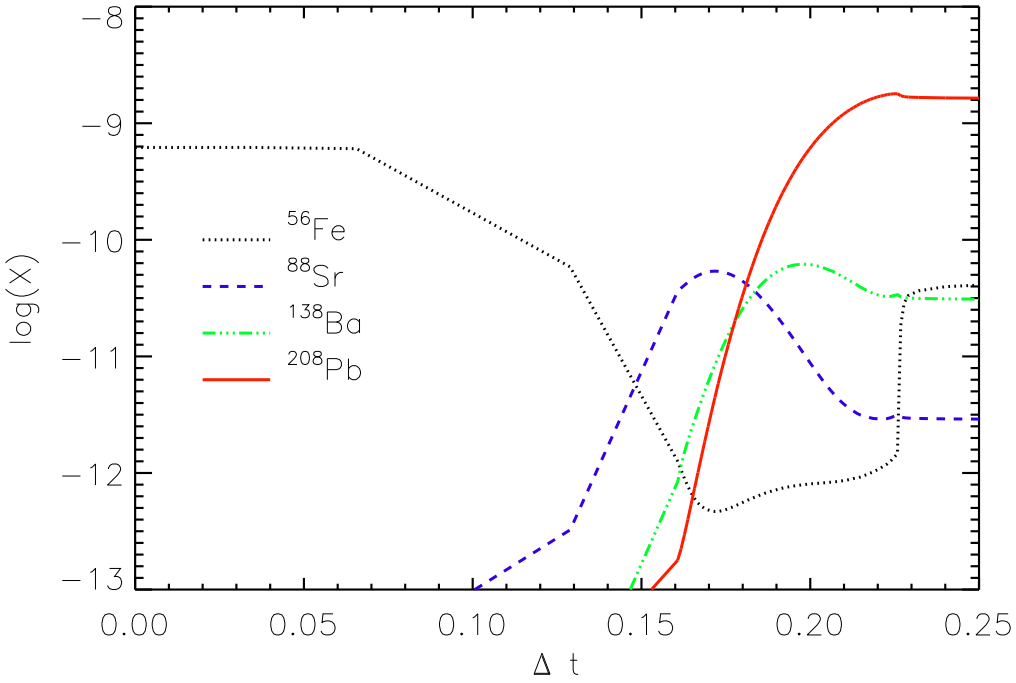

Figure 5.8: Evolution of the mass fraction of isotopes representative of the three s-process abundance peaks and $^{56}\mathrm{Fe}$ as a function of time. These abundances were sampled at the position 0.4 $\mathrm{M}_{\odot}$. They are representative of the entire convective zone and, after the splitting, are located in the HCZ which later comes into contact with the stellar envelope.

overall phase of s-process production and, thus, the relevant quantity for the final production is the averaged neutron exposure. Figure 5.7 shows the neutron exposure averaged over the convectively mixed zone (dashed lines). As it can be seen, the averaged neutron exposure is strongly reduced in the overshooting model (blue dashed line), but it is not much affected by the reduction in the mixing efficiency (black dashed line). This leads to small differences in the final production of s-process elements despite the 50% difference in the neutron exposure at the bottom of the HeCZ. Figure 5.9 shows the abundance distribution inside the HeCZ right before the splitting. As discussed above, the smaller neutron exposure of model M4 favors the production of elements from the first and second s-process peak and produces less Pb than models M2 and M3.

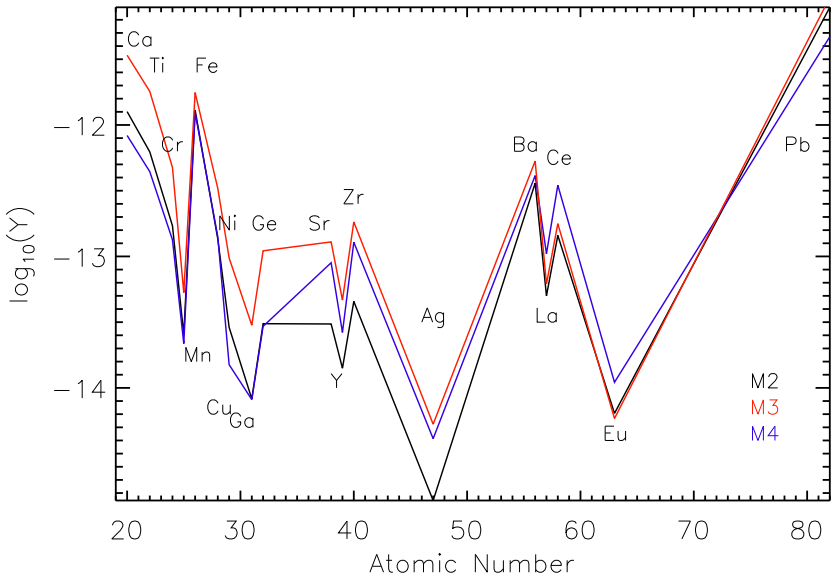

Figure 5.9: Abundance distribution inside the HeCZ right before the splitting.

5.5.2 The absence of iron-peak seeds: zero metallicity case

Goriely & Siess (2001) have studied the occurrence of s-process nucleosynthesis during the AGB phase of a $3M_{\odot}$ stellar model with initial zero metallicity. They found that, by parametrizing the formation of the ^{13}C-pocket during the third dredge-up, neutron densities of the order of $10^{9}\mathrm{cm}^{-3}$ can be reached. Furthermore, their results showed this is high enough for an efficient production of s-process elements to occur starting from lighter seeds (C-Ne), even in the complete absence of iron-peak elements.

The calculations of the 1 $M_{\odot}$ metal-free model presented in this thesis (model M1), show that low-mass stars can also produce light elements that might act as seeds of s-process nucleosynthesis. This occurs in two steps. First, during the transition from the subgiant to the red giant phase, the interior temperature is high enough to start helium-burning and produce carbon. Once the carbon mass-fraction is $X_c \sim 10^{-11}$, the CNO cycle is ignited and a small thermal runaway occurs due to the sudden increase in the efficiency of the CNO burning

(Weiss et al. 2000). Later, in the PIE, neutrons are captured by ^{12}C and ^{16}O creating Ne and Na isotopes.

In model M1, however, the HeCZ splits before s-process elements can be produced by neutron capture onto the light seeds and, since the splitting of the HeCZ is followed by an abrupt decrease of the availability of neutrons (Figure 5.5, top panel), s-process elements are not formed despite of the high neutron density ($n_n > 10^{13} cm^{-3}$) reached. In fact, the neutron exposure achieved at the position of maximum energy release by He-burning is ~ 25 mbarn^{-1}, which would be sufficient to produce s-process elements if the neutrons were captured in a radiative environment, as it happens during the third dredge-up in AGB stars (Goriely & Siess 2001).

5.6 Lithium Production

One important signature of the PIE is the production of ^{7}Li. Cristallo et al. (2009a), for instance, found an abundance of lithium of $\log(\epsilon(\mathrm{Li})) = 3.74$ for their model with mass $1.5\mathrm{M}_{\odot}$ and metallicity $\mathrm{Z} = 5 \times 10^{-5}$.

Figure 5.10 shows the chemical profiles for hydrogen, ^{3}He, ^{7}Be, and ^{7}Li at different times before and after the splitting of the HeCZ. Panel (a) shows that, during the PIE, ^{3}He nuclei are ingested within the convective zone, provided by the rich envelope ($\mathrm{X_{env}}(^{3}\mathrm{He}) \sim 10^{-4}$). After the splitting of the HeCZ, the temperature at the bottom of the HCZ is extremely high ($\log(\mathrm{T}) = 8.2$). At this temperature, the $^{3}\mathrm{He}(\alpha,\gamma)^{7}\mathrm{Be}$ reaction begins to create ^{7}Be. While the top of the HCZ expands and cools, ^{7}Be reaches mass-fraction values of $\mathrm{X}(^{7}\mathrm{Be}) \sim 10^{-7}$, and decays to produce a small amount of ^{7}Li (Panel b). When the envelope starts dredging up the elements present in the HCZ, ^{7}Be decays to ^{7}Li during the transport (Panel c). ^{7}Li is, then, mixed throughout the convective envelope, reaching an abundance of $\mathrm{X}(^{7}\mathrm{Li}) = 3.6 \times 10^{-8}$.

Contrary to ours and to previous results in the literature (Iwamoto et al. 2004; Picardi et al. 2004; Cristallo et al. 2009a), Campbell et al. (2010) found a low Li surface abundance in their PIE model ($\log(\epsilon(\mathrm{Li})) = 1.63$). In their evolutionary calculations, Campbell et al. (2010) used a simplified network with 6 isotopes and reaction rates from the old compilation by Caughlan & Fowler (1988), which resulted in a less violent H-flash. Table 7.6 in Campbell (2007) shows a maximum H luminosity of $\log_{10}(\mathrm{L_H}) = 8.2$ for their model with $1.0\mathrm{M}_{\odot}$ mass and metallicity $[\mathrm{Fe/H}] = -6.5$. The temperature at the bottom of the HCZ of a model with similar H luminosity ($\mathrm{M} = 0.85\mathrm{M}_{\odot}$/Z=0) is $\mathrm{T} = 10^{7.9}$, which is 50% smaller than the temperature found in our model. This difference in the temperature results in a much smaller rate for the reaction $^{3}\mathrm{He}(\alpha,\gamma)^{7}\mathrm{Be}$, as it is shown in Figure 5.11 and might be the source of the large differences in lithium production between Campbell et al. (2010) models and ours.

Another important quantity affecting the surface lithium abundance is the time between the H-flash and the dregde-up ($\Delta \mathrm{t_d}$). If $\Delta \mathrm{t_d}$ is long enough ^{7}Li is converted into ^{4}He through proton capture reactions. Table 5.5 shows the lithium surface abundance and $\Delta \mathrm{t_d}$ for our models. It can be seen that the longer it takes for the envelope to reach the HCZ, the lower is the lithium surface abundance. From Figure 7.7 of Campbell (2007) one can estimate $\Delta \mathrm{t_d}$ for their model with $1.0\mathrm{M}_{\odot}$ and metallicity $[\mathrm{Fe/H}] = -6.5$: $\Delta \mathrm{t_d} \sim 1.3$kyr. This larger dredge-up timescale should also contribute to lower the lithium abundance in their model.

Table 5.5 also shows the temperature at the bottom of the HCZ right after the splitting ($\mathrm{T_{HCZ}^{max}}$). All models with $1.0\mathrm{M}_{\odot}$ mass, except M1, have similar temperature, which is an indicative of $\Delta \mathrm{t_d}$(yr) influence in the final surface abundance. Our zero metallicity model

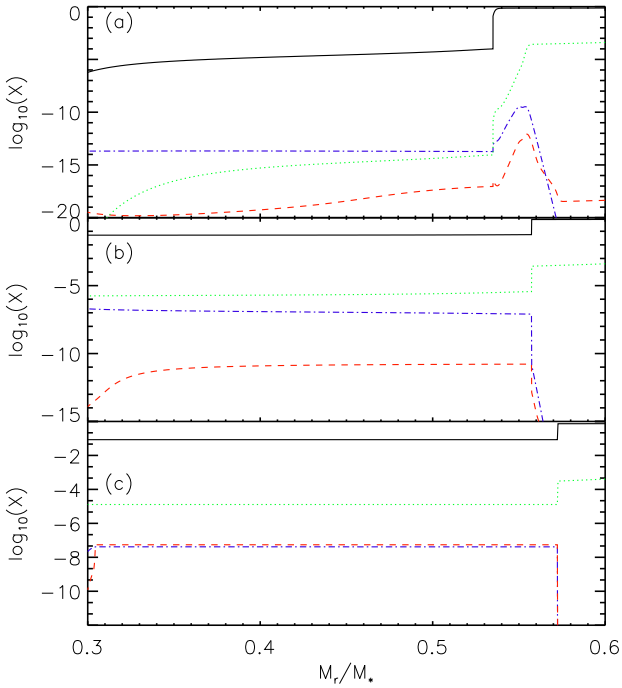

Figure 5.10: Chemical abundance profiles of protons (solid black line), ^{3}He (dotted green line), ^{7}Be (dashed red line), and ^{7}Li (dot-dashed blue line) as a function of mass coordinate in model M2. Each snapshot shows the time evolution of these quantities. Panel (a): t=1.5×10^{-3} yrs before the H-flash, Panel(b): t=0.013 yrs after the H-flash. Panel (c): t=308 yrs after the H-flash.

has the lowest lithium abundance, which is expected, since this model presents the lowest temperature and longest dredge-up timescale. Picardi et al. (2004) presented models for low-mass stars with zero and extremely low metallicity. Their model with mass $0.8M_{\odot}$ and metallicity $Z = 10^{-8}$ has a surface lithium abundance similar to the value found for model M6 ($\log\epsilon(\mathrm{Li}) = 5.21$). On the other hand, they have found a significantly larger abundance value for their zero metallicity $1.0M_{\odot}$ model ($\log\epsilon(\mathrm{Li}) = 4.03$).

Model	$\log\epsilon(\mathrm{Li})$	$\Delta t_{\mathrm{d}}(\mathrm{yr})$	$T^{\mathrm{max}}_{\mathrm{HCZ}}$	$T^{\mathrm{max}}_{\mathrm{HeCZ}}$
M1	-3.47	4329	8.00	0.22
M2	4.02	771	8.20	0.25
M3	2.96	1143	8.17	0.25
M4	4.55	537	8.19	0.25
M6	5.91	322	8.20	0.26
M7	4.95	220	8.21	0.26

Table 5.5: Surface lithium abundance for all low-mass models, except M5, is given as $\log\epsilon(\mathrm{Li}) = \log(N_{\mathrm{Li}}/N_{\mathrm{H}}) + 12$. Δt_{d} is the time between the H-flash and the onset of the dredge-up. $T^{\mathrm{max}}_{\mathrm{HCZ}} = \log_{10}(T)$ is the maximum temperature at the HCZ. $T^{\mathrm{max}}_{\mathrm{HeCZ}} = T(K)/10^{9}$ is the maximum temperature at the bottom of the HeCZ.

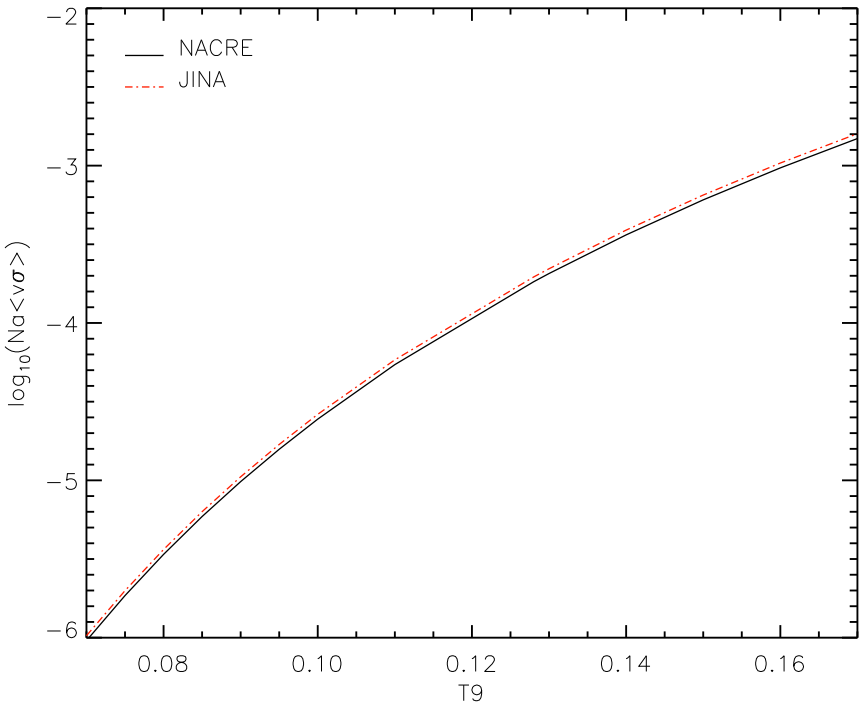

Figure 5.11: $^{3}\mathrm{He}(\alpha,\gamma)^{7}\mathrm{Be}$ reaction rates. The black solid line is the rate given by the NACRE compilation (used in our models) while the red dot-dashed line is the newest rate compiled by the JINA database which is based on Cyburt & Davids (2008). $\mathrm{T}_9 = \mathrm{T(K)}/10^9$.

5.7 Light elements

It has been suggested that the neutron-recycling reactions, $^{12}\mathrm{C}(\mathrm{n},\gamma)^{13}\mathrm{C}(\alpha,\mathrm{n})^{16}\mathrm{O}$, play an important role in the production of $^{16}\mathrm{O}$ during the PIE, since neutrons are more likely to be captured by $^{12}\mathrm{C}$ because of its large abundance in the HeCZ (Gallino et al. 1988; Jorissen & Arnould 1989). Figure 5.12 shows the contribution of some selected reactions on the production of $^{16}\mathrm{O}$. The values of the number fractions ($\mathrm{Y_i}$ and $\mathrm{Y_j}$) were taken from model M2 and represent the abundances at the bottom of the HeCZ. At this position, the proton abundance is quite low, because the mixing timescale is not large enough to carry protons down to the bottom of the HeCZ. Instead, hydrogen is burnt at an upward position which later becomes the splitting location. The $^{13}\mathrm{C}$ produced by hydrogen burning in the upper part of the HeCZ is, however, mixed throughout the entire HeCZ. The increasing $^{13}\mathrm{C}$ abundance at the bottom of the convective zone, increases the importance of the $^{13}\mathrm{C}(\alpha,\mathrm{n})$ reaction, and therefore, increases the neutron production.

From Figure 5.12 it can be seen that there are two main channels of $^{16}\mathrm{O}$ production: alpha and neutron captures by $^{12}\mathrm{C}$. The $^{13}\mathrm{C}(\alpha,\mathrm{n})^{16}\mathrm{O}$ reaction is faster by many orders of magnitude than the $^{12}\mathrm{C}(\alpha,\gamma)^{16}\mathrm{O}$. The final $^{16}\mathrm{O}$ abundance, however, depends on the competition between the reactions $^{12}\mathrm{C}(\mathrm{n},\gamma)$ and $^{16}\mathrm{O}(\mathrm{n},\gamma)$ (Figure 5.12). During the PIE, $^{16}\mathrm{O}$ abundance increases by three orders of magnitude (from $\sim 10^{-6}$ to $\sim 5\times10^{-3}$).

$^{17}\mathrm{O}$ is mainly produced by the reaction $^{16}\mathrm{O}(\mathrm{n},\gamma)^{17}\mathrm{O}$. Figure 5.13 shows the contribution

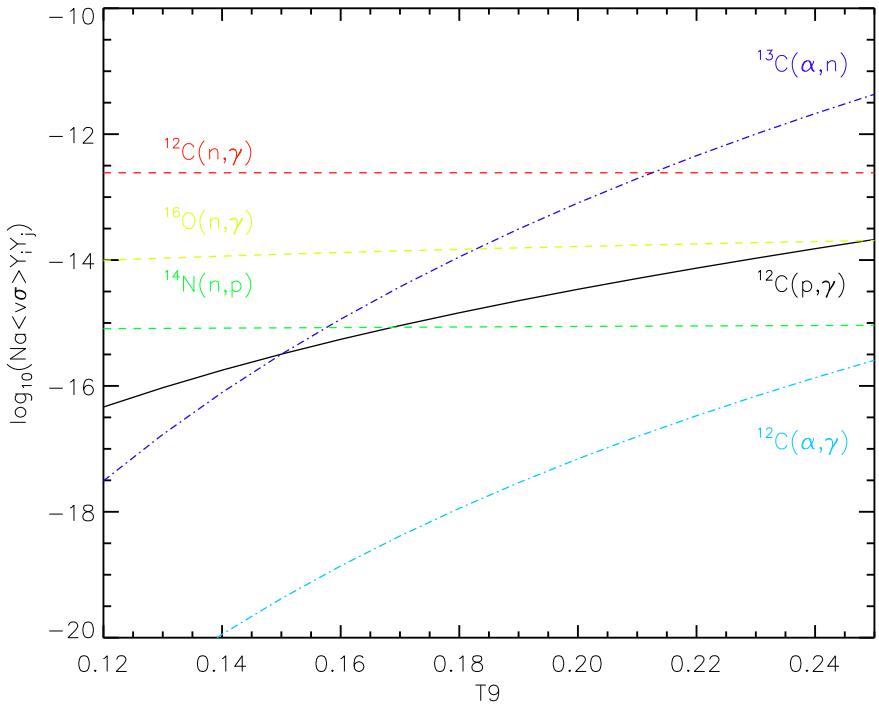

Figure 5.12: The rates of alpha, proton, and neutron captures as a function of temperature. The number fraction values (Y_i and Y_j) represent the values at the bottom of the HeCZ and were taken from model M2. $Na < \sigma v >$ is the Maxwellian-averaged reaction rate.

of the reactions involved in the production of the oxygen and fluorine isotopes inside the HeCZ. Each temperature and number fraction in this plot were taken at a point inside the HeCZ, as can be seen by the upper x-axis. In the inner part of the HeCZ, the neutron capture reactions dominate, producing ^{17}O which is partially transformed into ^{14}C. For the creation of ^{18}O, there are two main paths: $^{17}\mathrm{O}(\mathrm{p},\gamma)^{18}\mathrm{F}(\beta)^{18}\mathrm{O}$ and $^{17}\mathrm{O}(\mathrm{n},\alpha)^{14}\mathrm{C}(\alpha,\gamma)^{18}\mathrm{O}$. The dominating channel depends strongly on the adopted reaction rate of the alpha capture reaction. In Figure 5.13, the solid black line shows the contribution of the reaction $^{14}\mathrm{C}(\alpha,\gamma)$ using the reaction rate by Görres et al. (1992), while the dotted black line shows the contribution if the old values by Caughlan & Fowler (1988) were adopted. The old reaction rate can be up to five orders of magnitude larger than the one measured by Görres et al. (1992), which can lead to substantially different ^{18}O abundance.

The fluorine stable isotope (^{19}F) is produced by proton and alpha captures, $^{18}\mathrm{O}(\mathrm{p},\gamma)$ and $^{15}\mathrm{N}(\alpha,\gamma)$. Since the ^{18}O abundance is quite small, due to the much smaller reaction rates used in our calculations (Görres et al. 1992), its contribution for the creation of fluorine is quite small. The contribution of the alpha capture to the formation of ^{19}F in our models is also small, due to the use of new reaction rates with lower values in the temperature range relevant to the PIE.

For ^{20}Ne, the main paths are (n,γ) and (α,n) (Figure 5.14). However, the alpha capture of ^{17}O has a (α,γ) branch, which works as a neutron leakage out of the double neutron-recycling cycle, $^{12}\mathrm{C}(\mathrm{n},\gamma)^{13}\mathrm{C}(\alpha,\mathrm{n})^{16}\mathrm{O}(\mathrm{n},\gamma)^{17}\mathrm{O}(\alpha,\mathrm{n})^{20}\mathrm{Ne}$, (Nishimura et al. 2009). Once ^{21}Ne

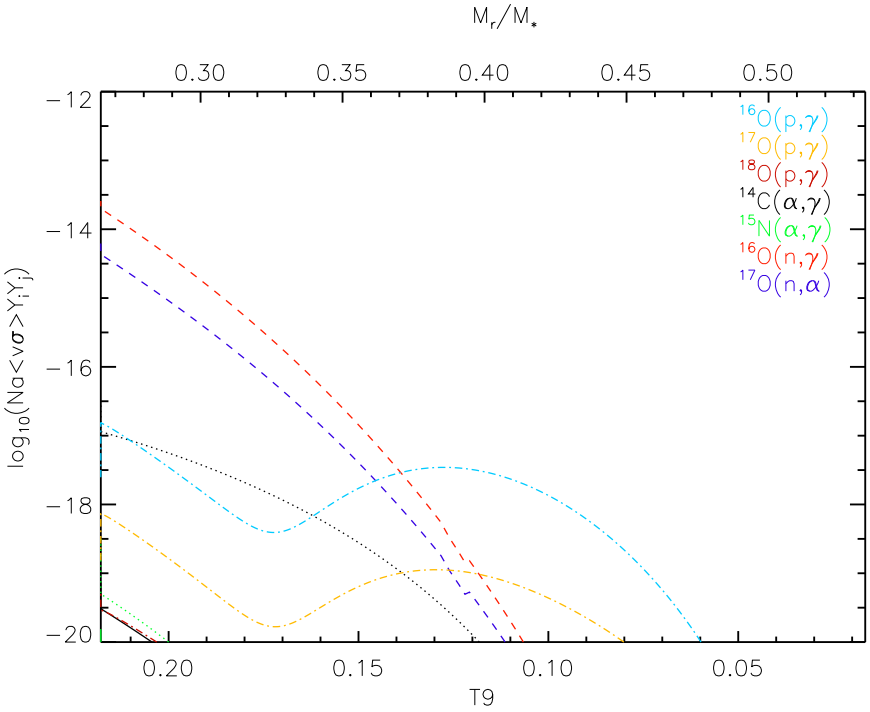

Figure 5.13: The rates of alpha, proton, and neutron captures inside the HeCZ in model M2 at t=0.183 yrs after the maximum He-burning luminosity was achieved. Dashed lines represent neutron capture reaction, dot-dashed lines represent proto capture reaction, solid and dotted lines represent alpha capture reactions.

is produced via $^{17}O(\alpha,\gamma)$, it is effectively converted into ^{22}Ne by neutron capture (Figure 5.14). The dominant process to produce ^{24}Mg is neutron capture by ^{23}Na. The two other channels of ^{24}Mg creation ($^{20}Ne(\alpha,\gamma)$ and $^{21}Ne(\alpha,n)$) are much less important in the typical temperatures achieved during the PIE. Neutron capture is also responsible for the formation of ^{25}Mg. On the other hand, the creation of ^{26}Mg is dominated by proton capture reactions (Figure 5.15). The contribution of the alpha capture channel for the production of (α,n) and (α,γ) is quite small when compared to the proton and neutron captures.

After the H-flash, the convective zone cool down and the neutron production is shut off. The nucleosynthesis in the HCZ is dominated by the CNO cycles and the NeNa and MgAl chains (Figure 5.16). The abundances of light elements in the HCZ slightly increases until the dredge-up. The main production, however, occurs prior to the splitting.

Nishimura et al. (2009) have computed parametrized nucleosynthesis models of zero metallicity stars during the PIE. They have used analytic solution of burning shell by Sugimoto & Fujimoto (1978) to calculate the development of the shell flashes. Models were obtained for masses $1.5M_\odot \leq M \leq 3.0M_\odot$. In these simulations, it was assumed that a constant amount of ^{13}C is mixed during a certain interval, Δt_{mix}, starting from the time the He-flash luminosty reaches its maximum. The amount of ^{13}C mixed and the mixing timescale are the free parameters in the calculations.

Some important conclusions regarding the production of light elements by Nishimura et al. (2009) were: 1) The abundances of elements beyond neon are strongly dependent on the

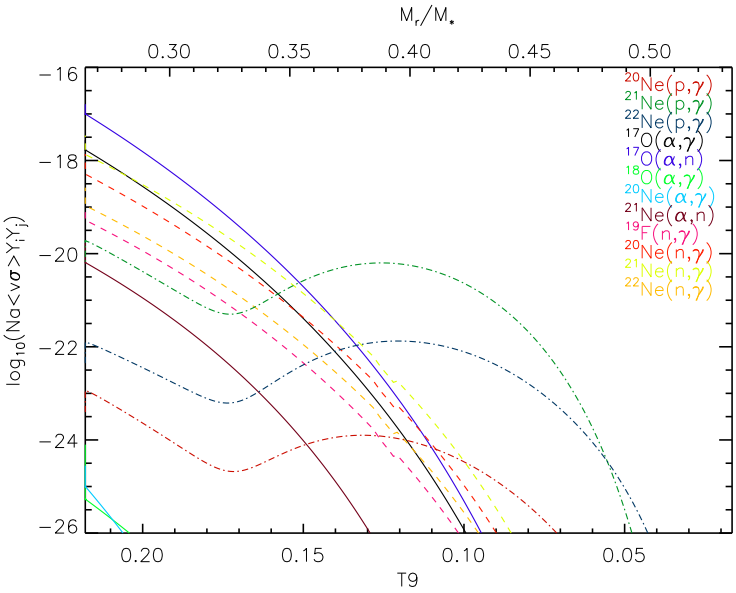

Figure 5.14: Same as Figure 5.13 for neon isotopes.

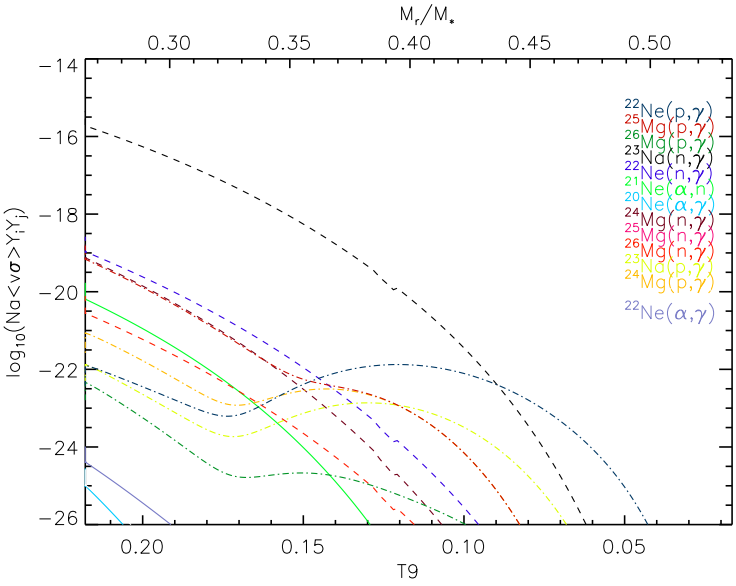

Figure 5.15: Same as Figure 5.13 for magnesium isotopes.

amount of mixed ^{13}C (which is an indicative of the amount of protons mixed), while oxygen, fluorine, and neon isotopes are mildly dependent on this property. 2) The abundance patterns are almost independent of the mixing duration if it is sufficiently long. If $\Delta t_{\rm mix}$ is

smaller than a certain value, depending on the maximum temperature in the convective zone, isotopes heavier than neon are not produced. Therefore, the final abundance of elements beyond oxygen dependens on the interplay between these two quantities. Also, the maximum temperature at the bottom of the HeCZ plays an important role in the abundance patterns of light elements produced during the PIE, because it determines the minimum Δt_{mix} necessary for the production of such elements. Nishimura et al. (2009) found Δt_{mix} values equal to 10^9 s and 10^{12} s for models with maximum temperatures $T_9 = 0.35$ and $T_9 = 0.2$, respectively. All our models have mixing timescales smaller than these values which might be the reason for the low abundances found in our models.

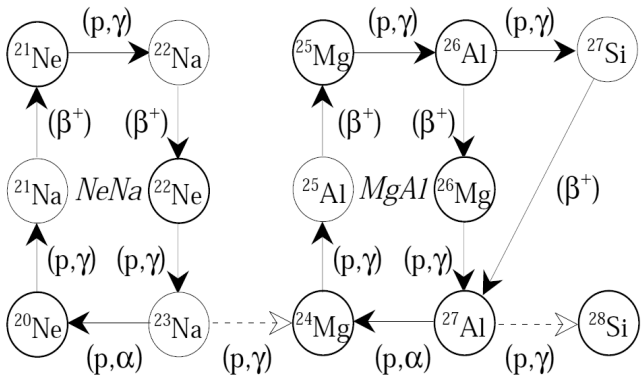

Figure 5.16: Reactions involved in the NeNa and MgAl chains.

We calculate that the amount of protons mixed into the HeCZ for model M2 is $\Delta H_{mix} \sim 5 \times 10^{-5}$ $M_\odot$. Models M1, M3, and M4 have $\Delta H_{mix} \sim 2 \times 10^{-5}, \sim 6 \times 10^{-4}, \sim 8 \times 10^{-4}$ $M_\odot$, respectively. Table 5.5 shows the maximum temperature at the bottom of the HeCZ (T^{max}_{HeCZ}) and Table 5.6 shows the surface abundance of some selected isotopes. Model M1 presents the lowest abundances amongst all models. This is the result of the combined effects of a lower proton mixing and a lower temperature. It can be seen that, for this model, the Δt_{PIE} is not sufficiently large to burn ^{18}O through alpha captures and build up heavier isotopes. Despite the larger ΔH_{mix} value found for model M4, the splitting timescale is much smaller than that found for model M2, which is the reason for a lower production of light elements in comparison to model M2.

Isotope	M1	M2	M3	M4	M6	M7
^{18}O	1.6×10^{-5}	4.0×10^{-9}	1.7×10^{-8}	2.3×10^{-9}	3.1×10^{-9}	5.9×10^{-9}
^{19}F	8.0×10^{-12}	2.6×10^{-10}	8.4×10^{-10}	1.4×10^{-10}	2.6×10^{-10}	5.2×10^{-10}
^{20}Ne	4.1×10^{-11}	3.6×10^{-8}	5.8×10^{-8}	2.1×10^{-8}	5.4×10^{-8}	1.1×10^{-7}
^{21}Ne	8.7×10^{-13}	7.6×10^{-11}	6.6×10^{-10}	2.6×10^{-11}	1.8×10^{-10}	6.3×10^{-10}
^{22}Ne	5.0×10^{-11}	9.6×10^{-9}	1.8×10^{-8}	5.0×10^{-9}	1.3×10^{-8}	3.8×10^{-8}
^{23}Na	8.3×10^{-13}	3.5×10^{-10}	5.3×10^{-10}	2.0×10^{-10}	5.3×10^{-10}	1.2×10^{-9}
^{24}Mg	6.8×10^{-13}	4.1×10^{-10}	9.9×10^{-10}	2.8×10^{-10}	2.7×10^{-10}	2.8×10^{-9}
^{26}Mg	9.2×10^{-14}	4.6×10^{-10}	1.4×10^{-9}	2.4×10^{-10}	2.7×10^{-10}	4.6×10^{-9}
^{27}Al	4.4×10^{-15}	7.0×10^{-11}	3.2×10^{-10}	4.0×10^{-11}	1.1×10^{-10}	9.8×10^{-10}
^{28}Si	2.0×10^{-14}	2.8×10^{-10}	3.0×10^{-10}	2.9×10^{-10}	2.6×10^{-10}	2.6×10^{-9}

Table 5.6: Surface abundance of light elements for all our models. Model M1 shows the largest ^{18}O abundance and the lowest abundance for all elements heavier than oxygen. This model have the lowest amount of protons mixed down into the HeCZ and the lowest maximum temperature. Model M1 would, then, need a much longer splitting timescale to enable a depletion of ^{18}O.

5.8 Discussion

The results presented in the previous sections show that the production of s-process elements in the models is mainly determined by the time spanned between the start of the PIE and the splitting of the convective zone (Δt_{PIE}) and the time evolution of the neutron flux. It is in this context that we discuss, in this section, our results and compare them to those from other authors.

Fujimoto et al. (2000) proposed a general picture for the enrichment of CNO and, potentially, s-process elements in extremely metal-poor stars. Although in their models stars with mass $M < 1.2M_{\odot}$ and metallicity [Fe/H] < -4 experience the PIE during the core He-flash, the splitting timescale for the HeCZ is so short that there is no s-process enhancement in the surface. In their models related to the PIE in the core He-flash, based on those by Hollowell et al. (1990), they find $\Delta t_{PIE} \approx 2.5 \times 10^{-3}$yr. In more recent results by the same group (Suda & Fujimoto 2010), the picture remains similar to the one proposed by Fujimoto et al. (2000), although there is no available information about Δt_{PIE}. On the other hand, Campbell et al. (2010) found a large s-process production during the PIE of a $M = 1\ M_{\odot}$ with metallicity [Fe/H] $= -6.5$. Our models for the core He-flash agree with results by Campbell et al. (2010) in terms of the existence of s-process production during this evolutionary stage. The level of production and of surface enrichment are, however, quantitatively different.

It should be stated that an important difference among calculations by different authors relates to the treatment of mixing during the PIE. As described before, our calculations with GARSTEC use a diffusive approach for convective mixing to account for the competition between mixing and nuclear burning. This is similar to the scheme used by Campbell et al. (2010). On the other hand, models computed by Fujimoto et al. (2000) and Suda & Fujimoto (2010) assume, during the PIE, homogeneous (instant) mixing down to a depth in the HeCZ determine by equating the convective turn-over and proton captures by ^{12}C timescales. Is it this less physical approach at the root of the qualitative differences in the results regarding s-process nucleosynthesis?

Different neutron fluxes lead to different s-process paths. Campbell et al. (2010) found a neutron superburst already at the beginning of the PIE, achieving maximum neutron density values of $\sim 10^{15}$cm^{-3}, which immediately produces large amounts of s-process elements. On the other hand, in our models, as the ingestion of protons progresses, the neutron density increases smoothly up to values above 10^{14}cm^{-3} (see Figure 5.5). This results in a slower production of s-process in the HeCZ than the one found by Campbell et al. (2010). Also, the larger size of our convective zone contributes to effectively slow down the production of s-process elements. The combination of a slower production and a shorter timescale for the splitting leads to surface abundances lower than those reported by Campbell et al. (2010): for instance, their Sr surface abundance is more than 2 dex larger than ours (Table 5.7). We note here that Campbell et al. (2010) had to extrapolate their results because of numerical problems which did not allow them to follow the dredge-up of processed material into the stellar envelope. On the contrary, our results are based on full models that follow in detail the enrichment of the stellar surface as a consequence of the merging between the HCZ and the convective envelope following the PIE. Although we do not believe the difference in the final enrichement are caused because of extrapolations done by Campbell et al. (2010) (based on reasonable assumptions), it is clear our calculations represent a qualitative step forward in modelling the PIE and subsequent enrichment of stellar envelopes.

We have compared our models with the hyper metal-poor (HMP) stars HE1327-2326 and HE0107-5240. It is clear that the self-pollution scenario cannot explain the abundance patterns observed in HE0107-5240 (this scenario is not suitable to HE1327-2326 since this star is not a giant and has not undergone the He-core flash yet): our models produce ~ 3 dex more [C/Fe] and at least 2 dex more Sr and Ba than observed in HE0107-5240 (see blue squares and black solid line in Fig. 5.17). In the binary scenario, on the other hand, there is no restriction to the evolutionary stage of the observed star and we can compare our models with both stars. In this scenario, material is transferred from the primary star (represented here by our models) and is expected to be diluted in the envelope of the companion star (the observed star). We assumed an initial solar-scaled composition of the same metallicity as our model M2 for the observed star and diluted the surface composition obtained in our models with this material by a factor that would match the resulting carbon abundance ([C/Fe]) to the observed value. This factor, f_D, represents the fractional mass of accreted material with respect to the mass of the accreting star over which the polluting material is mixed. Therefore, we used dilution factors $f_D = 2 \times 10^{-3}$ and $f_D = 6 \times 10^{-3}$ for HE1327-2326 and HE0107-5240, respectively.

Figure 5.17 shows the abundances derived for the two HMP stars along with the predictions from our models. Comparing with HE1327-2326 abundances, our model including dilution (see red symbols and red dashed line in Fig. 5.17), which by definition matches the observed C abundance, underproduces N by a factor of 7 and O by a factor of 9. The other elements shown in Fig. 5.17 are all underproduced by factors larger than 10 in comparison with the observations, except lithium. One interesting signature of the PIE is the ^{7}Li production (Iwamoto et al. 2004; Cristallo et al. 2009a). Our models produce Li surface abundance more than two orders of magnitude larger than the Spite plateau (Spite & Spite 1982). Therefore, Li is overproduced when comparing the diluted values with those observed in the HMP stars (Fig. 5.17). In any case, we do not account for the possibility that Li may be (partially) destroyed after being accreted.

For HE0107-5240 our model including dilution produces oxygen in agreement with the observed values, while N is strongly overproduced by a factor of ~ 60. Na, Mg, Al, Ca,

Ti, and Ni are underproduced in our models, however, they could come from an early supernova that polluted the cloud (blue symbols and blue dashed line in Fig. 5.17). For Sr and Ba observations allow only the determination of upper values for their abundances. Our model predicts abundances for these elements a factor of 4 smaller than the observed limits. Nishimura et al. (2009) have done a parameterized study of the PIE in zero metallicity stars. They parameterized the amount of ^{13}C mixed and the duration of the mixing epoch. They suggested that the primary star that polluted HE0107-5240 should have a mass in the range $1.5M_{\odot} < M < 3.0M_{\odot}$ and therefore suffered PIE during the AGB phase. Our models show that stars with smaller masses should not be discarded as the source of carbon and s-process enhancement for this star.

In our simple dilution model, we have assumed that mass was transferred before the star entered the AGB phase. Low-mass stars that suffered PIE during the core He-flash undergo a normal AGB evolution, i.e., there is no PIE during this phase. Therefore, the production of s-process elements should happen in a radiative environment if a ^{13}C pocket is formed. We might speculate on the possible consequence if the primary had not transferred mass to the companion star right after the PIE but rather during or after its AGB evolution. The main products carried to the surface after the third dredge-up (TDU) are carbon and s-process elements. Hence, before transferring mass, the primary would be even more enriched in these elements than prior to this phase. Nitrogen abundance would remain the same since Hot Bottom Burning (HBB) does not happen in stars with masses M = 1 M$_{\odot}$ and Li would be depleted during the TDU. In this way, a better match to the nitrogen and the lithium abundances of HE 0107-5240 could be obtained if the accreted mass is small enough. Also, the ^{12}C/^{13}C ratio would increase during the AGB evolution and could better match the observed lower limit for HE 0107-5240 (^{12}C/^{13}C > 50).

Element	M2	M3	M4	M6	M7
C	6.49	6.24	6.44	6.82	5.69
N	6.80	6.34	6.96	6.94	5.81
O	5.39	5.13	5.46	5.71	4.58
Sr	1.67	2.32	2.08	2.71	1.88
Y	2.04	2.58	2.45	3.11	2.23
Zr	2.14	2.78	2.59	3.26	2.33
Ba	3.37	3.65	3.85	4.30	3.13
La	3.69	3.72	4.15	4.39	3.24
Eu	3.33	3.36	3.79	4.08	2.18
Pb	5.02	5.05	4.93	4.82	5.31

Table 5.7: Surface abundances given in terms of: [X/Fe] $= \log_{10}(\mathrm{X/Fe})_{\star} - \log_{10}(\mathrm{X/Fe})_{\odot}$.

Concerning our zero metallicity model, we have found that only elements lighter than iron have been produced. In the viewpoint of the binary pollution scenario, this result does not support a low-mass zero metallicity star as the polluting companion of the two HMP stars discussed in this paper, if mass is transferred before it enters the AGB evolution.

In closing the discussion, we have done a simple test to determine if the production of s-process elements during the PIE is sensitive to the stellar mass. As stated before, Fujimoto et al. (2000) has found an upper limit of 1.2 M$_{\odot}$ for the occurrence of the PIE.

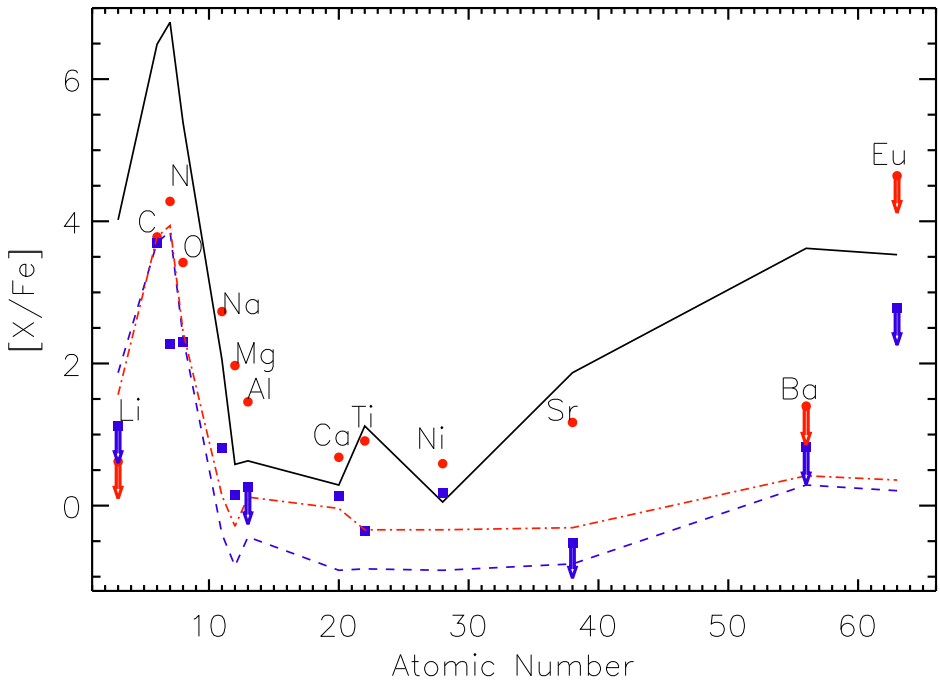

Figure 5.17: The abundance patterns of HE1327-2326 (filled red circles, taken from Frebel et al. (2008)) and HE0107-5240 (filled blue squares, taken from Christlieb et al. (2004) and Bessell et al. (2004)). The black line represent the surface abundance of our standard model (M2), while the red and blue lines represent the abundance of M2 after dilution by a factor of $f_D = 2 \times 10^{-3}$ and $f_D = 6 \times 10^{-3}$, respectively. Arrows indicate upper limits. Li abundance is given as $\log\epsilon(\mathrm{Li}) = \log(N_{Li}/N_H) + 12$.

On the low-mass range, we have computed the evolution of a 0.82 $M_\odot$ and Z=10^{-8} model (representative of the lowest stellar mass that has had time to evolve to the core He-flash in the lifetime of the Milky Way) and found that, in comparison to model M2, the splitting time is a factor of 3 shorter ($\Delta t_{PIE} =\sim 0.08$ yr), but still more than 30 times larger than models by Hollowell et al. (1990). The neutron flux increases more rapidly than in model M2 and just 0.03 yr after L^{He}_{max}, the neutron density at the bottom of the HeCZ is already larger than 10^{14} cm^{-3}. As a result we find that, associated with the PIE, there is a total neutron exposure at the bottom the HeCZ of 130 mbarn^{-1} and an average neutron exposure over the whole HeCZ of 30 mbarn^{-1}. We have performed post-processing nucleosynthesis for this model. The abundance pattern during the HeCZ is very similar to model M2 (and common to all models of equal metallicity undergoing the core He-flash) and the neutron exposure very large and within a factor of 2 of model M2. As can be seen in Table 5.7, s-process elements are efficiently produced with a abundance pattern more prominent towards the first and second s-process peak than model M2 due to its lower neutron exposure.

At the end of the PhD, it was realized that interpolation in metallicity used in GARSTEC underestimates the opacity for $0 < Z < 10^{-4}$. Although a test model showed that this caused difference in the results presented in this chapter, the differences are not sufficient high to change the main results and conclusions presented here.

5.9 Conclusions

We have performed evolutionary calculations for low-mass EMP and zero metallicity stars. Our models follow the proton ingestion episode (PIE) during the core He-flash and the subsequent hydrogen flash. We have then used these calculations as input to a post-processing unit, where we have performed calculations of s-process nucleosynthesis. A comparison with and among similar calculations found in the literature shows that the location at which the He-flash occurs varies among different stellar codes (varying from 0.15 (Schlattl et al. 2001), ~ 0.26 this paper to 0.41 (Hollowell et al. 1990)). This is indicative of the uncertainties in stellar modeling and is likely to impact results of the PIE modeling.

The production of s-process elements and subsequent surface enrichment during the PIE in EMP low-mass stars depends strongly on the efficiency of the convective mixing and on the general properties of the PIE (for instance, Δt_{PIE}). We do find large production of s-process elements in our models. The surface abundances after dredge- up are, however, about 2 dex smaller than those reported by Campbell et al. (2010). This is likely the result of the difference in the neutron density history between our models and those by Campbell et al. (2010); we do not find the neutron superburst reported by these authors. In more detail, our models produce 2-3 dex less first and second peak s-process elements whereas Pb production is smaller in our models by 1.3 dex. On the other hand, our results qualitatively agree that s-process production happens during the PIE in the core-He flash phase, which is in contrast with (Fujimoto et al. 2000; Suda & Fujimoto 2010) results who found no relevant s-process production during the PIE.

Our models produce C, N, and O surface abundances 2-3 dex larger than the abundance values observed in the HMP stars. The high CNO abundances in our models disfavor the self-enrichment scenario to explain the EMP abundance patterns, as other works on the topic have shown before. In the viewpoint of the mass-transfer scenario, our models support the idea that a low-mass star can be the donor star because the dilution of the transferred material

occurs in the secondary star envelope. In fact, our estimation of the dilution factors during the accretion process shows that the secondary needs to accrete a mass equal to only a few parts per thousand of its own envelope mass in order to match the observed carbon abundances.

Based on our results, and in qualitative agreement with those from Campbell et al. (2010), we conclude that stars with masses $M \leq 1\ M_{\odot}$ cannot be excluded as the binary companions of the two most iron deficient stars yet observed. In addition, the latest findings by Caffau et al. (2011, 2012) push the lowest metallicity at which low mass stars can form, increasing the need of detailed models for this class of stars. All these results reinforce the necessity of detailed studies of the PIE, both with hydrodynamic simulations and stellar evolutionary models, in order to achieve a more realistic picture of the its properties.

Chapter 6

Intermediate-Mass Stars

6.1 Models

We have performed evolutionary calculations from the zero-age main-sequence to the TP-AGB phase. The composition is solar-scaled with metallicities Z=0, Z = 10^{-8}, Z = 10^{-7}, and Z = 10^{-5}. Our standard models (I1, I2, I3, I7, I8, I9, I10, I11, I12) include overshooting, with the standard choice of the free parameter $f = 0.016$ (see Chapter 5 for more details), and low-temperature opacities with varying C/O ratio. Convection is modeled using the Mixing Length Theory (MLT) and the mixing length parameter $\alpha = 1.75$, similar to the one obtained from standard solar model calculations. Mass-loss is included as described in Chapter 3. OPAL equation of state (Rogers et al. 1996) was used. Radiative opacity tables are also from OPAL Iglesias & Rogers (1996). We have used the results by Itoh et al. (1983) for electron conduction opacities. For these models we have used updated reaction rates in the GARSTEC network. Most of the rates for the proton capture and some alpha capture reactions are from the newest compilation by Iliadis et al. (2010). The 3α reaction rate is taken from Fynbo et al. (2005).

In order to verify the impact of the main uncertanties in AGB modelling in the final composition, we have performed extra models using: 1) fixed C/O opacities, 2) the mass-loss rate according to Bloecker (1995), and 3) smaller overshooting parameter.

Model	Mass($M_\odot$)	Z	
I1	1.5	10^{-8}	Std
I2	2.0	zero	Std
I3	2.0	10^{-8}	Std
I4	2.0	10^{-8}	fixed opacity
I5	2.0	10^{-8}	f=0.008
I6	2.0	10^{-8}	BL95 mass-loss
I7	2.0	10^{-7}	Std
I8	2.0	10^{-5}	Std
I9	3.0	zero	Std
I10	3.0	10^{-8}	Std
I11	3.0	10^{-7}	Std
I12	3.0	10^{-5}	Std

Table 6.1: List of intermediate-mass stars models.

6.2 From ZAMS to the TP-AGB

In Pop. I and II[1] intermediate-mass (IM) stars, the H-burning during the MS is dominated by the CNO cycles. The path followed by these stars, during the MS, in the HRD is different from that followed by low-mass (LM) stars. While in the LM case the star moves towards larger effective temperatures ($T_{\rm eff}$) and luminosities, the IM star increases its luminosity towards lower $T_{\rm eff}$. In EMP and zero metallicity stars, due to the absence of CNO catalysts, the CNO cycles cannot operate and H-burning is then dominated by the p-p chains. This results in a significant change in the MS morphology of these stars. Figure 6.1 displays the evolution of our standard models in the HRD. As it can be seen, the MS path is similar to that followed by LM stars, as a result of the H-burning being powered by p-p chains.

In the zero metallicity models, the CNO cycles contribute to the H-burning only at the end of the MS. When the star reaches the turn-off, there is still a small amount of H in the core ($X_{\rm H} \sim 10^{-2}$). The temperature in the core is high enough to trigger some He-burning and to produce ^{12}C. Once the ^{12}C abundance reaches $\sim 10^{-12}$, a thermal runaway takes place and a small convective core is formed. The CNO flash can be seen in the HRD as a small loop at the turn-off (Figure 6.1). Figure 6.2 shows how the star reacts to the onset of the thermal runaway by the end of the MS. The density decreases, while the temperature is kept almost constant due to the expansion of the core. The now convective core, dredge-down new fuel, prolonging the MS in this model.

For a given mass, the different degrees of CNO catalysts result in large differences in the turn-off (TO) luminosities (up to ~ 0.25 dex in models with $3.0\,M_\odot$ and ~ 0.4 dex in models with $2.0\,M_\odot$). The larger the initial abundance of CNO elements, the faster their contribution to the H-burning increases and, thus, the smaller is the TO luminosity. The TO temperatures are also larger in models with less CNO catalysts, however, the difference between the models, in this metallicity range, is more modest (< 0.05 dex). The $3.0\,M_\odot$ model with metallicity

[1]Population I stars are young metal-rich stars. The Sun is an example of Pop. I star. They are found in the Disk of our Galaxy. Pop. II, on the other hand, are old metal-poor stars found mainly in the Halo. Pop. III are the primordial stars, without any metal.

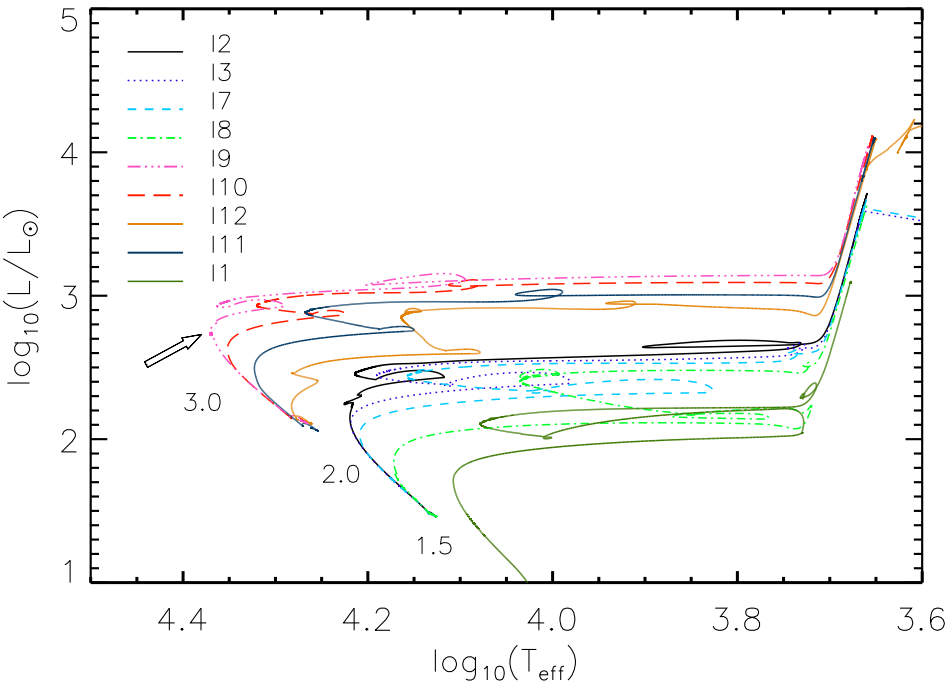

Figure 6.1: HR Diagram of intermediate-mass stars for our standard models. There are significant differences between EMP and Z=0 stars and the Pop I and II MS of IM stars. The arrow indicates the position of the CNO flash in model I9. Numbers indicate the initial stellar mass in $M_{\odot}$.

$Z = 10^{-5}$ have a different TO morphology: it presents a hook-like feature. This kind of structure indicates that a prominent convective core was formed due to the high efficiency of the CNO cycles in this model.

Almost all models avoid the RGB configuration (except model I8) and the core He-burning happens at lower central densities than those experienced by stars with larger metallicities. Moreover, due to the lack of the RGB configuration, the star only experiences one dredge-up episode: the second dredge-up (SDU). The main product brought-up to the surface by the SDU is He. The amount by which its abundance increases depends on the initial mass and the metallicity. The lower the metallicity, the larger the helium abundance after SDU. Figures 6.3 and 6.4 show the abundance profiles of hydrogen, helium and some CNO isotopes just before SDU sets in. It can be seen that SDU goes deeper in the zero metallicity models, reaching layers richer in helium than the model with $Z = 10^{-8}$. For models with the same metallicity, the larger the initial mass, the larger the helium abundance (Table 6.2). In comparison to other works in the literature (Campbell 2007; Suda & Fujimoto 2010), our He abundances agree with their values within less than 8% for any initial mass and metallicity. For instance, we found that the He mass-fraction increases from its initial value Y=0.245 to 0.309 in our $2.0\,M_{\odot}$ model with zero metallicity, while Campbell (2007) and Suda & Fujimoto (2010) found $Y = 0.31$ and $Y = 0.29$, respectively.

Regarding the $^{12}C/^{13}C$ ratio, in the IM models the ratio decreases from an initial value ~ 80 to similar values independent of the metallicity. In contrast, models with zero metallcity

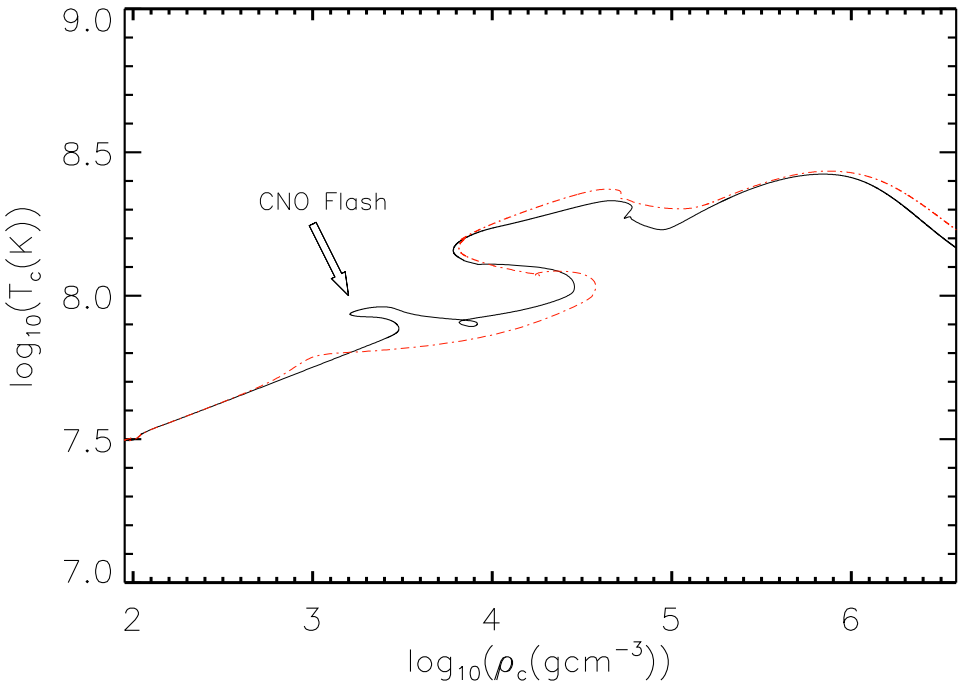

Figure 6.2: Central temperature versus central density for models I9 and I10. During the CNO flash, the central density decreases while the temperature is kept almost constant. Black line indicates models I9 (Z=0) while the red line indicates model I10.

have initially no carbon in its composition and have to produce it in situ. Although the envelope reaches regions where partial H-burning has happened, the burning in this region has been mainly powered by the p-p chains. SDU increases, then, the ratio to $^{12}C/^{13}C = 3$ (see Figures 6.3 and 6.4). Models by Campbell (2007) present similar trends with metallicity and mass, nevertheless, our models have ratios up to 40% smaller than their values. This could be explained by the fact that we have used the newest rate of the reaction $^{12}C(p,\gamma)^{13}N$ (Li et al. 2010) which is a factor of 2 larger than the rates used by Campbell (2007) in the typical temperatures of the H-burning shell.

6.2.1 Lifetimes

Table 6.3 shows the lifetimes of various evolutionary stages for all our standard models. We will compare our results mainly to Campbell (2007), since Suda & Fujimoto (2010) and Lau et al. (2009) do not provide values for these quantities. Our MS lifetimes are in reasonable agreement with the predictions by this study, never being more than $\sim 10\%$ different. Although the MS lifetime increases with decreasing metallicity, for a given mass, due to the increasing dominance of the p-p chains, the lifetimes do not vary more than $\sim 20\%$ between the different metallicities. In comparison to Marigo et al. (2001), our zero metallicity models have MS lifetimes 10-20% shorter than their models. This is the result of the smaller H

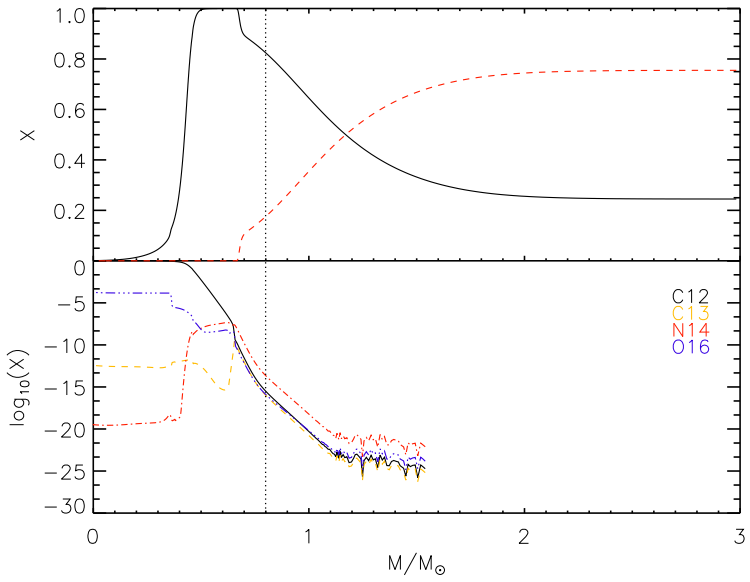

Figure 6.3: Upper panel: The hydrogen (Red line) and helium (Black line) abundances profile before the occurrence of the SDU in model I9. Lower panel: Same as the upper panel for some CNO isotopes. The dotted vertical line represents the maximum depth of the envelope during the SDU.

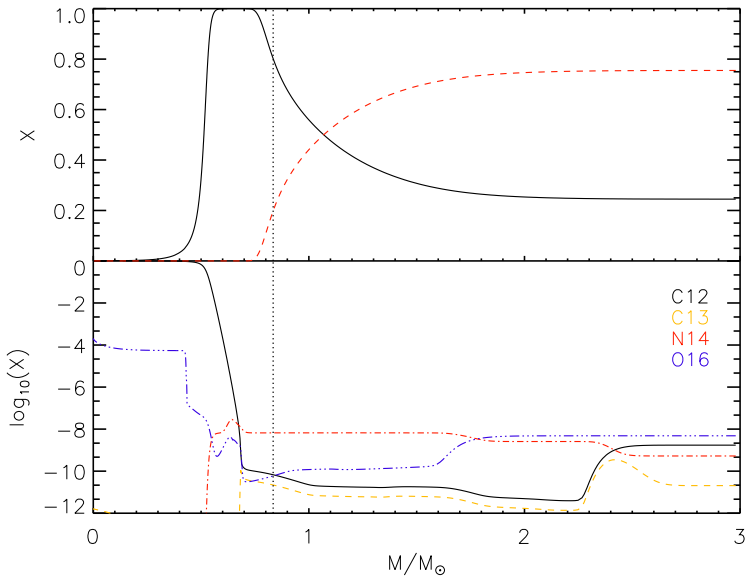

Figure 6.4: Upper panel: The hydrogen (Red line) and helium (Black line) abundances profile before the occurrence of the SDU in model I10. Lower panel: Same as the upper panel for some CNO isotopes. The dotted vertical line represents the maximum depth of the envelope during the SDU.

Model	Y	$^{12}C/^{13}C$
I1	0.265	23
I2	0.309	3
I3	0.295	18
I7	0.286	18
I8	0.264	17
I9	0.353	3
I10	0.325	15
I11	0.300	15
I12	0.264	15

Table 6.2: The surface abundances after SDU for all our standard models.

content in our models.

Model	t_{MS}	t_{SGB}	t_{RGB}	t_{CHeB}
I1	1465	102	zero	150
I2	634(-3)	15(-20)	zero	37(+23)
I3	581(-7)	52(+20)	zero	44(+10)
I7	553(-9)	91(+57)	zero	55(+10)
I8	516(+5)	115(-18)	3(-47)	93(-2)
I9	191(-13)	7(-13)	zero	12(0)
I10	176(-7)	22(+5)	zero	19(+12)
I11	179(+1)	36(+20)	zero	27(+13)
I12	185(0)	11(+39)	zero	48(+2)

Table 6.3: Lifetimes of various evolutionary stages for all our standard models. All ages are given in Myr. t_{MS}: lifetime for the main sequence, t_{SGB}: lifetime for the subgiant branch, t_{RGB}: lifetime for the red giant branch, and t_{CHeB} lifetime for the core He-burning. The numbers in the parenthesis indicate the differences (in percentage) between our lifetimes and those by Campbell (2007)

Following Campbell (2007), the SGB lifetime was defined, in the cases where there is no RGB, as the time between the turn-off and the He-burning ignition in the core. For the $2.0\,M_{\odot}$ models, there is an increase in the SGB lifetime with metallicity. The lower the metallicity, the lower is the density at which He-burning is ignited in the core. For the $3.0\,M_{\odot}$ models, the SGB lifetimes increase with metallicity up to a threshold above which the lifetimes decrease (our most metal-rich model - I12). This is probably related to the efficient convective core occurring in the MS of this model. In spite of the similar behaviour with metallicity and initial mass, the differences between our lifetimes and those by Campbell (2007) varies from 5 up to 57% in this evolutionary stage. The core He-burning, on the other hand, is consistently longer in our models. This can be explained by the inclusion of overshooting in our models that brings more fuel to the core, prolonging the He-burning phase.

6.3 Proton Ingestion Episode

As explained in Chapter 2, in IM stars PIE occurs at the beginning of the TP-AGB phase. In Figure 6.5 we show the evolution of one of our zero metallicity models (I2). PIE occurs after a series of weak pulses at the beginning of the evolution. Similarly to the LM case, the PIE is characterized by a peak in the H-burning luminosity (Figure 6.5). The He-flash, now in a shell, induces the formation of a convective zone (HeCZ) that breaks through the H-He discontinuity due to the low entropy barrier between the H and He layers. Protons are, then, dredge-down into the HeCZ and burnt at high temperatures, resulting in a secondary flash: the H-flash. It can be seen in Figure 6.5 that following the PIE the envelope deepens down and dredges-up material from the former HeCZ, increasing the surface abundance of CNO elements. The amount by which the envelope is enriched is smaller than in the LM case. While PIE in LM stars increases the CNO abundance to $X_{CNO} > 10^{-2}$, in IM stars the increase is more modest ($X_{CNO} \sim 10^{-4} - 10^{-3}$ - See Tab.6.4). Once the metal content in the envelope reaches values of $Z \sim 10^{-4}$, the TP-AGB evolution proceeds as in Pop.I and II stars.

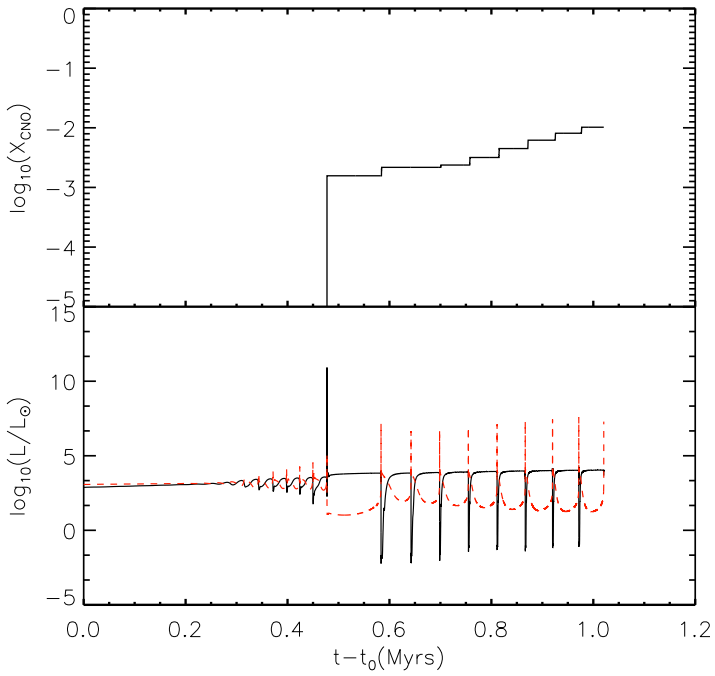

Figure 6.5: Upper panel: Time evolution of the surface abundance of the CNO elements in model I2. Bottom panel: Evolution along the AGB of the H-burning (Black Line) and the He-burning (Red line) luminosities.

Figure 6.6 shows the evolution of the convective regions from the formation of the HeCZ to the post-PIE dredge-up. The outer border of the HeCZ reaches H-rich regions, about 80 yrs after the formation of the HeCZ, and dredges-down protons into this zone. The H-flash causes a splitting of the HeCZ into two convective zone. The Hydrogen Convetive Zone (HCZ) continues expanding until the envelope deepens down and products of the nucleosynthesis

during the PIE are transported to the surface.

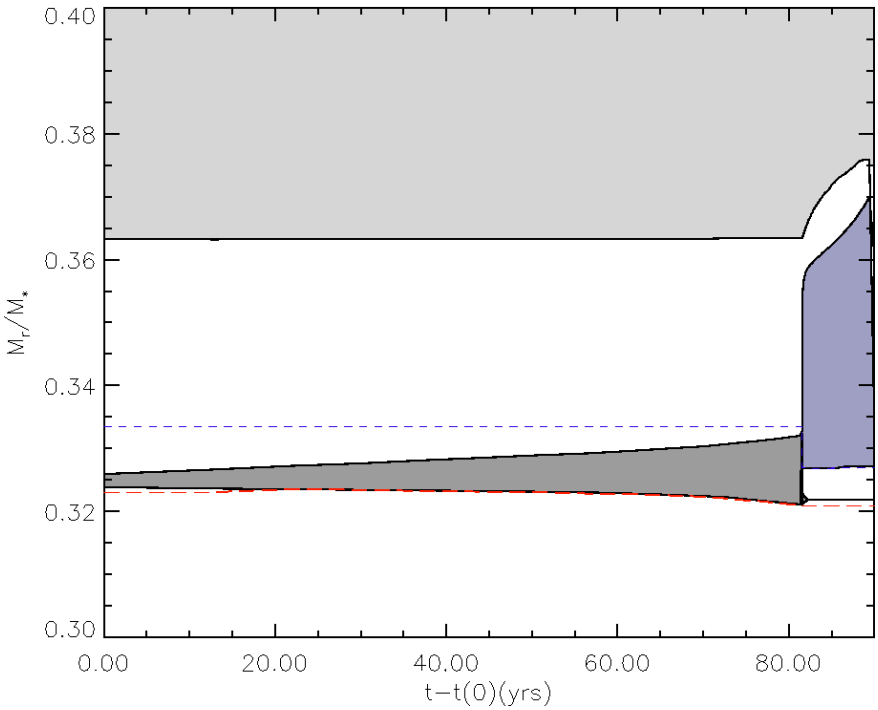

Figure 6.6: An example of PIE during the TP-AGB: Evolution of the convective zone during the PIE of the $2.0\,M_{\odot}$ model with $Z = 10^{-8}$. t_0 is the time at which the convective zone is formed. Blue line is the position of maximum energy released by H-burning. Red line is the position of maximum energy released by He-burning.

In our LM models, we have shown that during the PIE a large amount of neutrons are produced. This neutron production should happen in a similar way to that of LM stars. When protons are dredge-down into the HeCZ, ^{13}C is produced through proton capture by ^{12}C. The abundant ^{4}He is then captured by the newly produced ^{13}C, releasing neutrons into the convective zone. Iwamoto et al. (2004) have speculated the possibility of s-processing during the PIE at the TP-AGB. They have found neutron densities larger than 10^{13}cm^{-3} at the bottom of the HeCZ in their models. Using a network that included neutron production reaction, Campbell (2007) have found neutron production during the PIE. Our models agree with these studies, since they also show large amounts of neutrons inside the HeCZ. Figure 6.7 shows the abundance profile of some selected isotopes during the PIE in the HeCZ of model I7. As expected, neutrons were produced in a large amount ($N_n^{max} \sim 10^{12}$cm^{-3}) during this phenomenon.

6.3.1 Comparison with the literature

We will compare our models mainly to the works by Campbell (2007), Lau et al. (2009), and Suda & Fujimoto (2010) (see Figure 6.8). PIE happens in all our models. For the models with $2.0\,M_{\odot}$, we find that PIE occurs during the TP-AGB for metallicities up to $Z = 10^{-5}$. This is in agreement with the results by Suda & Fujimoto (2010) and Campbell (2007) that

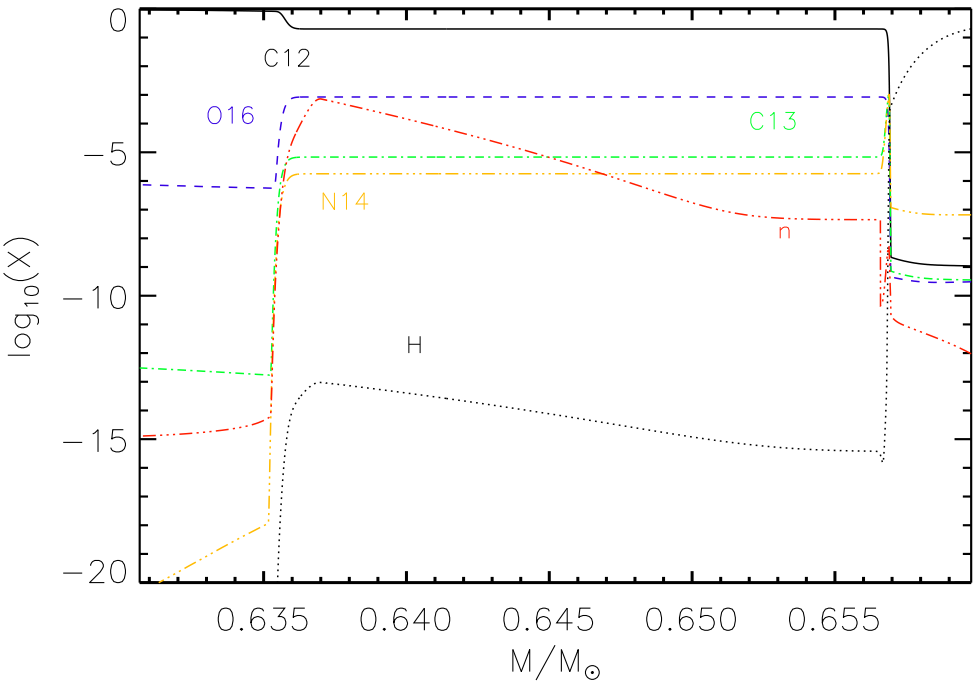

Figure 6.7: Chemical composition of the HeCZ during the PIE before the H-flash. To show the neutron abundance in the plot we added 12 to the logarithm of the neutron mass-fraction, therefore the real maximum neutron abundance in the HeCZ is $X_n \sim 10^{-16}$.

found PIE for metallicities [Fe/H] < -3.0. Nevertheless, for this initial mass Lau et al. (2009) models do not undergo PIE if [Fe/H] > -4.0. Furthermore, when overshooting is included in their model, PIE is supressed at even lower metallicities ($Z = 10^{-7}$).

Table 6.4 shows some properties of the PIE for all our models. The $2.0\,M_\odot$ models have core masses between $0.01\,M_\odot$ and $0.05\,M_\odot$ smaller than those found by Campbell (2007) for similar metallicities. In comparison to models by Suda & Fujimoto (2010), our core masses are usually larger by less than $0.08\,M_\odot$. Regarding the H-flash ignition point, our models have M^H_{max} smaller than the values found in Campbell (2007) models. This is probably a consequence of the inclusion of overshooting in our models. For instance, model I5 which has a smaller overshooting parameter has an H-flash ignition point $0.015\,M_\odot$ larger than model I3. Another signature from our models that was already observed in the LM models is the inner position of the He-flash. Our models have inner ignition points than those found in the literature. This can result in longer ingestion episodes which, in turn, should have an important impact in the s-process production during the PIE.

For the $3.0\,M_\odot$ models, PIE occurs up to metallicities 10^{-5}, however the model with $Z = 10^{-5}$ suffers a weak PIE. The largest discrepancies in the literature are found for this stellar mass. While Campbell (2007) found PIE for [Fe/H] < -4.0, Suda & Fujimoto (2010) metallicity boundary for the occurrence of the PIE is much smaller ([Fe/H] < -5.0). Lau et al. (2009), on the other hand, did not find PIE for any metallicity, but instead, their models undergo the carbon injection. In this phenomenon, a convective zone opens up on top of the

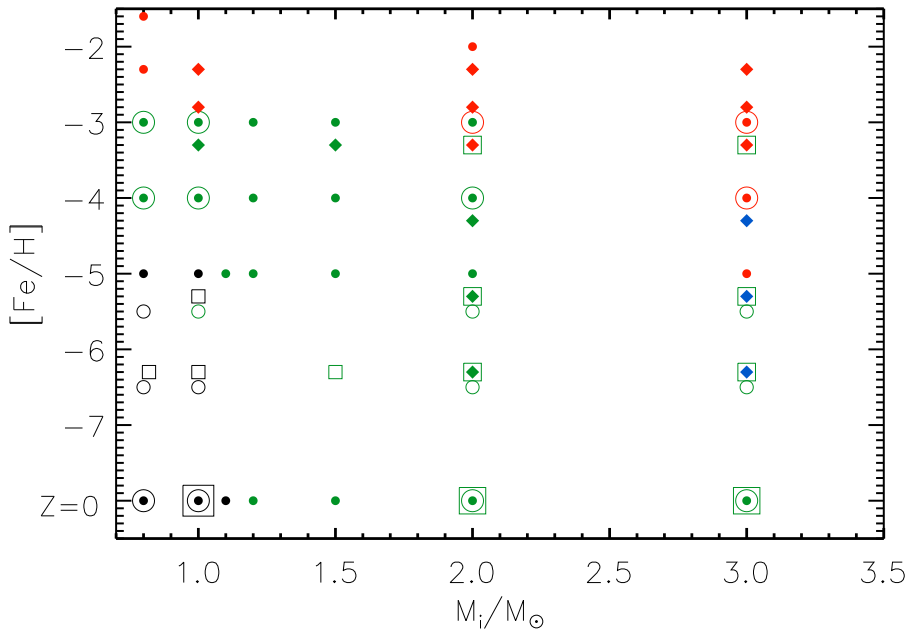

Figure 6.8: Updated version of the mass-metallicity diagram presented in Fig. 2.17 in Chapter 2 including our models. Black symbols represent models that undergo PIE during the core He-flash, green symbols represent models that undergo PIE during the TP-AGB phase, red symbols represent models that do not undergo PIE, and blue symbols represent models that undergo carbon injection during the TP-AGB phase. Open circles represent models by Campbell & Lattanzio (2008), filled circles represent models by Suda & Fujimoto (2010), filled diamonds represent models by Lau et al. (2009), and open squares represent our models.

H-burning shell and carbon from the intershell is dredged-up into the zone.

Concerning the CNO enrichment, we have discussed for the LM stars case that the difference between the core mass and the H-flash ignition point (ΔM_c) is a good diagnostic for the post-PIE enrichment. The smaller values of ΔM_c found by Campbell (2007) results in a much smaller CNO surface enrichment when compared to our models. For instance, our $3.0\,M_\odot$ model with Z=0 has $\Delta M_c = 0.001$ and $Z_{cno} = 0.0004$, while for the same metallicity, their model has $\Delta M_c = 3 \times 10^{-5}$ which increases the CNO abundance only to $Z_{cno} = 8 \times 10^{-6}$.

Table 6.5 shows the comparison of our CNO surface abundance after the PIE with previous works. For the $2.0\,M_\odot$ models with metallicity $Z > 0$ our carbon and nitrogen abundances are compatible with previous works within a factor of 2 or 4. Oxygen, on the other hand, has discrepancies larger than one order of magnitude. This can be related to the inclusion of the reaction $^{13}C(\alpha, n)^{16}O$ in our models which is an extra source of oxygen when ^{13}C is available. For the $3.0\,M_\odot$ models, only the Z=0 of Suda & Fujimoto (2010) can be used for comparison, since for larger metallicities their models do not undergo PIE. Again, except for oxygen our abundances are in agreement.

Model	L^{He}_{max}	L^{H}_{max}	M^{He}_{max}	M^{He}_{c}	M^{H}_{max}	ΔM_c	ΔM_{ig}	Z_{CNO}	Y_s
I1	6.371	11.09	0.504	0.549	0.544	0.005	0.045	0.0017	0.300
I2	5.115	10.92	0.624	0.690	0.641	0.048	0.056	0.0016	0.326
I3	5.551	11.03	0.622	0.640	0.639	0.001	0.018	0.0015	0.316
I4	4.867	11.27	0.621	0.640	0.626	0.014	0.019	0.0022	0.321
I5	5.526	10.77	0.628	0.651	0.641	0.010	0.023	0.0016	0.314
I6	5.215	10.69	0.620	0.640	0.639	0.001	0.020	0.0010	0.315
I7	5.736	11.10	0.636	0.656	0.652	0.004	0.020	0.0011	0.297
I8	7.423	10.82	0.623	0.652	0.640	0.012	0.029	0.0045	0.269
I9	5.971	11.10	0.784	0.791	0.789	0.002	0.007	0.0003	0.354
I10	5.826	11.22	0.823	0.829	0.828	0.001	0.006	0.0005	0.326
I11	6.346	11.16	0.831	0.836	0.833	0.003	0.005	0.0005	0.302
I12	6.072	5.365	0.811	0.821	0.820	0.001	0.010	0.0004	0.265

Table 6.4: Main properties of the proton ingestion episode. L^{He}_{max} and L^{H}_{max} are the logarithm of the maximum He-burning luminosity and the maximum H-burning luminosity in units of solar luminosity, respectively. M^{He}_{max} is the position of maximum energy released by He-burning. M^{He}_{c} is the core mass.M^{H}_{max} is the position of maximum energy release by H-burning. ΔM_c is the distance, in mass, that the H-shell moves inwards during the PIE. ΔM_{ig} is the distance, in mass, between the He-flash ignition point and the H-shell. All masses are given in units of solar mass. Z_{CNO} is the surface mass-fraction of CNO elements.Y_s is the surface helium abundance after the PIE.

6.3.2 S-process

It was discussed in Chapter 5 that during the PIE the amount of s-process elements produced is a function of the time integrated neutron flux, the neutron exposure, averaged over the entire convective zone. The neutron exposure, in turn, depends on the neutron flux and on the time between the start of the proton mixing and the splitting of the HeCZ (Δt_{PIE}). Figure 6.9 shows the surface abundance distribution for all our standard models with metallicities $Z \geq 10^{-8}$ after the PIE. For models with metallicity 10^{-8} (I1, I3, and I10), the largest differences in the abundance distribution can be seen in model I10. This model has Δt_{PIE} three to two orders of magnitude larger than models I1 and I3, respectively (See Table 6.6). S-process occurs in the three models, however, only model I10 has enough time to increase the s-process elements abundances in several orders of magnitude. The same bahaviour can be seen in models with metallicity $Z = 10^{-7}$ and $Z = 10^{-5}$.

The lower the metallicity the lower the number of iron-peak seeds available for neutron capture. If the same amount of neutrons are released in all the cases, the lower metallicity stars should produce a larger amount of heavier s-process than in the higher metallicity case, due to the larger neutron to seed ratio. Figure 6.10 shows the ratio between the different s-process components. During the PIE similar neutron densities are achieved at the bottom of the HeCZ by all models ($N_n > 10^{12} cm^{-3}$). From Figure 6.10 it can be seen that Δt_{PIE} plays a more important role in determining the final indices than the metallicity. The larger PIE timescale in models I7 and I8 results in larger s-process production than models I11 and I12, respectively. Moreover, the longer PIE timescale in model I8 in comparison to model I7 leads to larger neutron exposures and, therefore, to the production of heavier s-process elements in this model.

Reference	Mass	[Fe/H]	X_C	X_N	X_O
This work	1.5	-6.3	9.80×10^{-4}	7.40×10^{-4}	3.90×10^{-6}
This work	2.0	$-\infty$	1.10×10^{-3}	4.50×10^{-4}	1.90×10^{-5}
Siess et al. (2002)	2.0	$-\infty$	3.38×10^{-3}	6.72×10^{-5}	8.52×10^{-5}
Suda & Fujimoto (2010)	2.0	$-\infty$	1.39×10^{-4}	6.74×10^{-5}	8.52×10^{-5}
This work	2.0	-6.3	1.00×10^{-3}	5.00×10^{-4}	4.50×10^{-6}
This work	2.0	−5.3	7.30×10^{-4}	3.80×10^{-4}	6.20×10^{-6}
Suda & Fujimoto (2010)	2.0	−5.0	9.36×10^{-4}	8.87×10^{-5}	3.64×10^{-5}
This work	2.0	−3.3	4.10×10^{-3}	1.40×10^{-4}	8.30×10^{-4}
Iwamoto et al. (2004)	2.0	−2.7	9.84×10^{-4}	1.80×10^{-4}	6.95×10^{-5}
Suda & Fujimoto (2010)	2.0	−3.0	1.36×10^{-3}	1.08×10^{-4}	6.23×10^{-5}
This work	3.0	$-\infty$	1.30×10^{-4}	1.70×10^{-4}	1.70×10^{-7}
Siess et al. (2002)	3.0	$-\infty$	3.38×10^{-3}	6.72×10^{-5}	8.52×10^{-5}
Suda & Fujimoto (2010)	3.0	$-\infty$	1.39×10^{-4}	6.74×10^{-5}	8.52×10^{-5}
This work	3.0	-6.3	3.50×10^{-4}	1.40×10^{-4}	2.00×10^{-7}
This work	3.0	−5.3	3.80×10^{-3}	1.40×10^{-4}	3.70×10^{-6}
Suda & Fujimoto (2010)	3.0	−5.0	2.10×10^{-5}	4.47×10^{-7}	6.32×10^{-7}
This work	3.0	−3.3	3.90×10^{-3}	2.80×10^{-5}	1.10×10^{-5}
Iwamoto et al. (2004)	3.0	−2.7	4.94×10^{-5}	7.29×10^{-6}	1.71×10^{-5}
Suda & Fujimoto (2010)	3.0	−3.0	1.34×10^{-6}	4.34×10^{-6}	8.93×10^{-6}

Table 6.5: Comparison of CNO abundances after the PIE with previous works. We focus on the work by Suda & Fujimoto (2010) because they provide the abundance right after the post-PIE dredge-up, while other works only give the yields (Campbell & Lattanzio 2008) or the abundance in plots(Lau et al. 2009).

Model	Δt_{PIE}	Δt_d
I1	2.6×10^{-4}	57.17
I2	3.0×10^{-3}	11.33
I3	4.1×10^{-3}	8.53
I4	1.1×10^{-1}	0.68
I5	2.0×10^{-2}	6.14
I6	3.5×10^{-2}	23.38
I7	4.7×10^{-1}	4.68
I8	7.4×10^{-1}	4.45
I9	7.6×10^{-3}	0.59
I10	2.1×10^{-1}	0.20
I11	7.0×10^{-2}	0.20
I12	2.5×10^{-1}	15.50

Table 6.6: Δt_{PIE}: time between the onset of the PIE and the H-flash. Δt_d: time between the H-flash and the start of the post-PIE dredge-up. All times are given in yrs.

Another important property affecting the s-process production during the PIE is the size of the convective zone (ΔM_{ig}). In a convective environment, at each timestep the s-process products are mixed throughout the convective zone. This should lead to a smaller production

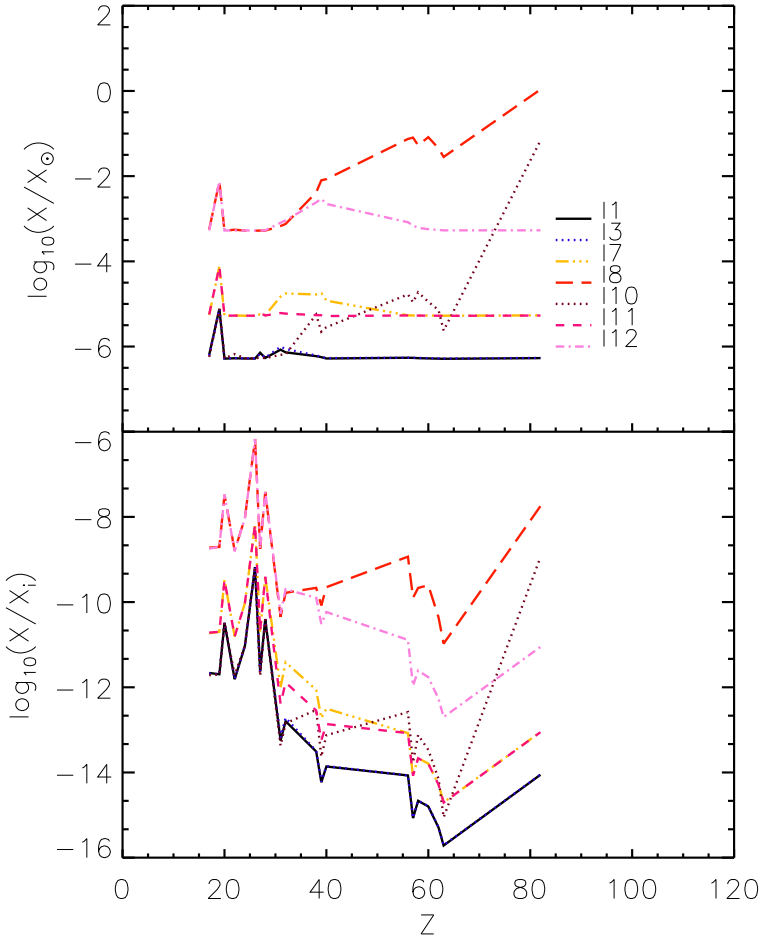

Figure 6.9: Bottom Panel: Total surface abundance distribution of some selected elements heavier than ^{30}Si after the PIE. Upper panel: The same as in the bottom panel, but relative to solar.

in comparison to a radiative s-process. As explained in Chapter 5, the average neutron exposure is the key quantity in the convective s-process. Therefore, a larger convective zone should imply in a smaller s-process production. Nevertheless, in our models, the main property controlling the average neutron exposure is the PIE timescale. In the models with $Z = 10^{-7}$, for instance, the five times longer PIE compensates the larger ΔM_{ig}. For models with masses $M \leq 2.0\,M_{\odot}$, we found $\Delta M_{ig} \leq 0.056\,M_{\odot}$. In the models presenting $\Delta t_{PIE} < 3.0 \times 10^{-3}\,yr$, however, the s-process production was almost absent.

Cristallo et al. (2009a) presented the evolution and nucleosynthesis of a star with initial mass $1.5\,M_{\odot}$ and metallicity $Z = 5 \times 10^{-5}$. Their model has a different behaviour for the s-process nucleosynthesis during the PIE. They have found that after the splitting of the HeCZ ^{13}C is burnt at smaller temperatures in the HCZ than at the bottom of the HeCZ leading to enrichment in light s-process elements. Our model I7 is the only model that presents a

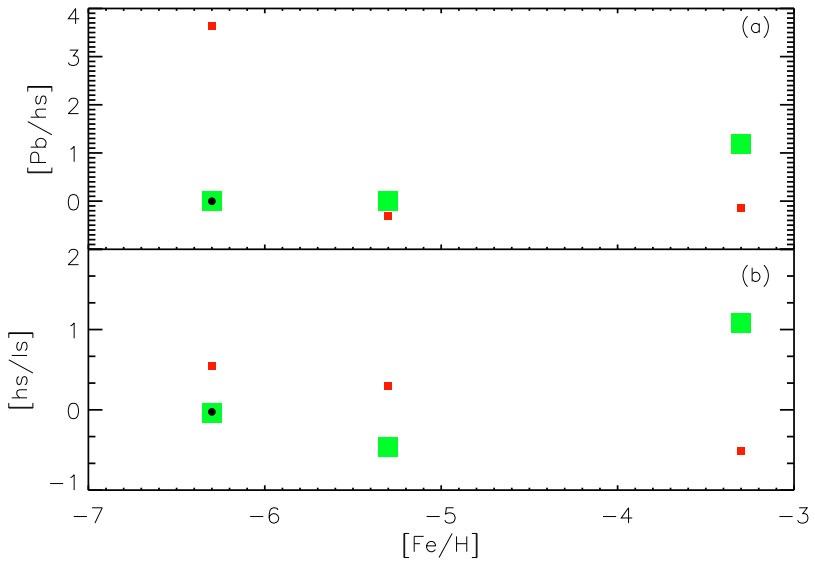

Figure 6.10: S-process indices predicted by our models. In panel (a) we report the [Pb/hs] index, while in panel (b) we plot the [hs/ls] index. Green squares indicate the $2.0\,\mathrm{M}_{\odot}$ models, red squares indicate the $3.0\,\mathrm{M}_{\odot}$ models, and the black circle indicates the $1.5\,\mathrm{M}_{\odot}$ model. We adopted the definition given by Bisterzo et al. (2010) for the light (ls) and heavy (hs) indices.

significant enhancement in light s-process elements after the PIE. However, this enrichment happens during the PIE because right after the splitting of the HeCZ, the ^{14}N abundance is already larger than the ^{13}C switching off s-processing in the HCZ (Figure 6.11).

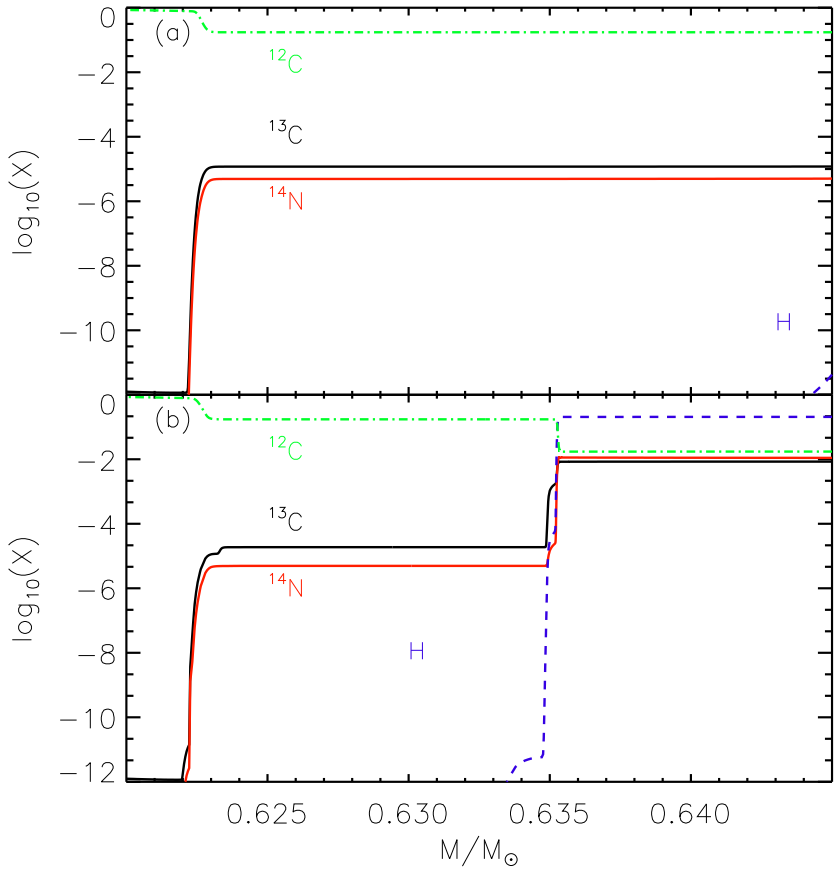

Figure 6.11: Panel (a): The profile of some selected isotopes involved in the production and destruction of neutrons in model I3 before the splitting ($\Delta t = -8.8 \times 10^{-5}\, yr$). Panel (b): Same as in panel (a) but after the splitting ($\Delta \mathrm{t} = 0.04\,\mathrm{yr}$).

6.4 Neutron Production after the PIE

After the post-PIE dredge-up, the envelope is enriched mainly in CNO elements and the surface metallicity increases to values larger than 10^{-4}. The subsequent TPs follow the "normal" AGB evolution found in more metal-rich models. Figure 6.12 shows the evolution of the convective zones in the third TP of model I3. Like in the more metal-rich AGB evolution, the HeCZ never reaches H-rich layers and thus, no proton ingestion occurs. In this case, neutrons might be produced during the interpulse period, after TDU brings down protons from the envelope, in a radiative layer above the intershell: the ^{13}C pocket. The amount of neutrons produced inside the pocket is usually much smaller than in the PIE.

In the models by Gallino et al. (1998), the ^{13}C pocket efficiency is treated as a free parameter, although the mechanism responsible for the creation of the pocket is still subject of debate. One of the proposed mechanisms for the ingestion of protons into the inter-

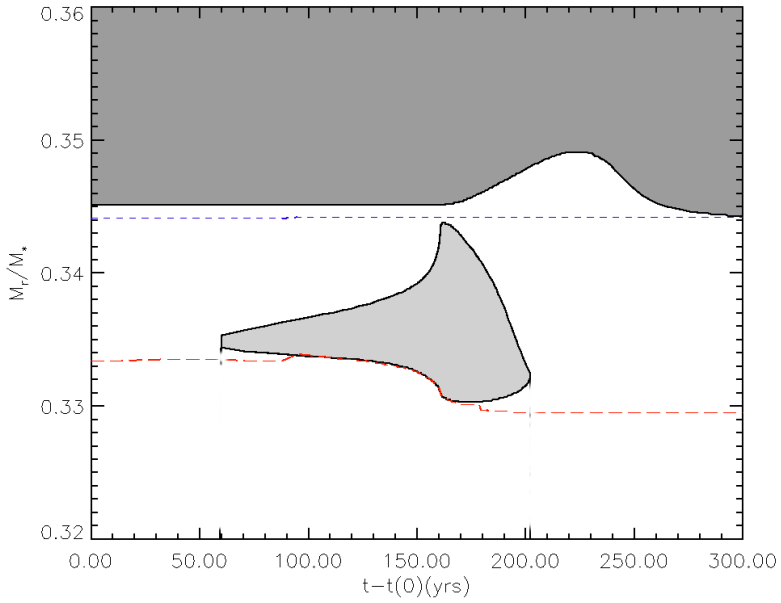

Figure 6.12: The evolution of TP number three of model I3. There is no PIE in this TP. The HeCZ never reaches the H-burning shell. Blue line is the position of maximum energy released by H-burning. Red line is the position of maximum energy released by He-burning. Time was shifted for clarity.

shell is the inclusion of diffusive overshooting at the lower border of the convective envelope (Herwig et al. 1997). We expect to find the ^{13}C pocket in our models, since diffusive overshooting is included. Also, at each TP another source of neutrons is expected to be activated: the $^{22}\mathrm{Ne}(\alpha,\mathrm{n})^{25}\mathrm{Mg}$. During the TP, the intershell material is mixed and ^{14}N is converted into ^{22}Ne through the reaction chain, $^{14}\mathrm{N}(\alpha,\gamma)^{18}\mathrm{F}(\beta^{+}\nu)^{18}\mathrm{O}(\alpha,\gamma)^{22}\mathrm{Ne}$. The ^{22}Ne neutron source is activated for temperatures $\mathrm{T} \geq 3.0 \times 10^{8}\,\mathrm{K}$. In most metal-rich models with masses $\mathrm{M} < 4.0\,\mathrm{M}_{\odot}$ this neutron source is only marginally activated (Iben & Truran 1978; Straniero et al. 1997; Gallino et al. 1998). Figure 6.13 shows the maximum temperature reached at the bottom of the HeCZ during the TP. All models reach after some TPs, the temperature of activation of the ^{22}Ne neutron source. Our $\mathrm{T}_{\mathrm{max}}$ are in agreement with the maximum temperatures found by Lugaro et al. (2012) when using the Stromlo evolution code for models $\mathrm{M} \geq 2.0\,\mathrm{M}_{\odot}$. However, it is important to keep in mind that the temperature at the bottom of the HeCZ increases with the TP number and some models might achieve $\mathrm{T} = 3.0 \times 10^{8}\,\mathrm{K}$ at the very end of the TP evolution (see Figure 6.14). This implies that this neutron source has differing degree of contribution to the s-process. The larger neutron fluxes resulting from the ^{22}Ne source activate s-process branching that are usually not active in the ^{13}C pocket.

Neutrons can also be produced at the bottom of the HeCZ by the reaction $^{13}\mathrm{C}(\alpha,\mathrm{n})^{16}\mathrm{O}$, if enough ^{13}C is left during the interpulse in the intershell. When the HeCZ is formed, ^{13}C is mixed into high temperature regions and it is captured by ^{4}He, releasing a large amount of neutrons.

In the s-process calculations by Bisterzo et al. (2010) and Lugaro et al. (2012), the parametrized efficiency of the ^{13}C pocket is kept constant in all TPs. However, models by Cristallo et al.

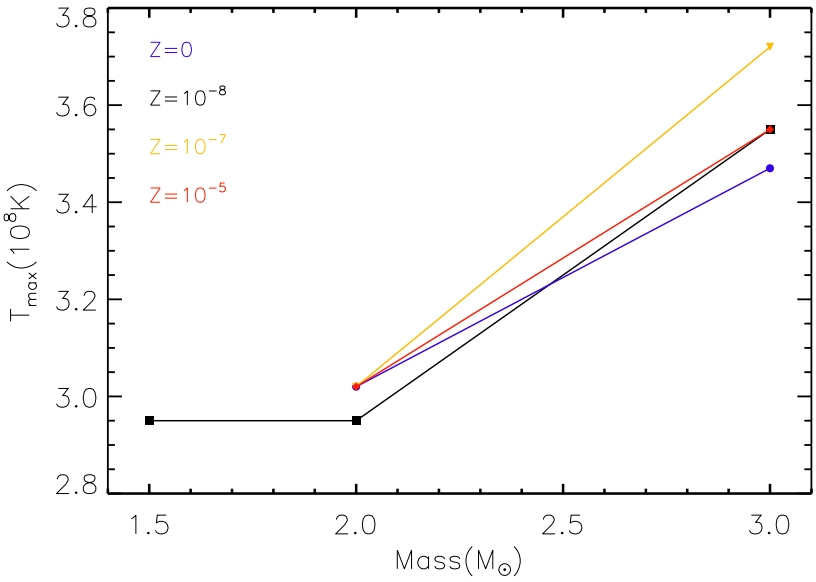

Figure 6.13: Maximum temperature at the bottom of the HeCZ during the TP as a function of the initial mass.

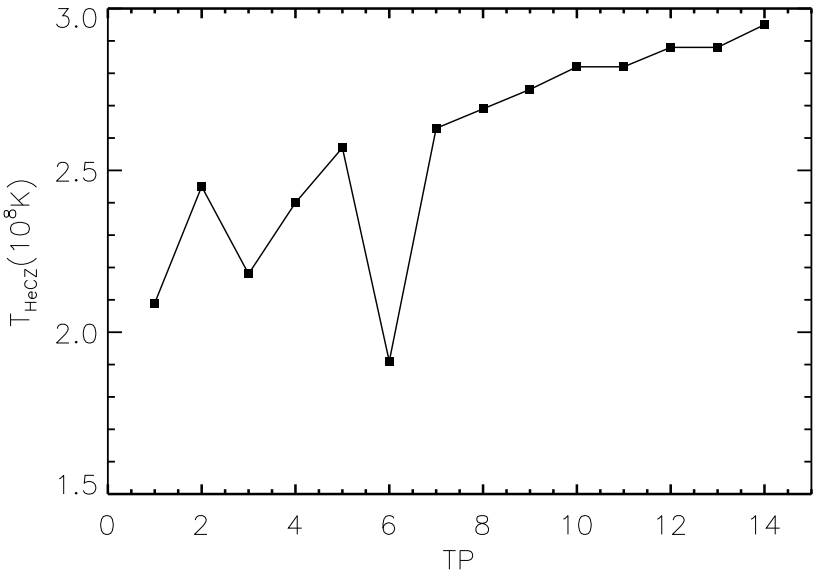

Figure 6.14: Temperature at the bottom of the HeCZ during the TP as a function of the TP number for model I1.

(2009b) performed with a code that have the s-process network coupled to the evolutionary code, have shown that this is not the case. Instead, they have found that the efficiency of the pocket decreases with the TP number. Therefore, the first TPs should have the largest

contributions to the s-process, defining the final abundance patterns in the surface.

Figures 6.15 shows the evolution of the maximum neutron density as a function of time for all the standard 2.0 $M_\odot$ models. The peaks in the neutron density represent the production at the bottom of the HeCZ. During the interpulse period after the PIE, the ^{13}C pocket seems to be more efficient than in the subsequents TPs, reaching a maximum neutron density $\sim 10^8\,cm^{-3}$. The subsequent TPs in some models never reach densities as high as $10^7\,cm^{-3}$.

The efficiency of the ^{13}C pocket depends on the amount of protons dredge-down into the intershell. If not enough protons are ingested in the intershell, ^{13}C is not produced in a sufficient amount to produce neutrons. However, if too many protons are dredge-down, ^{13}C is quickly converted into ^{14}N, leading to a very inefficient pocket. Herwig (2000) found ^{13}C pockets with masses $\sim 10^{-7}\,M_\odot$ in their calculations using f=0.016 which is around two orders of magnitude smaller than the mass required to model the main s-process component (Straniero et al. 1995). The choice of the overshooting parameter at the base of the convective envelope only affects the extent in mass of the pocket and not the abundance distribution. Lugaro et al. (2003) claims that a larger overshooting parameter ($f_{BCE} = 0.128$) at the bottom of the envelope is necessary in order to produce the required efficiency of the ^{13}C pocket. Moreover, they have argued that at the bottom of the HeCZ a less efficient overshooting ($f_{HeCZ} = 0.008$) is required in order to explain the s-process distribution in presolar meteoritic SiC grains, since a smaller overshooting parameter at this region should reduce the temperature at the bottom of the HeCZ, leading to a smaller efficiency of the ^{22}Ne neutron source.

Cristallo et al. (2009b) have shown that the pocket efficiency depends on the initial metallicity, being smaller in lower metallicity stars. Also, they have shown that the use of a diffusive mixing scheme instead should reduce the efficiency of the pocket. In their code they use a linear mixing scheme which can lead to a total mass of the ^{13}C within the pocket almost 20 times larger than in the diffusive mixing case.

The fact that we use the value f=0.016 for the overshooting parameter combined with the diffusive mixing scheme adopted in our code should help explaining the small efficiency of the ^{13}C pocket in our models.

6.4.1 S-process

The s-process production during the subsequent TPs depends strongly on the efficiency of the ^{13}C pocket. In most of our models, the maximum neutron density only reaches values smaller than $N_n = 10^6\,cm^{-3}$ inside the pocket (See Figure 6.15). As mentioned above, this is probably the result of the use of the 0.016 for the overshooting parameter. Also, based on models by Cristallo et al. (2009b), it is expected that the efficiency of the pocket decreases at lower metallicities.

Figure 6.16 shows the s-process production after each TP in model I3. The iron abundance in this model is extremely low which favors the production of lead with respect to the light (Sr-Y-Zr) and heavy s-process elements (Ba-La-Ce-Nd-Sm). In the first TP, in which PIE occurs, only light s-process elements are formed in a small amount due to the short duration of the PIE in this model. In the following TP, the neutron density in the pocket reaches $\sim 10^8\,cm^{-3}$ and heavy elements start to be produced. The lead abundance is already increased to [Pb/Fe] = 1.56 in the second TP, while the light and heavy elements abundance increase to [Ls/Fe] = 0.44 and [Hs/Fe] = 1.28, respectively. Despite the small efficicency of the ^{13}C

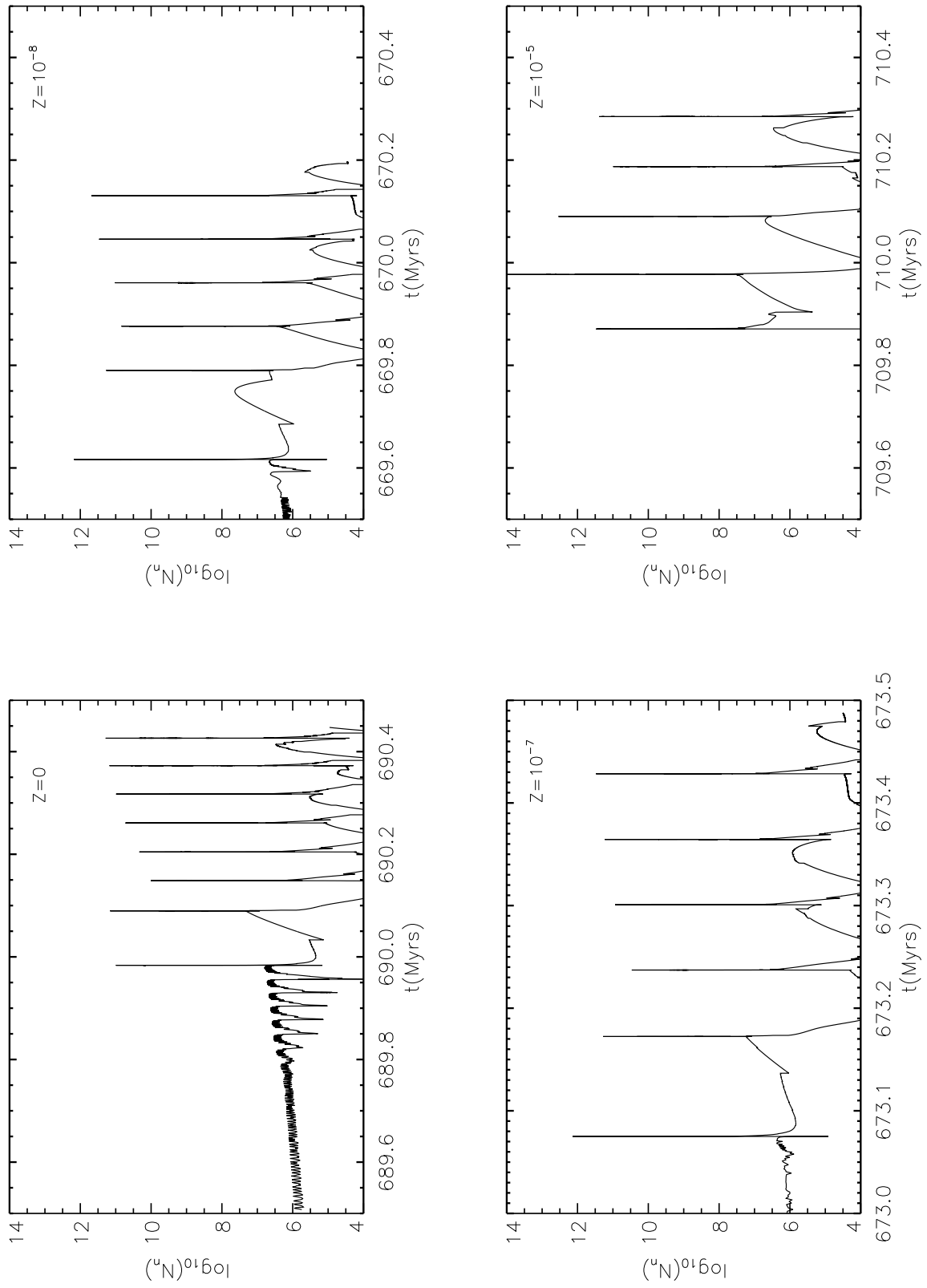

Figure 6.15: Time evolution of the maximum neutron density for the $2.0\,\mathrm{M}_{\odot}$ models.

pocket in the additional 5 TPs, the Pb abundance increases by almost 1.0 dex.

Table 6.7 shows the evolution of the surface abundance ratios and of some isotopic ratios at each TP. The large neutron densities reached during the PIE can already open some s-process branchings that are sensitive to the neutron density. Model I7 already overproduces ^{86}Kr and ^{87}Rb during the PIE probably due to the larger PIE timescale in comparison to model I3. Nevertheless, the ^{86}Kr/^{84}Kr and ^{87}Rb/^{85}Rb isotopic ratios in model I3 eventually reach values larger than 1, due to the high neutron densities achieved at each TP ($N_n > 10^{10}$ cm^{-3}).

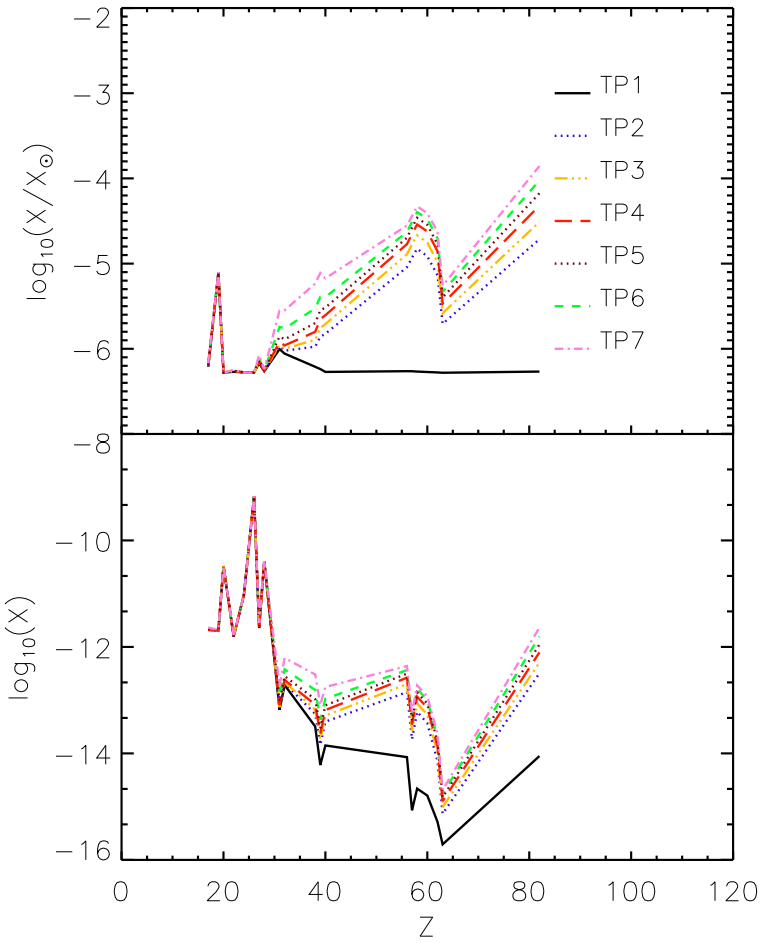

Figure 6.16: Bottom Panel: Surface abundance distribution of elements heavier than ^{30}Si after each TP of model I3. Upper panel: The same as in the bottom panel, but relative to solar.

TP	[Ls/Fe]	[Hs/Fe]	[Pb/Fe]	[Hs/Ls]	[Pb/Hs]	$^{86}Kr/^{84}Kr$	$^{87}Rb/^{85}Rb$	$^{134}Xe/^{132}Xe$	$^{142}Ce/^{140}Ce$
					Solar				
0	0.00	0.00	0.00	0.00	0.00	0.31	0.39	0.37	0.13
					Model I3				
1	0.02	0.01	0.01	-0.02	0.00	0.29	0.38	0.37	0.12
2	0.44	1.28	1.56	0.85	0.28	0.63	0.66	0.27	0.08
3	0.54	1.44	1.77	0.90	0.33	0.78	0.76	0.25	0.07
4	0.65	1.57	1.96	0.92	0.39	0.97	0.86	0.24	0.07
5	0.75	1.65	2.10	0.90	0.46	1.20	1.00	0.25	0.08
6	0.89	1.72	2.26	0.83	0.54	1.54	1.17	0.27	0.08
7	1.14	1.79	2.43	0.65	0.64	1.95	1.43	0.31	0.09
					Model I7				
1	0.44	0.01	0.01	-0.44	0.00	1.65	1.51	0.39	0.13
2	1.25	1.51	1.68	0.25	0.17	2.81	2.01	0.34	0.09
3	1.45	1.75	1.94	0.31	0.19	3.37	2.30	0.28	0.07
4	1.56	1.92	2.12	0.35	0.20	3.80	2.52	0.27	0.07
5	1.61	2.02	2.23	0.40	0.22	3.81	2.54	0.31	0.08
6	1.62	2.03	2.25	0.41	0.22	3.76	2.51	0.32	0.08

Table 6.7: Evolution of the surface abundance of heavy elements and of the surface branching isotopic ratios of the $2.0\,M_{\odot}$ models. The solar value of the branching isotopic ratios are also reported.

Variations in the mass of the ^{13}C pocket can lead to significant changes in the s-process predictions (Bisterzo et al. 2010; Lugaro et al. 2012). Bisterzo et al. (2010) treated the efficiency of the ^{13}C pocket as a free parameter in their calculations. This efficiency is varied in the calculations with respect to their standard case (ST). The ST model with Z=0.01 reproduces the solar system s-process abundances (Gallino et al. 1998). Predictions by Cristallo et al. (2009b) for [hs/ls] and [Pb/ls] are in good agreement with those of the ST case for high metallicities. On the other hand, for lower metallicities the predictions for these two indices are in better agreement with models using smaller ^{13}C pocket efficiencies. This can be explained by the smaller efficiency found in their low Z models. The same was found by Lugaro et al. (2012) when comparing their prediction with these two studies. In this work, they varied the mass of the proton mixing region. Models with smaller masses are in better agreement with predictions by Cristallo et al. (2009b).

Bisterzo et al. (2010) have found that [ls/Fe] has a non linear behaviour with metallicity. Their ST model shows a local maximum at [Fe/H] ~ -0.8. For metallicities smaller than [Fe/H] $= -0.8$, the s-process production shifts from the ls peak to the hs peak due to the reduction in the number of seeds, leading to a decrease in [ls/Fe]. In models with lower pocket efficiencies they have found that the location of the maximum is shifted towards lower metallicities due to the smaller amount of available neutrons. Finally, in their models, they have found a flat behaviour for metallicities [Fe/H] ≤ -2.0. Figure 6.17 shows our predictions for [ls/Fe] and [hs/Fe] in two 2.0 $M_\odot$ models. Our model with metallicity 10^{-7} (I7) shows larger [ls/Fe] than model I3. Model I7 have a more efficient PIE in which light elements were produced due to its longer ΔPIE. Also, model I3 have less efficient ^{13}C pockets in the subsequent evolution as it can be seen in Figure 6.15.

The trend found by Bisterzo et al. (2010) for [hs/Fe] is similar to that of [ls/Fe]. Our models I3 and I7 show similar [hs/Fe] values, although I7 presents slightly larger [hs/Fe] values due to larger ^{13}C pocket efficiencies in this model.

Figure 6.18 shows our predictions for [hs/ls] and [Pb/hs] in two 2.0 $M_\odot$ models. The predictions from Cristallo et al. (2009b) for all their standard models and from Bisterzo et al. (2010) for models with metallicities [Fe/H] $= -2.6$ and [Fe/H] $= -3.6$ are also plotted. The two conected symbols are the predictions for different pocket efficiencies. As it can be seen, they have found differences as large as 2.0 dex for the indices, depending on the efficiency used. Our models present both [hs/ls] and [Pb/hs] smaller than 1.0 dex. This is in agreement with the lower metallicity models calculated by Bisterzo et al. (2010) using efficiencies smaller than ST/12.

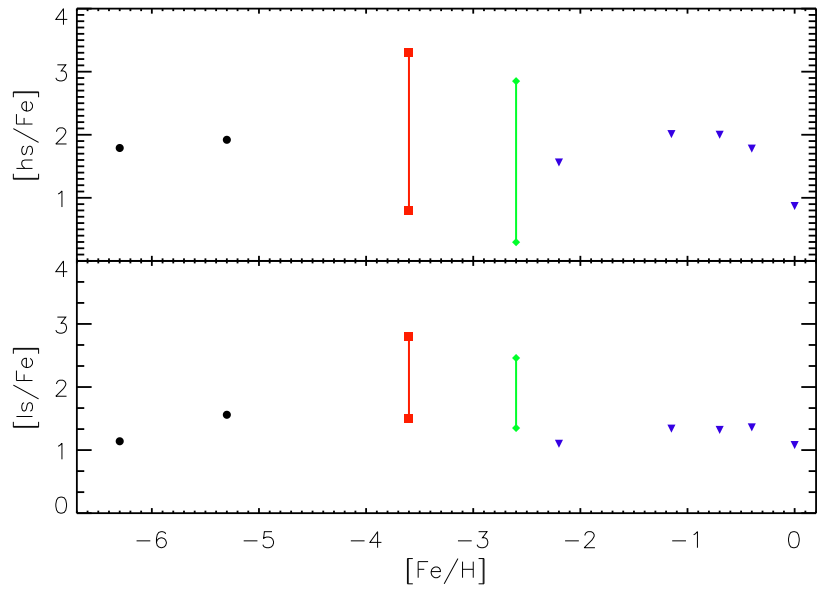

Figure 6.17: S-process indices as a function of metallicity. In the upper panel we report the [hs/Fe] index and in the bottom panel the [ls/Fe] index. Black symbols represent our predictions for models I3 and I7. Blue symbols represent the standard models from Cristallo et al. (2009b). Red and green symbols are predictions from Bisterzo et al. (2010). The lines conect the maximum and minimum predictions. At $[\mathrm{Fe/H}] = -2.6$ the maximum [hs/ls] is achieved by the model in which the efficiency is 1/3 of the ST case, while the minimum is achieved by the model ST/150.

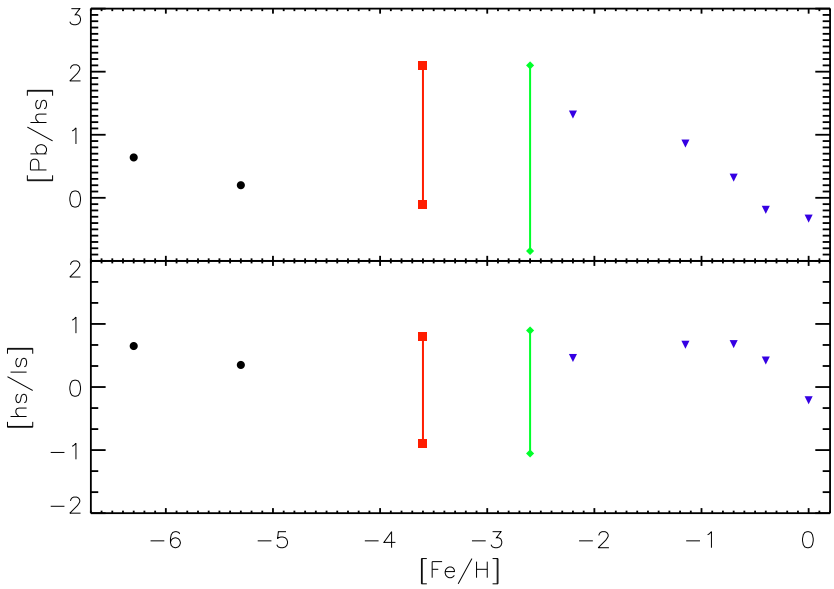

Figure 6.18: S-process indices as a function of metallicity. In the upper panel we report the [Pb/hs] index and in the bottom panel the [hs/ls] index. Black symbols represent our predictions for models I3 and I7. Blue symbols represent the standard models from Cristallo et al. (2009b). Red and green symbols are predictions from Bisterzo et al. (2010). The lines conect the maximum and minimum predictions. At $[\mathrm{Fe/H}] = -2.6$ the maximum [hs/ls] is achieved by the model in which the efficiency is 1/3 of the ST case, while the minimum is achieved by the model ST/150.

6.5 Light elements

The post-PIE dredge-up brings to the surface products of the nucleosynthesis during the PIE and of the nucleosynthesis after the splitting of the convective zone (happening in the HCZ). Figure 6.19 shows the surface abundance evolution of light elements ($A < 30$) for the $2.0\,M_\odot$ model with zero metallicity. The first abrupt increase in the abundances indicates the post-PIE dredge-up. Isotopes involved in the CNO cycles are the main product of this phenomenon. We have found that the most abundant isotope after the post-PIE dredge-up is ^{12}C, followed by ^{14}N. Nonetheless, for a model with the same mass and metallicity, Campbell (2007) have found that ^{16}O is the main product of the PIE (see their Figure 6.24). This difference might be explained by the inclusion of overshooting in our models. More ^{12}C from the core is brought to the HeCZ in the overshooting model, which should explain its dominance. Moreover, the inclusion of overshooting results in a faster splitting of the HeCZ, as it was shown in Chapter 5, which should slow the ^{16}O production through $^{13}C(\alpha, n)^{16}O$ and $^{12}C(\alpha, \gamma)^{16}O$. Further in the AGB evolution, the ^{12}C abundance continues to increase due to TDU, while the ^{14}N remains the same, resulting in an increase in the C/N ratio. The same happens with the $^{12}C/^{13}C$ ratio (Figure 6.19). This is in contrast with Campbell (2007) results. They found HBB in their model which converted ^{12}C into ^{14}N, decreasing the C/N ratio. HBB is not found in our model, since the temperature at the bottom of the convective envelope remains lower than 2×10^7 K during the entire TP-AGB. It is important to stress that the mass boundary for the occurrence of HBB strongly varies between studies. Whilst Campbell (2007) and Siess et al. (2002) found HBB in zero metallicity models with masses down to $M = 2.0\,M_\odot$, Lau et al. (2009) and Suda & Fujimoto (2010) did not find HBB for such low-mass stars.

The abundance of fluorine is enhanced during the PIE and continues to increase throughout the AGB. Ashes from the H-burning (^{13}C and ^{14}N) are mixed down in the intershell when a new TP occurrs and a new HeCZ is formed. ^{13}C is captured by the abundant ^4He and neutrons are produced. The released neutrons are captured by ^{14}N, producing protons through the reaction $^{14}N(n, p)^{14}C$. At the same time fluorine is formed via the reaction chain $^{18}O(p, \alpha)^{15}N(\alpha, \gamma)^{19}F$ with ^{18}O being provided by the $^{14}N(\alpha, \gamma)^{18}F(\beta^+\nu)^{18}O$ chain. Fluorine is then transported to the surface during TDU. Among the isotopes involved in the NeNa chain, ^{22}Ne is the most abundant during the PIE, due to the chain $^{14}N(\alpha, \gamma)^{18}F(\beta^+\nu)^{18}O(\alpha, \gamma)^{22}Ne$. It continues to be produced during the subsequents TPs due to the mixing of ^{14}N-rich layers into the newly formed HeCZ as explained above for the fluorine case. Since HBB does not happen in this model, ^{22}Ne is not destroyed in the envelope, in contrast to Campbell (2007) results.

Another element that is largely produced during the PIE is lithium. As explained in Chapter 5, the high temperature at the HCZ activate the reaction $^3He(\alpha, \gamma)^7Be$, producing ^7Be which in turn decays to produce ^7Li. In all our model with $M \leq 2.0\,M_\odot$ lithium is produced during the PIE in a large amount and it is preserved during the subsequent evolution, since the temperature at the bottom of the envelope is not high enough to activate the $^7Li(p, \alpha)^4He$ reaction ($T \sim 2.5 \times 10^6$ K). This is in agreement with Iwamoto et al. (2004) results for stars with $M \leq 2.0\,M_\odot$ and metallicity $[Fe/H] = -2.7$. Nevertheless, models with $3.0\,M_\odot$ reach temperatures larger than 2.5×10^6 K at the bottom of the HeCZ, leading to lithium depletion in the subsequent TPs.

Figures 6.20 and 6.21 show a comparison between our yields and those by Campbell (2007)

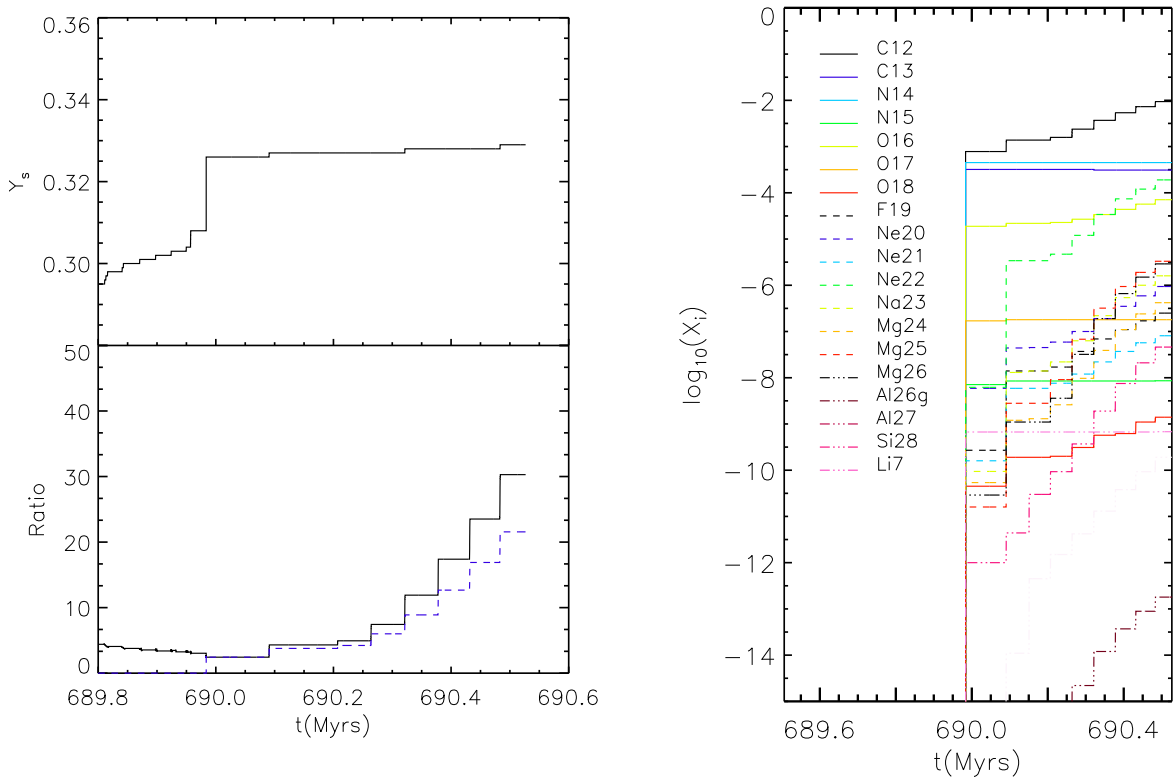

Figure 6.19: Left panel: Time evolution of the helium surface abundance and the abundance ratios: $^{12}C/^{13}C$ (Black line), C/N (Blue line). Right panel: Time evolution of the surface abundance of light elements.

for the zero metallicity models. It can be seen that the yields from Campbell (2007) models present strong HBB signatures. Whilst our models overproduce carbon with respect to the Sun, their models converted the carbon dredge-up after the PIE and in the first TDUs into ^{14}N. The same effect can be seen in the fluorine to magnesium isotopes. HBB predictions depend on, for instance, the adopted mass-loss rate. Campbell (2007) models have smaller mass-loss rates and undergo much more TPs than our models. The larger mass-loss rate in our models induces a faster cooling of the stellar structure, decreasing the chances of HBB to occur.

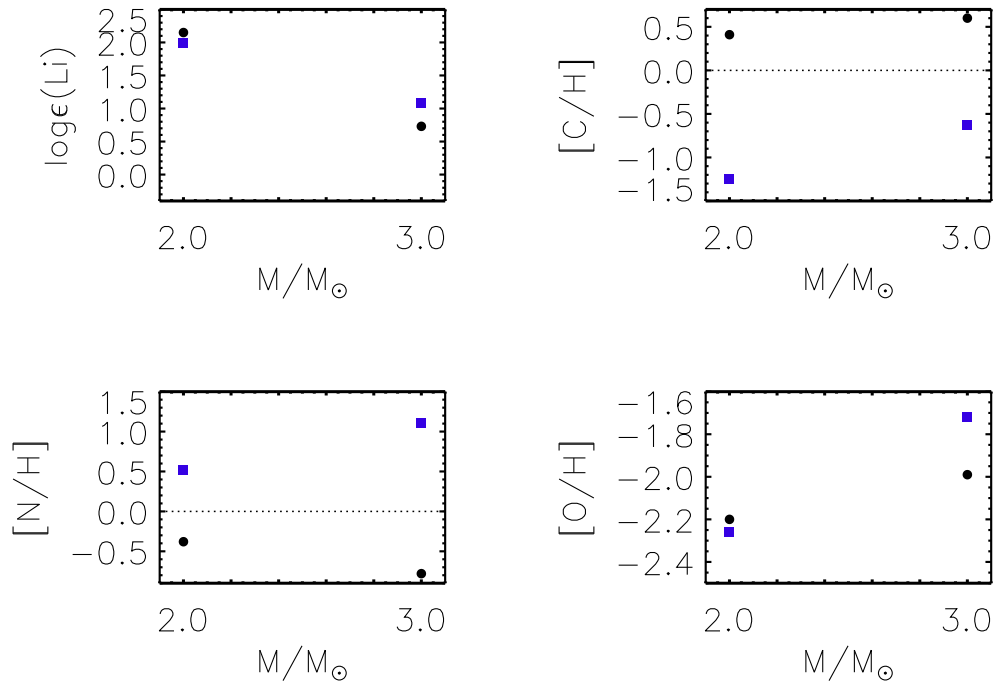

Figure 6.20: Elemental yields for our zero metallicity models against initial stellar mass. Blue squares represent the yields from Campbell (2007) and black circles represent our values. The solar abundance used on both yields is from Grevesse & Sauval (1998).

Except for lithium and nitrogen, the yields of all light elements increase with increasing mass. The lithium abundance after the PIE depends on the maximum temperature at the botttom of the HCZ, right after the splitting, and on the time between the splitting and the dredge-up Δt_d. The amount of nitrogen depends mostly on Δt_d. The longer it takes for the envelope to start dredging-up material from the HCZ, the larger the abundance of ^{14}N. The $3.0\,M_\odot$ model has Δt_d smaller than the $2.0\,M_\odot$ model which should explain the differences in ^{14}N abundance.

Figures 6.22 and 6.23 show the yields of all $2.0\,M_\odot$ models. In our models, the lithium abundance increases with metallitic, while in models by Campbell (2007) they decrease with metallicity. This is probably due to the fact that in their model with [Fe/H] $= -3.0$, PIE does not occur and lithium is produced only through HBB. The larger lithium abundance in our $Z = 10^{-5}$ model could be explained by the smaller Δt_d in this model. Therefore, ^{7}Li

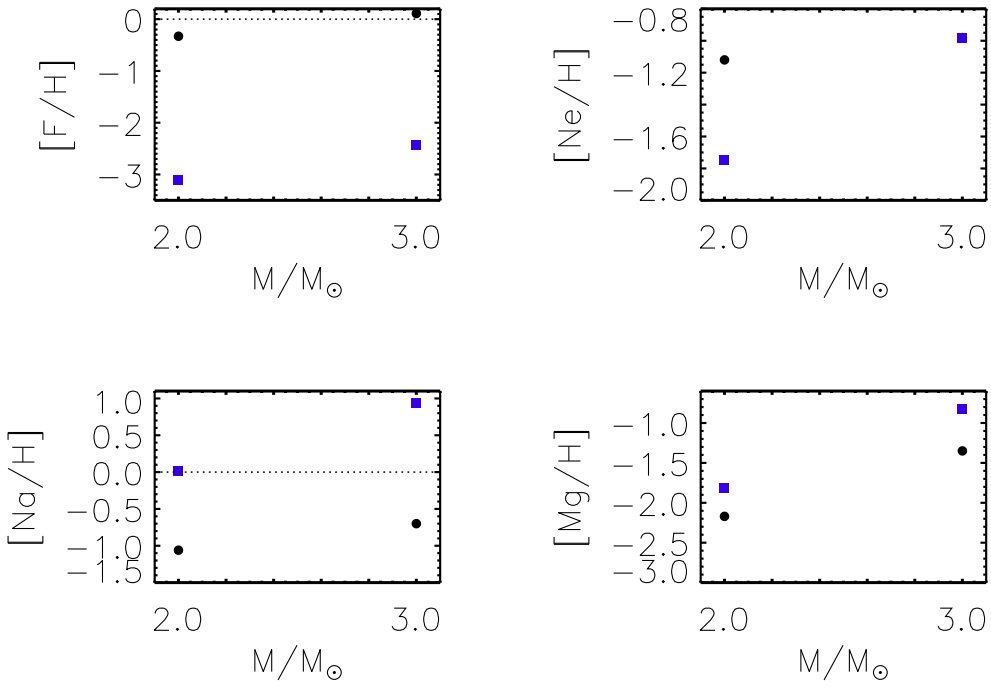

Figure 6.21: Elemental yields for our zero metallicity models against initial stellar mass. Blue squares represent the yields from Campbell (2007) and black circles represent our values.

is quickly carried to low temperature regions in this model where it cannot be destroyed by proton captures. On the other hand, the carbon yields are almost constant in this metallicity range. It is clear from these plots that all Campbell (2007) models show HBB signatures: large nitrogen content, small carbon abundance, large sodium abundance and small fluorine and neon abundances. Nevertheless, our models do not undergo HBB at any initial metallicity.

The ^{4}He abundance is dominated by the second the post-PIE dredge-ups since HBB does not occur in our models. Table 6.8 shows the final ^{4}He surface abundance. The SDU increase the initial abundance, $Y_s^0 = 0.245$, in 8-45%. PIE, on the other hand, increases the helium abundance in about 10%. Finally, the final abundance is increased by less than 1% in the subsequent TPs.

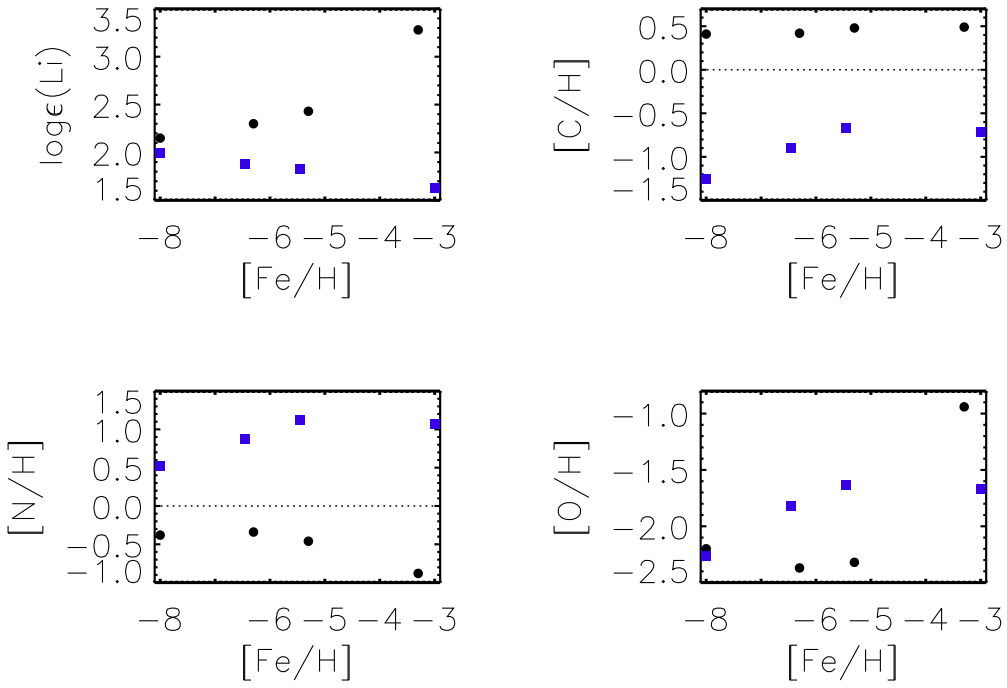

Figure 6.22: Elemental yields for our $2.0\,M_{\odot}$ models against initial metallicity. Blue squares represent the yields from Campbell (2007) and black circles represent our values. The solar abundance used on both yields is from Grevesse & Sauval (1998). The metallicity of Z=0 model was set to $[Fe/H] = -8.0$ in the plots for visualization purposes.

Model	No TPs	M_f	t_{TP-AGB}	Extra TPs	Y_s^{AGB}
I1	14	0.91	1.75	0	0.302
I2	13	1.11	0.64	0	0.329
I3	7	0.80	0.64	0	0.320
I4	7	1.06	0.54	0	0.325
I5	11	1.76	0.55	7	0.316
I6	10	1.02	0.68	0	0.319
I7	7	0.99	0.41	0	0.301
I8	5	0.65	0.50	0	0.272
I9	13	1.60	0.21	1	0.358
I10	10	2.37	0.14	4	0.329
I11	12	2.31	0.18	4	0.303
I12	10	2.04	0.20	2	0.269

Table 6.8: Selected AGB properties. All masses are given in solar mass units. Time is given in Myrs. For more details on the estimative of the remain TPs see Chapter 7. Y_s^{AGB} is the final helium abundance after the AGB evolution is over. In the cases additional TPs are expected, Y_s^{AGB} is the abundance in the last calculated model.

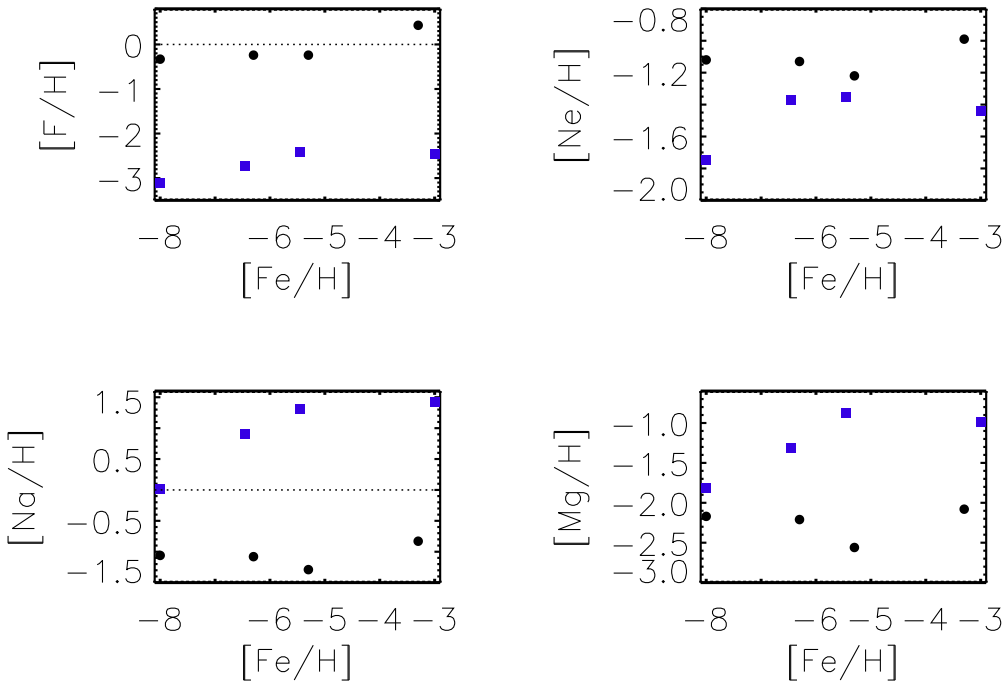

Figure 6.23: Same as in Figure 6.22.

6.6 Uncertainties in the Models

One of the main uncertanties in the AGB modelling is the mass-loss rate. We have performed an extra calculation using the mass-loss prescription from Bloecker (1995) with the free parameter $\eta = 0.02$ (I6). We have found that this model has a larger Δt_{PIE} than the standard model (I3) which implies in a larger s-process production during the PIE. In addition, this model undergoes three additional TPs. The two extra TDU episodes undergone by model I6 increases the overall s-process abundance. The abundances of the s-process elements are a factor of 2-3 larger in this model. The element that is most affected by the difference in mass-loss rate is nitrogen. The longer Δt_d after the PIE favors the production of ^{14}N in the HCZ before the post-PIE dredge-up. ^{14}N is then brought up to the surface. Moreover, since no HBB is found in both models, the difference in the nitrogen abundance can be totally atributted to the difference in Δt_d. The longer dredge-up timescale also influences the lithium abundance which is half of the value found in model I3. Campbell (2007) models suffer more than 200 TPs which is much larger than the number of TPs suffered by our models (~ 10).

One important difference between our models and those reported in the literature for this metallicity range is the use of low-temperature opacities for varying surface C/O ratios. Weiss & Ferguson (2009) have shown that these opacities can influence the evolution during the AGB in opposite directions depending on the initial metallicity. Metal-rich stars have smaller T_{eff} in the varying case after the C/O ratio reaches one. On the other hand, metal-poor stars present larger T_{eff} when varying C/O opacitites are used, and therefore, a longer

TP-AGB evolution. Figure 6.24 shows the evolution of the effective temperature in the calculations using the fixed C/O opacities (I4) and our standard model. After the PIE, the envelope is enriched mainly in CNO, leading to surface C/O ratios larger than one. Each subsequent TP brings up carbon to the surface, increasing the C/O ratio. Similarly to the predictions for $Z = 10^{-4}$ by Cristallo et al. (2007) and $Z = 5 \times 10^{-4}$ by Weiss & Ferguson (2009), the use of fixed or varying C/O opacities strongly influences the TP-AGB evolution. In our model, the varying C/O opacities prolongs the AGB evolution in 0.1 Myrs (see Table 6.8). One drawback of our models is the maximum C/O ratio in the opacity tables ($C/O_{max} = 20$), since our models can reach $C/O > 50$ after the PIE. Thus, when $C/O > 20$ the opacities with $C/O = 20$ is used. Nevertheless, the use of these opacities should be a better approximation than the fixed-C/O opacities. Regarding the surface abundance pattern, We have obtained similar results as in model I6. A larger abundance is found for the s-process elements. Nonetheless, the nitrogen in closer to that obtained for the standard model, due to the similar Δt_d.

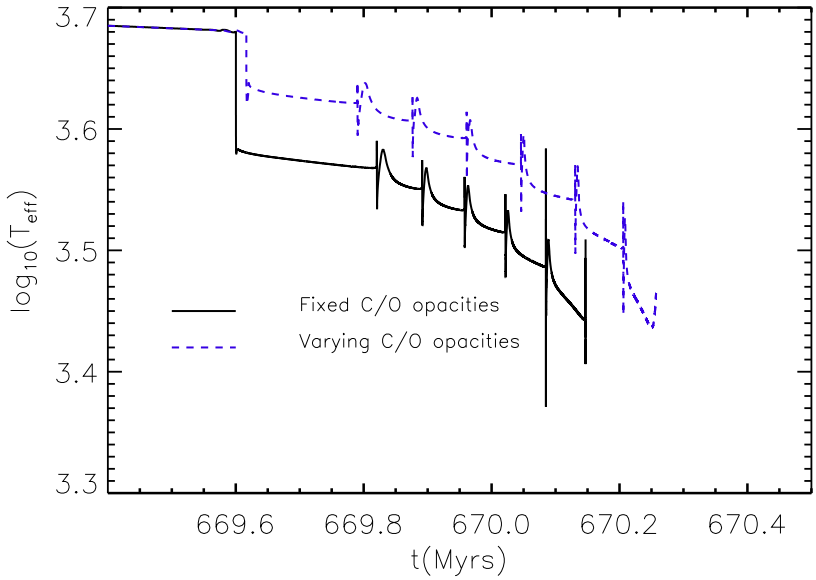

Figure 6.24: Evolution of the effective temperature for models using the varying C/O opacities (I3) and the fixed C/O opacities (I4).

Finally, we have performed an extra model using a smaller overshooting parameter (model I5). The first effect this change brings to the model is a larger position of the He-burning ignition point during the PIE ($^{I5}M^{He}_{max} -^{I3} M^{He}_{max} = 0.06\,M_{\odot}$). This results in ^{13}C being burnt at a lower temperature which, in turn, results in smaller neutron densities. Moreover, the lower overshooting parameter leads to smaller dredge-up and ^{13}C pocket efficiencies. Also, the temperature at the bottom of the HeCZ in the subsequent TPs is smaller than that found in model I3. This leads to smaller surface s-process abundances than in the standard model.

6.7 Can zero metallicity stars produce s-process elements?

In Chapter 5 we have discussed the possibility of s-process production during the PIE in low-mass stars. In zero metallicity stars, since iron-peak seeds are not initially present in the star, the production of heavy elements have to start from much lighter seeds. Neutron capture onto light elements (C, N, O, F, and Ne isotopes) produce elements up to ^{56}Fe that later might be used as seeds in the production of heavier elements. We have found, however, that in spite of the high neutron densities achieved in the the zero metallicity model the short duration of the proton ingestion only allows the production of elements up to iron. In models of the TP-AGB phase, the picture could be different since the star undergoes, after the PIE, several TPs in which s-process happens in radiative conditions in the ^{13}C pocket and in convective conditions at each TP.

For the 2.0M$_\odot$ model we have found that, like in the LM case, the PIE is too short to produce s-process elements. In the subsequent AGB evolution the efficiency of the ^{13}C pocket is too low to break through the bottleneck reaction $^{33}\mathrm{S(n,}\alpha)^{30}\mathrm{Si}$. The neutrons are all used to produce light elements. The abundance of silicon increases from zero to $\sim 10^{-11}$, while the abundance of sulfur reaches $\sim 10^{-14}$.

The 3.0 M$_\odot$ model also presents a short PIE evolution ($\Delta t_{PIE} \sim 10^{-3}\, yrs$) and therefore, there is no s-process production during this phenomenon.

The answer to the question in the title is no for the chosen overshooting parameter adopted in the current calculations. A detailed analysis of the role played by overshooting in the s-process production by zero metallicity stars might change this answer to yes.

6.8 Comparison with observations

In this section we will compare our 2.0 M$_\odot$ models with the stars HE0107-5240 and HE1327-2326. Nishimura et al. (2009) have done a parametrized study of the nucleosynthesis during the PIE. In this study they concluded that the abundance of light elements in HE0107-5240 might be the result of mass transfer from a zero metallicity star with initial mass between 1.5M$_\odot \leq$ M $\leq$ 3.0M$_\odot$. They argued that the small [C/N] ratio along with the large enrichment in sodium and carbon may require both PIE and TDU as initally proposed by Suda et al. (2004).

Figure 6.25 shows the abundance distribution of HE0107-5240 and HE1327-2326 over-plotted by our models. The dilution scheme is the same used for the low-mass case. We calculated the dilution coefficient requiring that the [C/Fe] abundance was a match to the observed value.

The first thing that can be observed in Figure 6.25 is the better agreement between the prediction for Li, Na, Mg and Al in the diluted material with the abundance of these elements in HE1327-2326. The O and N abundances, however, are a worst match to the observed values. The better agreement of the low-mass model for these O an N is related to the longer timescales for the PIE and the post-PIE dredge-up, respectively. Finally, our models do not reproduce the large Sr abundance found in this star, since our ^{13}C pocket are quite inefficient. A detailed study in the role overshooting plays in the ^{13}C pocket formation in such low metallicity environment is necessary.

For HE0107-5240, a better agreement between the predictions and its nitrogen abundance

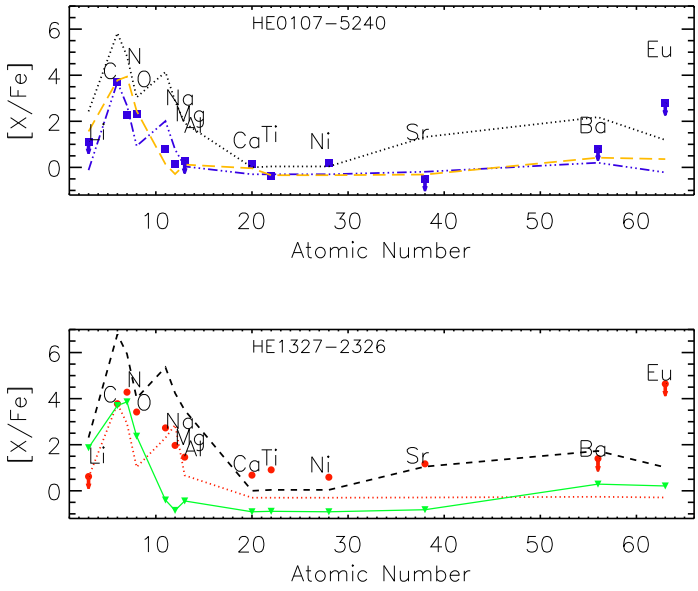

Figure 6.25: Comparison between the abundance distribution of HE0107-5240 (blue symbols - upper panel) and HE1327-2326 (red symbols 0 bottom panel) and our AGB models. Upper panel: The black dotted line indicates the final surface abundance after the last TDU of model I7. The blue line indicates the average abundance lost by the star diluted in the observed star material (I7). The orange line represents the diluted model M2 from Chapter 5. Bottom panel: The black dashed line indicates the final surface abundance after the last TDU of model I3. The red line indicates the average abundance lost by the star diluted in the observed star material (I3). The green line represents the diluted model M2 from Chapter 5.

is found for the $2.0\,M_{\odot}$ model. Nevertheless, the shorter PIE results in a worst agreement for the oxygen abundance. Moreover, intermediate elements (Mg, Al, Ca, Ti, Ni) are also in better agreement with the $2.0\,M_{\odot}$ model. For the s-process elements, the changes are not significant and this model is also able to reproduce the abundances within a factor of 4. It seems from our models that the suggestion by Nishimura et al. (2009) in which the primary star has a mass between $1.5M_{\odot} \leq M \leq 3.0M_{\odot}$ is the most favorable scenario. However, it is important to keep in mind that the large uncertainties regarding the modelling of the PIE must be studied in detail and low-mass stars cannot be discarded as a possible companion for HE0107-5240.

6.9 Summary

We have performed evolutionary and nucleosynthesis calculations of intermediate-mass EMP and zero metallicity stars. All our models undergo PIE. For masses $M \leq 2.0\,M_{\odot}$ we find a good agreement in the metallicity boundary for the occurrence of the PIE with the results from Campbell (2007) and Suda & Fujimoto (2010). For the $3.0\,M_{\odot}$ models large discrepancies are found between other literature studies and our models.

We have explored the nucleosynthesis of light and heavy elements in these stars, specially during the PIE. The nucleosynthesis during the PIE is strongly influenced by the duration of this phenomenon (Δt_{PIE}). Our models present a variety of values of Δt_{PIE}: from $\sim 10^{-4}$ up

to $\sim 7 \times 10^{-1}$ yrs. Amongst the models with $Z = 10^{-8}$, the $3.0\,M_{\odot}$ model shows a significant s-process production during PIE, while in models with $Z = 10^{-7}$ only light s-process elements are formed during the PIE. The $2.0\,M_{\odot}$ model with the highest metallicity presents the larger s-process production during the PIE, due to the large Δt_{PIE}.

For the nucleosynthesis post-PIE, our models confirm the trend found by Cristallo et al. (2009b) that the ^{13}C pocket efficiency should decrease with metallicity. However, it is important to stress that the overshooting parameter plays a major role in the ^{13}C pocket efficiency. Furthermore, the overshooting parameter also plays a role in the convective s-process. The large the overshooting parameter, the smaller is the He-burning ignition point during the PIE and at each new TP. We have also found that the interpulse period following the PIE have the stronger contribution to the s-process production.

Concerning the light elements, the evolution post-PIE is also of utmost importance for the final yields. Comparison between our yields and those by Campbell (2007) have shown that they can be extremely different. This difference is the result of the occurrence of HBB in their models. Our models do not undergo HBB, resulting in carbon enriched stars.

We have discussed the influence of the main uncertainties in the final abundances. The mass-loss rate by Bloecker (1995) does not alter the AGB evolution by a large fraction. However, the extra TDU episodes increases the s-process abundance by a factor of 2 to 4. The same can be discussed about the use of fixed C/O opacities instead of those with varying C/O. For the low metallicity range studied the varying C/O opacities tend to prolong the AGB evolution. In this particular model the use of fixed C/O opacities resulted in Δt_{PIE} and Δt_{d} approximately two orders of magnitude larger and one order of magnitude smaller than in model I3, respectively .

Chapter 7

Globular Clusters

7.1 Introduction

Globular clusters (GCs) are gravitationally bound groups of hundred of thousands (or millions) of stars confined to a volume of several tens to some hundreds light years in diameter. Traditionally, the stars in a particular globular cluster were considered to be coeval and to have the same metallicity (the observed spread in [Fe/H] is usually smaller than 0.05 dex - Carretta et al. 2009a). In this case, any difference in the abundances of light elements among the stars in the cluster should be attributed to the differences in evolutionary stages.

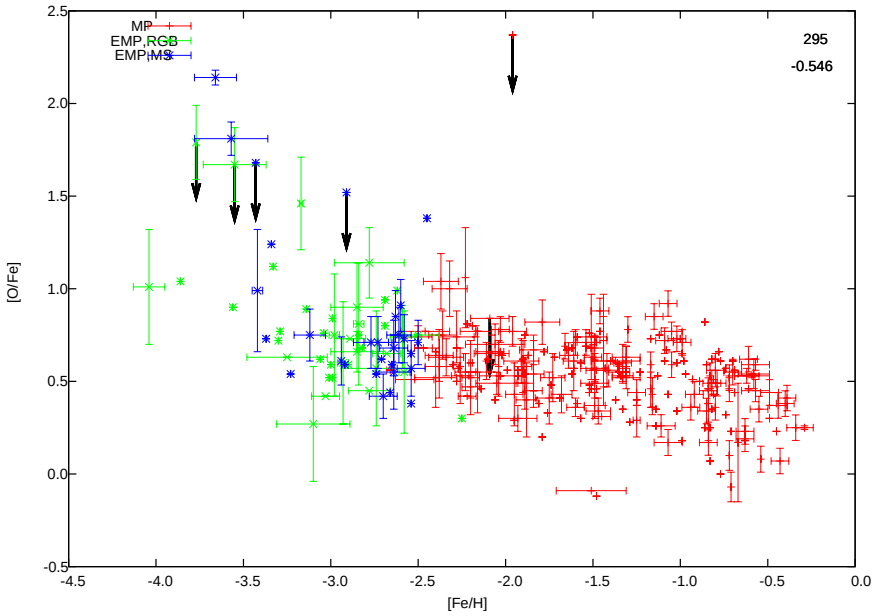

Figure 7.1: Oxygen abundance of field stars. Figure and data taken from the SAGA database (Suda et al. 2008). Despite the observed spread in oxygen abundance, metal-poor field stars are in general O-rich, due to alpha capture enrichment by SNe II.

Observations of field stars have shown that stars with metallicities [Fe/H] ≤ -1.0 exhibit an overabundance of alpha capture elements (O, Ne, Mg, Si, Ca, Ti) in comparison to the iron abundance ([α/Fe] ~ 0.4 - See Figure 7.1). Alpha capture elements are mainly produced by massive stars ($M > 10M_{\odot}$) when they end their lives as core-collapse type II supernovae (SNe II). Iron, on the other hand, is mainly produced by Type Ia supernovae (SNe Ia). The occurrence of SNe II and SNe Ia have quite different timescales. While SNe II occur within $t \leq 10^7$ yrs, SNe Ia have mean lifetimes larger than $t \sim 1$ Gyr. Therefore, the insterstellar medium contamination by SNe Ia occurs much later, reducing the abundance ratio [α/Fe] (at [Fe/H] ~ -1.0).

GCs are old objectcs (age > 10 Gyrs) with metallicities $-2.3 <$ [Fe/H] < 0.0. The abundances of light elements of individual stars in the cluster were expected to reflect the yields of SNe II and the internal changes due to their evolutionary stages. For instance, GC stars in the upper RGB were expected to have smaller $^{12}C/^{13}C$ ratios, due to the first dredge-up, than the ratios present in the MS stars. On the other hand, they were expected to be O-rich and Na-poor at any evolutionary stage preceding the AGB. Nevertheless, early investigations have shown that stars in GCs present abundance patterns that cannot be explained only by the expected surface abundance changes due to stellar evolution (Kraft 1994). More recent spectroscopic analysis of stars in GC have confirmed the existence of star-to-star abundance variations (Gratton et al. 2001; Ramírez & Cohen 2002; Carretta et al. 2004, 2009c,b). These variations, usually found to be anticorrelated: O-Na and Mg-Al anticorrelations, are not found in field stars (Gratton et al. 2000).

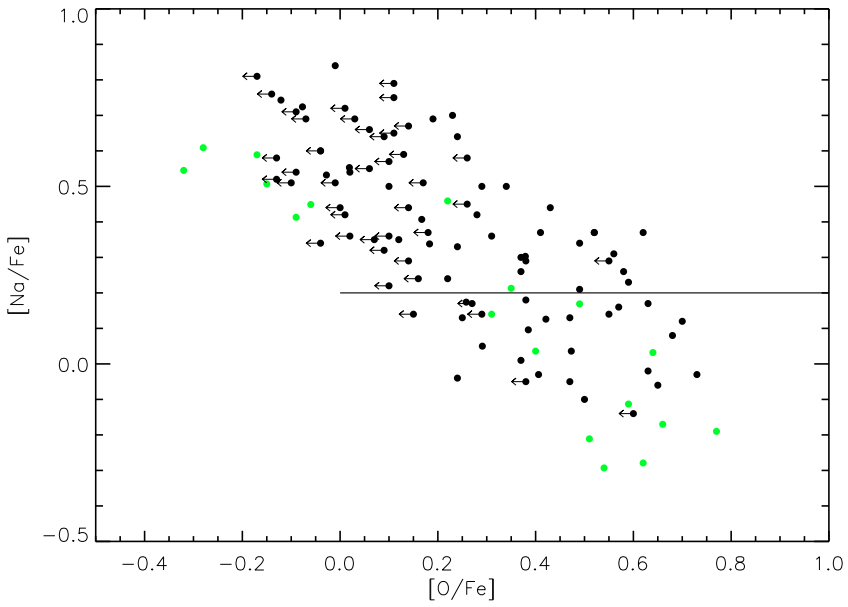

Figure 7.2: O-Na anticorrelation in NGC 6752. Black filled circles are measurements from Carretta et al. 2007. Green symbols are from Grundahl et al. 2002. The line indicate the separation between primordial and second generation as suggested by Carretta et al. 2009c.

Figure 7.2 shows the O-Na anticorrelation for NGC 6752. The stars below the horizontal line have oxygen and sodium abundances similar to those found in field stars with the same

metallicity ([Fe/H] ~ -1.5). As explained in Chapter 2, during the star ascension in the HR diagram, the envelope deepens down and products of H-burning are brought up to the stellar surface (FDU). However, standard evolutionary calculations of low-mass stars have shown that the changes in surface abundance due to FDU are very modest. The envelope does not reach deep enough regions where p-capture reactions might produce N from O (ON-cycle) and ^{23}Na from ^{22}Ne, in order to explain the O-poor and Na-rich stars observed above the horizontal line in Figure 7.2

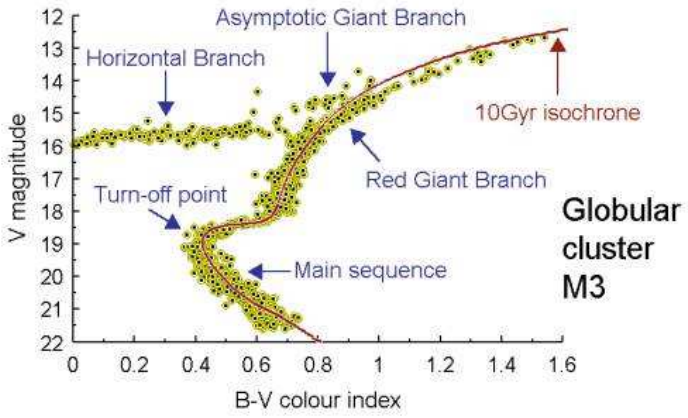

Figure 7.3: The color-magnitude digram of M3. Credit: http://www.astro.ljmu.ac.uk.

Since the general idea was that stars in GC belong to a single stellar population[1] it was natural to investigate if some non-canonical extra mixing during the RGB phase could explain the observed abundance anomalies (Denissenkov & Weiss 2001). Denissenkov & Weiss 1996 have explored the possibility that additional mixing in a region between the H-burning shell (HBS) and the bottom of the convective envelope (BCE) would explain the observed O-Na anticorrelation in GCs, the so called "deep mixing scenario". They were able to reproduce the O-Na anticorrelation for the giants in the clusters M92 and M13. Nonetheless, the discovery of anomalous abundances also in unevolved stars (Gratton et al. 2001) indicates that the surface abundance patterns were already present when these stars were formed.

Early photometric analysis of GC had also led to the believe that one single stellar population, i. e. one isochrone[2], could fit the color-magnitude diagram (CMD) of a globular cluster (Figure 7.3). Only the high quality photometry achieved in the last few years has been able to reveal that GC can present multiple main sequences and subgiant branchs in the CMD (Piotto et al. 2007; Piotto 2009): a clear evidence of multiple populations. Figure 7.4 shows the multiple main sequences found in the cluster NGC 2808 (Piotto et al. 2007). The different MSs in this cluster can be explained by different stellar populations, presenting different helium contents (see inner plot in Figure 7.4), since the spread in metallicity is not large enough to account for the presence of different MSs in the HRD. The high helium abundance of the bluest MS (Y ~ 0.38) can be explained by an ealier pollution of the cloud in which these stars were formed, since MS low-mass stars do not have a convective envelope able to transport H-burning material to the surface.

The abundance variations in GCs are expected to be reflected in the CMDs. Sbordone et al.

[1]Single stellar population is a group of stars, with different masses, having the same initial composition and

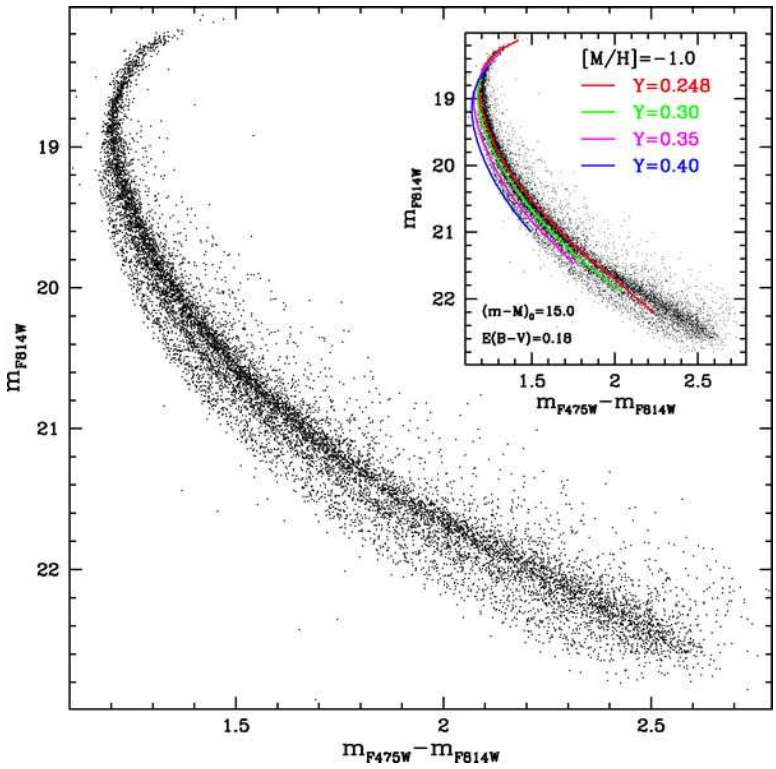

Figure 7.4: The color-magnitude diagram of NGC 2808. Taken from Piotto et al. 2007. The inner plot shows the superposition to the CMD of isochrones with different initial helium abundance.

2011 have performed theoretical calculations of the effect these variations have in the CMDs. They have found that different compositions affect the CMD in different ways. Moreover, depending on the filter used the effects can be large or negligible. For instance, they have shown that in the CMDs using the filters BVI, only a change in helium abundance would cause a splitting in the MS, while a variation of the C+N+O abundance should lead to a split in the SGB. This could help explaining, for instance, the empirical splitting in the SGB found for NGC 1851.

Finally, in the framework of multiple stellar populations, the horizontal branch (HB) morphology could also be explained by differing He abundances. Stars in the bluer HB should have a Helium abundance larger than those in the red HB (D'Antona et al. 2002; D'Antona & Caloi 2004).

In the light of the spectroscopic and photometric results discussed above, one possible scenario invokes the existence of at least two stellar populations in GCs. The more massive stars in the first stellar generation polluted the intra-cluster medium, via stellar winds, where later, a second generation of stars was formed. The nature of the polluting stars from the first generation is not yet established: they could be either massive AGB stars (Ventura et al. 2001) or rapidly rotating massive stars (Decressin et al. 2007). Massive AGB stars undergo hot bottom-burning (HBB - see Chapter 2 for more details) which is responsible for converting ^{12}C into ^{14}N. Furthermore, the high temperatures at the bottom of convective envelope activate

age.

[2]Lines in the HR diagram occupied by stars of different masses but the same age.

more advanced proton capture reactions: the NeNa and MgAl chains that, in principle, could account for the O-Na and Mg-Al anticorrelations.

Ventura et al. (2001) have performed the first full AGB calculations for intermediate-mass stars with metallicities compatible with the observed GCs. No quantitative results regarding the anticorrelations could be obtained due to the small network used in the calculations. However, they have found a strong depletion of ^{16}O in their models, which was an indication that advanced nucleosynthesis was occurring, and therefore producing Na and Al through proton capture. Fenner et al. (2004) have performed AGB calculations of stars with masses $M < 7.0M_{\odot}$ and metallicities [Fe/H] < -1.4. In this study, they have used a nuclear network including all elements involved in the advanced proton capture chains. Their models were able to reproduce the observed spread in Na and Al. However, neither O or Mg were sufficiently depleted in their models in order to match the observed O-Na and Mg-Al anticorrelations in GCs. In addition, the sum C+N+O did not remain constant in their models contrary to what is found for many GCs (Ivans et al. 1999). Denissenkov & Herwig (2003) models were also not able to reproduce the observed GCs patterns. They have found that the temperature at the base of the convective envelope necessary to deplete oxygen, leads to ^{25}Mg/^{24}Mg and ^{26}Mg/^{24}Mg ratios larger than the observed.

Denissenkov & Herwig (2003) and Fenner et al. (2004) claimed that it is unlikely that AGB stars are the polluters responsible for the abundance pattern observed in stars of the second generation. However, Ventura and collaborators argued that the use of a more efficienty convection theory in their models produces results more consistent with the observations. It is important to point it out that since 2004 mostly Ventura and collaborators have been publishing on the subject, while little work has been done by other groups. We have taken advantage of the newest GARSTEC nuclear network, including advanced H-burning, and have performed models of intermediate-mass stars with metallicities close to the observed GC. We have used the most up-to-date reaction rates, specially those involved in the advanced H-burning (Iliadis et al. 2010) and the low-temperature opacities for varying C/O-ratios.

7.2 The Models

We have performed evolutionary calculations from the ZAMS to the TP-AGB phase for stars with metallicities Z=0.001 and Z=0.004 and masses $3.0 \leq M/M_{\odot} \leq 5.0$. The initial composition is alpha-enhanced, which means that the abundances of O, Ne, Mg, and Si are enhanced by 0.4 dex. The physical inputs used in the models are the same as those used in Chapter 6 (Models G1-G6). Extra models using the mass-loss prescription by Bloecker (1995) and without overshooting have been performed (Models G7-G9). Table 7.1 shows the models and some selected AGB properties. In the second column the initial zero-age Main Sequence mass is given (M_{ZAMS}). The third column contains the initial metallicity (Z). The fourth and fifth columns give the total number of TPs experienced by the model (No TPs) and the final total mass (M_f), respectively. Further in this Chapter, we will estimate the amount of remaining TPs, not computed due to convergence problems. The number of TPs actually simulated and the final total mass, in Table 7.1, will give us an idea of how much further in the evolution we were able to simulate.

Model	M_{ZAMS}	Z	No TPs	M_f
G1	3.0	0.001	13	1.59
G2	4.0	0.001	20	2.74
G3	5.0	0.001	63	3.67
G4	3.0	0.004	10	1.26
G5	4.0	0.004	18	3.20
G6	5.0	0.004	51	3.39
G7	5.0	0.001	57	1.60
G8	3.0	0.001	24	0.86
G9	4.0	0.001	38	1.58

Table 7.1: List of computed models and selected AGB properties. All masses are given in solar mass units.

7.3 Results

Intermediate-mass stars undergo the so-called HBB phenomenon. During the AGB, the bottom of the convective envelope can reach high temperatures: $T_{bce} = (0.5 - 1.0) \times 10^8$ K. These high temperatures activate advanced H-burning in this region, leading to the surface depletion of carbon and oxygen and the enrichment of nitrogen. Figure 7.5 shows the temperature at the bottom of the convective envelope along the AGB evolution for our standard models. Our $3.0M_\odot$ models (black lines in Figure 7.5) present mild temperatures, which should imply in a negligible contribution from HBB to the abundance patterns in these stars. This can be seen in Figure 7.6 by the surface time evolution of carbon and nitrogen. If HBB was operating efficiently in this model, ^{12}C should be converted into ^{14}N. Instead, ^{12}C abundance increases at each TP due to the dredge-up of intershell material. ^{22}Ne and the Mg isotopes are also enhanced by TDU. ^{22}Ne is synthesised via α captures in the convective shell during the TP. It is, then, partially converted to ^{23}Na after the dredge-up, increasing the surface ^{23}Na abundance.

The higher mass models, on the other hand, show significant HBB signatures in their surface. This can be seen clearly in the surface abundance evolution of ^{12}C and ^{14}N in Figure 7.7. TDU is also efficiently operating in this model, bringing freshly dredged-up ^{12}C to the surface which is partially destroyed by HBB. The larger temperatures in the higher mass models are also responsible for depleting ^{16}O. In the beginning of the AGB evolution, ^{22}Ne is converted into ^{23}Na which is later destroyed, when the rate of destruction exceeds that of production. Regarding the magnesium isotopes: ^{24}Mg is strongly depleted during the evolution, while ^{25}Mg and ^{26}Mg abundances increase. This results in an overall increase of the total Magnesium abundance. In addition, further in the evolution due to TDU, the abundance of ^{24}Mg increases again, contributing to the increase in total Mg abundance.

The sum of carbon, nitrogen, and oxygen abundances is found to be approximately constant in many GCs (Ivans et al. 1999). Figure 7.8 shows the evolution along the AGB of C+N+O in our $5.0M_\odot$ models. It is clear from Figure 7.8 that our models cannot reproduce this observational signature, since they show a large increase in C+N+O. Another feature from our models that poses a problem to AGB stars as the polluters stars in GCs is the Magnesium abundance. Figure 7.8 reveals that Magnesium is produced instead of destroyed in our models, contrary to what is observed in GCs (MgAl anticorrelation). These results are

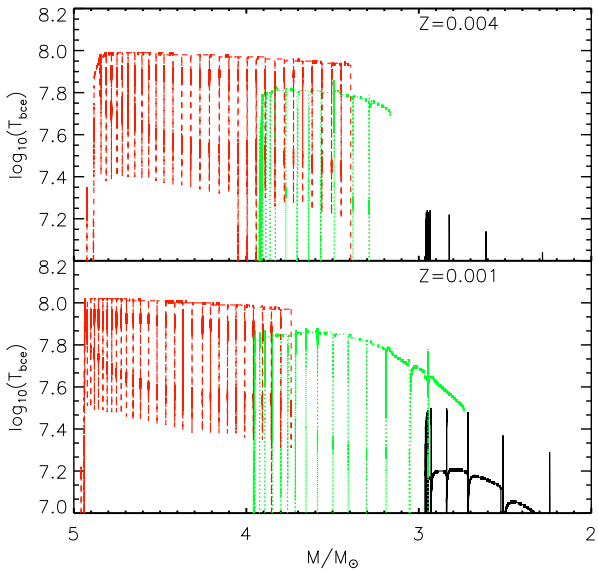

Figure 7.5: Temperature at the bottom of the convective envelope along the AGB evolution of our models. Red lines represent $5.0\mathrm{M}_{\odot}$ models (G3 and G6), green lines represent $4.0\mathrm{M}_{\odot}$ models (G2 and G5), and black lines represent $3.0\mathrm{M}_{\odot}$ models (G1 and G3).

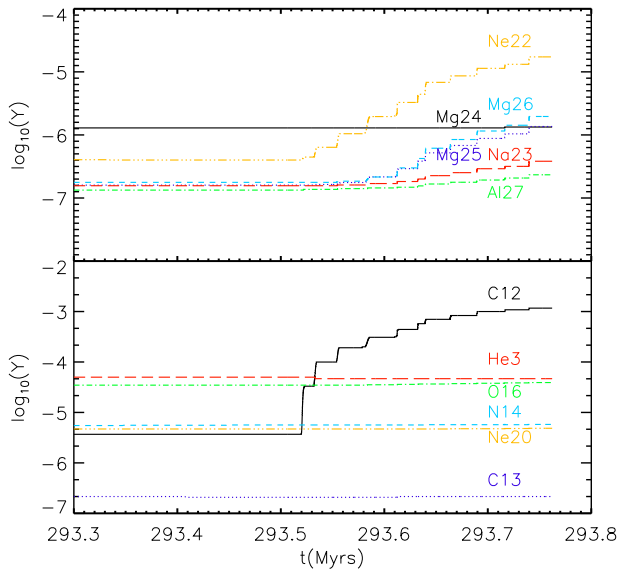

Figure 7.6: The surface abundance evolution of some of the CNO, Ne, Na, and Mg isotopes in model G1. $\mathrm{Y_i} = \mathrm{X_i}/\mathrm{A_i}$ is the number fraction.

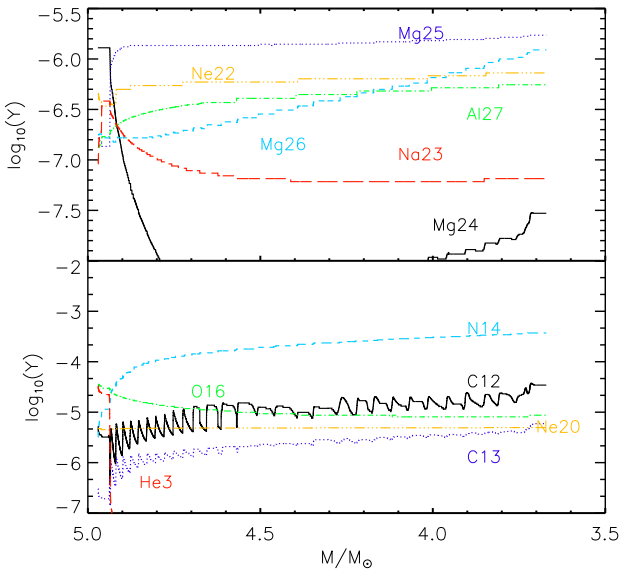

Figure 7.7: The surface abundance evolution of some of the CNO, Ne, Na, and Mg isotopes in model G3. $\mathrm{Y_i = X_i/A_i}$ is the number fraction.

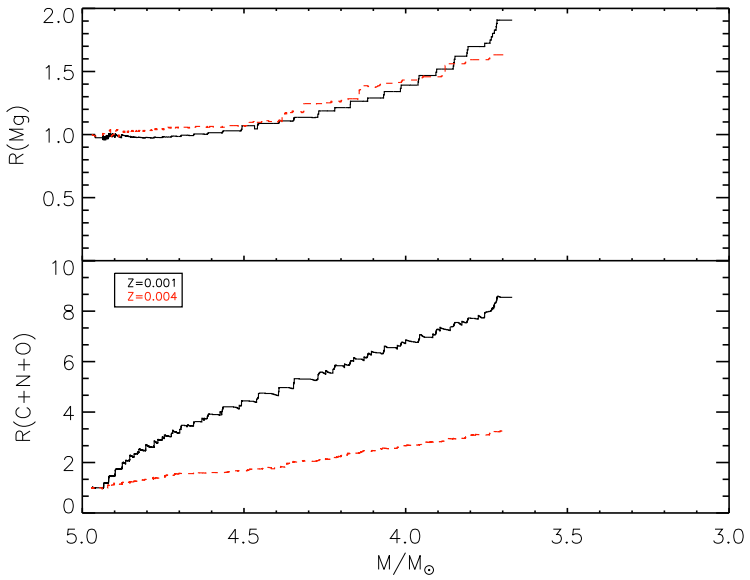

Figure 7.8: Upper Panel:The surface abundance evolution of Mg for models G3 and G6. It is shown in the y-axis the quantity $(\mathrm{X_{Mg}/X^0_{Mg}})$, where $\mathrm{X^0_{Mg}}$ is the initial Magnesium abundance. Bottom Panel: The surface abundance evolution of C+N+O for models G3 and G6. It is shown in the y-axis the quantity $(\mathrm{X_C + X_N + X_O})/(\mathrm{X^0_C + X^0_N + X^0_O})$, where $\mathrm{X^0_i}$ is the initial abundance of element i.

in agreement with previous calculations by Fenner et al. (2004).

Ventura & D'Antona (2005a) have explored the role of convection in the discrepancies between the results by different groups. They have shown that the efficiency of the convection model adopted has a strong influence on the nucleosynthesis that happens at the bottom of the convective envelope. They found that models adopting the Full Spectrum of Turbulence (FST) treatment of convection developed by Canuto & Mazzitelli (1991) achieve larger luminosities than models adopting MLT. Therefore, models adopting FST have a shorter AGB evolution. Moreover, they have found that FST models have steeper radiative temperature gradient profiles, which favors a more internal position of the inner border of the convective envelope which may overlap the CNO burning shell. This has a strong impact in the nucleosynthesis at the bottom of the convective envelope, leading to a strong depletion of oxygen and magnesium.

Our models using MLT achieve temperatures at the bottom of the convective envelope as large as those found by Ventura & D'Antona (2005a) using FST (for instance, see their Figure 2). This should lead to similar oxygen depletion in our models. Furthermore, Ventura & D'Antona (2005b) have argued that the difference in convection efficiency between their models and Fenner et al. (2004) is in the core of the increase in C+N+O observed in the models simulated by the latter. In fact, in their models using MLT, Ventura & D'Antona (2005a) have found an increase in C+N+O of 0.4-0.8 dex, depending on the value chosen for the mixing length parameter, contrary to their FST model that shows no increase in the C+N+O abundance.

Our models present similar T_{bce} as those found in models by Ventura & D'Antona (2005a) using FST, but have much stronger TDU efficiencies than their models (this can be seen in the sudden increase in ^{12}C abundance observed at each TP in our models - Figure 7.7). In order to test whether our models using MLT would also present CNO enhancement if the TDU efficiency is reduced, we have performed additional models without overshooting.

Model G7 uses the same physical inputs as our standard models (see Table 7.1), except that in this model no overshooting was included and the mass-loss rate is calculated according to Bloecker (1995) with a free parameter $\eta = 0.02$, which is the same used by Ventura & D'Antona (2005b). As it can been seen by the large decrease in the ^{12}C abundance in Figure 7.9, the absence of overshooting supress the TDU at the beginning of the AGB. ^{16}O and ^{24}Mg are depleted, while the ^{14}N and ^{25}Mg surface abundances increase. TDU sets in later on, slightly increasing ^{12}C abundance. The lack of fresh ^{12}C due to the low efficiency of TDU, leads to a smaller increase in ^{14}N abundance when compared to our standard models. While the ^{14}N abundance increases by ~ 2.0 dex in model G3, it increases by only ~ 1.0 dex in model G7.

The upper panel in Figure 7.9 shows that, contrary to our standard models, the sum of the CNO abundances does not increase. Moreover, the total magnesium abundance slightly decreases in the model without overshooting. In their calculations, Ventura & D'Antona (2005b) do not include overshooting in the inner border of the convective envelope. Thus, the main difference between their models and model G7 would be the convection model adopted and the low temperature opacities used. Model G7 indicates that the inclusion of overshooting in the inner border of the convective envelope, which determines the efficiency of TDU, plays a more important role in the final C+N+O sum and in the total Mg abundance than the convection model used.

Recent measurements of the C+N+O abundance have confirmed earlier findings that this quantity is constant in GCs (Carretta et al. 2005; Villanova et al. 2010). Observations by Yong et al. (2009) for NGC 1851, however, have shown a variable C+N+O in this cluster. Al-

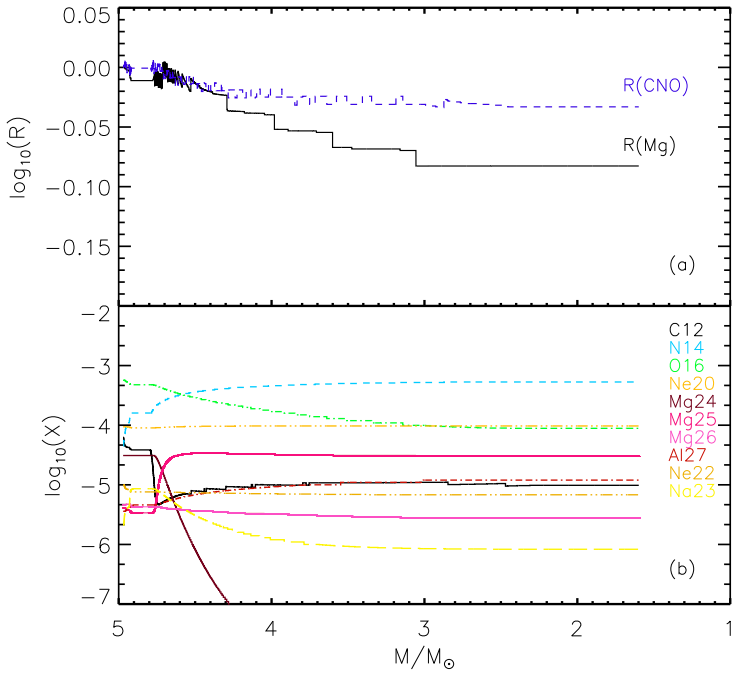

Figure 7.9: Panel (a) shows the quantity $\log_{10}(X_i/X_i^0)$ for the sum of carbon, nitrogen, and oxygen isotopes, and for the total magnesium abundance of a model not including overshooting (G7). Panel (b) shows the surface abundance evolution of CNO, Ne, Na, and Mg isotopes of the same model.

though, Villanova et al. (2010) have argued that the variable C+N+O observed in NGC 1851 is the results of the measurement of CNO abundance in mismatched AGB stars, Milone et al. (2008) have found a splitting in the SGB of this cluster which is an indication of variations in C+N+O (Cassisi et al. 2008; Ventura et al. 2009). If the variable CNO abundance is real in this cluster, our models without overshooting would not match the observations. A small amount of overshooting at the inner border of the convective envelope might be necessary.

Other physical inputs play an important role in the nucleosynthesis of massive AGB stars. Ventura & D'Antona (2005b) have explored the uncertanties in the mass-loss and in the proton capture cross-sections. In this work they have used the cross-sections of two standard compilations: NACRE and Caughlan & Fowler (1988). Regarding the heavy elements, they have found that there is little variation between the yields of most heavy elements. Sodium, on the other hand, is more efficiently produced when the NACRE reaction rate is used, since for the typical temperatures achieved at the bottom of the convective envelope, the NACRE rate of the reaction $^{22}\mathrm{Ne}(\mathrm{p},\gamma)^{23}\mathrm{Na}$ can be up to 3 orders of magnitude larger than the values given by Caughlan & Fowler (1988).

Figure 7.10 shows the rates of the reactions involved in the production and destruction of ^{23}Na by the NACRE compilation, El Eid & Champagne (1995), and Iliadis et al. (2010) (used in our models). For the reaction $^{22}\mathrm{Ne}(\mathrm{p},\gamma)^{23}\mathrm{Na}$, the old values by El Eid & Champagne (1995) can be up to 8 orders of magnitude larger than the NACRE values and 10 orders of magnitude larger than the Iliadis et al. (2010) values in the temperature range of HBB. More-

over, in this temperature range, the rates of the destruction reactions are always smaller than the production rates in the NACRE and El Eid & Champagne (1995) cases. On the other hand, for high temperatures ($0.07 \leq T_{bce}/T_9 \leq 1.1$) the rate for the reaction $^{22}Ne(p,\gamma)^{23}Na$ becomes smaller than the rates for the reactions $^{23}Na(p,\gamma)^{24}Mg$ and $^{23}Na(p,\alpha)^{20}Ne$ in the newest compilation (Iliadis et al. 2010). This could explain, for instance, the ~ 1.0 dex difference between Fenner et al. (2004) and our sodium yields for the $5.0M_\odot$ models, since they used the rate values by El Eid & Champagne (1995) and we used the newest rates by Iliadis et al. (2010).

Yong et al. (2003) have reported that ^{24}Mg is the most abundant Mg isotope in the GC NGC 6752. They have found that in the least polluted stars the Mg isotopic ratio is $^{24}Mg : {}^{25}Mg : {}^{26}Mg \sim 80 : 10 : 10$, while in those most polluted it is $^{24}Mg : {}^{25}Mg : {}^{26}Mg \sim 60 : 10 : 30$. Yong et al. (2006) have found similar Mg isotopic ratios for the GCs M13 and M71. Our predictions are in conflict with these observations, since ^{24}Mg is extremely depleted due to HBB, while ^{25}Mg is produced. Our surface isotopic ratios are $^{24}Mg : {}^{25}Mg : {}^{26}Mg \sim 1 : 57 : 42$ and $^{24}Mg : {}^{25}Mg : {}^{26}Mg \sim 1 : 91 : 8$ for models G3 and G7, respectively. These inconsistencies were also obtained by other author in the literature (e.g. Denissenkov & Herwig (2003)). D'Ercole et al. (2008) have performed hydrodynamical simulations of star formation for the second generation in GCs. They have explored in their models the possibility that the second generation (SG) stars were formed from material containing a mixing of the AGB and super-AGB[3] ejectas with the pristine matter. Using this assumption they were able to reproduce the observed helium distribution for the SG stars of NGC 2808. For this reason, Ventura et al. (2011) have argued that in the framework of a dilution model the Mg isotopic-ratios problem could be solved. The pristine matter is expected to have the ^{24}Mg abundance enhanced by 0.4 dex, while ^{25}Mg and ^{26}Mg have solar-scaled abundances. Hence, dilution between the AGB ejecta and the pristine material should result in a decrease in ^{25}Mg abundance.

One possible way to discriminate between the two polluters (AGB stars or fast-rotating massive stars) is a comparison between the lithium abundance in the first and second generation stars (D'Antona et al. 2012). AGB stars produce lithium at the beginning of the HBB, while massive stars destroy it. This difference should be reflected in the lithium abundance in the SG stars. Recent lithium abundance measurements in stars of NGC 6752 have shown that there is a correlation between lithium and oxygen (Shen et al. 2010). However, it was observed that the Li depletion is smaller than the O depletion. This means that lithium must be produced in the polluting stars. The high temperatures at the bottom of the convective envelope activate the reaction $^3He(\alpha,\gamma)^7Be$. ^7Be is then converted into ^7Li while being transported to the surface, where it survives because the temperature is too low for the occurrence of proton capture. Figure 7.11 shows the ^7Li abundance for models G1-G3 and G7. It can be observed an initial phase of lithium production, where lithium abundance reaches the maximum value of $\log\epsilon(Li) = 4.0$, that lasts until the exhaustion of ^3He in the envelope. Figure 7.11 also shows that the smaller the initial stellar mass, the slower is the decrease of the lithium abundance. Moreover, our $3.0M_\odot$ model never reaches values of $\log\epsilon(Li)$ larger than ~ 1.0 dex. Models by Ventura & D'Antona (2008) for the same metallcitiy, on the other hand, show similar maximum lithium surface abundances for all masses ($\log\epsilon(Li) \sim 4.0$). This difference is the result of the larger T_{bce} values found by Ventura & D'Antona (2008) for their

[3]Super-AGB stars are stars with masses $M \sim 7 - 11\,M_\odot$, in the TP-AGB phase, which are the progenitors of oxygen-neon white dwarfs.

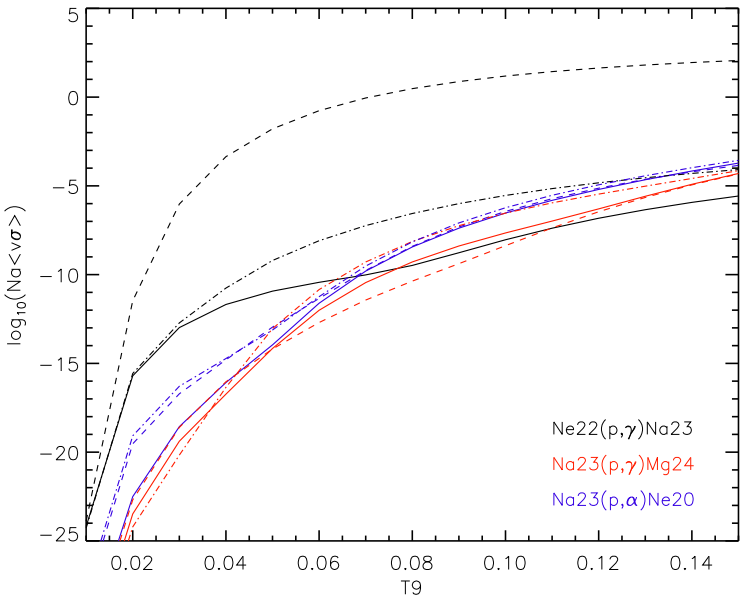

Figure 7.10: Reaction rates involved in the production and destruction of ^{23}Na. Solid lines are the rates values by Iliadis et al. (2010), dashed lines by the NACRE compilation, and dotted-dashed lines by El Eid & Champagne (1995).

3.0 $M_\odot$ models. While their 3.0 $M_\odot$ model reaches $T_{bce} > 60 \times 10^6$ K, the temperatures in our models with the same mass never exceed $\sim 40 \times 10^6$ K.

7.3.1 Yields

In order to compare our predictions with the observations it is necessary to estimate the surface abundances for the remaining TPs not simulated due to convergence problems. To evaluate the number of remaining TPs, we have assumed that the mass-loss rate is constant over the remaining interpulse periods (see Figure 7.12). Therefore, the amount of mass ejected at each interpulse period can be calculated as:

$$\Delta M = \frac{dM}{dt} * \tau_{ip}, \tag{7.1}$$

dM/dt is the mass-loss and τ_{ip} is the interpulse period. The interpulse period is assumed to be constant for the rest of the AGB evolution. We have evaluated the interpulse period, the effective temperature (T_{eff}), and the luminosity between the last two calculated TPs and kept these quantities constant. The luminosity and T_{eff} were used to estimate the mass-loss rate for the remaining TPs. Table 7.2 shows the number of remaining TPs estimated. The amount of remaining TPS given in Table 7.2 is a rough estimation and should be treated as

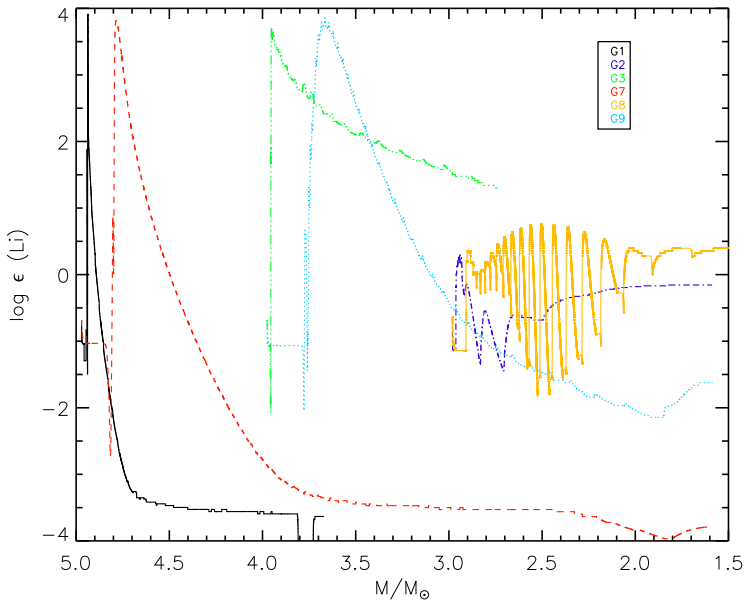

Figure 7.11: Lithium surface abundance ($\log\epsilon(\mathrm{Li}) = \log(\mathrm{N_{Li}/N_H}) + 12$) evolution for models G1-G3 and G7. The lithium-rich phase lasts while ^{3}He is not exhausted in the surface. M represents the total mass of the star as a function of time (M(t)).

an upper limit. For instance, the effective temperature is expected to decrease with each TP, which in turn should increase the mass-loss rate of the following TP.

Model	Extra TPs	λ
G1	1	0.90
G2	4	1.51
G3	17	1.21
G4	0	0.74
G5	10	1.08
G6	17	1.18
G7	3	0.11
G8	0	0.11
G9	7	0.11

Table 7.2: Number of remaining TPs.

To estimate the enrichment of the envelope from the remaining TPs, we need four pieces of information from the detailed AGB calculations: 1) the TDU efficiency (λ), 2) the composition of the intershell, 3) the composition of the envelope in the last calculated model, and 4) the mass by which the H-exhausted core grows ($\Delta\mathrm{M_H}$). λ, $\Delta\mathrm{M_H}$, and the composition of the intershell are assumed constant during the remaining TPs.

The efficiency of the TDU is defined as the ratio of the mass dredged-up by the envelope,$\Delta\mathrm{M_d}$, to the increase in the H-free core mass due to H-burning during the interpulse period, $\Delta\mathrm{M_H}$

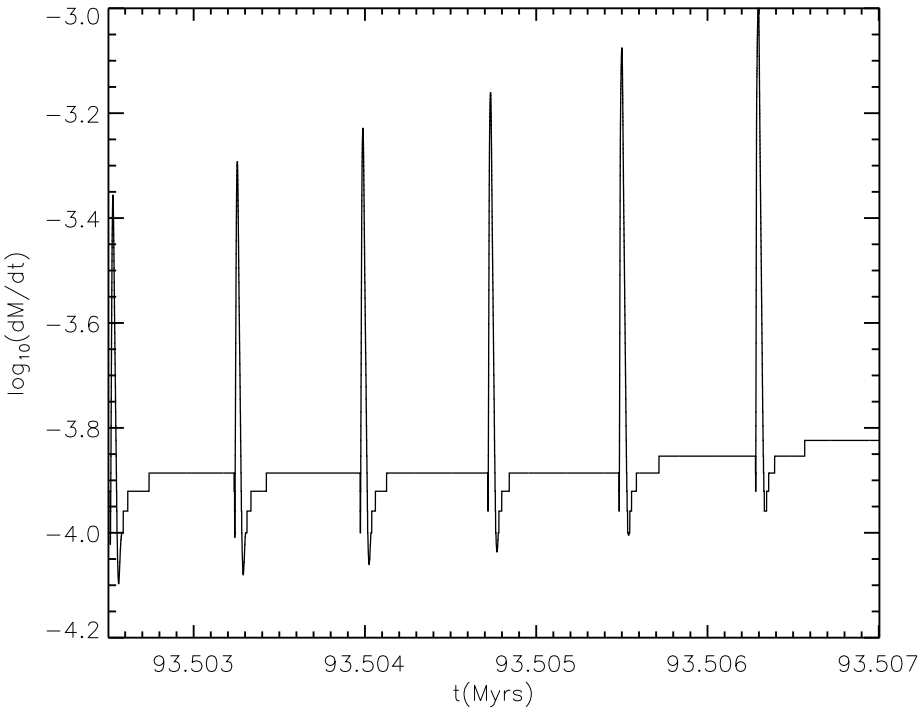

Figure 7.12: Mass-loss rate as a function of time. Zoom in at the end of model G7. It can be seen that the rate is aproximately constant over the interpulse period.

(See Figure 7.13),

$$\lambda = \frac{\Delta M_d}{\Delta M_H}, \tag{7.2}$$

The value λ depends on physical parameters such as core mass, the total mass of the star, and metallicity. Karakas (2003) have found that maximum efficiency λ_{max} increases with the initial mass up to $4.0M_\odot$, regardless of the metallcity. For higher masses it seems to be constant. This is true in our models for Z=0.001. For the higher metallicity case, the maximum efficiency is achieved by the model with mass $M = 5.0M_\odot$. Furthermore, the absence of overshooting decreases the dredge-up efficiency, as expected.

Assuming that the intershell abundances remain constant at each remaining TP, we can estimate the mass of isotope i that is mixed into the envelope at a given TDU episode:

$$\Delta M_i = X_i^{shell} \lambda \Delta M_H. \tag{7.3}$$

Therefore, the mass-fraction of isotope i at the surface for the n^{th} interpulse period is given by:

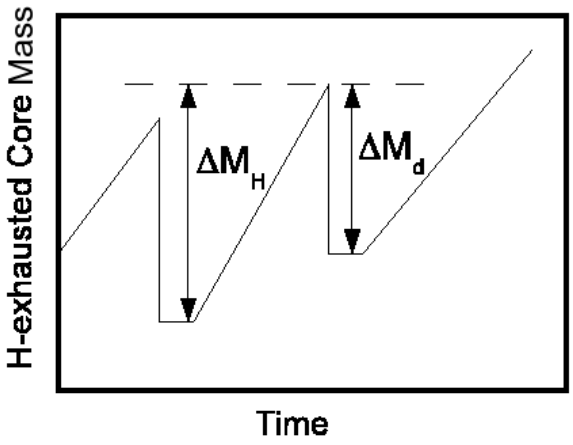

Figure 7.13: Schematic definition of the dredge-up efficiency.

$$X_i^n = \frac{(M_{env}^n - \lambda\delta M_H)X_i^{n-1} + \Delta M_i}{M_{env}^n}, \tag{7.4}$$

X_i^{n-1} is the mass-fraction of isotope i at the surface for the $(n-1)^{th}$ interpulse period and M_{env}^n is the current envelope mass.

The surface abundance estimated is an upper limit for many isotopes, since we are assuming that only TDU is happening, and that HBB is neglegible, which is not true in the high mass models ($M \geq 4.0 M_\odot$).

Figure 7.14 shows the variation in the lithium integrated abundance in the ejecta as a function of initial mass for our models and for models by (Ventura et al. 2009; Ventura & D'Antona 2010) of metallicity Z=0.001. Except for $M = 4.0\,M_\odot$, our models underproduce lithium in comparison to Ventura et al. (2009) models. However, the largest differences are found when comparing the standard models. As explained in Section 7.3, models with $3.0\,M_\odot$ achieve temperatures at the bottom of the convective envelope much smaller than those found by Ventura et al. (2009). For instance, the maximum temperature achieved in our model G8 is $T_{bce}^{max} = 35 \times 10^6$ K, while Ventura et al. (2009) found $T_{bce}^{max} = 73 \times 10^6$ K for their $3.0\,M_\odot$ model. The difference in the rate of the reaction $^3He(\alpha,\gamma)^7Be$ between these two temperatures is of about three orders of magnitude, which should explain the smaller lithium production in our $3.0\,M_\odot$ models.

For the $5.0\,M_\odot$ model, the longer lithium production phase in the model without overshooting is responsible for the discrepancies between model G3 and G7 (see Figure 7.11). The average lithium content of the ejecta is determined by the mass lost during the production phase (Ventura & D'Antona 2008). The larger the mass lost during the lithium-rich phase is, the larger is the final yield.

The final sodium abundance of the ejecta is determined by the efficiency of TDU in dredging-up ^{22}Ne from the ashes of He-burning shell, increasing ^{23}Na abundance, and by

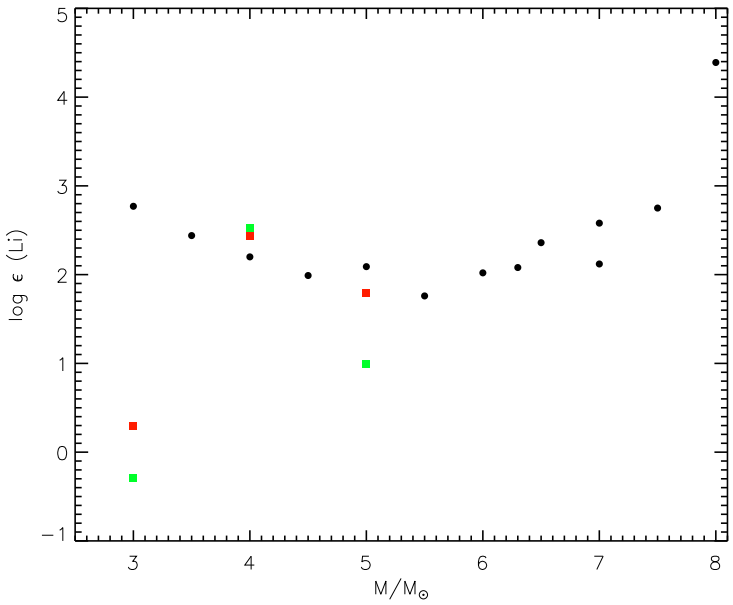

Figure 7.14: Lithium yields as a function of the initial mass. Black filled circles indicate the yields by (Ventura et al. 2009; Ventura & D'Antona 2010). Red filled squares are the results for our models without overshooting (G7-G9). Green filler squares are the yields of our standard models (G1-G3).

the HBB. If the temperature is smaller than $\sim 70 \times 10^6$ K, sodium is produced. For larger temperatures, the destruction rates are larger than the production one. The much smaller TDU efficiency found in our models without overshooting explains the ~ 0.5 dex differences between these models and the standard ones. That should also explain the difference between our yields and those by Ventura et al. (2009). For instance, in model G3, the TDU efficiency parameter reach values larger than $\lambda = 1$, while model G7 has $\lambda = 0.11$. The model with the same metallicity and mass from Ventura et al. (2009) have $\lambda = 0.5$.

In the case of oxygen, the models without overshooting are not able to dredge-up from the underlying layer fresh ^{16}O. This results in a considerable depletion of this elements due to HBB. Our models without overshooting present a stronger depletion in comparison to models by Ventura et al. (2009).

Figure 7.16 compares the observed anticorrelations for the clusters NGC6752, NGC2808, M3, M5, M13, M15, and NGC 3201 to our predicted yields. It is clear that our models including overshooting produces too much magnesium in order to match the MgAl anticorrelation. Moreover, oxygen is not sufficiently depleted to explain the low oxygen abundances found in these GCs. However, the model without overshooting seems to give more promissing results. Dilution of G7 yields with the pristine matter could help explaining the less extreme abundances.

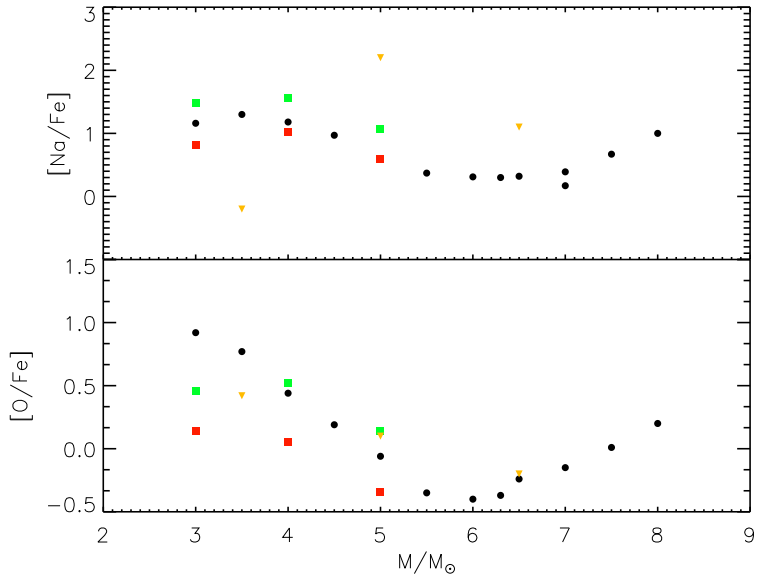

Figure 7.15: Upper Pannel: Sodium yields as a function of the initial mass. Bottom Pannel: Oxygen yields as a function of the initial mass. Black filled circles indicate the yields by (Ventura et al. 2009; Ventura & D'Antona 2010). Red filled squares are the results for our models without overshooting (G7-G9). Green filler squares are the yields of our standard models (G1-G3). Orange filled triangles indicate the yields by Fenner et al. (2004).

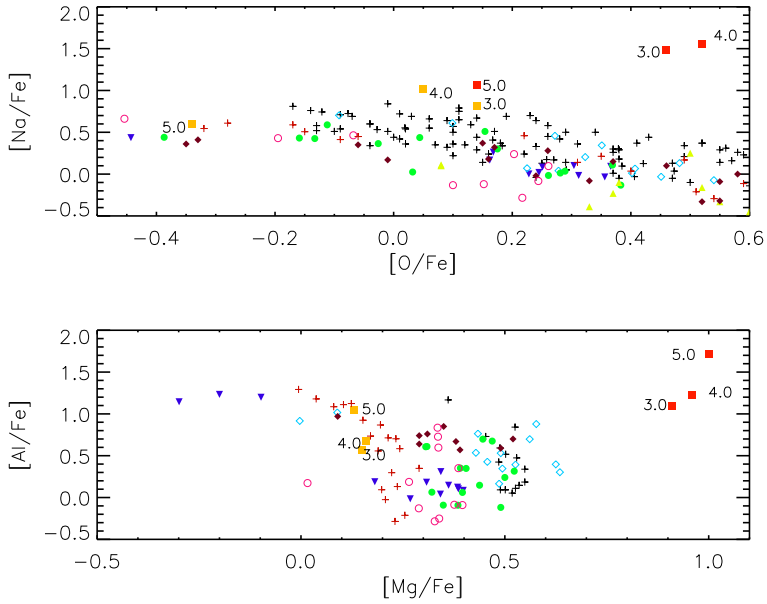

Figure 7.16: The O-Na and the Mg-Al anticorrelations in GCs: NGC6752 (black crosses - Carretta et al. 2009b, red crosses - ?), NGC2808 (inverted blue triangles - Carretta et al. 2009b), M3 (yellow triangles - Cohen & Meléndez 2005), M13 (filled diamonds - Cohen & Meléndez 2005), M5 (filled green circles - Carretta et al. 2009b), M15(open diamonds - Carretta et al. 2009b), and NGC3201(open circles - Carretta et al. 2009b). Our models including overshooting are represented by the red open squares, while the model without overshooting is represented by the orange filled square.

7.4 Conclusions

We present AGB models of intermediate-mass stars with metallicities Z=0.001 and Z=0.004. We have used in these calculations the most up to date reaction rates, specially for those reactions involved in the NeNa and MgAl chains. Our standard models uses the variable C/O low-temperature opacities and different mass-loss rates for c-rich and o-rich atmospheres. Overshooting was used in all convective boundaries in these models.

Our standard models present similar problems as earlier publications (Denissenkov & Herwig 2003; Fenner et al. 2004): a large increase in the C+N+O values and an increase in the total magnesium abundance. Our models produce much stronger sodium enhancement than the observed in GCs. However, our $5.0M_{\odot}$ models do not produce as much sodium as found by Fenner et al. (2004). This is probably due to the use of up to date reactions rates for the reaction $^{22}\mathrm{Ne}(\mathrm{p},\gamma)^{23}\mathrm{Na}$. The old values used by them, can be several orders of magnitude larger than those used in our calculations. Moreover, the new reaction rate values show that for high temperatures the sodium production reaction is smaller than its destruction reaction, which causes a decrease in the sodium abundance towards the end of the AGB evolution.

In attempt to understand the role extra mixing in the inner border of the convective envelope plays in these results, we have performed models without overshooting. This model is able to reproduce some of the observed features. In figure 7.16, it can be seen that the non-overshooting model matches the observed O-Na and Mg-Al anticorrelations much more than our standard models. The Mg istopic-ratio is quite different form the observed value. While in our models ^{25}Mg is most abundant isotope, the observations show that ^{24} is the most abundant. Recent hydrodinamical simulations of the second generation star formation, however, show that it is possible that the AGB and super-AGB ejectas are mixed with pristine material. This should solve the isotopic-ratio problem.

Concerning the question whether AGB stars are responsible for the star-to-star variations observed in GCs: they still cannot be ruled out as the possible GC polluters. Although overshooting is expected to occur, it is not clear by how far must the convective zone overshoot. The amount of overshooting should depend on the stellar parameters and it could be sufficiently small in the envelope of massive AGB stars in order to match the observations. Moreover, our results shows that the amount if extra mixing plays a more important role in the differences between our yields and those from Ventura and collaborators work than the difference in convection theory used.

Chapter 8

Summary and Conclusions

In the course of this thesis we have explored the evolution and nucleosynthesis of extremely metal-poor and zero metallicity stars. Stars with a tiny amount of metal in their composition usually suffers the, so called, proton ingestion episode. The conditions in which this phenomenon happens strongly depends on the treatment of convection and mixing. For stars with initial mass $2.0\,M_{\odot}$ our results are in good agreement with previous studies regarding the metallicity boundaries for such phenomenon. Our models with stellar mass $3.0\,M_{\odot}$ undergo PIE up to $Z = 10^{-5}$. This is very different from what has been found in the literature. In fact, for this mass, there is a large discrepancy between all the studies.

The ingestion of protons into the C-rich convective zone results in a substantial production of neutrons, and therefore, s-process elements. This neutron production was found for both low- and intermediate-mass stars in our models. Fujimoto et al. (2000) have claimed that low-mass stars, which undego PIE during the He-flash, do not produce s-process due to the short duration of the PIE. Our models, however, agree with the findings by Campbell et al. (2010) that s-process production does occur in low-mass stars. Nevertheless, the final surface enrichment resulting from this phenomenon is significant different from that found Campbell et al. (2010). The neutron superburst found in their models was not reproduced in our calculations. The nature of this superburst is rather puzzling, since the zone where it occurs is extremely rich in ^{12}C which is an important neutron poison in this condition.

In Chapter 5 we have expanded the work by Campbell et al. (2010) to more metallicities and masses. Our models have surface s-process enrichment ≥ 2.0 dex smaller than that found in this work. This leads to different conclusions concerning the two most iron-poor stars (HE1327-2623 and HE0107-5240). Whilst their model can reproduce the abundance pattern of HE1327-2623, the smaller production in our model matches the pattern of HE0107-5240. We also addressed the main uncertainty in the PIE modelling: convection. Using different overshooting parameters, we have found that the neutron exposure averaged across the convective zone is one of the key quantities determining the final s-process abundance. Moreover, the neutron density time evolution is the major difference between our model and Campbell et al. (2010). For the light elements, we have shown that some have their final abundance determined by the PIE conditions, while others (Li,N) depend strongly on the time between the splitting of the convective zone and the start of the post-PIE dredge-up.

In Chapter 6 we have performed for the first time s-process calculations for the PIE phase in EMP and zero metallicity intermediate-mass stars. We have found once again that s-

processing during the PIE depends on the duration of the proton ingestion (Δt_{PIE}). Our models present a large range of Δt_{PIE}: varying from $\sim 10^{-4}$ yrs to $\sim 7 \times 10^{-1}\, yrs$. The results do not seem to have a trend with mass, however, for the $2.0\,M_{\odot}$ models, we found that this quantity increases with metallicity. This leads to significant larger enhancements in s-process elements after the PIE in the high metallicity models (for instance, models I3 and I8 have [Ba/Fe]=0.01 and 2.15, respectively). We also explore the s-process production after the PIE. Our models have small ^{13}C pocket efficiencies leading in unexpressive neutron densities during the interpulse period. This low efficiency can be ascribed to the low metallicity of our models, since in this conditions ^{22}Ne becomes an important neutron poison ($^{22}(n,\gamma)^{23}$Ne) as was demonstrated by Bisterzo et al. (2010) for models with initial metallicity significantly higher than ours. Furthermore, our models show that the interpulse period following the TP in which PIE occurs has the most efficient ^{13}C pocket. For this reason, the bulk of the s-process is formed in these two TPs. However, further investigation into the role played by the chosen overshooting parameter in the pocket efficiency in this low metallicity regime is necessary.

We have compared the $2.0\,M_{\odot}$ models with abundances from HE1327-2623 and HE0107-5240. We found that the model with $Z = 10^{-7}$ is in better agreement with the abundance patterns observed in HE0107-5240. This agrees with the mass range for the companion star suggested by Nishimura et al. (2009) based on their parametric study of the PIE. Nonetheless, the large uncertainties in the PIE modelling do not allow low-mass stars to be dismissed as the HE0107-5240. For HE1327-2623, the $2.0M_{\odot}$ model has a better agreement than the LM case. However, we did not find the large enhancement in Sr observed in this star.

For the light elements, large discrepancies between our results and those reported by Campbell (2007) were found. The differences for most of the light elements can be ascribed to the occurrence of HBB in their models found in none of the models in our grid. Our code uses the new varying C/O opacities which play an important role in the evolution. They are important in such low metallicity environment due to the enrichment in CNO elements in the post-PIE dredge-up, enhancing the metallicity to $Z \sim 10^{-4}$ already in first TP(s). Also, we use a mass-loss prescription for C-rich stars which result in a large difference in the number of TPs compared to Campbell (2007) results.

Finally, we made use of the new extended proton-capture network in GARSTEC to address the globular cluster anomalies issue. Stars in globular clusters (GC) were believed to be part of one single population. However, detailed spectroscopic analysis have shown that large star-to-star variations are found among the stars in the cluster, suggesting that cluster are composed by more than one stellar population. High accuracy photometry backed up this idea when multiple main sequences and red giant branchs were found. The abundance variations found in GCs are usually anticorrelated: Na-O and Mg-Al anticorrelations.

One of the possible scenarios to explain these abundance patterns assumes that intermediate-mass stars from the first generation of star polluted the intracluster medium with the material that has been subjected to advanced H-burning. Evolutionary calculations for the stars in the first generation were mainly performed over the years by Ventura and collaborators. other groups have reported that their models could not reproduce the observed abundance patterns (Denissenkov & Tout 2003; Fenner et al. 2004). Moreover, they have found that magnesium was produced instead of destroyed as expected. Ventura & D'Antona (2005a) have claimed that sucess of their models in reproducing the observed anticorrelations can be ascribed to the use of more efficient convection theory. We have performed AGB calculations for stars with $3.0 \leq M/M_{\odot} \leq 5.0$ and metallicities $Z = 0.001$ and $Z = 0.004$. We found that when over-

shooting is included in the calculations our models overproduces Mg. Furthermore, the sum C+N+O that is found to be constant in many GCs is considerably altered during the evolution. Additional models without overshooting, however, have shown that it plays a major role in the final yields. The absence of overshooting supresses the TDU at the beggining of the AGB and, thus, ^{12}C can be transformed into ^{14}N, ^{16}O is also depleted, while ^{25}Mg is converted into ^{27}Al. Our yields can reproduce the overall Na-O and Mg-Al anticorrelations observed.

Bibliography

Abel, T., Bryan, G. L., & Norman, M. L. 2002, Science, 295, 93

Adelberger, E. G., Garía, A., Robertson, R., et al. 2011, RvMP, 83, 195

Alexander, D. R. & Ferguson, J. W. 1994, ApJ, 437, 879

Althaus, L. G., Serenelli, A. M., Panei, J. A., et al. 2005, A&A, 435, 631

Angulo, C., Arnould, M., Rayet, M., Descouvemont, P., & et al. 1999, Nucl. Phys. A, 653, 3

Aoki, W., Beers, T. C., Sivarani, T., et al. 2008, ApJ, 678, 1351

Aoki, W., Norris, J. E., Ryan, S. G., Beers, T. c., & Ando, H. 2002, ApJ, 567, 1166

Beers, T. C. & Christlieb, N. 2005, ARA&A, 43, 531

Beers, T. C., Preston, G., & Shectman, S. 1985, AJ, 90, 2089

Beers, T. C., Preston, G., & Shectman, S. 1992, AJ, 103, 1977

Beers, T. C., Rossi, S., Norris, J. E., Ryan, S. G., & Shefler, T. 1999, AJ, 117, 981

Bessell, M. S., Christlieb, N., & Gustafsson, B. 2004, ApJL, 612, L61

Bidelman, W. & MacConnell, D. 1973, AJ, 78, 687

Bisterzo, S., Gallino, R., Straniero, O., Cristallo, S., & Käppeler, F. 2010, MNRAS, 404, 1529

Bisterzo, S., Gallino, R., Straniero, O., Cristallo, S., & Käppeler, F. 2011, MNRAS, 418, 284

Bloecker, T. 1995, A&A, 297, 727

Bond, H. 1970, ApJS, 22, 117

Bond, H. 1980, ApJS, 44, 517

Bond, H. 1981, ApJ, 248, 606

Boothroyd, A. I., Sackmann, I. J., & Ahern, S. C. 1993, ApJ, 416, 762

Bowen, G. H. 1988, ApJ, 329, 299

Bromm, V., Coppi, P. S., & Larson, R. B. 2002, ApJ, 564, 23

Bromm, V. & Loeb, A. 2003, Nature, 425, 812

Bromm, V. & Loeb, A. 2004, New Astronomy, 9, 353

Busso, M., Gallino, R., & Wasserburg, G. J. 1999, ARAA, 37, 239

Caffau, E., Bonifacio, P., François, P., et al. 2011, Nature, 477, 67

Caffau, E., Bonifacio, P., François, P., et al. 2012, ArXiv e-prints

Campbell, S. W. 2007, Sructural and Nucleosynthetic Evolution of Metal-Poor and Metal-Free Low and Intermediate Mass Stars (Monash University, Australia)

Campbell, S. W. & Lattanzio, J. C. 2008, A&A, 490, 769

Campbell, S. W., Lugaro, M., & Karakas, A. I. 2010, A&A, 522, L6

Canuto, V. M. & Mazzitelli, I. 1991, ApJ, 370, 295

Carretta, E., Bragaglia, A., & Cacciari, C. 2004, ApJL, 610, L25

Carretta, E., Bragaglia, A., Gratton, R., D'Orazi, V., & Lucatello, S. 2009a, A&A, 508, 695

Carretta, E., Bragaglia, A., Gratton, R., & Lucatello, S. 2009b, A&A, 505, 139

Carretta, E., Bragaglia, A., Gratton, R. G., et al. 2009c, A&A, 505, 117

Carretta, E., Bragaglia, A., Gratton, R. G., Lucatello, S., & Momany, Y. 2007, A&A, 464, 927

Carretta, E., Gratton, R. G., Lucatello, S., Bragaglia, A., & Bonifacio, P. 2005, A&A, 433, 597

Cassisi, S., Castellani, V., & Tornambe, A. 1996, ApJ, 459, 298

Cassisi, S., Salaris, M., & Irwin, A. W. 2003, ApJ, 588, 862

Cassisi, S., Salaris, M., Pietrinferni, A., et al. 2008, ApJL, 672, L115

Caughlan, G. R. & Fowler, W. A. 1988, Atomic Data and Nuclear Data Tables, 40, 283

Chieffi, A., Domínguez, I., Limongi, M., & Straniero, O. 2001, ApJ, 554, 1159

Christlieb, N. 2003, RvMA, 16, 191

Christlieb, N., Green, P. J., Wisotzki, L., & Reimers, D. 2001, A&A, 375, 366

Christlieb, N., Gustafsson, B., Korn, A. J., et al. 2004, ApJ, 603, 708

Clayton, D. D. 1983, Principles of stellar evolution and nucleosynthesis, ed. Clayton, D. D.

Cohen, J. G. & Meléndez, J. 2005, AJ, 129, 303

Cristallo, S., Gallino, R., & Straniero, O. 2004, Mem. Soc. Astron. Italiana, 75, 174

Cristallo, S., Piersanti, L., Straniero, O., et al. 2009a, PASA, 26, 139

Cristallo, S., Straniero, O., Gallino, R., et al. 2009b, ApJ, 696, 797

Cristallo, S., Straniero, O., & lederer, M. T. 2007, ApJ, 667, 489

Cyburt, R., Amthot, A. M., Ferguson, R., et al. 2010, ApJS, 189, 240

Cyburt, R. H. & Davids, B. 2008, Phys. Rev. C, 78, 064614

D'Antona, F. & Caloi, V. 2004, ApJ, 611, 871

D'Antona, F., Caloi, V., Montalbán, J., Ventura, P., & Gratton, R. 2002, A&A, 395, 69

D'Antona, F., D'Ercole, A., Carini, R., Vesperini, E., & Ventura, P. 2012, ArXiv e-prints

Dantona, F. & Mazzitelli, I. 1982, A&A, 113, 303

Decressin, T., Meynet, G., Charbonnel, C., Prantzos, N., & Ekström, S. 2007, A&A, 464, 1029

Denissenkov, P. A. & Herwig, F. 2003, ApJL, 590, 99

Denissenkov, P. A. & Tout, C. A. 2003, MNRAS, 340, 722

Denissenkov, P. A. & Weiss, A. 1996, A&A, 308, 773

Denissenkov, P. A. & Weiss, A. 2001, ApJL, 559, L115

D'Ercole, A., Vesperini, E., D'Antona, F., McMillan, S. L. W., & Recchi, S. 2008, MNRAS, 391, 825

Dillmann, I., Heil, M., Plag, R., Rauscher, T., & Thielemann, F. K. 2006, AIP Conf. Ser., 819, 123

El Eid, M. F. & Champagne, A. E. 1995, ApJ, 451, 298

Fenner, Y., Campbell, S., Karakas, A. I., Lattanzio, J. C., & Gibson, B. K. 2004, MNRAS, 353, 789

Ferguson, J. W., Alexander, D. R., Allard, F., et al. 2005, ApJ, 623, 585

Forestini, M. & Charbonnel, C. 1997, A&AS, 123, 241

Frebel, A., Collet, R., Eriksson, K., Christlieb, N., & Aoki, W. 2008, ApJ, 684, 588

Freytag, B., Ludwig, H. G., & Steffen, M. 1996, A&A, 313, 497

Fujimoto, M. Y., Iben, I. J., & Hollowell, D. 1990, ApJ, 349, 580

Fujimoto, M. Y., Ikeda, Y., & Iben, Jr., I. 2000, ApJL, 529, L25

Fynbo, H. O. U., Diget, C. A., Bergmann, U. C., et al. 2005, Nature, 433, 136

Gallino, R., Arlandini, C., Busso, M., et al. 1998, ApJ, 497, 388

Gallino, R., Busso, M., Picchio, G., Raiteri, C. M., & Renzini, A. 1988, ApJ, 334, L45

Goriely, S. & Siess, L. 2001, A&A, 378, 25

Görres, J., Graff, S., Wiescher, M., et al. 1992, Nuclear Physics A, 548, 414

Gratton, R. G., Bonifacio, P., Bragaglia, A., et al. 2001, A&A, 369, 87

Gratton, R. G., Sneden, C., Carretta, E., & Bragaglia, A. 2000, A&A, 354, 169

Greif, T. H., Springel, V., White, S. D. M., et al. 2011, ApJ, 737, 75

Grevesse, N. & Sauval, A. J. 1998, SSRv, 85, 161

Grundahl, F., Briley, M., Nissen, P. E., & Feltzing, S. 2002, A&A, 385, L14

Hale, S. E., Champagne, A. E., Iliadis, C., et al. 2002, Phys. Rev. C, 65, 015801

Hale, S. E., Champagne, A. E., Iliadis, C., et al. 2004, Phys. Rev. C, 70, 045802

Heger, A. & Woosley, S. E. 2010, ApJ, 724, 341

Herwig, F. 2000, A&A, 360, 952

Herwig, F. 2001, ApJL, 554, L71

Herwig, F. 2005, ARAA, 43, 435

Herwig, F., Blöcker, T., Schönberner, D., & El Eid, M. 1997, A&A, 324, L81

Herwig, F., Pignatari, M., Woodward, P. R., et al. 2011, ApJ, 727, 89

Hollowell, D., Iben, I. J., & Fujimoto, M. Y. 1990, ApJ, 351, 245

Iben, Jr., I. & Truran, J. W. 1978, ApJ, 220, 980

Iglesias, C. A. & Rogers, F. J. 1996, ApJ, 464, 943

Iliadis, C., Longland, R., Champagne, A. E., Coc, A., & Fitzgerald, R. 2010, Nuclear Physics A, 841, 31

Itoh, N., Mitake, S., Iyetomi, H., & Ichimaru, S. 1983, ApJ, 273, 774

Ivans, I. I., Sneden, C., Kraft, R. P., et al. 1999, AJ, 118, 1273

Iwamoto, N., Kajino, T., Mathews, G. J., Fujimoto, M. Y., & Aoki, W. 2004, ApJ, 602, 377

Iwamoto, N., Umeda, H., Tominaga, N., Nomoto, K., & Maeda, K. 2005, Science, 309, 451

Jaeger, M., Kunz, R., Mayer, A., & et al. 2001, Phys. Rev. Lett., 87, 202501

Jorissen, A. & Arnould, M. 1989, å, 221, 161

Käppeler, F., Beer, H., & Wisshak, K. 1989, Rep. Prog. Phys., 52, 945

Karakas, A. I. 2003, Asymptotic Giant Branch Stars: their influence on binary systems and the interstellar medium (Monash University, Australia)

Karakas, A. I. 2010, MNRAS, 403, 1413

Karakas, A. I. & Lattanzio, J. . C. 2007, PASA, 20, 279

Karakas, A. I. & Lattanzio, J. C. 2003, PASA, 24, 103

Kippenhahn, R. & Weigert, A. 1990, Stellar Structure and Evolution, ed. Kippenhahn, R. & Weigert, A.

Kitsikis, A. 2008, Theoretical AGB and post-AGB Models for Synthetic Population Studies (Ludwig Maximilians Universitaet, Munich)

Kraft, R. P. 1994, PASP, 106, 553

Kubono, S., Abe, K., Kato, S., & et al. 2003, Phys. rev. Lett., 90, 062501

Kunz, R., Fey, M., Jaeger, M., et al. 2002, ApJ, 567, 643

Langer, N., Heger, A., Wellstein, S., & Herwig, F. 1999, A&A, 346, L37

Lau, H. H. B., Stancliffe, R. J., & Tout, C. A. 2009, MNRAS, 396, 1046

Lederer, M. T. & Aringer, B. 2008, in Evolution and Nucleosynthesis in AGB stars, ed. R. Guandalini, S. Palmerini, & M. Busso, AIP Conf.Ser., 1001, 11

Li, Z., Su, J., Guo, B., et al. 2010, Science in China G: Physics and Astronomy, 53, 658

Lucatello, S., Tsangarides, S., Beers, T. C., et al. 2005, ApJ, 625, 825

Luck, R. E. & Bond. 1991, ApJS, 77, 515

Lugaro, M. 2001, Nucleosynthesis in AGB stars (Monash University, Australia)

Lugaro, M., Herwig, F., Lattanzio, J. C., Gallino, R., & Straniero, O. 2003, ApJ, 586, 1305

Lugaro, M., Karakas, A. I., Stancliffe, R. J., & Rijs, C. 2012, ApJ, 747, 2+

Magic, Z., Serenelli, A., Weiss, A., & Chaboyer, B. 2010, ApJ, 718, 1378

Marigo, P. 2002, A&A, 387, 507

Marigo, P., Girardi, L., Chiosi, C., & Wood, P. R. 2001, A&A, 351, 152

Masseron, T., Johnson, J. A., Plez, B., et al. 2010, A&A, 509, 93

Mattsson, L., Wahlin, R., & Höfner, S. 2010, A&A, 509, 14

Mattsson, L., Wahlin, R., Höfner, S., & Eriksson, K. 2008, A&A, 484, 5

Meyer, B. S. 1994, ARAA, 32, 153

Milone, A. P., Bedin, L. R., Piotto, G., et al. 2008, ApJ, 673, 241

Moazen, B. H., Bardayan, J. C., Blackmon, K. Y., Chae, K. Y., & et al. 2007, Phys. Rev. C, 75, 065801

Munakata, H., Kohyama, Y., & Itoh, N. 1985, ApJ, 296, 197

Nishimura, T., Aikawa, M., Suda, T., & Fujimoto, M. Y. 2009, PASJ, 61, 909

O'shea, B. W. & Norman, M. L. 2007, ApJ, 654, 66

Picardi, I., Chieffi, A., Limongi, M., et al. 2004, ApJ, 609, 1035

Piotto, G. 2009, in IAU Symposium, Vol. 258, IAU Symposium, ed. E. E. Mamajek, D. R. Soderblom, & R. F. G. Wyse, 233–244

Piotto, G., Bedin, L. R., Anderson, J., et al. 2007, ApJL, 661, L53

Ramírez, S. V. & Cohen, J. G. 2002, AJ, 123, 3277

Reimers, D. 1975, Circumstellar envelopes and mass loss of red giant stars (Problems in stellar atmospheres and envelopes.), 229–256

Rogers, F. J., Swenson, F. J., & Iglesias, C. A. 1996, ApJ, 456, 902

Rossi, S., Beers, T. C., & Sneden, C. 1999, ASPC, 165, 264

Sbordone, L., Salaris, M., Weiss, A., & Cassisi, S. 2011, A&A, 534, A9

Schaller, G., Schaerer, D., Meynet, G., & Maeder, A. 1992, A&A, 96, 269

Schlattl, H., Cassisi, S., Salaris, M., & Weiss, A. 2001, ApJ, 559, 1082

Schlattl, H., Salaris, M., Cassisi, S., & Weiss, A. 2002, A&A, 395, 77

Schneider, R., Ferrara, A., Salvaterra, R., Omukai, K., & Bromm, V. 2003, Nature, 422, 869

Schöier, F. L. & Olofsson, H. 2001, A&AS, 368, 969

Seeger, P. A., Fowler, W. A., & Clayton, D. D. 1965, ApJS, 11, 121

Serenelli, A. 2006, Nucleosynthesis in Low Mass Very Metal Poor AGB Stars, ed. S. Randich & L. Pasquini, 322

Shen, Z.-X., Bonifacio, P., Pasquini, L., & Zaggia, S. 2010, A&A, 524, L2

Siess, L., Livio, M., & Lattanzio, J. 2002, ApJ, 570, 329

Spite, F. & Spite, M. 1982, A&A, 115, 357

Stacy, A., Greif, T. H., & Bromm, V. 2010, MNRAS, 403, 45

Stacy, A., Greif, T. H., & Bromm, V. 2012, MNRAS, 422, 290

Stancliffe, R. J., Dearborn, D. S. P., Lattanzio, J. C., Heap, S. A., & Campbell, S. W. 2011, ApJ, 742, 121

Straniero, O., Chieffi, A., Limongi, M., et al. 1997, ApJ, 478, 332

Straniero, O., Gallino, R., Busso, M., et al. 1995, ApJ Lett., 440, 85

Suda, T., Aikawa, M., Machida, M. N., Fujimoto, M. Y., & Iben, J. I. 2004, ApJ, 611, 476

Suda, T. & Fujimoto, M. Y. 2010, MNRAS, 405, 177

Suda, T., Fujimoto, M. Y., & Itoh, N. 2007, ApJ, 667, 1206

Suda, T., Katsuta, Y., Yamada, S., et al. 2008, PASJ, 60, 1159

Suda, T., Yamada, S., Katsuta, Y., et al. 2011, MNRAS, 412, 843

Sugimoto, D. & Fujimoto, M. Y. 1978, PASJ, 30, 467

Takahashi, K. & Yokoi, K. 1987, At. Data Nucl. Data Tables, 36, 375

Tomkin, J., Lamnert, D. L., Edvardsson, B., Gustafsson, B., & Nissen, P. E. 1989, A&A, 219, L15

van Loon, J. T., Cioni, M. R. L., Zijlstra, A. A., & Loup, C. 2005, A&A, 438, 273

Vassiliadis, E. & Wood, P. R. 1993, ApJ, 413, 641

Ventura, P., Caloi, V., D'Antona, F., et al. 2009, MNRAS, 399, 934

Ventura, P., Carini, R., & D'Antona, F. 2011, MNRAS, 415, 3865

Ventura, P. & D'Antona, F. 2005a, A&A, 431, 279

Ventura, P. & D'Antona, F. 2005b, A&A, 439, 1075

Ventura, P. & D'Antona, F. 2008, A&A, 479, 805

Ventura, P. & D'Antona, F. 2010, MNRAS, 402, L72

Ventura, P., D'Antona, F., & Mazzitelli, I. 2002, A&A, 393, 215

Ventura, P., D'Antona, F., Mazzitelli, I., & Gratton, R. 2001, ApJL, 550, L65

Villanova, S., Geisler, D., & Piotto, G. 2010, ApJL, 722, L18

Wachter, A., Schröder, K. P., Winters, J. M., Arndt, T. U., & Sedlmayr, E. 2002, A&A, 384, 452

Wachter, A., Winters, J. M., Schröder, K. P., & Sedlmayr, E. 2008, A&A, 486, 497

Weiss, A., Cassisi, S., Schlattl, H., & Salaris, M. 2000, A&A, 533, 413

Weiss, A. & Ferguson, J. W. 2009, A&A, 508, 1343

Weiss, A. & Schlattl, H. 2008, Ap&SS, 623, 99

Weiss, A., Schlattl, H., Salaris, M., & Cassisi, S. 2004, A&A, 422, 217

Whitelock, P. A., Feast, M. W., van Loon, J. T., & Zijlstra, A. A. 2003, MNRAS, 342, 86

Willson, L. A. 2000, ARA&A, 38, 573

Winters, J. M., Le Bertre, T., Jeong, K., Nyman, L.-A., & Epchtein, N. 2003, A&A, 409, 715

Yong, D., Aoki, W., & Lambert, D. L. 2006, ApJ, 638, 1018

Yong, D., Grundahl, F., D'Antona, F., et al. 2009, ApJL, 695, L62

Yong, D., Grundahl, F., Lambert, D. L., Nissen, P. E., & Shetrone, M. D. 2003, A&A, 402, 985

Yoshida, N., Omukai, K., & Hernquist, L. 2008, Science, 321, 669

Acknowledgments

This work was only possible due to the scientific and moral support from many people.

First. I would like to thank Achim for the opportunity to come to Germany, to MPA and learn so much. I would like also to thank the MPA directors, the Max-Plack society, and the IMPRS school for the finantial support and the opportunity to grow as a scientist.

I cannot describe how grateful I am to Aldo Serenelli, not only for the scientific support, but also for understanding my difficult moments during the course of this work.

I will be eternally grateful to Silvia Rossi for being so kind and finding a working space for me to finish this thesis. *Gostaria de agradecer o carinho e suporte quase materno que senhora me dedicou todos esses anos.*

I am pleased to thank the kind and efficient secretaries: Maria Depner, Gabi Kratschmann, and Cornelia Rickl. You were always helpful, kind, and cheerful. Thanks!

I would like to thank my parents (Dorival and Ednalda), and my brothers, Murilo and Nícolas, for the love, support and understanding; *Ao meu painho e a minha mainha (Dorival e Ednalda) e aos meus irmãos, Murilo e Nícolas, pelo amor, carinho e compreensão*;

my fiancèe, Nelson, for the love and patience to wait for me all these years, even with an ocean between us =D. For believing in me, even when I didn't do it myself; *meu noivo, Nelson, por todo amor a mim dispensado. Por ser meu maior companheiro, em todos os momentos. Por aguentar meu gênio retado e me fazer rir de qualquer bestage*;

my friends Ania Raiter - for all the time we spent together dancing, talking nonsense, laughing, eating sweets and the support in the moments of great need, Rodrigo Vieira *pelas conversas no skype e e-mails divertidos que sempre trocamos e que me fazem rir. Pelo suporte e carinho em 10 anos de amizade.*, and Nop Wongwathanarat - for all the great moments inside and outside MPA. For being a great supportive friend. Laura Porter - always providing me with chocolate, good books and series, and with nice words =D, for reading this thesis and helping me to improve it, Martin Henze - for all the good moments on the dance floor (bailando salsa!), for all the nice (or nonsense) movies we have watched together =D, Paula Jofré - for the support in difficult moments, for reading this thesis, and for the friendship. *Gostaria de agradecer pelo carinho e companheirismo nesses anos.* Stephan Hachinger - for being such a nice and good person. Alan Alves Brito - pelas palavras de incentivo e as danças maravilhosas =D.

Marcianita, Marcionildo, Pam, and all the good friends that I have met over the years that, even being so far away, found a way to make my life more cheerful. Um muito obrigado

também ao Rodolfo que foi, juntamente com a Ania, um anjo me abrigando na casa deles.

" ... Somos muitos Severinos iguais em tudo na vida: na mesma cabeça grande que a custo é que se equilibra, no mesmo ventre crescido sobre as mesmas pernas finas e iguais também porque o sangue, que usamos tem pouca tinta.

... Somos muitos Severinos iguais em tudo e na sina: a de abrandar estas pedras suando-se muito em cima, a de tentar despertar terra sempre mais extinta,

a de querer arrancar alguns roçado da cinza. Mas, para que me conheçam melhor Vossas Senhorias e melhor possam seguir a história de minha vida, passo a ser o Severino que em vossa presença emigra."

João Cabral de Melo Neto em *Morte e Vida Severina*